CONTROL OF NEAR-WALL COHERENT STRUCTURES IN A TURBULENT BOUNDARY LAYER USING SYNTHETIC JETS

A THESIS SUBMITTED TO THE UNIVERSITY OF MANCHESTER
FOR THE DEGREE OF DOCTOR OF PHILOSOPHY
IN THE FACULTY OF ENGINEERING AND PHYSICAL SCIENCES

2016

By
Emanuele Spinosa
School of Mechanical, Aerospace and Civil Engineering

Contents

List of Tables

List of Figures

Abstract

The University of Manchester

Emanuele Spinosa

Ph.D. in Aerospace Engineering

Thesis Title: ***Control of Near-Wall Coherent Structures in a Turbulent Boundary Layer Using Synthetic Jets***

October 11, 2016

The increase in CO_2 emissions due to the significant growth of the level of air traffic expected in the next 40 years can be tackled with new technologies able to reduce the skin friction drag of the new generation aircraft. The ACARE (Advisory Council for Aeronautical Research in Europe), within the Flightpath 2050 Vision, has established stringent targets for drag reduction, which can be achieved only with innovative flow control methods.

Synthetic jets are a promising method of flow control, especially for their ability to control the flow without the need of a bleed air supply. The application of synthetic jets for flow separation control has been already proven [165, 166, 171]. Their application can also be extended to skin friction drag reduction in a turbulent flow. Indeed, most of turbulence production in a turbulent boundary layer is related to the dynamics of streamwise streaks and vortices in the near-wall region. Synthetic jets can be used to weaken these structures, to reduce turbulence production and consequently skin friction drag. The effectiveness of synthetic jets for skin friction drag reduction in a turbulent boundary layer has already been explored in a few works [94, 119, 92, 84]. However, there is a lack of understanding on the physical mechanism by which this effect is achieved. The aim of this work is to provide further insight on this.

A series of experimental investigations are carried out, using three main measurement techniques: Particle Image Velocimetry, Liquid Crystal Thermography and Constant Temperature Anemometry. The effectiveness of a single round synthetic jet in controlling near-wall streamwise streaks and vortices in a laminar environment, in particular those that develop downstream of a circular cylinder, is verified. Turbulent boundary layer forcing is attempted using a synthetic jet array that produces coherent structures of the same scale as the streamwise vortices and streaks of a turbulent boundary layer. The synthetic jet array is able to create regions of lower velocity in the near-wall and of lower skin friction. A possible physical mechanism behind this has been proposed. With a few minor modification, it is believed that the performance of the synthetic jet array could be significantly improved. This can be achieved especially if the array is installed in a feed-forward control unit, which is only briefly explored in this work. In this case the information on the flow field gathered real-time with wall sensors can help to consistently improve the synthetic jet array performance in terms of skin friction drag reduction.

Declaration

No portion of the work referred to in this thesis has been submitted in support of an application for another degree or qualification of this or any other university or other institute of learning.

Copyright

Acknowledgements

I would like to thank my supervisor, Dr. Shan Zhong, for her constant help and advice during these years.
My project has been funded by the University of Manchester and by Airbus Group Innovations UK (AGI-UK). I would like to thank Dr. Stephen Rolston, head of the Aeromechanics division at AGI-UK, for his support and for encouraging my participation in a number of interesting meetings in the UK and abroad regarding the fascinating and challenging research field of flow control and drag reduction.

I have to thank particularly two experimental officers, who really helped during these years: Dr. Shanying Zhang and Dr. Andrew Kennaugh. My experimental work would have been much harder without their guidance and assistance.
A special thanks also to Martin Hyde an Amine Koched, working with TSI©, for their valuable suggestions about my PIV experiments.
I would like to thank a few technicians: Mike Carroll, Phil Oakes, Dave Golding and especially Eddie Whitehouse, who has always been very kind with me and helpful.
During my Ph.D. I also had the pleasure and the honour of working as a teaching assistant for the experimental Fluids laboratory held by Professor Brian Launder and Dr. Tim Craft. I would like to thank Professor Launder for making some time to discuss some aspects of my research with me. Thanks also to Dr. Craft and for our valuable conversations about a few theoretical questions related to my project.

During these years in Manchester I have made many friends, with whom I have spent a wonderful time. Sometimes they made me even forget the lack of sun in the sky and the absence of a proper espresso coffee. I cannot mention them all, but I cannot avoid naming some of them. Thanks to my dear friends and colleagues Fernando and Pablo. Thanks also to my colleagues Adam, Fay, Nick, Mariam, Dean and Umair. Thanks to my flatmates Tommaso, Claudio and the twins Enrico and Alessandro. Thanks to my

friends Daniele Teresi, Alessandro, Isabella, Marialaura, Francesca, Giovanni, Flavia, Cintia and Yasaman.

Grazie alla mia famiglia, a mia madre Rosanna, a mio padre Enrico e a mia sorella Letizia, che mi hanno sempre supportato in questi lunghi anni e nei momenti di difficoltà ed incertezza che fare un Dottorato all'estero comporta. Sono convinto che questi sacrifici saranno ripagati e spero di avere dimostrato soprattutto a voi che con la perseveranza e la determinazione si possono raggiungere sempre nuovi traguardi.

List of Acronyms and Symbols

Main Acronyms

Acronym	Description
BL	Boundary Layer
LBL	Laminar Boundary Layer
TBL	Turbulent Boundary Layer
ZPG	Zero Pressure Gradient
SJ	Synthetic Jet
SJA	Synthetic Jet Actuator
PIV	Particle Image Velocimetry
LCT	Liquid Crystal Thermography
LC	Liquid Crystals
CTA	Constant Temperature Anemometry
DNS	Direct Numerical Simulation
LES	Large Eddy Simulation
RMS	Root Mean Square
CCD	Charged Coupled Device
RGB	Red Green Blue
HSV	Hue Saturation Value
DR	Drag Reduction
LMS	Least Mean Squares
SISO	Single Input Single Output
MISO	Multiple Input Single Output
MIMO	Multiple Input Multiple Output

Main Symbols

Symbol	Units	Description
$\vec{v}$	$\mathrm{m/s}$	velocity vector
x, y, z	m	streamwise, wall-normal, spanwise spatial coordinate
u, v, w	$\mathrm{m/s}$	streamwise, wall-normal, spanwise velocity component
t	s	time variable
p	Pa	pressure
ρ	$\mathrm{Kg/m^3}$	density
μ	$\mathrm{Kg/(m\,s)}$	dynamic viscosity
ν	$\mathrm{m^2/s}$	kinematic viscosity
u_∞	$\mathrm{m/s}$	freestream velocity
T_∞	K	freestream temperature
T_W	K	wall temperature
τ_W	$\mathrm{N/m^2}$	wall shear stress
D	N	drag force
C_{fx}	–	skin friction coefficient
δ	m	boundary layer thickness
δ^*	m	BL displacement thickness
θ	m	BL momentum thickness
u_τ	$\mathrm{m/s}$	friction velocity
L_τ	m	viscous length
T_τ	s	viscous time
f_τ	Hz	viscous frequency
q^+	–	general variable scaled in wall units
T_b	s	bursting period
f_b	Hz	bursting frequency
D_0	m	SJA orifice diameter
h	m	SJA orifice neck height
D_c	m	circular SJA cavity diameter
H	m	SJA cavity height
f	Hz	SJA oscillation frequency
Δ	m	SJA oscillation amplitude
T	s	SJA oscillation period
L_0	m	SJ stroke length

L	–	SJ dimensionless stroke length
$\overline{U_0}$	–	averaged (synthetic) jet velocity during the blowing stroke
VR	–	jet-to-freestream velocity ratio
St	–	Strouhal number
S	–	Stokes number
Re_q	–	Reynolds number based on q
M	m/pixels	(image) magnification factor
Δt	s	PIV time separation
$\vec{r}$	pixel	PIV pixel displacement
$\bar{q}$	[q] units	time or ensemble averaged quantity
q'	[q] units	fluctuating component of q
$< q >$	[q] units	phase-locked average of q
$\tilde{q}$	[q] units	periodic component of q i.e. $< q > -\bar{q}$

Chapter 1

Introduction

1.1 Skin Friction Drag Reduction in Aeronautics

The level of air traffic is expected to significantly grow within the next 40 years, in response to the increasing demand for reasonably fast point-to-point connections, which only aviation is able to guarantee. In Europe alone the number of commercial flights is expected to rise up to 25 million in 2050, compared to 9.4 million in 2011 [34]. This factor, combined with increasing fuel prices and the need for proper environmental protection, poses major challenges to the aircraft manufacturing industry. The Advisory Council for Aeronautical Research in Europe (ACARE), within the Flightpath 2050 Vision, has therefore set a number of targets that need to be pursued by the new generation of aircraft. In 2050 the new technologies and procedures available must allow a reduction of CO_2 emission by 75% per passenger kilometre and a 90% reduction of NO_x emissions compared to the levels in 2000 [34]. In addition, the perceived sound noise emission of commercial aircraft has to be reduced by 65%. In order to achieve these objectives, an extensive program of Research and Development has been started in industry and in academia.

In particular drag reduction methods have received considerable attention in the last decades, as they provide a means for an aircraft to require less engine power at the same speed and altitude, giving rise to improved aircraft efficiency and to a reduction of fuel burn rates up to 50% [8]. The current technology of airframe design, wings and fuselage, has reached a technological saturation, so only with the introduction of innovative flow control methods it is possible to achieve a further drag reduction and an improved aircraft performance.

In the context of civil and commercial transport aircraft, skin friction drag and lift-induced drag represent the two main sources of drag, approximately 50% and 30% of the total drag at cruise conditions respectively. Since cruise conditions are maintained for the longest percentage of time (more than 90%) of a flight mission, a small reduction in skin friction drag (even a few percent) eventually produces large gains. Flow control methods aiming to reduce skin friction drag have broadly progressed in two directions: laminar flow control (LFC) and turbulent drag reduction (TDR). Extensive reviews on the historical developments of these methods can be found in [45, 24, 121]. Laminar flow control is based on the development of technologies to delay or suppress the boundary layer laminar-turbulent transition. Since skin friction drag is higher in turbulent flows (compared to laminar ones at the same free-stream velocity) and a turbulent boundary layer covers great portion of the aircraft wing and fuselage surfaces, maintaining the boundary layer laminar results in an overall significant skin friction drag reduction. However, in typical flight conditions, in which the Reynolds number is very high, laminar flow control can hardly be applied. Even exploiting very promising recent advancements, with the current technology only a limited portion of the total surface of wings and fuselage can be provided with an effective Laminar Flow Control system. For this reason, turbulent drag reduction strategies, which aim to mitigate of skin friction drag in a turbulent flow, have aroused the interest of academia and industry. The development of efficient turbulent drag reduction strategies is also very challenging. In a turbulent boundary layer (TBL), most of the turbulence production occurs in the near-wall region and is mainly related to large scale streamwise structures that naturally form and reside there. These structures are streamwise streaks of local lower and higher velocity, which are observable in the vicinity of the wall, and streamwise vortices, which are believed to induce the streaks and are located just above them. It is believed that the dynamics of the streamwise streaks and vortices are responsible for most of turbulence production within the boundary layer. The streaks are indeed observed to destabilise and burst into structures of much smaller size. This bursting process contributes significantly to the production of the turbulent velocity fluctuations, which lead to an increased velocity gradient near the wall compared to a laminar boundary layer and hence to a higher skin friction drag. Therefore, a flow control method able to weaken/disperse these structures will probably effectively achieve a reduction of turbulence production and ultimately a skin friction drag mitigation.

1.2 Turbulent Drag Reduction Methods

As stated above, only with the introduction of innovative flow control methods it is possible to achieve the objective of skin friction drag reduction in a turbulent boundary layer. According to Gad-el-Hak [45] flow control is any mechanism or process through which a fluid flow is caused to behave differently than it normally would do in the absence of it. Gad el Hak proposed a classification of the flow control strategies, based on energy expenditure and the control loop involved [43]. In passive strategies no auxiliary energy is added to the flow field. In active strategies energy is added to the flow field by means of flow actuators. Active control strategies can be further divided into predetermined control and reactive control strategies. In predetermined control, also simply referred to as forcing, the actuators input steady or unsteady energy into the flow without regard to the particular state of the flow itself. Following again Gad-el-Hak definition [43], in reactive control the operating conditions of the actuators are continuously adjusted based on measurements of some kind. Reactive control can be achieved by a feed-forward strategy (or open-loop) or by a feedback strategy (or closed loop). In feed-forward control the control variables and the measured variables may differ and are typical at different locations in the flow field. On the other hand, in feed-back control the control variable and the measured variable are the same and are measured at the same point. The control system is automatically regulated to produce flow control effects on that flow variable at that exact location.

Examples of passive flow control strategies that yield turbulent drag reduction are riblets [47] or superhydrophobic surfaces [127, 50]. These two strategies aim to suppress the turbulent production in the near-wall region by inhibiting the normal behaviour of the near-wall coherent structures. Also large eddy break up (LEBU) devices have been extensively used, in this case to mitigate the turbulence production related to the coherent structures in the outer part of the boundary layer [7]. Passive strategies are simple to design and require minor technological development, however they cannot be switched off and therefore might cause a decrease in the aerodynamic performance at off-design conditions.

Active strategies are believed to be advantageous because they can offer on-demand control and can be optimised to provide higher drag reduction effects.
An early example of an active control strategy is the application of suction and blowing at the wall. Uniform blowing and suction at the wall from a spanwise oriented slot was

first tested by Park and Choi [108] using direct numerical simulations. With uniform blowing the streamwise vortices in the near-wall region are lifted up, and thus their interaction with the streamwise streaks is weakened. This ultimately leads to a skin friction drag reduction. The application of periodical suction and blowing at the wall also produces skin friction drag reduction, as reported in Park, Lee and Sung [109], Park and Sung [110] and Tardu [149]. The periodic generation of spanwise vortices creates regions of reverse flow in the near-wall region, which decrease the velocity gradient at the wall. Gad-el-Hak and Blackwelder [44] and more recently Kerho [77] used selective suction and blowing at the wall to target and suppress the streamwise streaks directly. In all cases of suction/blowing, a skin friction drag reduction up to 40% could be achieved and the power saved was observed to be much higher than the ideal fluid power input. The main disadvantage of such method however is the need of a source of compressed air.

In recent years significant levels of drag reduction with spanwise oscillating walls have been demonstrated in direct numerical simulations [73, 113]. The spanwise wall motion modifies the interaction between the streamwise vortices and the streamwise streaks, breaking up the mechanism of turbulence production. The technique is able to provide a skin friction drag reduction up to 40%. The drag reduction was also confirmed experimentally by Laadhari et al [88], K.S. Choi et al [31] and Ricco et al [125, 122]. However its application in flight conditions does not seem viable given the high frequency oscillations needed and the difficulty in implementing the technology for example on an aircraft wing.

Similar solutions using spinning or oscillating discs at the wall were tested with direct numerical simulations by Ricco et. al [123, 161]. Also the imposition of spanwise and streamwise travelling velocity waves seems effective in turbulence drag reduction [37, 115].

1.3 Synthetic Jets and Their Application for Skin Friction Drag Reduction

A synthetic jet is a stream of fluid into a flow system, which does not require the need of an external fluid (air/water) supply but is produced entirely from the flow system it is deployed in. Given that, a synthetic jet is able to transfer linear momentum to the flow system without net mass injection across the flow boundary [49]. Typically the jet is synthetised by continuous alternate oscillations of a diaphragm within a cavity

that communicates with the flow system through a small orifice. Figure 1.3 shows the typical geometry of a synthetic jet actuator. The diaphragm can be set in motion

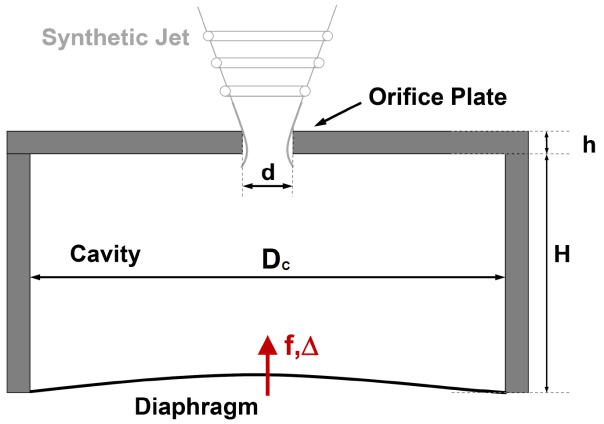

Figure 1.1: Schematic of a synthetic jet actuator

by a magnetic shaker or by a similar device. The interest in synthetic jets aroused from the fact that they are produced without the need of a fluid supply, which makes their implementation for flow control much easier, avoiding complex piping and fluidic packaging. In addition, synthetic jets also guarantee on-demand control and low energy consumption compared with the energy saving they can produce. Referring to Figure 1.3, during a single oscillation when the diaphragm shed out of the cavity. In this phase usually the flow separates and a free shear layer is formed at the location of the orifice. If the jet is sufficiently strong, the free shear layer tends to roll up and form a coherent vortical structure, which propagates away from the orifice.

The interaction of synthetic jets with a boundary layer produces a train of coherent structures (hairpin vortices, vortex rings etc.). The types of coherent structures produced depends on the synthetic jet operating conditions, in particularly on the amplitude and frequency of oscillation of the diaphragm, and on the properties of the boundary layer into which the jet is issued. Extensive studies have been carried out at the University of Manchester to determine the operating conditions at which the different types of coherent structures are produced [170, 66]. It has been observed that in certain operating conditions these structures are able to redistribute momentum inside the boundary layer, bringing low momentum fluid upwards and high momentum fluids downwards. In doing so, the boundary layer is energised and is found more resistant to withstand adverse pressure gradient, giving rise to a delay of flow separation. The

application of synthetic jets for flow separation control has been extensively studied also at the University of Manchester for several years [173, 165].

Since synthetic jets, in some specific operating conditions, produce coherent structures that are essentially elongated in the the streamwise direction, it is believed that these structures may interact with the streamwise streaks and vortices in the turbulent boundary layer and they may suppress or at least weaken their formation, yielding a local skin friction drag reduction. However, the application of synthetic jets for skin friction drag reduction in turbulent boundary layers has not yet been systematically explored.

The effect of small scale forcing on a turbulent boundary layer was experimentally investigated by Lorkowski et al [94], using a single synthetic jet actuator, with an orifice slot oriented in the streamwise variation. While the convection velocity of the near-wall coherent structures was not influenced by the forcing, an increase of their inclination angle was observed, which could be followed by a reduction in wall shear stress: this reduction was not tested in this work.

Direct numerical simulations on the forcing effect exerted by an array of synthetic jets in a turbulent boundary layer were carried out by Lee and Goldstein [92]. The array is composed of four slot orifices oriented in the streamwise direction, in which each pair of adjacent slots functioned as a single unit powered by a common diaphragm. Even if no skin friction drag reduction was observed, this study has given valuable insight on the performance of a synthetic jet array in a turbulent boundary layer and on the possibility of influencing the events related to specific near-wall coherent structures.

Rathnasingham and Breuer [119, 118] attempted turbulent boundary layer control using an array of three synthetic jets, similar to that used by Lorkowski [94]. They also used an array of three wall-shear stress sensors and developed a linear feed-forward control strategy. They showed a reduction of streamwise velocity fluctuations of 30%, a reduction of wall pressure fluctuations of 15% and a net reduction of wall shear stress of 7%. The authors stressed however that this is just a crude estimation of wall-shear stress reduction, as the evaluations were based on the slope of the velocity profile in the near-wall region and not on a direct measurement of the wall-shear stress.

Even if these preliminary studies have shown the capability of synthetic jets to control the near-wall coherent structures in a turbulent boundary layer, there is a lack of understanding on how the near-wall coherent structures are modified and the physical mechanism by which the turbulence production process is inhibited. The motivation

of the present project is to gather this information through experimental activities.

1.4 Research Methodology

1.4.1 Development of a TBL Control System using Synthetic Jets

The first logical step towards the development of a turbulent boundary layer control system using synthetic jets is the evaluation of their capability to control artificially-created streamwise streaks and vortices in a laminar environment. A way to create these streaks and vortices is to mount a circular cylinder vertically across a laminar boundary layer, as shown in Figure 1.2. The cylinder produces two counter-rotating

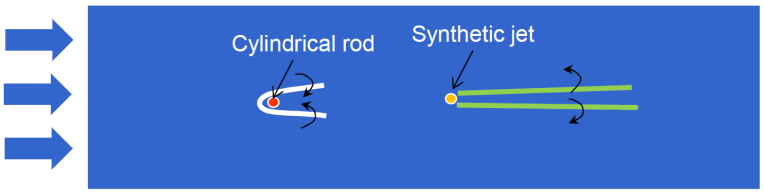

Figure 1.2: Control of streamwise vortices and streaks in a laminar boundary layer with a synthetic jet

streamwise vortices downstream in the near-wall region. A synthetic jet can be placed in the same flow, aligned with the cylinder in the streamwise direction and its capacity to control the vortices downstream of the cylinder can be evaluated. The application of flow actuators similar to a synthetic jet (a cantilever beam actuator) to study this type of flow control problem is reported in Jacobson and Reynolds [67].

As a successive step, the more general case of a turbulent boundary layer can be examined. As the coherent structures in a turbulent boundary layer are distributed in space, typically a control system adopting a synthetic jet array is believed to be more effective. Synthetic jets can be employed in different types of control strategies, of increasing complexity, from predetermined control to feed-forward and feed-back control. Examples of predetermined, feed-forward and feed-back control strategies of a turbulent boundary layer are shown in Figure 1.3. A predetermined control system only consists of a synthetic jet array. The flow is forced by the actuators, but no sensors are installed in the flow. The operating conditions of the synthetic jets are chosen based on knowledge of the flow physics and by trial and error adjustments. In reactive control the information gathered from flow sensors is used to automatically optimise

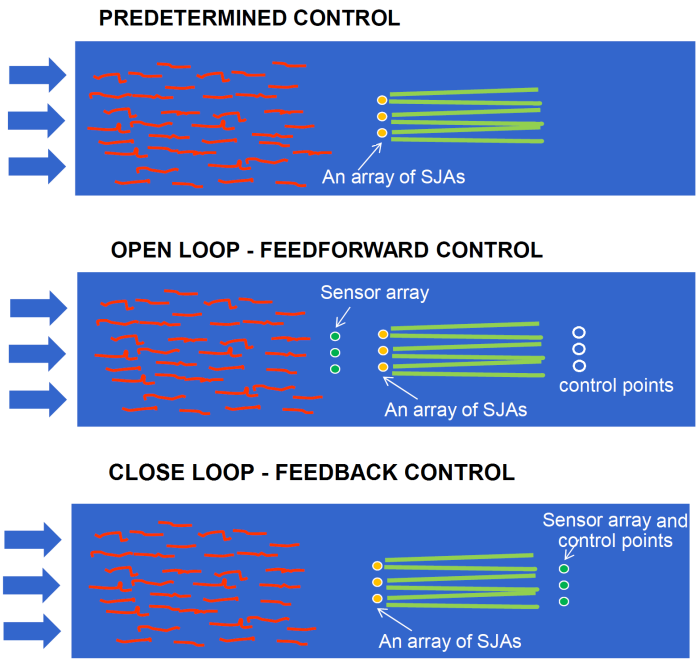

Figure 1.3: Predetermined, feed-forward and feed-back control of a turbulent boundary layer with a synthetic jet array (view from the top)

the operating conditions of the synthetic jets. In feed-forward control only the information from sensors upstream of the synthetic jet actuators is used to achieve pre-defined control effects at the control points (for example the reduction of the level of fluctuation in velocity at the control points). Further sensors are placed downstream of the actuators at the location of the control points to design the feed-forward control algorithm. These sensors can also be used a posteriori to evaluate the effectiveness of the control strategy, but they are not strictly needed during the control operation. The design of a feed-forward turbulent boundary layer control strategy is reported in Rathnasingham and Breuer [119]. In feed-back control the sensors are located at the control points and the feed-back routine has the objective of automatically adjusting the operating conditions of the actuators in order to achieve a certain control objective at these locations.

1.4.2 Experimental Work

For this thesis experimental work is undertaken toward the design of a turbulent boundary layer control system using synthetic jet actuators. All the experiments are performed in a water flume, operated at u_∞=0.1 m/s. The free-stream velocity is measured using Particle Image Velocimetry, with a relative uncertainty of about 1.25% (see Section 3.5.3). The turbulence intensity in the free-stream is estimated to be lower than 1% of the value of the free-stream velocity.

The work consists of the following parts:

1. An experimental study assessing the capability of a single round synthetic jet to control the vortices that develop in the near-wall region of a circular cylinder mounted vertically across a laminar boundary layer. This study is carried out using PIV. The velocity field with and without synthetic jet in a plane parallel to the wall, 3 mm above it, is analysed.

2. An experimental campaign using Liquid Crystal Thermography (LCT) in a turbulent boundary layer without any forcing. The use of Liquid Crystal Thermography allows the properties of the sublayer streaks to be examined, in particular their footprints at the wall. Liquid Crystal Thermography also allows not only a spatial but also a temporal characterisation of the turbulent streaks at the wall.

3. The design of a simple predetermined control system, with a synthetic jet array. The array is dimensioned to produce vortical structures of the same scale as the sublayer streaks, determined at the point above. The array is tested in details using Particle Image Velocimetry (PIV), which enables the analysis of the velocity field on a series of longitudinal planes, i.e. normal to the wall and aligned to the flow direction. Long-time averaged and phase-locked averaged PIV is used. Flow visualisations with liquid crystals are also preliminarily performed and allow the impact of the forcing at the wall to be examined.

4. The design of the first leg of the feed-forward control system, i.e a feed-forward predictor, which allows the potential optimal sensor arrangement to be determined. The experimental study is carried out using Liquid Crystal Thermography and Constant Temperature Anemometry with hot-film probes.

1.5 Objectives of the Research Project

The objectives of the present research project are:

- to assess the capability (in terms of modification of the velocity field) of a single synthetic jet actuators to control streamwise vortices and streaks in a laminar boundary layer and to determine the operating conditions at which the control effects are optimal.
- to study the properties of the near-wall coherent structures in the turbulent boundary layer to be controlled.
- to examine the forcing effect of an array of circular synthetic jets on the near-wall region of a turbulent boundary layer and to identify the operating conditions that yield skin friction drag reduction.
- to gain some knowledge about the physical mechanism which produces skin friction drag reduction/increase due to the synthetic jet array forcing;
- to lay the basis for the design of a feed-forward control system of a turbulent boundary layer based on wall-sensors and on an array of circular synthetic jets.

1.6 Thesis Outline

This thesis reports the experimental work carried out in order to achieve the objectives specified above. The discussion is organised as described herein.
Chapter 2 provides a literature review relevant to this project. As this is the first project carried out at the University of Manchester related to turbulence control for drag reduction with synthetic jets, an extensive review of turbulent boundary layers and the organised motion in it are reported. In addition, an overview of flow control methods of turbulent boundary layers is present. Finally the concepts related to synthetic jets are reviewed.
Chapter 3 describes the experimental facilities and the measurement techniques used to meet the above-mentioned objectives.
The results obtained and their discussion are divided into four chapters, namely Chapters 4,5,6 and 7.
Chapter 4 presents the experimental study of the interaction between a synthetic jet and the near-wall vortices that develop downstream of a circular cylinder;

Chapter 5 presents a characterisation of the properties of the near-wall coherent structures in a turbulent boundary layer using Liquid Crystal Thermography;
Chapter 6 presents a study on the turbulent boundary layer forcing with a round synthetic jet array. Extensive results obtained with Particle Image Velocimetry are reported as well as some preliminary flow visualisations with liquid crystals. A simple physical model of the flow field during different operating conditions of the synthetic jets is drawn.
Chapter 7 contains a preliminary study on the the development of a feed-forward predictor in a turbulent boundary layer. Finally Chapter 8 summarises the conclusions drawn in the previous chapters and reports a few suggestions for future work.

Chapter 2

Literature Review

The aim of this chapter is to review some basic concepts related to turbulent boundary layer and the coherent motions in them. The basic concepts needed to understand the results presented in the thesis are provided, the necessary definitions are given, with the nomenclature used also in the following chapters. In addition background information on flow control methods for drag reduction are also reviewed, to introduce this wide research area to the reader. Finally, the basic concepts relating to synthetic jets are reviewed.

2.1 Wall-Bounded Turbulence

Turbulence is considered as one the great unsolved problems of classical physics. The challenge of understanding the behaviour of turbulent flows aroused the interests of many scientists and philosophers in history. The study of turbulence is indeed of great practical importance: turbulent flows are ubiquitous in nature and a clear understanding of their features would have a great impact in aeronautical and naval engineering applications as well as in climate studies, weather forecasting and also in astrophysics. The study of turbulence has lead to great progress over the years, however nowadays even though the equations which rule the motion of turbulent flows are well known, a general physical theory of turbulence does not yet exist.

Among all types of turbulent flows, a full comprehension of wall-bounded turbulent flows, which means in the vicinity of a solid boundary, would provide an advantage in many engineering applications. It has been estimated that half of the energy spent for the transportation of fluids and gases through pipes and canals or for the propulsion of

vehicles through air and water is dissipated by turbulence near the wall. This review focuses mainly on incompressible wall-bounded turbulent flows. For more details on this subject it is possible to refer to [111] and [100].

2.1.1 Energy Cascades in Wall-Bounded Turbulence

One of the principal school of thoughts in the study of turbulence is based on breaking the complex turbulent flow field into more elementary organized motions, usually referred as eddies and coherent structures. An eddy is usually a single swirling motion, which usually has neither temporal nor spatial coherence. A coherent structure is a region of space where one or more flow variables retain both a spatial and a temporal degree of correlation with each other. A more detailed definition of coherent structures and their role in turbulent boundary layer dynamics is given in Section 2.2.

In a turbulent flow, eddies of different sizes exist, interact, exchange energy, split and merge to build smaller or larger structures. This process is typical of all turbulent flows. Quoting Jimenez [11] "*energy is injected into the largest eddies, but they become unstable and transfer energy to smaller eddies, which repeat the process to even smaller sizes. As long as the the eddies are large the transfer is inviscid and no energy is dissipated, but as they become smaller with successive instabilities, so do their based Reynolds numbers. Eventually energy reaches an eddy size for which viscosity cannot be neglected. It is at this point that energy is dissipated.*" The process outlined is often referred to as the energy cascade, see figure 2.1. The energy cascade process

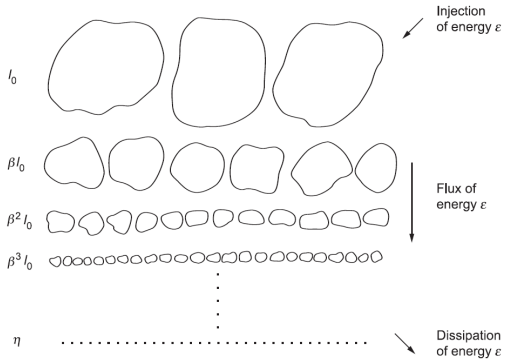

Figure 2.1: Energy cascade in turbulent flows (figure taken from [40])

is typical of all turbulent flows, such as free shear flows, mixing layers, shear layers and wall-bounded flows. It occurs from the largest eddies to the smallest ones and

shows an increasing trend within an inertial range i.e. a range of scales in which the net energy coming from the largest eddies is in equilibrium with the net energy cascading to smaller eddies. It is usually referred to as the self-similar Richardson energy cascade, because it assumes that the energy transfer is local in scale and there are no significant interactions between eddies of different size. Within this framework, Kolmogorov derived how energy is distributed among the eddies and also estimated the smallest length scale η at which the energy cascade process ends, also known as the Kolmogorov length scale:

$$\eta = \left(\frac{\nu^3}{\varepsilon}\right)^{1/4}. \tag{2.1}$$

where ε is the rate of kinetic energy transfer and ν is the kinematic viscosity of the fluid. Below the Kolmogorov length scale, the kinetic energy contained in the eddies is dissipated into heat.

The energy cascade process locally occurs also in wall-bounded turbulent flows. However, the range of scales spanned in the cascade is function of the distance from the wall y, as the largest eddy size depends on y [69] . In Figure 2.2 (taken from [69]) two spectral density maps for a turbulent channel flow, obtained by a DNS simulation are shown The spectral density is plotted for two quantities: the kinetic energy of the streamwise velocity fluctuations (shaded contours), which is related to the largest eddies that contain kinetic energy, and the surrogate dissipation (line contours), which is related to the eddies that dissipate kinetic energy into heat. Maps are plotted as functions of the streamwise wavelength λ_x^+ and of the distance from the wall y^+. The symbol $+$ means that the quantities are normalised in wall units, using the length scale L_τ, defined in Section 2.1.3. The energy cascade process occurs from the scale of the energy containing eddies (red peak in the shaded contours) to the scale of the dissipative eddies (red peak in the line contours). Therefore, the range of scales of interest is a function of y. In the near-wall region the two scales are similar in size and so the cascade process does not occur. Between $y^+ = 80$ and 1000 there is a sufficient separation between the two scales for the cascade process to occur. For y^+ larger than 1000 the scale separation decreases again and the cascade process is limited.

In addition, due to the flow inhomogeneity, in wall-bounded turbulence energy is not only transferred between different scales, but also from one region to another. Momentum is also transferred. We can refer to this second cascade process as the spatial

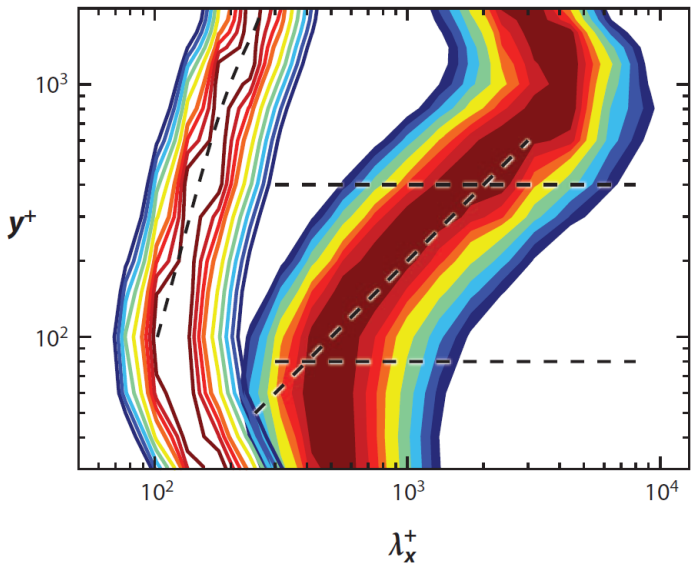

Figure 2.2: Power spectral density of the kinetic energy of the streamwise velocity fluctuations (shaded contours) and of the surrogate dissipation (line contours) computed from a direct numerical simulation of a channel flow at $\mathrm{Re}_\tau = 2000$ (figure taken from [69])

cascade. The spatial cascade may occur not only between eddies of same sizes, but also between eddies of different sizes. The smallest scales are generally isotropic, so the spatial cascade does not involve them. Since there are only small scales in the region closer to the wall, the spatial cascade does not occur and is only typical of the outer region of wall-bounded flows. This co-existence of these two cascade processes in wall-bounded flows gives rise to a complex scenario, which makes the problem of understanding wall-bounded turbulent flow more challenging [69, 11].

2.1.2 Reynolds Decomposition

The most popular description of turbulence was introduced and developed by Osborne Reynolds (1895) and is commonly referred to as the Reynolds decomposition. The Reynolds decomposition is based on an Eulerian frame. In the following discussion, x is the Cartesian coordinate in the streamwise direction, y is in the wall-normal direction and z in the spanwise direction. Reynolds observed that all the flow variables show a certain degree of random fluctuation superimposed to a mean value. Given that, the

generic variable q of the Navier-Stokes equations can be decomposed as:

$$q \doteq \bar{q} + q'. \tag{2.2}$$

In the case of an incompressible flow, the Reynolds decomposition can be applied to all the velocity components $\vec{v} = (u, v, w)$ and to pressure p. Given that, $u \doteq \bar{u} + u'$, $v \doteq \bar{v} + v'$, $w \doteq \bar{w} + w'$, $p \doteq \bar{p} + p'$. The mean value should be calculated as an ensemble average, which means on different realizations of the same flow field. However, the ergodicity hypothesis is often considered valid, for which the time average at a given point can be used as a substitute for the ensemble average. The time average can be computed as:

$$\bar{q} = \lim_{T \to +\infty} \frac{1}{T} \int_{t_0}^{t_0+T} q(t)\, dt. \tag{2.3}$$

After introducing the decomposition of all the variables, substituting the decomposed variables into the Navier-Stokes equations and taking the time average of both left-hand and right hand side, it is possible to derive the so-called Reynolds Averaged Navier-Stokes equations or RANS:

$$\nabla \cdot \bar{\vec{v}} = 0 \tag{2.4}$$

$$\rho \frac{D\bar{\vec{v}}}{Dt} = -\nabla p + \nabla \cdot \tau_{ij}. \tag{2.5}$$

The unknowns of the RANS equations are the mean flow variables. The mathematical problem is properly closed only after proper initial and boundary conditions are imposed. The main difference from the classical Navier-Stokes equations is that in the RANS the term τ_{ij} reads:

$$\tau_{ij} = \tau_{\mathrm{v}\,ij} - \rho \overline{u_i' u_j'} \tag{2.6}$$

where $\tau_{\mathrm{v}\,ij}$ is the mean shear stress tensor, which for an incompressible flow is equal to

$$\tau_{\mathrm{v}\,ij} = \mu \left(\frac{\partial \bar{u}_i}{\partial x_j} + \frac{\partial \bar{u}_j}{\partial x_i} \right). \tag{2.7}$$

Therefore, in the RANS equations there is an additional contribution to the viscous stress tensor, known as the Reynolds stress tensor, also referred to as τ_{Re}. The Reynolds stress term adds six further unknowns to the mathematical problem, which are the six tensor components. In order to close the problem, therefore, these additional unknowns

have to be modelled by means of turbulence models.

The kinetic energy for the mean part of the velocity is defined as (see for example [111])

$$\bar{k} \doteq \frac{\bar{u}_i \bar{u}_i}{2} = \frac{\bar{u}^2 + \bar{v}^2 + \bar{w}^2}{2}. \tag{2.8}$$

The kinetic energy for the fluctuating part of the velocity is defined as

$$k \doteq \frac{\bar{u_i'} \bar{u_i'}}{2} = \frac{(u')^2 + (v')^2 + (w')^2}{2}. \tag{2.9}$$

An equation for turbulent kinetic energy transport both for the mean part and for the fluctuating part can be derived (see [111]) . The latter can be expressed in the following form (steady state):

$$u \frac{\partial k}{\partial x} + v \frac{\partial k}{\partial y} = P_k + D_k + \varepsilon. \tag{2.10}$$

The term ε is the viscous dissipation of kinetic energy into heat. The term D_k represents the turbulent transport of kinetic energy through the system boundaries; the term P_k is associated with the production of turbulent kinetic energy. If one writes the transport equation for the kinetic energy for the mean motion, it is possible to see that a term identical to P_k also appears, but with the opposite sign. Indeed, P_k represents the transfer of kinetic energy from the mean motion to the turbulent fluctuations. It is interesting to understand what mechanisms produce this term and what are the regions in the turbulent boundary layer where this term is more significant.

2.1.3 Turbulent Boundary Layers

In the case of turbulent boundary layer flows, the RANS equations can be simplified using arguments related to the order of magnitude of each term (see [132] for a detailed treatment). In particular in the two-dimensional case[1], the y-component of the Navier-Stokes momentum equation simply reduces to $\frac{\partial p}{\partial y} = 0$, whereas the x-component is simplified as:

$$\bar{u} \frac{\partial \bar{u}}{\partial x} + \bar{v} \frac{\partial \bar{u}}{\partial y} = -\frac{1}{\rho} \frac{dp}{dx} + \frac{1}{\rho} \frac{\partial \tau}{\partial y}. \tag{2.11}$$

[1]The mean flow in a turbulent boundary layer is assumed to be two-dimensional. The instantaneous flow field is however three-dimensional and also $w' \neq 0$.

In the incompressible case, the shear stress term τ is:

$$\tau = \mu \frac{\partial \bar{u}}{\partial y} - \rho \overline{u' v'}. \tag{2.12}$$

The shear stress can be divided into a viscous term and in a Reynolds stress term.
For zero-pressure gradient boundary layers (ZPG) the first term on the right-hand side vanishes and the momentum equation in the x-direction becomes:

$$\bar{u} \frac{\partial \bar{u}}{\partial x} + \bar{v} \frac{\partial \bar{u}}{\partial y} = \frac{1}{\rho} \frac{\partial \tau}{\partial y}. \tag{2.13}$$

The turbulent kinetic energy equation is not reported here. It is interesting however to mention how the term related to energy production for a turbulent boundary layer is expressed as:

$$P_k = -\frac{\partial \bar{u}}{\partial y} \overline{u' v'} \tag{2.14}$$

The importance of the form of relation (2.14) on the dynamics of a turbulent boundary layer flow is addressed below.

The boundary layer thickness is the distance δ at which the velocity $\bar{u}$ is equal to 0.99 u_∞, where u_∞ is the free-stream velocity, outside the boundary layer. [132, 22]. Based on δ the displacement thickness δ^* and the momentum thickness θ of the boundary layer are defined as:

$$\delta^* \doteq \int_0^\infty \left(1 - \frac{\bar{u}}{u_\infty}\right) dy \qquad \theta \doteq \int_0^\infty \frac{\bar{u}}{u_\infty} \left(1 - \frac{\bar{u}}{u_\infty}\right) dy \tag{2.15}$$

For more details on the physical meaning of θ and δ please see [132, 22, 111]. The wall shear stress, which is the value of τ at the wall, is:

$$\tau_w \doteq \tau|_{y=0}. \tag{2.16}$$

The skin friction coefficient is defined as

$$C_{fx} = \frac{\tau_w}{\frac{1}{2} \rho u_\infty^2}. \tag{2.17}$$

In this thesis, if not differently specified, in a turbulent boundary layer the wall shear stress and the skin friction coefficient are assumed to be mean values.

Some empirical correlations are commonly used for a first estimation of all these parameters in a turbulent boundary layer [22, 15]. These correlations assume that the a completely turbulent boundary layer develops from the leading edge of a flat plate, with zero-pressure gradient, and x is the distance from the leading edge:

$$\delta(x) \approx \frac{0.37x}{\mathrm{Re}_x^{0.2}} \qquad \delta^*(x) \approx \frac{0.046x}{\mathrm{Re}_x^{0.2}} \tag{2.18}$$

$$\theta(x) \approx \frac{0.036x}{\mathrm{Re}_x^{0.2}} \qquad C_{fx}(x) \approx \frac{0.059}{\mathrm{Re}_x^{0.2}} \tag{2.19}$$

where Re_x is the Reynolds number based on x and on the free-stream velocity u_∞

The turbulent boundary layer is a composite layer, in which an overall scaling for the flow variables cannot be found, unlike a laminar boundary layer. A turbulent boundary layer can be divided into:

- an inner layer, where the effect of the external inviscid flow on the boundary layer is negligible and the shear stresses are predominant;
- an outer layer, in which the effect of the external flow on the boundary layer is not negligible.

Given that, it is possible to find scaling laws that apply to each layer separately [132, 111]. More details on each layer are provided hereafter.

Inner Layer In the inner layer, which extends from the wall to typically 10-20% of the boundary layer thickness, the momentum fluxes are negligible with respect to the shear stress term on the right-hand-side of equation (2.13). Therefore, for a zero-pressure gradient case, it is possible to re-write it as:

$$\frac{\partial \tau}{\partial y} = \frac{\partial}{\partial y}\left(\mu \frac{\partial \bar{u}}{\partial y} - \rho \overline{u' v'}\right) \approx 0. \tag{2.20}$$

In this region, the sum of the viscous shear stress and of the Reynolds shear stress is approximately constant along y. Through dimensional analysis, it is possible to show that the average velocity distribution depends solely on the wall shear stress τ_w, the kinematic viscosity ν and the distance y from the wall. A viscous velocity can be

defined, also called friction velocity as

$$u_\tau \doteq \sqrt{\frac{\tau_w}{\rho}}. \tag{2.21}$$

Hence, the relation between the friction velocity and the freestream velocity is

$$\frac{u_\tau}{u_\infty} = \sqrt{\frac{C_{fx}}{2}}. \tag{2.22}$$

obtained by simply comparing (2.21) with (2.17). A viscous length and a viscous time-scale can also be defined respectively as

$$L_\tau \doteq \frac{\nu}{u_\tau} \qquad T_\tau \doteq \frac{\nu}{u_\tau^2}. \tag{2.23}$$

Given these definitions, two dimensionless groups for velocity and length scale can be formed

$$u^+ \doteq \frac{\bar{u}}{u_\tau} \qquad y^+ \doteq \frac{y}{L_\tau} = \frac{y u_\tau}{\nu}. \tag{2.24}$$

Lengths and velocity normalized by these groups are commonly said to be expressed in wall units and this scaling procedure is commonly referred to as the inner scaling. Dimensional analysis leads to a relation between these two dimensional groups, of the form

$$u^+ = f\left(y^+\right), \tag{2.25}$$

which is known as the law of the wall and applies in the whole inner layer.

A further decomposition is usually performed according to the relative magnitude of the Reynolds stress term with respect to the viscous shear stress term. In this way, typically three regions can be identified:

- *viscous sublayer* ($0 < y^+ < 5$), in which the shear stress is purely viscous and therefore a linear relation is assumed between u^+ and y^+ (i.e. the law of the wall is linear):

$$u^+ = y^+; \tag{2.26}$$

- *buffer layer* ($5 < y^+ < 30$), an intermediate region in which the two types of stress have the same order of magnitude;

- *logarithmic layer* ($30 < y^+ < 0.1 - 0.2\delta$)[2], in which the viscous shear stress is negligible compared to the Reynolds stress. This implies that the velocity distribution is independent of viscosity. Dimensional arguments lead to a logarithmic relationship between u^+ and y^+

$$u^+ = \frac{1}{K} \log y^+ + C. \tag{2.27}$$

where K is also known as the von Karman constant and its value is approximately 0.4 [3]. The parameter C is approximately $5.0 - 5.5$ for a smooth wall. This value depends on the surface roughness, and increases with it.

In Figure 2.3 the velocity profile expressed in the wall units in the inner layer is plotted.

Some theoretical relationships exist, which can describe the scaled form of the velocity profile in the inner layer. For example, the law of the wall provided by White in [159], which is derived from the definition of eddy viscosity and from the Prandtl

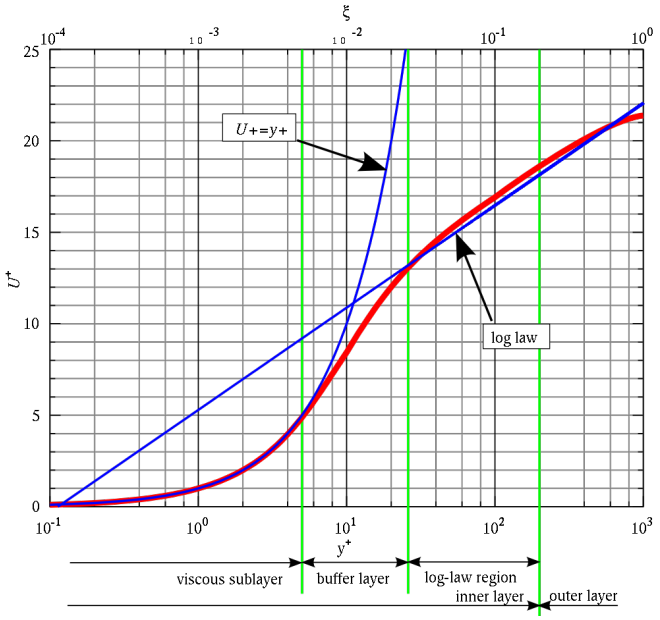

Figure 2.3: The velocity profile of a turbulent boundary layer, normalised in wall-units

[2] According to Spalart [141] the logarithmic layer extends from y^+=30 to y/δ=0.15. Spalart also claims that the existence of the logarithmic layer is dubious below Re_θ=400, even if an 'apparent log layer' might appear in the scaled velocity profile, in which probably the buffer layer and the wake region are partially overlapped.

[3] Many authors consider the value of the von Karman constant as universal, whereas other cast doubts on this universality [99]

mixing-length model, reads:

$$u^+ = \int_0^{y^+} \frac{2\,ds}{1+\left\{1+4K^2s^2\left[1-\exp(-s)\right]^2\right\}^{1/2}} \tag{2.28}$$

where K is still the von Karman constant and $A \approx 26$. The advantage of such a relation (2.28) is that it describes the turbulent boundary layer velocity profile in the inner layer with a single formula. Another relationship is the Spalding profile, which is a power series interpolation joining the viscous sublayer law to the logarithmic layer law [142]:

$$y^+ = u^+ + \exp(-kC)\left[\exp\left(ku^+\right) - 1 - ku^+ - \frac{\left(ku^+\right)^2}{2} - \frac{\left(ku^+\right)^3}{6}\right], \tag{2.29}$$

where $K = 0.4$ and $C = 5.0$ again. Another relationship is provided by the Musker profile, also based on the eddy-viscosity turbulence model [102, 76], which reads:

$$\frac{du^+}{dy^+} = \frac{\frac{\left(y^+\right)^2}{K} + \frac{1}{s}}{\left(y^+\right)^3 + \frac{\left(y^+\right)^2}{K} + \frac{1}{s}}, \tag{2.30}$$

where $K = 0.4$ and $s = 0.001093$ [76].

Outer Layer In the other layer, which extends for the remaining 80-90% of the boundary layer thickness, the external inviscid flow affects the boundary layer, therefore another scaling needs to be applied. The natural scaling variables in this layer are the boundary layer thickness δ and the freestream velocity u_∞. This scaling is commonly referred to as the outer scaling and the quantities normalised with these variables are said to be scaled in outer variables. The velocity profile in this region can be expressed with the so-called velocity-defect law, which reads:

$$\frac{u_\infty - u}{u_\tau} = f\left(\frac{y}{\delta}\right). \tag{2.31}$$

It is possible also to show that the logarithmic law of the wall also satisfies this scaling. This means that the logarithmic layer is actually an overlap region, where both the inner and the outer scaling apply. Using the the inner scaling for the variables in equation

(2.31), the velocity profile can be expressed as

$$u^+ = \frac{1}{K}\log y^+ + C + g(\frac{y}{\delta}) \tag{2.32}$$

where $g(\frac{y}{\delta})$ is the deviation from the pure logarithmic law. For the case of a ZPG turbulent boundary layer, g is well estimated by the Cole's law of the wake

$$g\left(\frac{y}{\delta}\right) \approx \frac{\Pi(x)}{k} 2 sin^2\left(\frac{\pi}{k}\frac{y}{\delta}\right) \tag{2.33}$$

where the coefficient $\Pi(x)$ is also known as the Cole Π coefficient or amplitude of the wake, which is weakly dependent on the Reynolds number, approaching the value of 0.55 for high Reynolds numbers.

2.1.4 Re_τ or Karman Number in Turbulent Boundary Layers

It can be shown that in turbulent boundary layers the viscous length L_τ, defined before is of the same order of magnitude of the Kolmogorov length scale, which is the smallest scale of the turbulent flow (see Section 2.1). On the other hand, the largest scale in the boundary layer is of the order of the boundary layer thickness δ, which is also the natural length scale in the the outer scaling. It is particularly significant to consider the ratio of the inner to the outer scaling length, because it represents the order of magnitude of the ratio of the largest to the smallest scales in the turbulent boundary layer. This ratio has the form of a Reynolds number, therefore in literature it is often indicated as Re_τ:

$$\mathrm{Re}_\tau = \frac{L_\tau}{\delta} = \frac{\delta u_\tau}{\nu}. \tag{2.34}$$

This quantity is also called the Karman number or alternatively indicated as δ^+, because it is also equal to the boundary layer thickness scaled in wall units. It is possible to easily show that Re_τ is actually proportional to the Reynolds number based on the boundary layer thickness Re_δ. In fact, we find that substituting (2.22) into (2.34)

$$\mathrm{Re}_\tau = \mathrm{Re}_\delta \sqrt{\frac{C_{fx}}{2}}. \tag{2.35}$$

The larger Re_τ, the larger is the ratio of the order of magnitudes between the maximum and minimum turbulent scales (in other words the larger is the so-called scale separation) . The scale separation plays a crucial role in the dynamics of the boundary

layer, therefore the behaviour of turbulent boundary layers at different values of Re_τ is significantly different.

2.1.5 Reynolds Stresses and Increase in Skin Friction in Turbulent Boundary Layers

It is well known that the wall shear stress, and so skin friction, in a turbulent boundary layer is higher than in a laminar one. This is due to the Reynolds stress term $\overline{u'v'}$ in equation 2.12. In fact, $\overline{u'v'}$ is the only term that distinguishes the equations of a turbulent boundary layer from those of a laminar boundary layer. The Reynolds stress profile therefore is responsible for the modification of the velocity profile in a turbulent boundary layer with respect to a laminar one, and to the increase in skin friction at the wall.

The typical Reynolds shear stress profile is shown in Figure 2.4, along with the root-mean-square values of u',v' and w'. The value of $\overline{u'v'}$ is negative, starts from zero at the

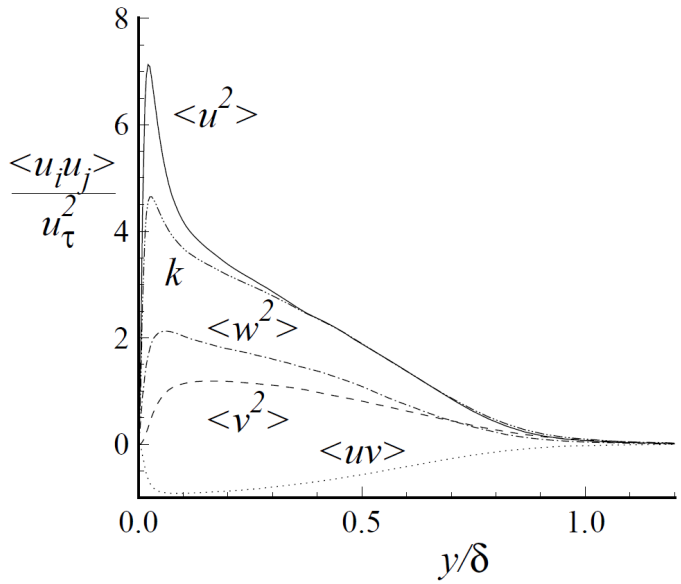

Figure 2.4: Turbulence intensity profiles and Reynolds stress profile in a turbulent boundary layer (figure taken from [111])

wall, reaches a minimum at about y^+ =12-15, in the buffer layer, and then approaches again the value of zero in correspondence of the boundary layer edge.

The reason why $\overline{u'v'}$ is negative is shown in Figure 2.5. The fluid particle originally

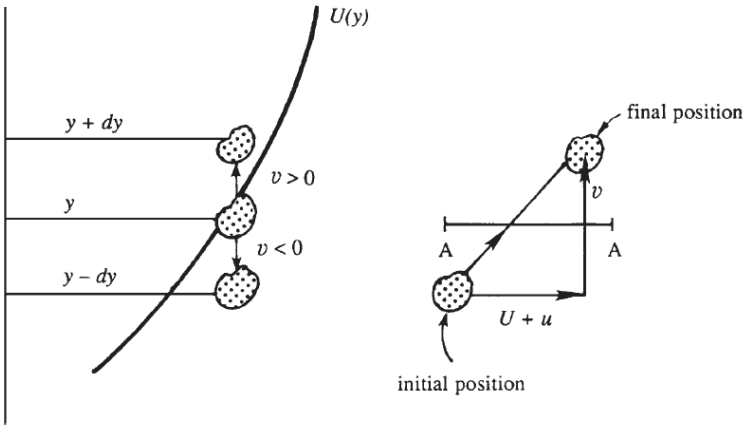

Figure 2.5: Relationship between u' and v' in presence of a velocity gradient in a turbulent boundary layer (figure taken from [87])

located at position y moves upwards to the final position $y+dy$, because of a positive velocity fluctuation $v > 0$. On the average, the particle tends to keep its original velocity u and when it is in in the position $y+dy$, being in a region of larger velocity $(\bar{u} + \frac{\partial \bar{u}}{\partial y} dy)$, tends to slow down the neighbouring fluid particles, causing an instantaneous negative u fluctuation, $u' < 0$. This means that a positive v' is generally correlated with a negative u'. Similarly it is possible to show that a negative v' is generally correlated with a positive u'. The value of $\overline{u'v'}$ is negative in both cases.

If the values of u' and v' in a turbulent boundary layer at a certain y are recorded on a scatter plot, the situation is that shown in part (b) of Figure 2.6. The case of isotropic fluctuations, in which $\overline{u'v'}$=0, is also shown in part (a) of Figure 2.6.

The quadrant splitting scheme, first proposed by Wallace [156] and Willmarth and Wu [160], can be used to characterise the single events which produce the $u' - v'$ scatter plot. The $u' - v'$ plane is divided into four quadrants. The nomenclature used is shown in Figure 2.7. Figure 2.7 refers to the typical case of a turbulent boundary layer, in which the fluctuations lie mainly on quadrants 2 and 4. In particular, quadrant 4 events are also called sweeps or Q4 and whereas quadrant 2 are called ejections or Q2. It is interesting to observe that being the production term for the turbulent kinetic energy in turbulent boundary layers expressed as $P_k = -\frac{\partial \bar{u}}{\partial y} \overline{u'v'}$, see equation (2.14), both sweeps (Q2) and ejections (Q4), for which the product $\overline{u'v'}$ is negative, are events

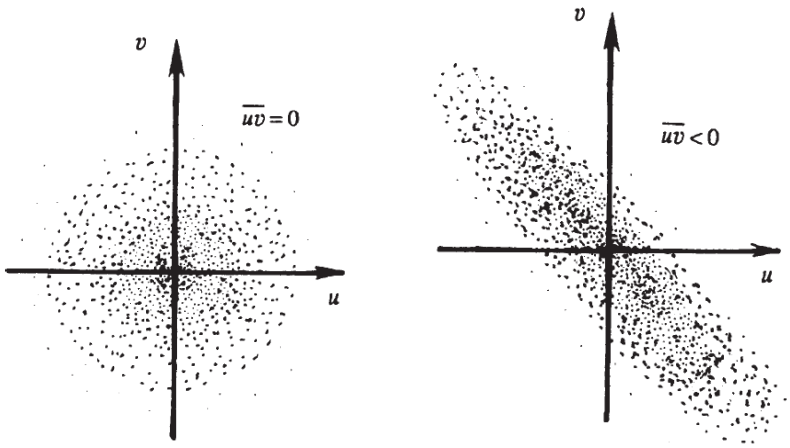

(a) $\overline{u'v'}=0$ (b) $\overline{u'v'}<0$

Figure 2.6: $u'-v'$ scatter plots in the case $\overline{u'v'}=0$ and in the case $\overline{u'v'}<0$ (Figure adapted from [87])

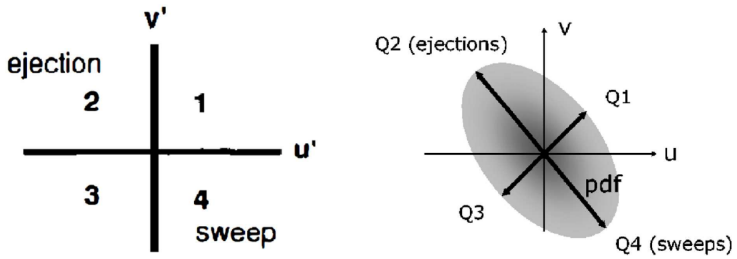

Figure 2.7: Quadrant splitting scheme and related events in turbulent wall-bounded flows (figure taken from [2])

providing a positive contribution to the production of turbulent kinetic energy because of the minus sign and because in a boundary layer the term $\frac{\partial \bar{u}}{\partial y}$ is positive.

The shape of Reynolds stress shown in Figure 2.4 is related the velocity fluctuations in the turbulent boundary layer and, as explained in Section 2.2, it can be related to the coherent structures present in the boundary layer itself. With qualitative arguments (see [2]) it is possible to show that that specific Reynolds stress profile causes an increase of skin friction at the wall, see Figure 2.8. y_p is the value at which the Reynolds

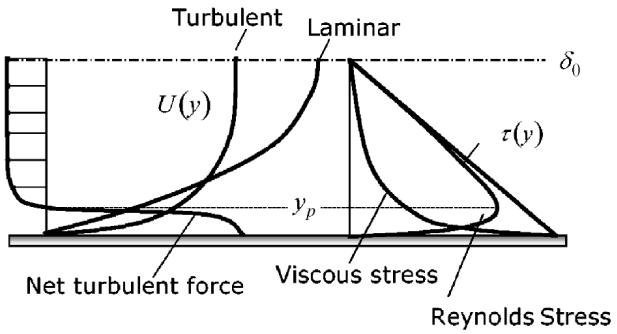

Figure 2.8: Profiles of shear stresses and net force due to Reynolds stresses in wall-bounded turbulent flows (adapted from [2])

stress is maximum. By substituting the shear stress relation for a turbulent boundary layer (2.12) into (2.11), assuming $dp/dx = 0$:

$$\rho\left(\bar{u}\frac{\partial \bar{u}}{\partial x} + \bar{v}\frac{\partial \bar{u}}{\partial y}\right) = \frac{\partial}{\partial y}\left(\mu\frac{\partial \bar{u}}{\partial y} - \rho\,\overline{u'v'}\right). \tag{2.36}$$

The left-hand-side of the equation represents the variation of the streamwise velocity component $\bar{u}$, all the terms on the right-hand side represent the forces that cause this variation, the resultant of which is referred to as the net shear force. The net shear force is composed of two parts: a viscous part and another part due to *Reynolds stresses*, which we refer to as the *turbulent net shear force*

$$\text{net turbulent force} = \frac{\partial}{\partial y}\left(-\rho\overline{u'v'}\right). \tag{2.37}$$

Hence, what really matters in terms of the dynamics of a turbulent boundary layer is not the *Reynolds stress* but its derivative. According to the variation of the Reynolds shear stress shown in Figure 2.8, the turbulent net shear force is negative and roughly constant above y_p and positive below y_p. Therefore, under the effect of the turbulent

net shear force the mean momentum increases near the wall with respect to the case of a laminar boundary layer and decreases in the region away from the wall. If the mean velocity is increased near the wall, the velocity gradient is also increased, because the presence of the wall imposes a zero velocity at the wall and so the slope of the velocity profile at the wall is higher. Therefore, the wall shear stress , defined as

$$\tau_w = \left(\mu \frac{\partial \bar{u}}{\partial y} - \rho \overline{u'v'} \right) \Bigg|_{y=0} = \mu \frac{\partial \bar{u}}{\partial y} \tag{2.38}$$

is higher, because $\overline{u'v'}$ is null at the wall.

Another way of accounting for the effect of the Reynolds stresses on the wall shear stress and on the skin friction coefficient at the wall is to make use of the *FIK identity* (Fukagata-Iwamoto-Kasagi) also simply known as the *Fukagata identity*, introduced in [41]. In [41] it is shown that in the case of a zero-pressure gradient turbulent boundary layer the FIK identity can be written as:

$$C_{fx} = 0.664\,\mathrm{Re}_x^{-0.5} + \frac{4}{\delta^2 u_\infty^2} \int_0^\delta (y-\delta)\, \overline{u'v'}\, dy \tag{2.39}$$

This identity shows that the skin friction coefficient in a turbulent boundary layer can be expressed as the sum of two terms: the first one is also present in a laminar boundary layer, see for example [22, 15]; the second term depends on the Reynolds shear stress and is therefore related to the turbulent velocity fluctuations. If one is able to measure accurately the Reynolds shear stress profile, then it is possible to estimate the skin friction coefficient after evaluating the integral in equation (2.39). The FIK identity can also be used for the analysis of drag modifications using a flow control strategy, as described in detail in [41].

2.2 Organised Motion in Turbulent Boundary Layers

Classical studies on turbulent flows, which followed the pioneering work of Osborne Reynolds at the beginning of the 20th century, regarded turbulence as a completely random phenomenon, which could be therefore studied only on a statistical basis. However, from the 1960s it was noticed especially through flow visualization and experiments, that turbulent flows contain large coherent motions that can actually be

observed and are not completely chaotic. Since then, the study of coherent or organised motion has received more and more attention. As pointed out in Section 2.1.5, a proper understanding of the dynamics of these structures is today considered extremely important, because they significantly contribute to the production of turbulent kinetic energy, Reynolds stress and therefore affect the shape of the mean velocity profile. This new perspective in the study of turbulent flows is not at all disjoint from the early statistical approach, rather it is a complementary view.

Although the concept of *coherent structure* is quite intuitive, a very precise definition has not been yet universally reached [3, 111, 153]. A good qualitative definition was given by Robinson [126], who defined a coherent structure as a "*three dimensional region of the flow over which at least one fundamental flow variable (velocity component, pressure, temperature) exhibits significant correlation with itself or with another flow variable over a range of space and time, both significantly larger than the smallest local scales of the flow*". This definition, even if not rigorous, is sufficient to understand the concepts illustrated in this chapter. Early developments on this subject are summarized in [26, 126, 107]. More recent developments can be found in [2, 139, 138, 147]. Today, even if many points are still unclear and need to be studied in more detail. A general agreement has been reached concerning the basic nature of the coherent structures present in a turbulent boundary layer, and some mechanisms related to their origin and evolution have been sketched [2, 107].

Figure 2.9 shows a couple of flow visualization of a turbulent boundary layer, in which some of the coherent structures are marked. According to the most recent reviews on this subject [139, 2], the coherent structures in a turbulent boundary layer can be classified into three broad categories:

- *streamwise streaks/vortices*, located in the viscous sublayer and buffer layer. These structures are associated to the near-wall cycle and their dynamics accounts for the peak of Reynolds stress and turbulent kinetic energy production at the edge of the buffer layer, already mentioned in Section 2.1.3;
- *hairpin packet/vortex cluster organisation* in the logarithmic and outer region of the boundary layer, believed to be related to the Large Scales of Motions (LSMs);

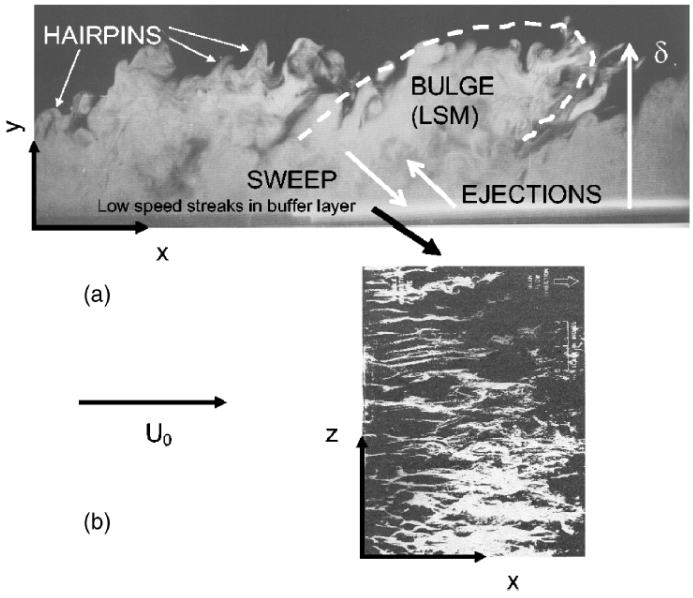

Figure 2.9: Flow visualization of the most relevant coherent structures in a turbulent boundary layer (figure taken from [2])

- *Very Large Scales of Motions (VLSM)*, also termed superstructures, which populate the logarithmic region of turbulent boundary layers at high Reynolds number.

2.2.1 Streamwise Streaks, Vortices and the Near-Wall Cycle

The organised motion in the near-wall region has been studied extensively since the late 1950s. The first attempts to characterise it were made by Favre et al [38] and subsequently by Willmarth and Woolridge [162, 160]. In their studies autocorrelations and cross-correlations of wall pressure and velocity with separation vectors in all streamwise, spanwise and wall-normal directions were measured. Their main conclusion was that the near-wall region contains flow disturbances that are continuously generated, convect downstream essentially along the streamwise direction and finally decay.

Successive studies, especially carried out by Runstadler et al. [128] and Kline et. al [83] at the end of the 1960s revealed that the most dominant structures or eddies in the near-wall region are alternating streamwise streaks of higher and lower speed, which appear randomly in space and time and produce a spanwise modulation of all

the flow variables at the wall. The streaks move essentially along the streamwise direction. However their motion is not indefinite, as the single streaks at a certain point are observed to lift-up, destabilize and breakup into much finer structures. During these events low speed fluid is ejected towards the outer region (ejection event) and successively high speed fluid is swept towards the inner region (sweep event), in a quasi-cyclic sequence also referred to as bursting. The peak in the Reynolds stress profile and on the turbulent kinetic energy production profile, which is observed at the edge of the buffer layer at $y+ \approx 12-15$, is believed to be associated with the streak bursting. The presence of the streamwise streaks is now considered a peculiar characteristic of any turbulent wall-bounded flow. The spanwise spacing between two adjacent streaks is approximately $100L_\tau$ and this value is weakly dependent on the Reynolds number, up to $\mathrm{Re}_\theta \approx 6000$. The streamwise extent of the streaks is at least 5-10 times larger, approximately $500-1000L_\tau$, but less agreement has been reached about this value.

The streamwise streaks are induced by a distribution of streamwise vortices, which populate the region immediately above the viscous sublayer. These vortices are also continuously generated and travel downstream essentially along the streamwise direction. Extensive studies have shown that the streamwise vortices have a diameter scaling in wall units, approximately between 20 and 50 L_τ [79, 81] Each vortex is much shorter than the streamwise streak it generates. This leads to the conclusion that each streak is generated by more than one streamwise vortices, as sketched in Figure 2.10. It is also

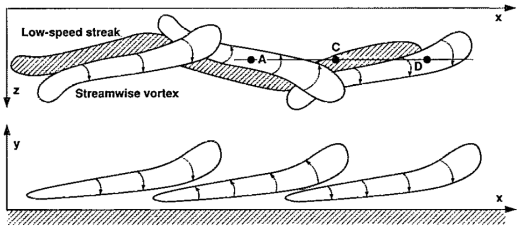

Figure 2.10: Conceptual model of streak generation by a series of streamwise vortices (figure taken from [80])

observed that streaks can be generated also by single streamwise vortices, not always arranged in a counter-rotating pair, as early conceptual models described.

In Figure 2.11 results from a numerical simulations are reported, which show the features of a turbulent channel near-wall region. On the top of the figure a contour-map of the spanwise vorticity at the wall is shown. The map shows regions of alternate

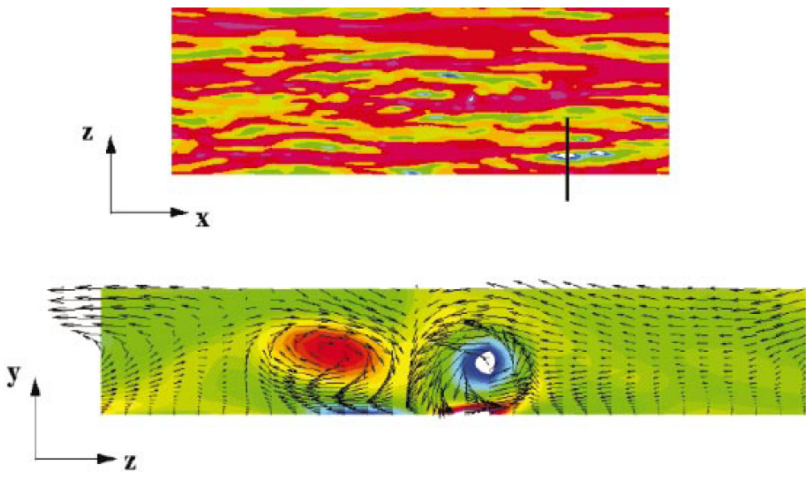

Figure 2.11: Evidence of streamwise streaks and streamwise vortices in the flow field obtained with a numerical simulation (figure taken from [78])

higher and lower vorticity. At the bottom of the figure the flow in the indicated cross section is shown. In this plot the colours denote the magnitude of streamwise vorticity, the vectors indicate the wall-normal and spanwise components of the velocity in the plane. The regions of higher and lower vorticity are associated with two counter-rotating streamwise vortices. These vortices are observed to induce a streak of lower and a streak of higher velocity underneath them, very close to the wall. The relation between the streamwise vortices and streamwise streaks was also examined by Kravchenko et al. [85] using data from direct numerical simulations of a fully developed turbulent channel flow at Reynolds number 3300, based on the centreline velocity and the channel half-width. They showed that the high skin-friction regions at the wall are strongly correlated with the streamwise vortices above them and that they constitute their footprints. A time sequence in the evolution of near-wall streamwise vortices and high skin-friction regions on the wall is shown in 2.12. In the figure, the contours lines indicate skin-friction on the wall, and the grey and black regions indicate iso-surfaces of negative and positive streamwise vorticity above the wall respectively. This figure highlights the the correlation between streamwise vortices and streamwise streaks. The three events marked by A, B, and C are regions of high skin-friction followed in time. It is important to stress how only the event C is related to counter-rotating streamwise vortices near a high skin-friction region, while the other two events are associated with a single streamwise vortex. Recent PIV investigations by Adrian and co-workers [2] have also shown that streamwise vortices may be attached to the

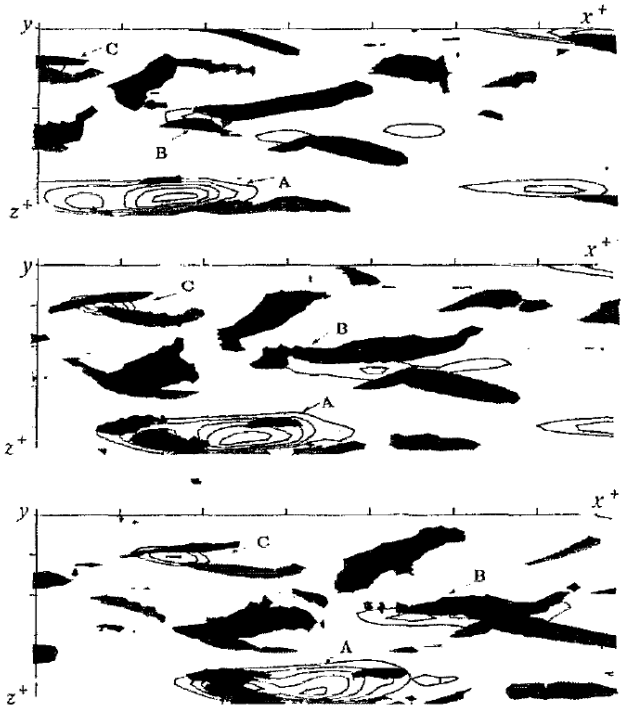

Figure 2.12: Time evolution of the streamwise vortices and of the skin friction lines at the wall (figure taken from [85])

legs of the single legged or double legged hairpin/horseshoe vortex packets (aligned essentially along the streamwise direction) that populate the logarithmic and the outer region of the boundary layer. The packet organisation of the hairpins would account for the longer streamwise extent of the streamwise streaks with respect to any single detected streamwise vortex.

It is generally accepted that, at least at low Reynolds number, the mechanism of turbulence production occurs within a cyclic series of events (see Figure 2.13), commonly referred to as the near-wall cycle. The near-wall cycle involves both the streamwise vortices and the streaks, see part (a) of figure 2.13. Streamwise vortices induce the streaks by interaction with the mean shear. The streaks lift-up and burst, creating streamwise-dependent disturbances which perturb and destabilise the mean velocity profile, as shown in part (b) of figure 2.13. This instability is at the basis for the generation of new streamwise vortices and so on [70, 133, 155]. It is believed that this process is autonomous, which means independent of the outer region of the boundary layer, and that the presence of the wall itself does not play a direct role in the process [79, 70].

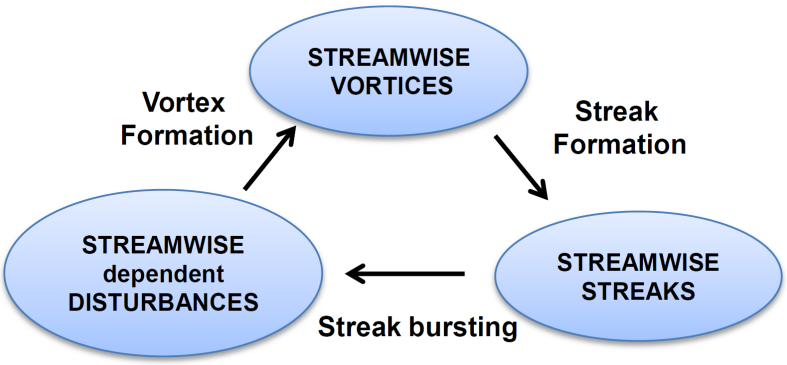

(a) Near-wall cycle events

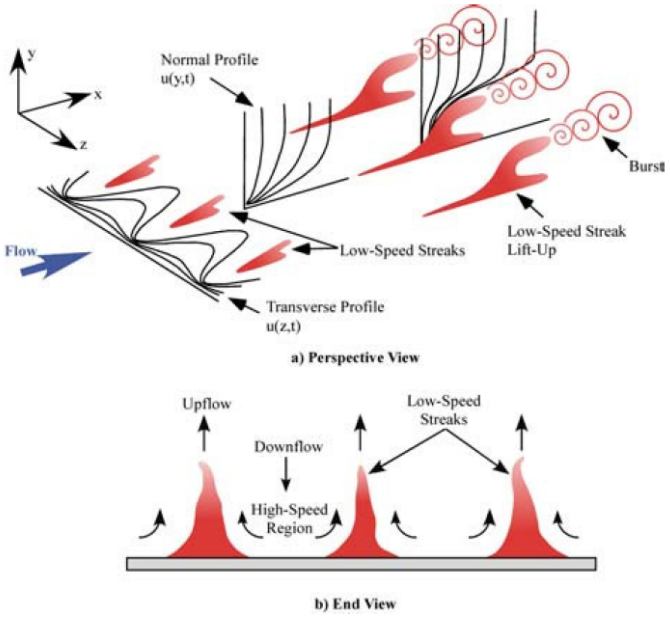

(b) Streak generation and bursting (figure taken from [77])

Figure 2.13: Near-wall cycle events

A controversial topic, which has not been fully clarified is the scaling of the bursting period T_b, which is the period between two successive bursting events extracted in time at a fixed location. The bursting frequency is the inverse of the bursting period i.e. $f_b = 1/T_b$. Finding a proper scaling for the bursting period would have a crucial importance in understanding whether the dynamics of the near-wall region of a turbulent boundary layer is actually affected or not by the outer region. Unfortunately, a definite answer to this question has not yet been given, especially at high Reynolds number. A vast group of researchers, among which Blackwelder et al. [17], reported a scaling law in wall-units:

$$T_b \approx \frac{1}{400} T_\tau. \tag{2.40}$$

This scaling law was found appropriate for low-Reynolds number flows, which have a limited scale separation. On the other hand, Rao et al. [117] reported a relationship for the bursting period on outer variables:

$$T_b \approx 6 \frac{\delta}{u_\infty}. \tag{2.41}$$

To resolve this controversy, attempts were made to find a mixed scaling law [4], using both inner and outer variables. In the last decades more and more experimental investigations have shown that an outer scaling is more appropriate than an inner scaling, although the studies still cover a Reynolds number range not large enough to be considered conclusive. Very recently, Matzger et. al [101] built a new scaling of the bursting period based on the Taylor micro-scale, which removes both the observed Reynolds number and wall-normal trends in the scaling. This normalisation also makes the bursting period and duration independent of Reynolds number.

2.2.2 Hairpin packet / Vortex Cluster Organisation and LSMs (Large Scales of Motions)

The region slightly farther away from the wall, above the buffer layer, is also characterised by the presence of large lower and higher momentum coherent structures. The scale of these structures is of the order of the boundary layer thickness δ. They are referred to as Large Scales of Motions or briefly LSM. They are forward-leaning structures, which extend typically up to the edge of the boundary layer, where they are believed to create the bulges that appear in flow visualisations (see Figure 2.9).

As also reported by Klewicki [82], there are two schools of thought regarding the origin of these structures:

- Adrian and other researchers associate the LSMs with *hairpin vortex packets* [2, 131], which are well-defined in shape and are capable of self-regeneration;
- Jimenez and co-workers [69] believe that the LSMs are associated with the wakes of *vortex clusters*, less defined in shape.

The two models have many common points and many features of one model can be interpreted also as manifestation of a phenomenon in the other model. It is believed however that at low Reynolds number the theory of hairpin vortex packets better represents the physics of the flow, whereas at higher Reynolds number the theory of vortex clusters is more appropriate.

Hairpin Vortex Packets In the last decades the attention of large part of the research community has focused their studies on the hairpin packet model, especially after the extensive experimental studies by Adrian [2, 107, 138]. Hairpin-like and horseshoe vortices are considered as the key element of the dynamics of turbulent boundary layers. A hairpin vortex represents the simplest possible conceptual model that accounts for the essential features of turbulent dynamics near the wall.

Part (a) in Figure 2.14 [126] shows the expected shape of a hairpin vortex at different Reynolds number. The hairpin vortex shown is asymmetric and has a longer vortex leg, which is connected to a quasi-streamwise vortex underneath. In part (b) a conceptual model is presented, about how a single hairpin vortex is capable of generating regions of lower momentum underneath and how it is able to produce single ejection and sweep events, associated to turbulence production.

This conceptual model has been recently revisited by extensive Particle Image Velocimetry studies carried out by Adrian [2] using conditional sampling techniques[4]. Figure 2.15 shows the an instantaneous velocity vector field in the x-y plane. Adrian confirmed that the single hairpin vortex has an asymmetric structure and showed that

[4]conditional sampling is a selective criterion able to isolate the fluctuations of velocity which met a pre-defined condition, for example it is possible to select the velocity fluctuations which give a positive contribution to Reynolds stress production

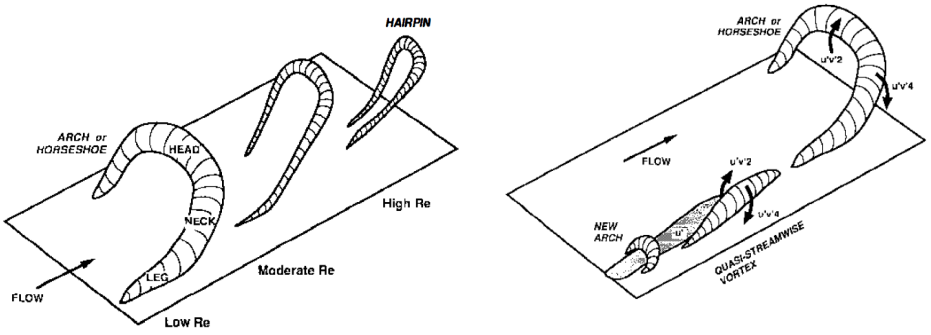

(a) Hairpin Vortex Shapes

(b) Dynamics associated with a single hairpin vortex at low Reynolds number

Figure 2.14: Robinson's hairpin vortex conceptual model (figure taken from [126])

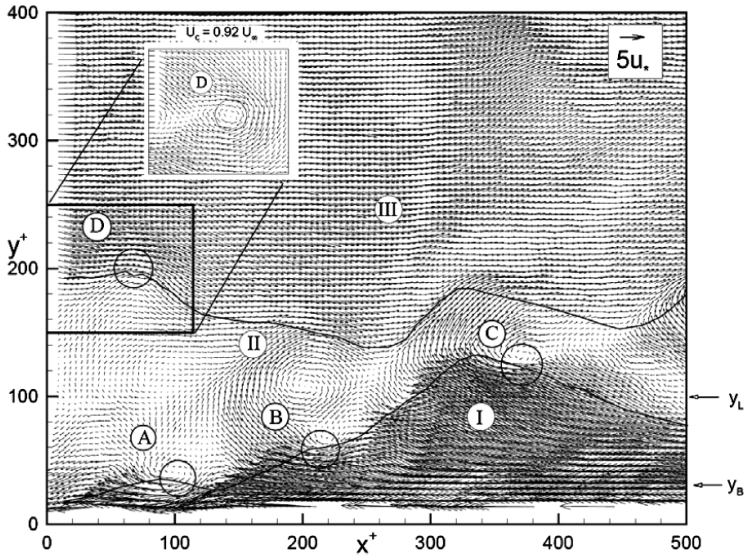

Figure 2.15: Velocity flow field obtained with Particle Image Velocimetry showing hairpin vortices in a turbulent boundary layer. The letters A,B,C,D indicate different hairpin vortices (figure taken from [2])

its legs tend to tilt away from the wall, with an inclination angle of about 45°. Also the presence of streamwise vortices attached to the two legs is confirmed. In addition, it was observed that hairpin vortices are not isolated, but are organized in hairpin vortex packets, which are aligned in the streamwise direction with increasing size downstream. This pattern is visible in Figure 2.15, where a hairpin vortex packet with three vortices A, B, C is observed. A single group of hairpins tends to propagate in the streamwise direction, with the single hairpin travelling at nearly the same speed. Within this framework, the formation of new hairpin vortices is accomplished by a process of auto-generation, described in detail in [2, 1].

While travelling downstream, the hairpin vortex packets tend to grow and to move towards the edge of the boundary layer. The growth in the wall-normal direction is observed to scale with the distance y from the wall, consistently an the Townsend's attached eddy model, which is an early model describing the dynamics of vortical structures in turbulent boundary layers [26, 126]. In addition, the single hairpin vortices appear to diffuse under the effect of the flow shear. Figure 2.16 shows an instantaneous snapshot of the flow field, in which three hairpin vortex packets appears. The

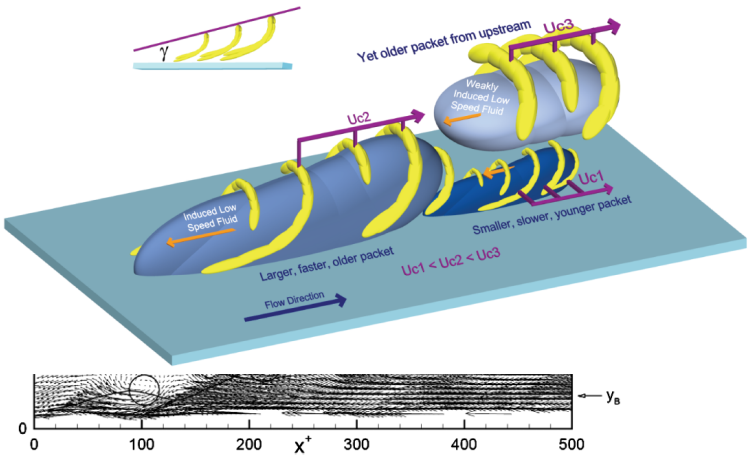

Figure 2.16: Conceptual instantaneous picture of hairpin vortex packet dynamics in a wall-bounded flow (figure taken from [2])

packet labelled as 2 travels at a velocity of U_{c2}. Closer to the wall, a younger packet is born at a velocity U_{c1}: being younger it is smaller and, being closer to the wall, its convection velocity is lower. The third packet is the oldest, so it is larger and its convection velocity U_{c3} is higher. It is important to observe that each hairpin vortex

packets is associated with a region of lower velocity in its interior, induced by the vorticity in the hairpin vortex legs and in the hairpin vortex head.

As the hairpin packets grow, they eventually end up meeting adjacent packets. When this happens, the packets are believed to interact and eventually merge, forming larger packet structures. The mechanism of merger are different and are summarized in Figure 2.17.

The hairpin packet organization is able to explain two important features related to

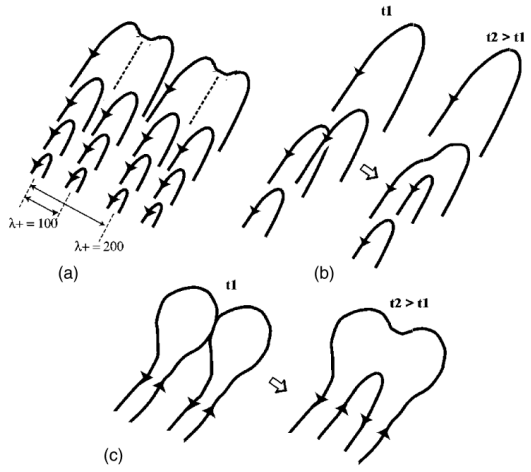

Figure 2.17: Different merging mechanisms of hairpin vortices (figure taken from [2])

the dynamics of the turbulent flow:

- *the long extent of streamwise sublayer streaks compared with the streamwise extent of the single streamwise vortices*: it is possible to assume that the streamwise streaks in the viscous sublayer are generated by the hairpin packets that travel closer to the wall, just above the buffer layer. The streamwise vortices described in Section 2.2.1 may be the streamwise vortices attached to the legs of the single hairpin vortices of these packets. It is therefore evident that a single streak is related to more than one streamwise vortex. Within this framework, the bursting phenomenon can also be regarded as the break-up of the flow produced by the passage of a hairpin vortex packet, associated to ejection and sweep events [2, 3].

- *the nature of the Large Scales of Motions LSMs*: in the hairpin vortex packet model, the LSMs appear to be the interior of the hairpin vortex packets which

travel in the region above the buffer layer up to the edge of the boundary layer, as shown in Figure 2.16. The bulges at the edge of the boundary layer may be associated to the passage of hairpin packets that have migrated to the outer region and have reached the edge of the boundary layer itself.

Although the hairpin vortex packet model is able to explain several features associated to the dynamics of a turbulent boundary layer, numerical simulations and experiments have shown the presence of hairpins only at low or moderate Reynolds number. For example, Schlatter et. al [131] performed DNS of a zero-pressure gradient turbulent boundary layer developing on a flat plate. The simulation was performed on a long domain, with Re_θ based on the boundary layer displacement thickness up to 4300. A visualisation of the turbulent boundary layer at low Reynolds number (Re_θ=60) is shown in part (a) of Figure 2.18, a visualisation at high Reynolds number (Re_θ=4300) is shown in part (b). Vortical structures are visualised by plotting iso-contours of swirling

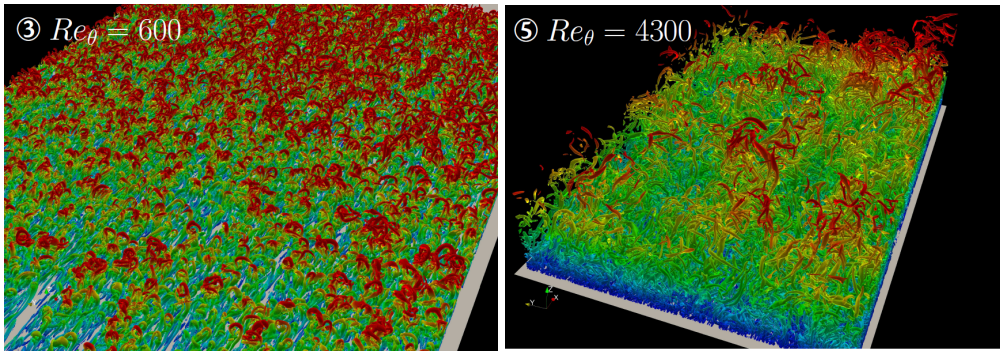

(a) DNS at Re_θ=600 (b) DNS at Re_θ=4300

Figure 2.18: Hairpin vortex organisation at low and high Reynolds number in a turbulent boundary layer computed with direct numerical simulations (figure taken from [131])

strength [5] coloured with a streamwise velocity magnitude. At low Reynolds number a hairpin vortex organisation is visible, with a well defined shape, especially the hairpin vortex head. However, at high Reynolds number, the vortical structures in the flow appear much more disorganised, and the individual hairpin cannot be seen any longer. In addition, large regions of higher and lower velocity appear, especially at the edge of the boundary layer. Therefore, the model of hairpin vortex packets does not appear to

[5]The swirling strength is the imaginary part of complex eigenvalues of velocity gradient tensor. It is positive if and only if the discriminant is positive and its value represents the strength of swirling motion around local centres

hold at high Reynolds number and more detailed studies are needed to identify what types of coherent structures are present in this case.

Vortex Clusters The vortex cluster model was outlined by Jimenez and co-workers on the basis of extensive DNS simulations [69]). According to this model, the vortex organisation above the buffer layer is not characterised by well defined hairpin vortex packets, but by vortex clusters, whose shape is amorphous and not well-defined. An example of a vortex cluster is shown in Figure 2.19. In part (a) the yellow object rep-

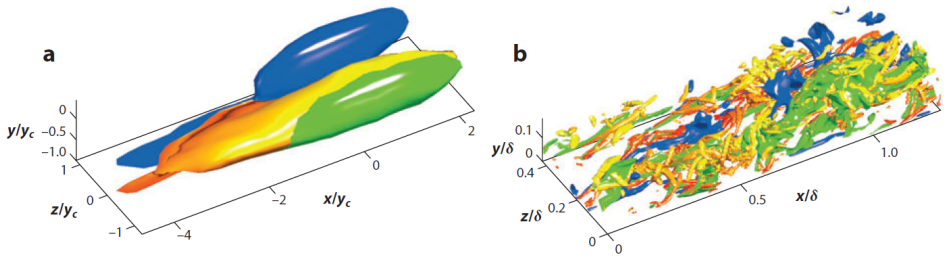

Figure 2.19: (a) Model of vortex cluster and associated regions of sweep (blue) and ejection. (b) Instantaneous realisation of vortex cluster in a DNS of a turbulent channel flow at Re_τ=934 (figure taken from [69])

resents a region of strong vorticity, associated to the vortex cluster. The blue and green regions at each side represent the structure of the averaged Reynolds shear stress, conditioned to the presence of a sweep events and ejection events respectively; in other words, the green and blue regions are regions in which sweeps and ejections have a high probability to occur. Part (b) of the Figure shows an instantaneous realisation of the flow field described in part (a), obtained from a DNS simulation of a turbulent channel flow at Re_τ=934.

These clusters are also believed to align in streamwise groups, probably much longer than the hairpin vortex packets. Vortex clusters can be distinguished as wall attached and wall detached. Wall attached vortex clusters populate the region just above the buffer layer and are found to be self-similar, in the sense that their dimension scales linearly with the distance from the wall. They present many features also attributed to the hairpin vortex packets. Their dynamics does not seem to be influenced much by the events below the buffer layer. Wall detached vortex clusters populate instead the outer region of the turbulent boundary layer. The large scales of motion arise from this

organisation, being the "wakes" of the vortex cluster motions. These wakes should be interpreted as a momentum field redistributions associated with the advection of the vortex clusters themselves [36, 82].

The vortex cluster model seems to better represent what happens in turbulent boundary layers at higher Reynolds number and in the region above $y^+ = 200$. Probably the differences between the vortex cluster and the hairpin vortex packet model are not substantial and in future the models could be also be reconciled in a single broader model. For instance, quoting Jimenez [69] "*individual hairpin vortices can correspond to the instabilities of the shear layers around the streaks created by the ejections, especially if hairpins were allowed to be irregular or incomplete and the respective emphases on vortices and on larger eddies might be influences by the relatively coarse resolution of many experiments, which cannot resolve individual vortices*". This means that the vortex cluster model may be related to the hairpin vortex model, however the limited spatial resolution of the current field measurement techniques could not resolve the single hairpin vortices and the packet organisation, especially because the shape of the single vortical structures is believed to be much more irregular and asymmetric than what described in the earliest conceptual models.

2.2.3 VLSMs (Very Large Scales of Motion in the Outer Layer)

The Very Large Scale of motions (or VLSMs, also called superstructures) are very large scale structures, which are observed in the logarithmic region of turbulent wall-bounded flows at high Reynolds number. Experimental at high Reynolds number studies indeed revealed the presence very long and meandering streaks of lower/higher velocity, whose streamwise extent is of the order of 5-10δ, occasionally extending up to 20δ. Figure 2.20 shows the shape of a VLSM, identified with sonic anemometer measurements in an atmospheric boundary layer at very high Reynolds number, Re_τ=660,000 The dimension and and the contribution of the VLSMs to the dynamics of the flow increases considerably with the Reynolds number. They can be clearly identified only at Re_τ higher than 10,000. These structures are believed to carry a significant fraction of the total turbulent kinetic energy [99, 98, 2].

The effect of the VLSMs on the streamwise turbulence intensity is illustrated in Figure 2.21, taken from [98] The streamwise turbulence intensity, normalised in wall units, is plotted versus the distance from the wall, also normalised in wall units and indicated

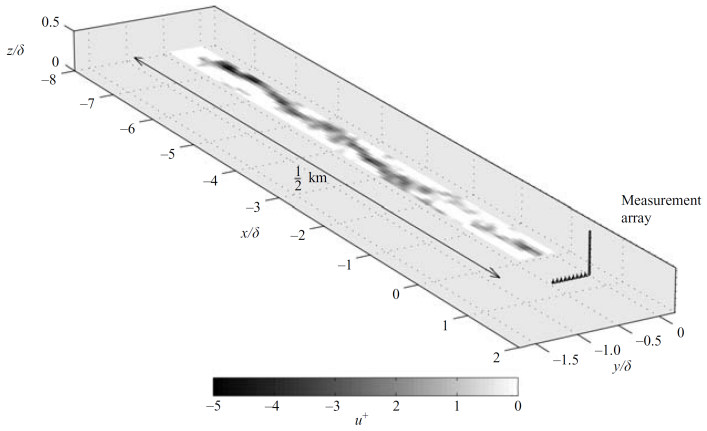

Figure 2.20: Long and meandering structure of a VLSMs identified in an atmospheric boundary layer at Re_τ=660000 (Figure taken from [59])

with z^+ in this case. Cases at different Reynolds number are plotted from Re_τ=500 to 19000. The turbulence intensity profile at low Reynolds number, Re_τ=500 , presents a

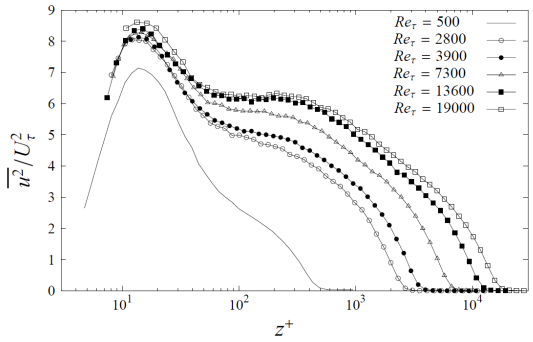

Figure 2.21: Streamwise turbulence intensity profile at different Reynolds numbers (figure taken from [98])

peak in correspondence of the edge of the buffer layer ($y^+ \approx 12$), which is related to the turbulence production within the near-wall cycle. As the Reynolds number increases, the magnitude of this peak increases too and, in addition, the turbulence intensity values between z^+=100 and 1000 (so in the logarithmic layer) strongly increases. At Re_τ=13,600 a second turbulence intensity peak is present at $z^+ \approx 200$. The appearance of this second peak is believed to be related to the appearance of the VLSMs, which increases the level of velocity fluctuations in the logarithmic layer.

The mechanism of formation of the VLSMs in high Reynolds number flows is not

clear, although it seems plausible that they might be a concatenations of hairpin vortex packets or vortex clusters. They might also arise from some large scale instability associated with the turbulent/non-turbulent interface at the the edge of the boundary layer.

Even if they affect the velocity fluctuations mainly in the logarithmic region, the VLSMs appear to have an influence that extends down to the wall, where a large-scale velocity footprint is superimposed on the near-wall turbulence. These structures appear to affect the near-wall cycle, challenging the classical view that this is independent of the outer region [96]. This interaction resembles that of an amplitude modulation of the small scales by the large scales [98, 96]. In Figure 2.22 a diagram illustrating this concept is shown [96]. The picture can be interpreted as an instantaneous snapshot of

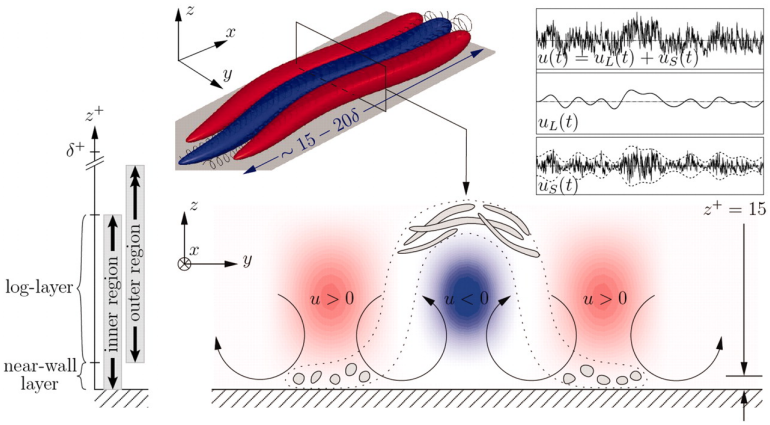

Figure 2.22: Interaction between the VLSMs and the near-wall structures across the turbulent boundary layer (figure taken from [96])

the flow field in the cross-flow plane indicated at the top. The VLSMs in the logarithmic region impose a velocity modulation on the flow in the near-wall cycle. Within a large scale low-speed event (blue region) close to the wall, the near-wall cycle is actually inhibited, whereas farther from the wall the small scale fluctuations are amplified. The reversed scenario is observed within a high speed fluctuation, indicated in red.

The current understanding of the dynamics of the VLSMs is very basic and further studies are therefore necessary to fully characterise their impact in the dynamics of the flow, especially because high Reynolds number flows are of greater technological importance than low Reynolds number flows.

2.3 Skin Friction Drag Reduction Methodologies

In the last decades, many developments on the field of flow control for skin friction drag reduction have been achieved. This Section contains a review of the most promising flow control methods, focusing on the reduction of drag in turbulent wall-bounded flows.

The flow control strategies aiming to achieve drag reduction have historically progressed in two directions: laminar flow control (LFC) and turbulent drag reduction (TDR). Laminar flow control (LFC) is a strategy based on the delay or prevention of the boundary layer laminar-turbulent transition. Indeed a laminar boundary layer is associated with a lower skin friction drag. Laminar flow control can be achieved by either by properly shaping the body to mitigate adverse and destabilizing pressure gradients (Natural Laminar Flow) or by using passive or active control systems to damp the disturbance modes leading to instability and transition (Active Laminar Flow Control). The greatest advantage of LFC is the fact that the control strategy is implemented in a laminar flow, in which the level of fluctuation of the flow variables is much lower than in a turbulent flow. This makes the control system operation much easier. The greatest disadvantage is that in many situations LFC is not at all applicable. Among others, such situations include flow at very high Reynolds number, flows in high-noise environments, flows over surfaces with large roughness, flows around intersection regions or "contamination areas" etc. These situation limit the applicability of LFC to a portion of the wing or fuselage total area. If a laminar flow cannot be maintained, it is possible to achieve a mitigation of skin friction drag in a turbulent boundary layer: this strategy is also referred to as turbulent drag reduction. In this section a review of the research activities focused on turbulent drag reduction is presented. Research on this subject is vast and quite different according to the field of application (aeronautics, bluff bodies, wind turbines etc.), so it has been decided to focus more on the aeronautical applications, mainly following the review of Bushnell [24].

2.3.1 Turbulent Drag Reduction

The starting point in the development a turbulent drag reduction strategy is the definition of skin friction drag

$$D = \tau_w S_w = \frac{1}{2} \rho u_\infty^2 S_w C_f.$$

It is clear that skin friction drag can be lowered by reducing combinations of wetted area S_w, skin friction coefficient C_f or the local dynamic pressure $\frac{1}{2}\rho u_\infty^2$. These three approaches are summarized in Figure 2.23.

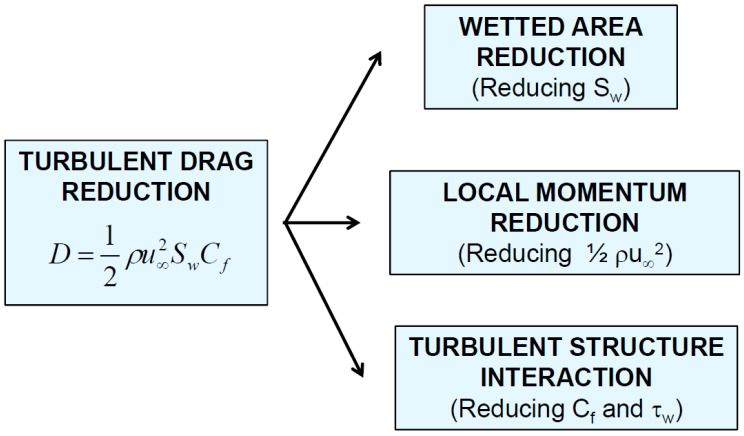

Figure 2.23: Approaches to pursue turbulent drag reduction (TDR)

A wetted area reduction can be obtained using active control or thrust vectoring devices, which produce reductions in the control surface wetted area, and innovative configuration approaches such as blended wing bodies, which obviate much of the fuselage wetted area [24]. The latter approaches also are referred to as shape optimisation.

Skin friction drag reduction can also be achieved through a local reduction of dynamic pressure $\frac{1}{2}\rho u_\infty^2$ or equivalently of longitudinal momentum ρu_∞. This can be obtained by reducing either the local freestream velocity u_∞ or the local density ρ. The most developed flow control techniques within this category are the wall heating and the wall injection/suction strategies. Wall heating is only applicable to air flows. The increase in the air temperature near the wall results in a decrease in local density, but also in reduction of Reynolds number, which causes a thickening of the boundary layer and a reduction of C_f as a further benefit. Sources of heat in an aircraft are available, for example, by exploiting the "waste heat" from engine cooling system or heat generated by fuel cells. Wall injection/suction consists in injecting low-momentum air parallel to the stream direction, so that for a certain distance downstream the wall senses a lower

freestream velocity. This results in a reduction of the overall momentum and in a reduction of drag. Even if this technology has been proven quite effective, it has never been implemented in practice, essentially due to the difficulties in obtaining low-loss air to be injected and due to the substantial modifications required to the airframe [24].

The most interesting and promising methods of achieving turbulent drag reduction are based on reduction of the skin friction coefficient at constant dynamic pressure and wetted area. This can be achieved by modifying the dynamics of the turbulent boundary layer. This research field is also referred to as turbulent structure interaction. The development of such methods is strongly related to the organised motion of the turbulent boundary layer. Different flow control strategies based on this principle are presented in more detail in Section 2.3.2.

2.3.2 Turbulent Drag Reduction via Turbulence Structure Interaction

We can group the flow control strategies for skin friction drag reduction via turbulence structure interaction into different categories.

- as for the presence or not of energy injection into the flow, we can distinguish between *passive strategies*, in which no energy is added to the flow field (hence no actuator is present) and *active strategies*, in which energy is added to the flow field, by means of one or more actuators;
- as for the region of application of the active/passive flow control device, following the review by Choi [30], we can distinguish between *near-wall control strategies*, involving an intervention on the near-wall turbulence structures (streamwise streaks and vortices) by forcing the flow at the wall itself and *outer-layer control strategies*, based on an intervention on the coherent structures resident in the outer region of the turbulent layer.
- as for the type of intervention on the turbulent boundary layer coherent structures, we can in addition distinguish between *global control* in which the flow is forced globally, without targeting the single coherent structures, and *targeted control* in which the single coherent structures (streaks, vortices, hairpin packet

etc.) are be identified and then weakened/suppressed singularly. Passive strategies can be only global, because no actuator is present and therefore an intelligent targeting of the single coherent structures cannot be achieved.

Figure 2.24 illustrates this classification.

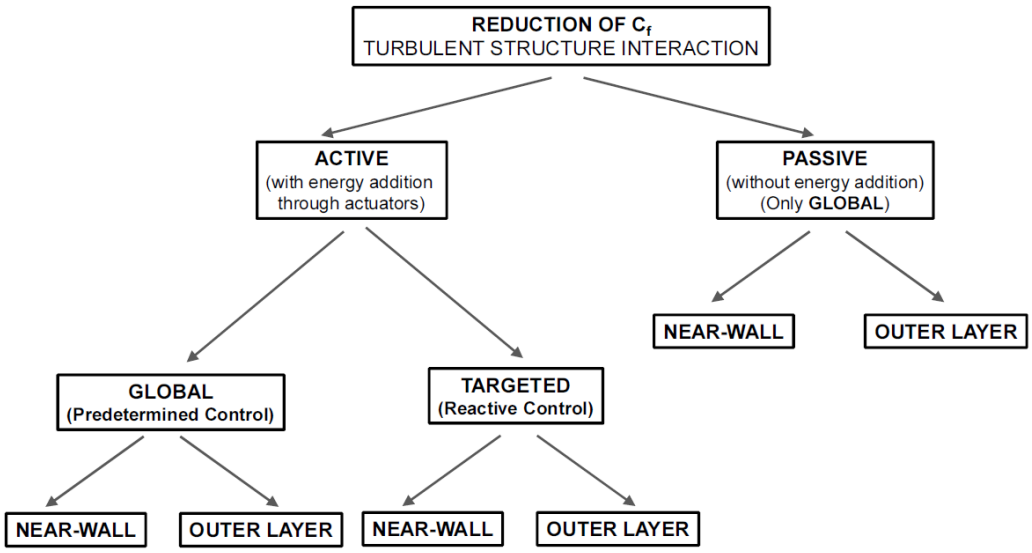

Figure 2.24: Classification of skin friction drag reduction strategies via turbulence structure interaction

Passive Strategies

Riblets The most popular passive strategy, studied and tested for at least three decades is riblets. Riblets are very small longitudinal striations, typically with a reversed V shape, which are superimposed to the wetted surface, see Figure 2.25. The develop-

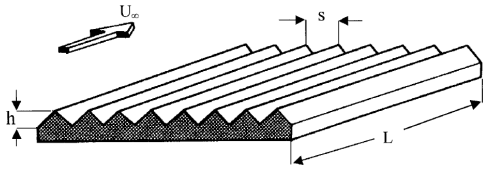

Figure 2.25: Classical riblet geometry

ment of riblets started in late 1970s at the NASA Langley Research Centre [24]. Riblet solutions have also been pursued by nature: indeed, the fastest sharks have a riblet-like skin. Many studies have been carried out in the last decades on the optimal shape of riblets. Alternative geometries have been proposed, among which are three-dimensional

riblets with a finite streamwise length.

The skin friction drag reduction associated with riblets results from the net effect of two important changes: a drastic increase in wetted area and a consistent reduction of skin friction coefficient per unit area. The reduction in skin friction drag due to riblets strongly depends on the parameter s^+, the riblet spacing normalised in wall units. Figure 2.26 shows experimental data of wall shear stress reduction as a function of s^+ The

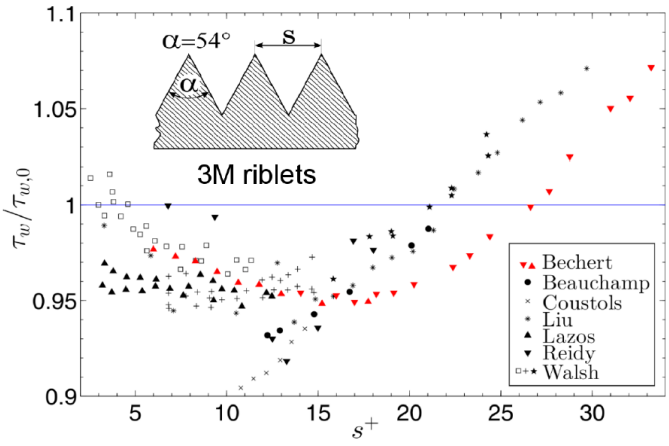

Figure 2.26: Experimental data reporting wall shear stress reduction achieved with riblets as a function of s^+ (figure taken from [39])

maximum skin wall shear stress reduction is about of 5-6%, but this value is reduced in practice to 2-3% because only the 40-50% of the total wetted surface of an airplane or of a vessel can be covered by riblets. The beneficial effect has been observed over a great range of Reynolds number and also in the presence of moderate longitudinal pressure gradients. A minor sensitivity to the yaw angle has been shown up to 30°, but for yaw angle higher than this value riblets are not effective any longer.

Drag reduction associated with riblets is not observed in laminar flow, so it is believed that riblets affects the dynamics of the coherent turbulent boundary layer structures, especially the structures in the near-wall region (stremaiwse streaks and vortices). One school of thought is that riblets act as small longitudinal fences impeding the lateral movements of the streamwise vortices, causing a reduction of the bursting duration and intensity. Other researchers believe that riblets literally shift the boundary layer origin a little bit further away from the wall. This reduces the effect of down-wash during burst events [47].

Riblets can be applied to the surface of a wing/fuselage using special adhesive films. In aeronautics, Boeing and Airbus applied the riblet technology to up to 60% of the

wetted aircraft surface, showing a drag reduction of 2-3%. The most important disadvantage of riblet technology is the application time and the direct cost both for their application and maintenance. Latest assessments have concluded that, with the current fuel price and the cost of installing and maintaining riblet coatings, the performance benefits are minor. However by improving the technology, it may be possible to make riblet technology viable in future.

Super-hydrophobic surfaces The use of super-hydrophobic surfaces has also received a great deal of attention recently as a means of turbulent drag reduction for naval applications. Although it is not very relevant to aeronautics, it is worth mentioning something about this drag reduction method. The idea of super-hydrophobic surfaces comes from nature, as many biological surfaces are super-hydrophobic. For a quite comprehensive review on this technology one can refer to [127].

A superhydrophobic surface is essentially a micro-textured surface (see Figure 2.27), in which several micro-protrusion elements are manufactured. If the textured surface is immersed in water it entraps pockets (or bubbles) of air. If the groove size is small enough, the bubbles can lodge within the texture grooves, and the overlying water flow is mostly in contact with the entrapped air, instead of with the solid surface. This air layer can act as a lubricant for the outer flow, which can then effectively slip over the wall, experiencing reduced friction compared to conventional surfaces.

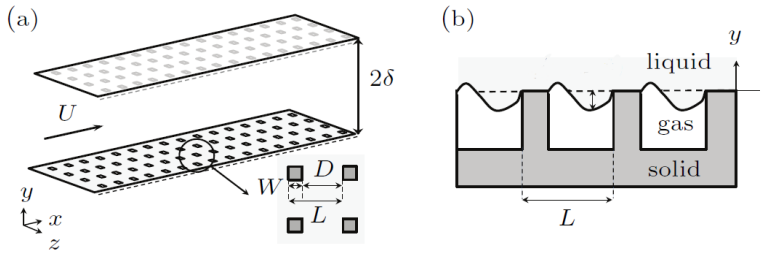

Figure 2.27: Superhydrophobic textures surface and interaction bewteen gas and liquid phases (figure taken from [46])

In principle super-hydrophobic surface can reduce skin friction also in a laminar boundary layer [127]. The theoretical work of Fukagata et al [42] explains how superhydrophobic surfaces alter the viscous sublayer in turbulent boundary layers. Numerical simulations have shown a reduction of skin friction at the wall as well as a reduction of

the peak of turbulence intensity at the edge of the buffer layer. Experimental works (especially that of Gogte et al [50]) report a combined reduction of skin friction/pressure drag of about 15%. The drag reduction effect is expected to increase with increasing Reynolds number, although this has not been yet established by experiments.
The main disadvantage of using super-hydrophobic surfaces is their fragility and the difficulty of their manufacturing process.

Large Eddy Breakup devices Large Eddy Breakup device, or synthetically LEBUs, are thin ribbon-like miniature aerofoils designed to be mounted within the boundary layers of the wing or fuselage surface of an aeroplane. One of the typical arrangement for LEBUs is illustrated in Figure 2.28: one or more splitter plates are placed in tandem in the outer region of a turbulent boundary layer. The development of LEBUs

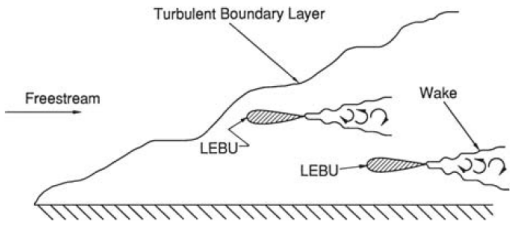

Figure 2.28: Typical gemoetry of Large eddy break up (LEBU) devices

started and continued in parallel to the riblet technology [7]. The main objective of LEBUs is to break up artificially the large scale structures in the outer region of the boundary layer. These devices have been shown to produce large skin friction drag reductions in several low-speed experiments, with peaks of the order of 30-40% and over long distances downstream. It is believed that a LEBU acts as an aerofoil operating in a gusty atmosphere, caused by the presence of vortical structures within the turbulent boundary layer: the starting vortex shed at the trailing edge of a LEBU, as a result of an incoming vortex upstream, produces a vortical structure of opposite sign. This structure cancels out the effect of the incoming vortex and so reduces the level of velocity fluctuation and of turbulence production.
The issues of LEBU technology are mainly related to two factors: an extreme sensitivity to flow conditions and the generation of a non-negligible pressure drag, which overwhelms the beneficial effects of their skin friction drag reduction.

Streamline Curvature Early studies by Bradshaw (see [23]) showed that streamline curvature has an important effect on turbulence production and, as a consequence, on skin friction drag. Bradshaw noticed that a concave longitudinal curvature tends to promote turbulence production because it triggers the formation of the so-called Gortler streamwise vortices[6]. The flow-field associated with these vortices strongly increases entrainment and enhances mixing, leading to an increase in turbulence production. On the contrary, a longitudinal convex curvature has been proved to give significant benefits in terms of reduced turbulence production as well as a lower skin friction drag.
Also in this case, the main disadvantage is the generation of a significant pressure drag, higher than the reduction of skin friction drag.

Introduction of Foreign Substances The introduction of foreign substances such as polymers [16, 154] is seen to be effective only in liquid flows, such as water or oil. Therefore, the interest in this type of drag reduction techniques is much more relevant for flows in pipe and channels. It is possible to apply this technology also to water vessels such as ships, boats or submarines. For more information the reader can refer to [45].

Active Strategies

In active strategies energy is injected into the flow by means an external device, such as an actuator. As shown in Figure 2.24 it is possible to distinguish between global and targeted strategies. In general, first a strategy is applied globally and then it may be refined by the application of sensors to improve its efficiency. In this case it becomes targeted, because the purpose of sensors is to identify a single of a group of coherent structures to control. Also a distinction between near-wall and outer layer control strategies can be made, although nowadays almost exclusively near-wall control strategies are developed.

In terms of the architecture of the control system, Gad El Hak [45] classified the active control strategies into two sub-categories: predetermined control and reactive control,

[6]Gortler vortices are secondary flows that appears in a boundary layer along a concave wall. If the boundary layer thickness is thin compared to the radius of curvature of the wall, the pressure remains constant across the boundary layer. On the other hand, if the boundary layer thickness is comparable to the radius of curvature, the centrifugal action creates a pressure variation across the boundary layer, which leads to a centrifugal instability, the Gortler instability, and the consequent formation of streamwise vortices, also called Gortler vortices.

as shown in Figure 2.29. Reactive control can be achieved by an open-loop strategy (or feed-forward) or by a closed-loop strategy (or feedback). In predetermined control, the

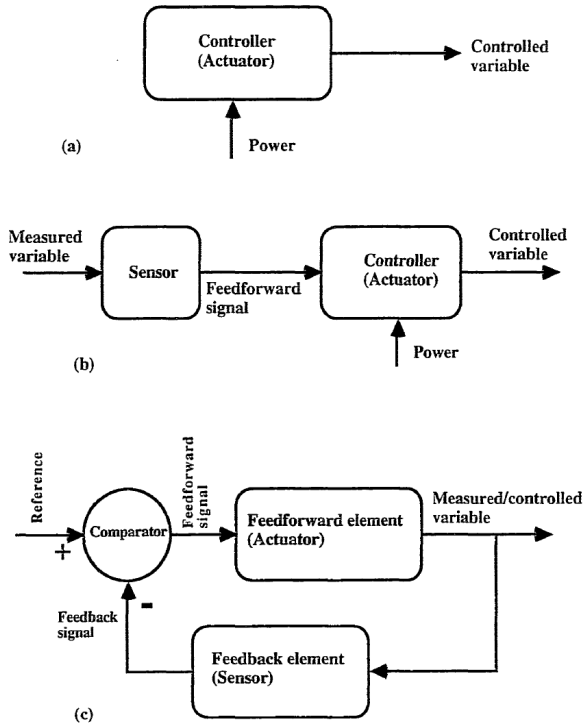

Figure 2.29: Active flow control strategies: (a) predetermined control, (b) feed-forward control, (c) feed-back control (figure taken from [45])

actuators input steady or unsteady energy into the flow without regard to the particular state of the flow itself. The operating parameters of the control system are set a priori. Case (b) and (c) are referred to as reactive control because in this case the input is adjusted based on measurements with sensors, which gather information on the state of the flow. In this case the operating parameters of the control systems are automatically regulated based on the information provided by the sensors. Reactive control can be divided into:

- *open-loop* or *feed-forward*, case (b): in this case the control variables and the measured variables may differ. For example, the pressure or velocity are measured using a sensor at a certain location, say x_1: this signal is used together with an appropriate control law to trigger an actuator, which in turn influences the velocity at a downstream position, say x_2;

- *closed-loop* or *feedback*, case (c): in this case the control variable and the measured variable must be the same (for example the velocity or pressure at a particular position x_1): this variable needs to be measured, fed back and compared with a reference input.

All the strategies reviewed in the next paragraph are near-wall control strategies. Outer control strategies are presented in the last paragraph.

Suction and Blowing from the Wall Uniform blowing and suction at the wall from a spanwise oriented slot was first tested by Park and Choi [108] using direct numerical simulations. The slot was 125 L_τ wide. The ratio of the blowing/suction velocity to the free-stream velocity was below 10%. With uniform blowing the streamwise vortices in the near-wall region downstream of the slot are lifted up, and thus their interaction with the streamwise streaks is weakened. This ultimately leads to a skin friction drag reduction. The opposite effect is observed in the case of suction. In the case of blowing, the skin friction however tends to increase further downstream of the slot because the streamwise vortices diffuse less and become stronger just downstream of the slot. The opposite behaviour occurs further downstream of the slot in case of suction.
Tardu [149] examined the effect of unsteady blowing from a spanwise slot, with blowing jet velocity varying from 0 and 5 u_τ. The forcing frequency was set to $f^+ = 0.017$, nearly the double of the bursting frequency of the turbulent boundary layer. The effect of the forcing was mainly that of a relaminarisation of the boundary layer in the region immediately downstream of the slot (for about 40 L_τ). This is due to the displacement of the streamwise vortices away from the wall and the formation of a thin vortex sheet of opposite sign in front of the wall. Downstream this region this vortex sheet tends to roll up so that the skin friction and the turbulent fluctuations grow.
Park, Lee and Sung [109], Park and Sung [110] investigated the possibility of using periodical blowing and suction from a spanwise slot in a water flow, first using hot-wire anemometry and then using Particle Image Velocimetry. The effect of the forcing frequency and amplitude was analysed. The jet to freestream velocity ratio was set to 0.4 and 0.6. It was found that the periodical forcing causes a region of skin friction reduction just downstream of the slot, about 100 L_τ long, after which the skin friction recovers the unforced boundary layer values. They concluded that the effect of blowing during the forcing cycle is predominant. The skin friction reduction appears to increase with the forcing frequency. The most effective forcing frequency was $f^+ = 0.088$. Phase-Locked PIV measurements showed that the structures responsible

of the drag reduction are periodically generated spanwise vortices which form in the vicinity of the wall and that gradually move away from the wall. Each periodical vortex creates a region of reversed flow in the near-wall region, which is responsible for drag reduction. If the forcing frequency is increased, two successive vortices are closer and their effect on skin friction reduction is increased.
Gad-el-Hak and Blackwelder [44] investigated the possibility of a targeted control using blowing and suction at the wall. Experiments were carried out in a laminar and turbulent boundary layer. Artificial streamwise streaks were created in the flow. In this case therefore the streak location is known a priori. An array of actuators operating suction and blowing at the wall was then employed to withdraw fluid after the passage of a low speed streak and to inject fluid after the passage of a high speed streak. In this way, the bursting process was inhibited. In addition, the spanwise velocity field of the controlled flow appeared to be more uniform, and therefore more stable. Very low values of the suction rate, 0.6 - 0.15% of the streamwise velocity, were proven to be effective for the purpose. These effects are illustrated in Figure 2.30.

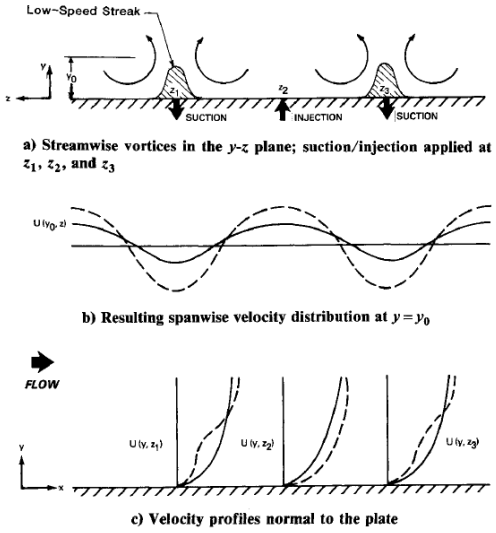

a) Streamwise vortices in the y-z plane; suction/injection applied at z_1, z_2, and z_3

b) Resulting spanwise velocity distribution at $y = y_0$

c) Velocity profiles normal to the plate

Figure 2.30: Effects of suction/injection on local velocity profiles: dashed lines are reference profiles and solid lines are profiles with suction/injection applied (figure taken from [44])

The strategy was resumed and extended to a turbulent boundary layer by Kerho [77]. Experimental activities first in a water tunnel and then in a wind tunnel were performed. In this case also flush mounted hot-film sensors were installed in order to identify the passage of low speed streaks. The actuation system was based on suction at the wall.

Due to the small dimension of the streaks and the high bursting frequencies involved, a MEMS based micro-valve were employed for the active suction port actuator. The basic unit of the system is shown in Figure 2.31. The streak is visualised using smoke.

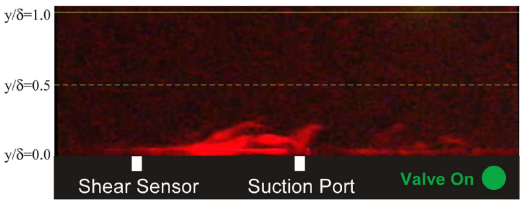

Figure 2.31: Basic unit of the flow control system developed by Kerho (figure taken from [77])

The bursting of the streak is visible and also the streak cancellation at the suction port. The study shows the feasibility of the selective suction approach.
Another similar targeted method to reduce skin friction drag is *opposition control*, which consists in imposing a velocity at the wall, opposite to that detected in the plane at y^+=12-15 i.e. in correspondence of the peak of turbulence production at the edge of the buffer layer. The imposed opposite velocity has the effect of counteracting the single sweep and ejection events in the buffer layer and consequently of reducing the turbulence production. The concept is illustrated in Figure 2.32. The method was de-

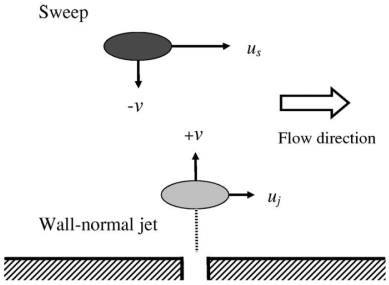

Figure 2.32: Working principle of the opposition control technique (figure taken from [120])

veloped by Choi, Moin and Kim [28], employing blowing and suction at the wall in a direct numerical simulation of a channel flow at Reynolds number 1800 and 3200 based on the centre-line velocity and the channel half-width. Numerically the strategy was implemented through a modification of the wall boundary condition. A skin friction drag reduction of 20 - 30% was achieved. Opposition control was also attempted with experiments by Choi and Rebbeck [120], in a wind tunnel using a hot-wire sensor

and a wall-normal jet actuator. In this case the experimental method only detects the most significant sweep and ejection events at a certain position on the wall and creates an opposite velocity at a point downstream, applied with a certain time delay, due to the convection velocity of the near-wall disturbances. The experiments showed that a "virtual wall" was created by the jet actuator, able to stop the advancement of sweep events.

In-Plane Wall Motion A significant levels of drag reduction can be achieved also with in-plane wall motion, which includes spanwise wall oscillations, spanwise travelling waves and streamwise travelling waves.
Spanwise wall oscillations were first investigated using direct numerical simulations by Jung, Mangiavacchi and Akhavan [73]. They showed that if the oscillation period is about $100\,T_\tau$ a drag reduction up to 40% can be achieved. The numerical simulations performed by Quadrio and Ricco [113, 124] revealed that the spanwise wall motion breaks the "coherency" between the streamwise vortices and the streamwise streaks, which results in an inhibition of the bursting process and in a decrease of turbulence production. The drag reduction was also confirmed experimentally by Laadhari et al [88], K.S. Choi et al [31] and Ricco [125, 122].
Turbulent boundary layer forcing with spanwise travelling waves was first proposed by Du et. al [37]. The application of spanwise travelling waves can achieve a skin friction drag up to 30% for low Reynolds numbers, however the efficiency is reduced as the Reynolds number increases. Xu and Choi [163] carried out an experimental study to reproduce this strategy, and obtained similar results in terms of skin friction drag reduction. The spanwise travelling waves were observed to spread the low-speed streaks and to amalgamate them in larger inactive areas in terms of turbulence production. Spanwise oscillation and spanwise travelling waves, have been also implemented through the utilisation of dielectric barrier discharge (DBD) plasma actuators. More details on these new actuators are reported for example in [32].
Streamwise travelling waves of spanwise wall velocity were also employed for skin friction drag reduction, see [37, 115, 114]. Waves which slowly travel forward produce a large drag reduction of drag, which can relaminarise the flow at low Reynolds numbers. The same effect is also observed for backward travelling waves.
The efficiency of in-plane wall motion to produce drag reduction also inspired recent innovative solutions, such as spinning or oscillating discs at the wall, which were tested with direct numerical simulations by Ricco et. al [123, 161]. In this case a drag

decrease up to 23% was obtained, with a net power saved of 10%. Although quite promising, these new approaches have not been tested yet with experiments.

Zero-Averaged Mass Flow Actuators Another widely used manipulation method consists in using mass-less flow actuators, or synthetic jets, in which periodical vortical structures essentially streamwise-oriented are produced without the necessity of an air or a water pneumatic source.

Jacobson and Reynolds [67] designed a control strategy using a piezo-ceramic cantilever beam actuator, installed flush with the wall. The beam is mounted over a small cavity and is driven at its resonant frequency. The beam does not exactly produce a zero-averaged mass jet, but its effect is that of producing periodical streamwise vortices, similarly to zero-averaged mass jets. The strategy was first applied to control steady disturbances generated downstream of a finite length cylinder mounted vertically across a laminar boundary layer in water flow. An illustration of these experiments is shown in Figure 2.33. If the Reynolds number based on the cylinder diameter

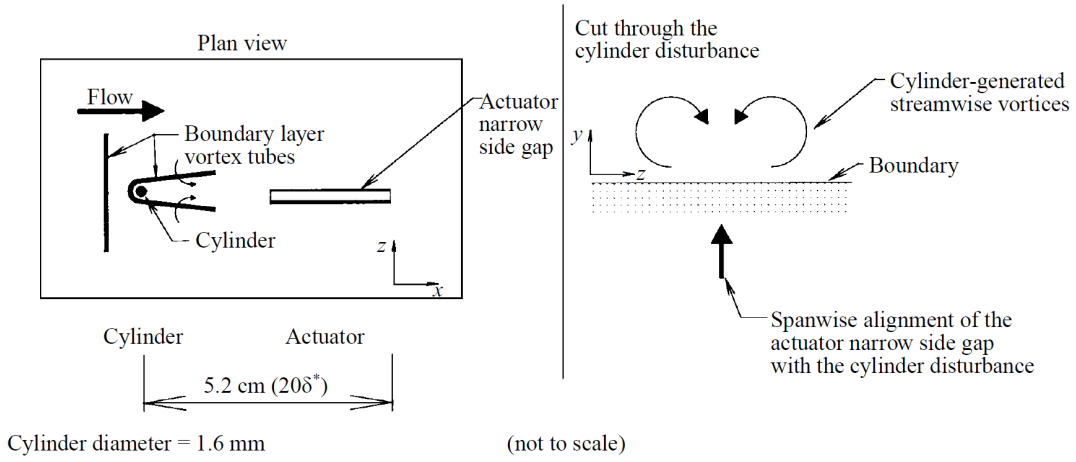

Figure 2.33: Schematic of the flow-control problem and of the position of the actuator (taken from [67])

d, $Re_d \doteq \frac{ud}{\nu}$ is larger than 40-50, the physics of flow around such a cylinder is illustrated in Figure 2.34. The interaction of the flat plate boundary layer with the boundary layer which develops around the lateral surface of the cylindrical rod generates a horseshoe vortex in the region just upstream. The trailing legs of the horseshoe vortex then

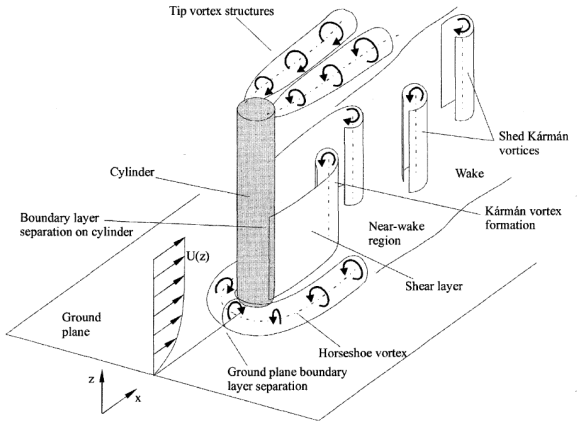

Figure 2.34: Flow structures around a circular cylinder in a boundary layer at $Re_d > 40$

develop downstream in the near-wall region forming two counter-rotating streamwise vortices. The flow structure also includes a von Karman vortex street, with vortices that are periodically shed in a region slightly farther away from the wall, and tip vortices that develop from the upper free end of the cylinder. The two streamwise vortices arising from the horseshoe vortex also induce two streamwise streaks close to the wall. Although the streamwise vortices rapidly decay, the streaks remain coherent for a large part of the flow-field downstream of the cylinder itself and eventually trigger the transition of the boundary layer. Jacobson and Reynolds carried out some measurements with a Laser Doppler Anemometer to derive the velocity field downstream of the cylinder, on a plane normal to the flat plate and located 20 δ^* downstream of it, where δ^* is the displacement thickness of the boundary layer of the undisturbed flow at the location of the cylinder. Their results are shown in Figure 2.35. In part (a) of Figure 2.35 the

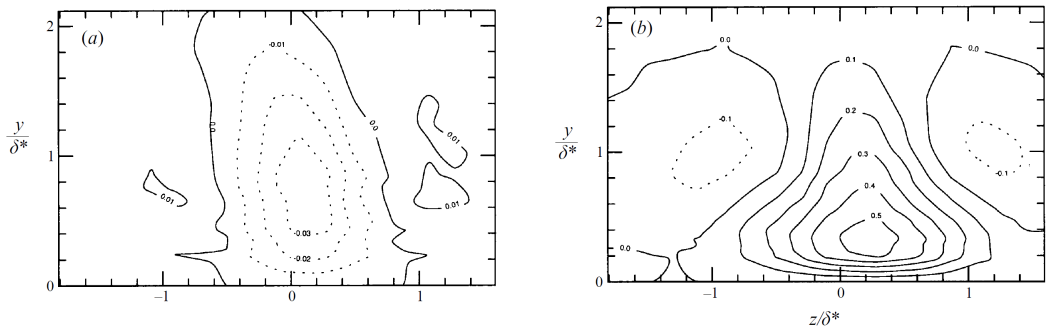

Figure 2.35: Velocity disturbance generated by the cylindrical rod 20δ^* from the location of the rod itself: (a) contour of the spanwise disturbance velocity (b) contour of the streamwise disturbance velocity (taken from [67])

contour of the spanwise disturbance velocity $\frac{v-v_{\text{und}}}{U_\infty}$ is plotted, whereas part (b) shows the contour of the streamwise disturbance velocity $\frac{u-u_{\text{und}}}{U_\infty}$, where u_{und} and v_{und} represent respectively the streamwise and spanwise velocity of the undisturbed flow (i.e. the laminar boundary layer developing over a flat plate). The disturbance velocity field is compatible with the existence of two streamwise vortices located approximately $y = \delta^*$ from the wall. The vortex signature is visible especially as a reduction of the streamwise disturbance velocity. In addition, there are two regions of alternating higher and lower velocity with respect to the undisturbed flow in the near-wall region up to 0.4 δ^* from the wall. Jacobson and Reynolds' objective was to introduce an artificial pair of counter-rotating streamwise vortices, in opposition to the vortices generated by the cylinder, in order to weaken the trailing legs and therefore delay the boundary layer transition caused by them. In order to estimate the beneficial effect of this interaction, they measured how far downstream the transition was delayed. Their set-up was mounted in a low turbulence level (with $u_{\text{RMS}} \approx 6\%$) water tunnel, with a free-stream velocity of 0.20 m/s. The diameter of the cylinder was $d = 1.6m$, yielding a Reynolds number based on the diameter of Re_d=320. By using this actuator they were able to delay the transition downstream by about 40 δ^*: their conclusion was that an actuator able to produce artificial coherent structures over a limited scale range can also be used to control disturbances over a wider scale range, which is the typical situation occurring in the general case of a turbulent boundary layer.
Successively Jacobson and Reynolds also employed the same type of actuator to control the flow downstream of an array of suction holes, which produces an artificial array of unsteady streamwise streaks downstream. The configuration of the control unit is shown in Figure 2.36. An array of sensors was placed downstream the suction hole to drive the array of actuators. When the control was switched on, the velocity modulation due to the suction holes was strongly weakened and a reduction of turbulence production and skin friction drag was obtained. To do this, a feed-forward open-loop control strategy was employed.

Lorkowski et al [94] attempted small-scale forcing of a turbulent boundary layer using a single synthetic jet actuator, with an orifice slot oriented in the streamwise direction. The convection velocity of the near-wall coherent structures was not influenced by the forcing. However an increase of their inclination angle was observed, which could be followed by a reduction in wall shear stress. This reduction was not however assessed in these experiments.

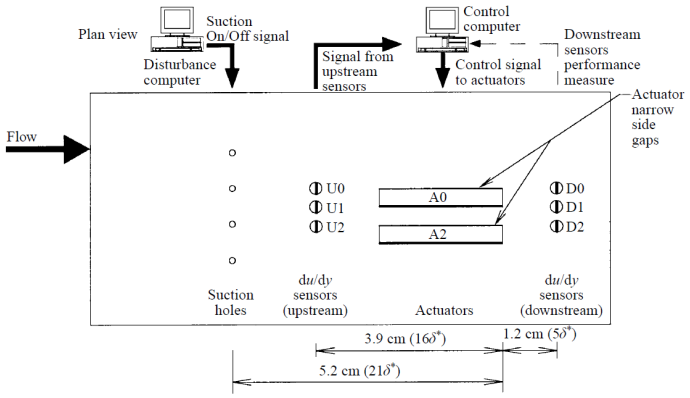

Figure 2.36: Schematic of the feed-forward control system developed by Jacobson and Reynolds (figure taken from [67])

Direct numerical simulations on the forcing effect exerted by an array of synthetic jets in a turbulent boundary layer were performed by Lee and Goldstein [92]. The array is composed of four slot orifices oriented in the streamwise direction. Each pair of adjacent slots functioned as a single unit, powered by a common diaphragm. The study was only preliminary and only a few operating conditions were tested. Therefore, a skin friction drag reduction was not observed in these cases. However the possibility of influencing the events related to specific near-wall coherent structures with the synthetic jet array was confirmed .

Rathnasingham and Breuer [119] developed a feed-forward control strategy of turbulent boundary layer using the same type of actuators used by Lorkowski [94]. The strategy employed an array of sensors followed by an array of actuators, see Figure 2.37. The feed-forward control method that they developed was linear, based on the assumption that the evolution of the near-wall disturbances can be predicted for a short period of time and for a short space extension, by means of linear equations. The control system is designed using a system-identification method and its objective was the reduction of the streamwise velocity and pressure fluctuation at a series of control points downstream of the array of actuators. They showed a reduction of streamwise velocity fluctuations of 30% and of a reduction of wall pressure fluctuations of 15% at the control points. As a by-product a net reduction of wall shear stress of 7% was also achieved.

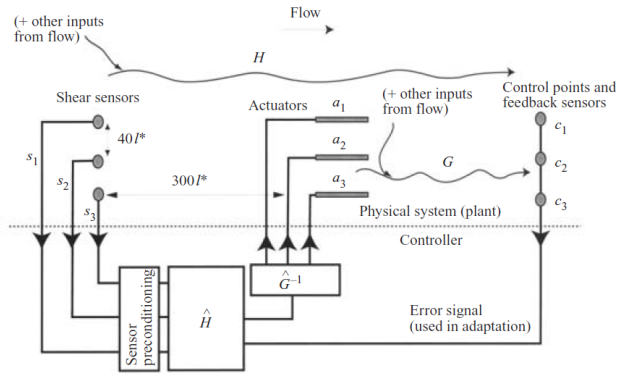

Figure 2.37: Schematic of the feed-forward control system developed by Rathasingham and Breuer (figure taken from [119])

Other Near-Wall Control Strategies Schoppa and Hussain [134] proposed a global strategy of near-wall control. They tested the strategy with DNS of a turbulent channel flow at Reynolds number 1800, based on the channel half-width. The strategy is based on a stabilisation of the near-wall flow by the imposition of an artificial low cross-flow motion (6% of the freestream streamwise velocity) . The cross-flow motion generates weak streamwise vortices, which act as stabilisers for the streak bursting. The effects of the control are shown in Figure 2.38. It is interesting to notice how the control

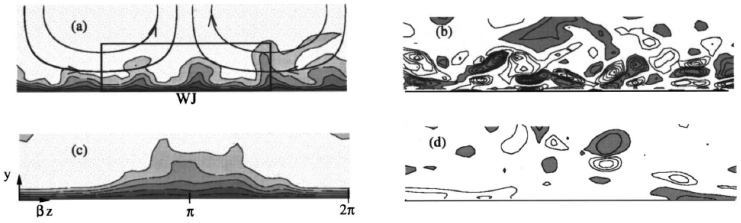

Figure 2.38: Large scale control strategy proposed by Schoppa and Hussain. Part (a) and (c): distribution of u in the cross flow without and with control respectively. Part (b) and (d): streamwise vorticity in the cross flow without and with control respectively (figure taken from [134])

techniques causes the disruption of the streaks and the attenuation of the streamwise vortices near the wall, resulting in a reduction of skin friction drag of 20%. The method was then experimentally reproduced with a similar configuration by Hutchins and Choi [58]. Although they were able to achieve a slight reduction of skin friction drag, not a complete agreement with the numerical results by Schoppa and Hussain was obtained, due most probably to the difficulty in setting a long lasting vortical motion in experiments with minimum device drag penalty.

Carlson and Lumley [27] used wall deformation to achieve a global boundary layer forcing. They numerically simulated a Gaussian bump actuator, approximately 12 L_τ high, which emerges from one of the channel walls. The effect of the actuator is to push the high-speed streaks away from the wall. The forcing is applied to a so-called minimal flow unit[7]. As a result, the surrounding low-speed streaks tend to spread, the near-wall cycle is weakened and, as a consequence, turbulence production is inhibited. Also in this case Yoshino, Suzuki and Kasagi tried to reproduce a similar set-up experimentally [164] by implementing MEMS (Micro-Electro-Mechanics Systems) sensors and actuators, achieving a drag reduction of 6%.

Outer Layer Control Strategies It has been already pointed how the near-wall control strategies tend to be less effective as the Reynolds number of the flow increases. In these cases, it might be more convenient to act on the large scales of motions of the flow, which mostly reside the outer part of the boundary layer. It has been already pointed out how passive devices, such as the LEBUs, acting on these structures, actually provide a significant positive contribution to the reduction of wall shear stress.
Kang and Choi [74] tried to implement this technique through an active strategy. By assuming that the LSMs are prevalently generated by the hairpin vortex packets, they named their control strategy as "direct intervention on hairpin structures". The technique is similar in concept to the opposition control technique previosuly described and addressing to the sweep events in the near-wall region. In fact, it basically consists in counteracting the up-wash motion of the hairpin vortices with jets issued from a nozzle, placed in the outer region of the turbulent boundary layer. The technique involves the detection of hairpin vortex packets, followed by an opposition control that directly counteracts the up-wash of low speed flow. The detection is performed by sensing the increase of streamwise velocity that occurs over the head of the hairpin packets as they pass near the edge of the boundary layer. The first effect achieved by the control system is to reduce the circulation around the hairpin legs. An exploratory study was presented in [74], in which experiments in a water tunnel were performed. Although the control parameters were not fully optimized, there was a strong indication of a significant skin friction drag reduction. The reduction of circulation around the hairpin legs may have a weakening effect on the streamwise vortices generating the streaks in the near-wall cycle. For more details on the implementation of this strategy it is possible to refer to [74, 30].

[7] A minimal flow-unit is essentially a box just large enough to sustain a turbulent flow: it contains only a pair of low and high streaks and a pair of streamwise of vortices

2.4 Introduction to Synthetic Jets

Synthetic jet actuators are flow control devices that are able to produce mass-less jets (or literally synthetic jets) by means of a diaphragm, which oscillates within a cavity. A schematic of a round synthetic jet actuator together with its fundamental dimensions and relative nomenclature is shown in Figure 2.39. The orifice plate is in direct contact

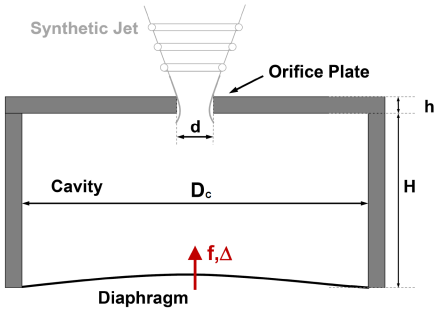

Figure 2.39: Schematic of a synthetic jet actuator

with the flow that one wishes to control. H is the cavity height, whereas h is the orifice depth. In the case of a round synthetic jet, the cavity is a circular cylinder; D_c is the diameter of the cavity, D_0 is the orifice diameter. The oscillation of the diaphragm is in regulated by the user through a shaker or a similar actuator. If the driving oscillation is sinusoidal, the frequency and amplitude of the oscillation are respectively indicated with f and Δ.

During a sinusoidal oscillation when the diaphragm moves downwards, it creates a depression which draws fluid from the external environment into the cavity. Conversely, when the diaphragm moves upwards, fluid is pushed out of the cavity; in this phase usually the flow separates and a free shear layer is formed at the location of the orifice. If the jet is sufficiently strong, the free shear layer tends to roll up and to form a coherent structure.

The behaviour of a synthetic jet can be described using non-dimensional numbers, based on the actuator geometry cavity, on the fluid properties, such as the kinematic viscosity ν, the fluid density ρ, and the quantities describing the oscillation of the diaphragm. The considerations reported below are valid for macro-scale synthetic jets operating at frequency f sufficiently far for the Helmholtz-resonance frequency of the

cavity. In case of micro-scale synthetic jets or synthetic jets operating at frequencies close to the resonance frequency of the cavity, more complex models need to be adopted (see for more information [170]).

2.4.1 Synthetic Jets in Quiescent Conditions

In case the synthetic jet is employed in a quiescent fluid, its behaviour is mainly characterized by two parameters, namely the Stokes number, defined as

$$S \doteq \sqrt{\frac{2\pi f D_0^2}{\nu}} \tag{2.42}$$

and the dimensionless stroke length, which is the height of the column of fluid pushed out of the orifice during the blowing part of the sinusoidal cycle, equal to:

$$L \doteq \frac{L_0}{D_0} \tag{2.43}$$

where L_0 is the dimensional stroke length, defined as:

$$L_0 \doteq \overline{U_0}\, T \tag{2.44}$$

and where T is the period of the diaphragm oscillation (equal to $1/f$) and $\overline{U_0}$ is the time-averaged blowing velocity during a sinusoidal oscillation of the diaphragm. Synthetic jets operating at frequencies f sufficiently far from the Helmholtz resonance frequency of the cavity can be modelled with a dynamic incompressible model: as a result, referring to Figure 2.39, $\overline{U_0}$ can be estimated as:

$$\overline{U_0} = \alpha \Delta f \left(\frac{D_c}{D_0}\right)^2. \tag{2.45}$$

where the coefficient α depends on the diaphragm material. Common values for α are about 0.25-0.3. In case a rigid diaphragm is used α is equal to 1. As a consequence of relation (2.45), the stroke length L can be estimated as:

$$L = \frac{L_0}{D_0} = \alpha \left(\frac{\Delta}{D_0}\right) \left(\frac{D_c}{D_0}\right)^2. \tag{2.46}$$

In some studies also another parameter appears, the Reynolds number based on the stroke length L, defined as

$$\mathrm{Re}_L \doteq \frac{\overline{U_0} L_0}{\nu}, \tag{2.47}$$

however it is easy to prove that this parameter is not independent of L and S, being

$$S = \sqrt{\frac{2\pi \mathrm{Re}_L}{L^2}}. \tag{2.48}$$

Every description involving two of the three parameters can be considered equivalent.

Each parameter can be related to a certain characteristic of the synthetic jet dynamics. In particular, it has been shown (see [170] for more details) that the Stokes number S affects the characteristic of the vortex roll-up. If S is lower than 10, the orifice exit velocity profile is of parabolic type; with this type of velocity profile a sufficient roll-up to create a vortex cannot occur. Therefore, a correct operation requires to achieve $S > 10$. In this case the orifice exit velocity profile assumes a top-hat profile, compatible with the generation of a vortex. The dimensionless stroke length L affects the amount of circulation that is contained in the primary vortex[8]: if L is lower than 0.5, the primary vortex cannot move sufficiently away and it is drawn back into the cavity again during the suction part of the cycle. If L is larger than 4, the circulation stored in the primary vortex becomes saturated and secondary vortices start to shed from it. Therefore an ideal value for L should be slightly higher than 0.5 and sufficiently lower than 4. The actuator geometry also affects the roll-up of the structures: indeed the vortex roll-up is enhanced if the ratio of the orifice height to the orifice diameter is lower than 1 i.e. $h/D_0 < 1$. The optimal value of h/D_0 has been found to be about 0.5 [170].

2.4.2 Synthetic Jets in a Laminar Boundary Layer

The interaction of the synthetic jet with a cross-flow (such as a laminar or a turbulent boundary layer) introduces other significant length, time and velocity scales, which must be kept into account when trying to characterize the behaviour of synthetic jet actuators by means of non-dimensional parameters. In the case of the interaction of the synthetic jets with a boundary layer flow, the actuator still produces periodical vortical

[8] In this discussion, a primary vortex is the largest and strongest vortex that is generated by the roll-up of the shear layer during the blowing part of a sinusoidal cycle. A secondary vortex is a smaller vortex which still develops during the blowing part of the cycle. Usually it is is undesired.

structures, but in this case after their generation these structures are convected downstream by the external flow. It is important to establish the dynamics and the evolution of the structures, which are also strongly influenced, in the case of a shear flow, by the interaction with the shear stresses.

The dimensionless parameters related to the synthetic jet performance are:

- the jet-to-freestreeam velocity ratio, also indicated by VR and defined as

$$\mathrm{VR} \doteq \frac{\overline{U_0}}{U_\infty}. \tag{2.49}$$

  This value represents the relative strength between the jet and the freestream velocity and characterises the trajectory of the jet itself within the boundary layer as well as that of the vortical structures as they start propagating downstream.

- the ratio of the boundary layer thickness δ to the diameter of the synthetic jet orifice D_0. As mentioned above, the synthetic jet structures also interact with the shear inside the boundary layer. The shear stress distribution depends on how thick the boundary layer is at the location of the synthetic jet with respect to the diameter of the jet itself.

- The magnitude of the wall shear stress itself and so the correspondent dimensionless parameter, which is the skin friction coefficient C_{fx}.

In addition, also the other parameters influencing the behaviour of the synthetic jet in quiescent condition play a role: these are L, S and h/D_0. It is also possible to form another non-dimensional parameter from the dimensionless stroke length and the velocity ratio: this is the Strohual number, which is widely used in the description of periodical phenomena in fluid flows and is equal to:

$$\mathrm{St} = \frac{\mathrm{VR}}{L} = \frac{f D_0}{U_\infty}. \tag{2.50}$$

The Strouhal number can be regarded as a dimensionless frequency and can be related to the frequency of the coherent structure shedding from the synthetic jet during its operation.

Studies have been carried out at the University of Manchester to understand in detail

the type of coherent structures produced by synthetic jets as a function of the dimensionless parameters defined above [66, 170, 174, 65]. Emphasis has been placed not only on the type of structures generated, but also on the conditions that ensure their formation. These studies have led to the construction of the parametric map shown in Figure 2.40. The map shows in abscissa the dimensionless stroke length and in

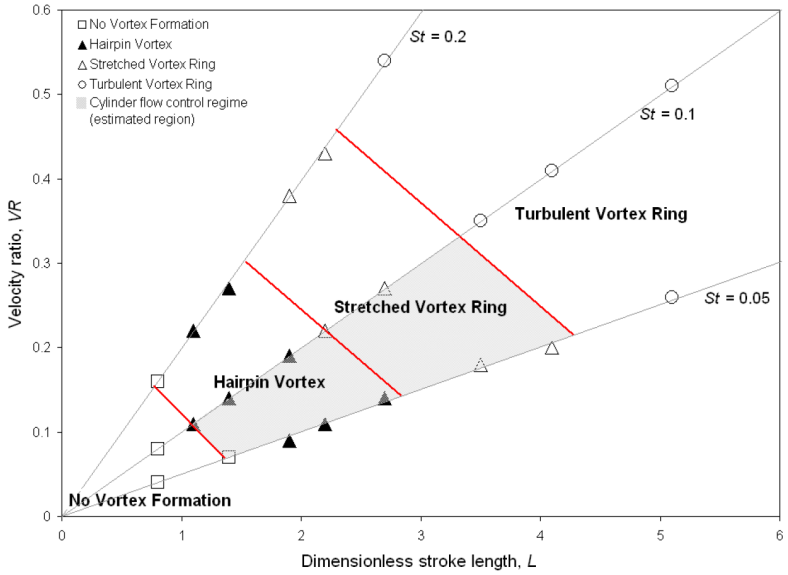

Figure 2.40: VR - L parametric map showing the different vortical structures produced by a synthetic jet in a laminar boundary layer, obtained with experiments (figure taken from [170])

ordinate the velocity ratio: the straight lines passing through the origin are lines at constant trouhal number, being St=VR/L. The same map has been also extended by Zhou through a number of detailed numerical simulations [172] and is shown in Figure 2.41. From both maps, it is possible to see how the combination of these two parameters yields different types of structures. It is evident the presence of a parametric region, resulting from a combination of low values both for velocity ratio VR and stroke length L, in which no structure formation is possible. For higher values of VR and L mainly three type of structures have been observed, described below. In Figure 2.42 a schematic drawing of two of these vortical structures is shown. The same structures educed in a numerical simulation with the Q-criterion [9] is reported in Figure 2.43. These structures can be classified into three categories:

[9] Q is a scalar used to visualize turbulent fields especially in boundary layer flows (or mixing layera) in which the vorticity due to vortex motion is overshadowed by the vorticity component due to velocity

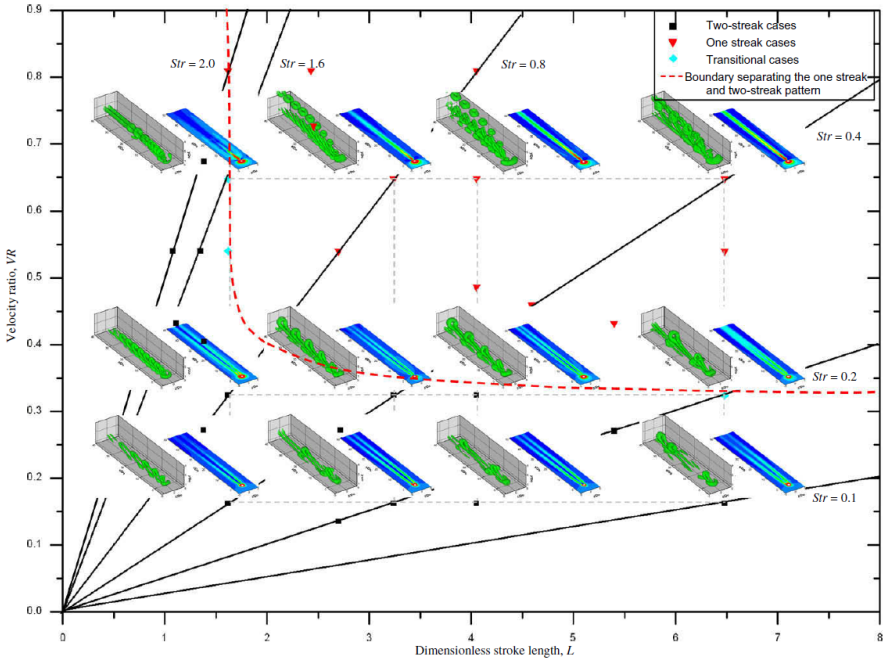

Figure 2.41: VR-L parametric map showing the different vortical structures produced by a synthetic jet in a laminar boundary layer, obtained with numerical simulations. The corresponding time-averaged wall shear stress pattern is also shown. One-streak cases correspond to tilted vortex rings, two-streak cases correspond to hairpin vortices (figure taken from [172])

.

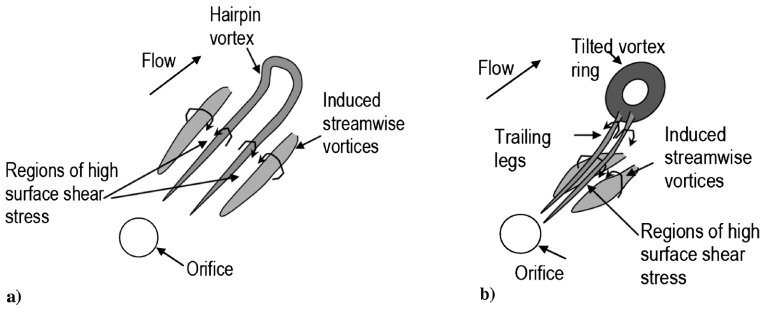

Figure 2.42: Schematic of (a) a hairpin vortex and of (b) a tilted vortex ring and related induced secondary structures produced by a single round synthetic jet (taken from [165])

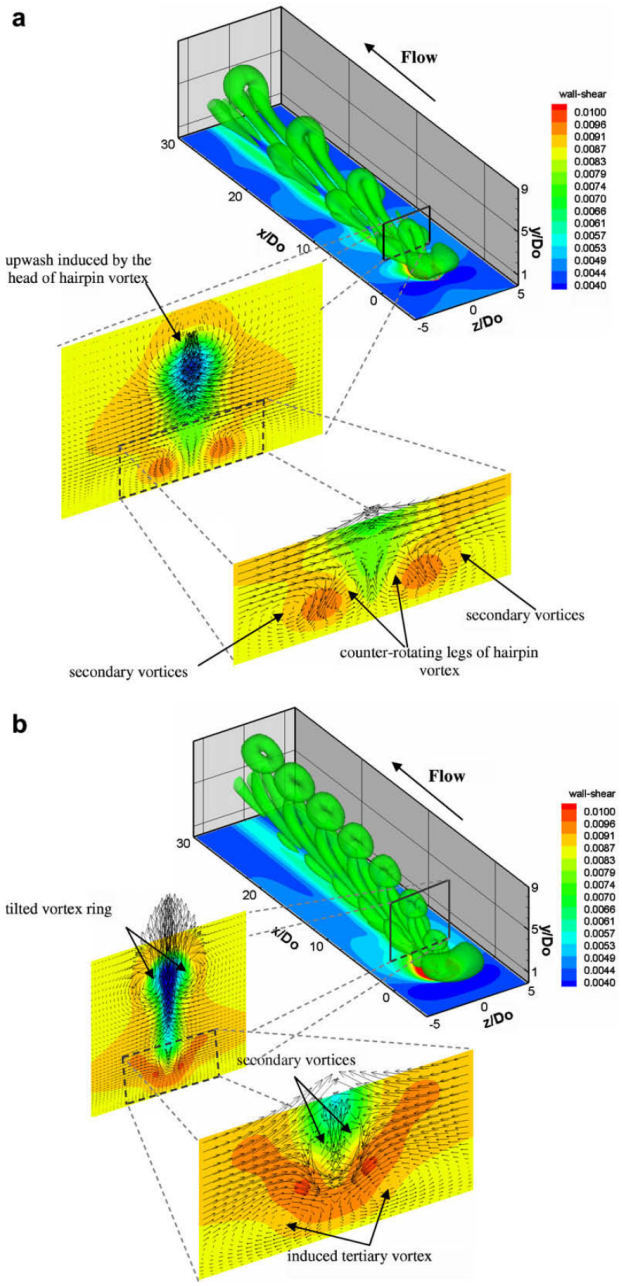

Figure 2.43: Instantaneous iso-surfaces of Q = 0.1 of (a) hairpin vortices and (b) tilted vortex rings (figure taken from [172])

- *hairpin vortices*: these have an elongated shape, formed by two legs which connect to a head (see part (a) of Figure 2.42). After they form, they start to convect downstream, at a velocity which is more or less equal to that of the local flow. Because of the low value of VR, these structures tend to stay in the near-wall region of the boundary layer. For this reason their development is strongly affected by the higher level of shear stress typical of the near-wall region and their legs experience a significant vortex stretching. In addition hairpin vortices also formed for low values of the dimensionless stroke length: this means that the suction stroke is dominant for them, because they cannot move sufficiently downstream during the blowing part of the cycle to become unaffected by the successive suction part. This can be noticed by observing that the hairpin vortex legs can be tracked back to the orifice during dye visualisation experiments or in numerical simulations. Hairpin vortices are the weakest structures that are produced by a synthetic jet and, because of that, their ability to affect the outer region of the boundary layer region appears limited. The two hairpin legs also produce two counter-rotating streamwise vortices located laterally to the primary vortex legs (see again part (a) of Figure 2.42): these structures are created by induction by the hairpin legs themselves. The presence of these structures is confirmed both by experimental tests [66] and by numerical simulations [174];

- *stretched vortex rings*, which form for higher values of VR and *L*. The difference with hairpin structures are mainly two: an increased roll-up of the head of the structure and a well defined detachment of the legs of the vortices from the wall, which is due to a much lower influence by the suction part of the cycle. The effect on the dynamics of the near-wall region is similar to that of the hairpin structures, however their impact is larger, due to the fact that they are stronger.

- *tilted vortex rings* are formed essentially in the parametric region in which the velocity ratio is approximately higher than 0.4 and L is higher than 1-1.5. A schematic of a tilted vortex ring is shown in part (b) of Figure 2.42. Tilted vortex rings are characterised by an intense roll-up of the head of the structures, much more evident than in stretched vortex rings. This leads to the formation of a

gradients, quite high in these cases. Given that, it is possible to use the parameter Q, defined as:

$$Q \doteq -\frac{1}{2}\frac{\partial u_i}{\partial x_j}\frac{\partial u_j}{\partial x_i}.$$

Areas of positive Q represent regions in the flow where the rotation dominates strain and shear.

ring-like structure. The high value of VR ensures that the structure penetrates well the boundary layer, reducing the effect of the boundary layer shear on it. These structures are not as stable as the hairpin vortices and stretched vortex rings: this results in an almost immediate formation of secondary structures. As also mentioned above, secondary structures are observed to form at $L > 4$. Another interesting characteristic of tilted vortex rings is the fact that they also generate a tertiary structure, namely a pair of two side-by-side counter-rotating vortices located below the primary structures and downstream of the orifice (see part (b) of Figure 2.42). It is believed that these vortices are responsible for the generation of a region of high wall shear stress located downstream of the orifice, visible in wall shear stress visualisations. The tilted vortex rings are the strongest structures produced by a synthetic jet and, as such, they are expected to have the strongest effects in affecting the flow behaviour.

2.4.3 Synthetic Jets in a Turbulent Boundary Layer

At present, the knowledge of the interaction of synthetic jets with a turbulent boundary layer is not as detailed as for a laminar one, but some studies have been undertaken to evaluate the differences between these two cases. As also reported in [66], it is expected that the type of vortical structures produced by synthetic jet in a turbulent boundary layer is qualitatively similar to those produced in a laminar one: the main difference is believed to be the dissipation rate of the structures in the near-wall region due to the higher shear stresses present in a turbulent boundary layer.

The coherent structures produced by synthetic jets in a turbulent boundary layer strongly interact with the coherent structures that naturally form inside it. For instance, it has been shown [158] that the turbulent boundary layer hairpin vortices present very similar characteristics to those produced by the synthetic jets, in terms of shape, induced secondary structures and evolution process. The interaction between the two kinds of structures has to be taken into consideration carefully in each single case.

At the University of Manchester some studies have been carried out in a wind tunnel at a free-stream velocity of 28 m/s, to establish the effect of interaction of a single round synthetic jet on a boundary layer. The results are documented in [170] and also shown in Figure 2.44. The velocity field was measured with a hot-wire anemometer. The oscillation frequency was set to 1.6 kHz and the velocity ratio was estimated to be

about 0.5. In part (a) of Figure 2.44 velocity contours of the streamwise velocity on a streamwise plane passing through the centre of the synthetic jet orifice are shown. The boundary layer is periodically disturbed by the vortical structures generated by

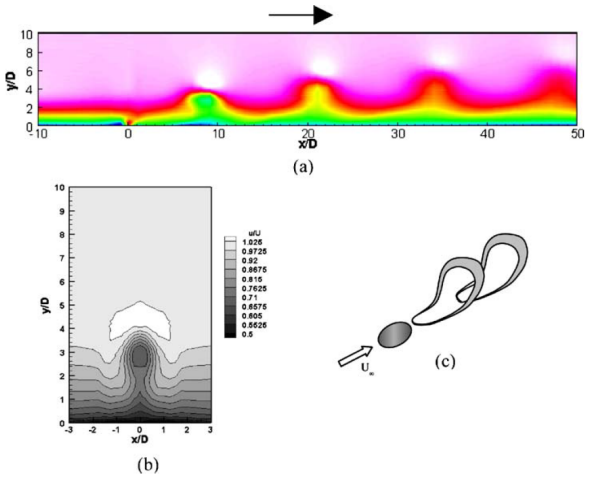

Figure 2.44: Interaction of a synthetic jet and a turbulent boundary layer operated at $S = 29$, $St = 0.07$ and VR=5. (a) velocity contour map obtained with Hot-Wire Anemometry in the longitudinal plane (b) velocity contour map in cross-flow (c) schematic of the expected coherent structures produced by the synthetic jet (figure taken from [170])

the synthetic jet. In part (b) velocity contours on a cross-stream spanwise plane during the passage of a vortical structure are shown. These results are interpreted in part (c) of Figure 2.44, in which a sketch of the vortical structure responsible for the observed velocity field is shown. The structure looks like a highly stretched vortex ring, whose size increases as it convects downstream. In any case, the structure remains coherent at least for a distance of 50 D_0 from the synthetic jet orifice. These structures have also been shown to provide beneficial effects in terms of delaying flow separation.

A large eddy simulation of a synthetic jet operating at VR=0.17 and L=1.7 was also carried out by Tang [158]. The results of this simulation are compared directly to those of a laminar boundary layer at the same free-stream velocity. It was found that in both cases hairpin vortices are produced by the synthetic jet. In the case of the turbulent boundary layer the hairpin vortices travel faster and have a more bent shape than in laminar flow. Due to the presence of many background coherent structures, the shape of the hairpin vortex in the turbulent boundary layer is asymmetric and presents a lateral oscillation while it moves downstream. In addition, due to the higher level of

shear, the hairpin vortex in the turbulent boundary layer tends to dissipate faster with respect to that in a laminar boundary layer. A comparison of the two cases is shown in Figure 2.45. In both cases secondary structures are also observed. In the case of

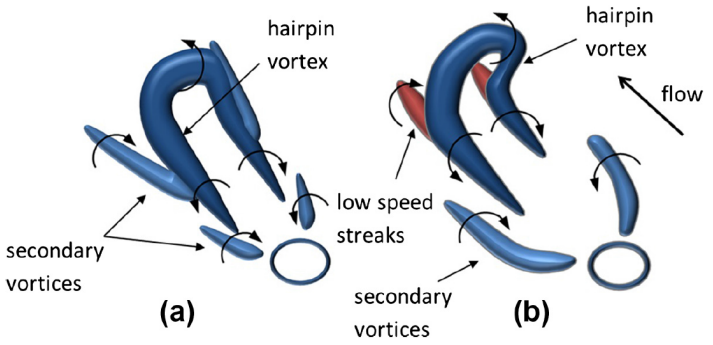

Figure 2.45: Comparison of the shape of a hairpin vortex generated by a synthetic jet in (a) a laminar boundary layer and (b) in a turbulent boundary layer (figure taken from [158])

a laminar boundary layer the secondary streamwise vortices are more largely spaced than in the case of a turbulent boundary layer and are located laterally with respect to the hairpin legs. In the case of a turbulent boundary layer these structures are located just underneath the hairpin legs. Figure 2.46 shows the time averaged excess of wall shear stress with respect to the base flow (no synthetic jet present). The impact of the hairpin vortices on the near-wall can be deduced from it. The wall shear stress footprints appear to be symmetric in the case of a laminar boundary layer and asymmetric in the case of a turbulent boundary layer. The impact is wider in the case of a turbulent boundary layer, but it is weaker and not extended much downstream. Similar considerations can be drawn by looking at the plots at the bottom of Figure 2.46. Therefore it can be concluded that if one wants to achieve the same effect on flow separation control in a turbulent boundary layer a stronger jet is required in a turbulent boundary layer.

Finally, an array of synthetic jets was employed in flow separation control experiments in a turbulent boundary layer by Zhang and Zhong [166, 171]. The array was composed of three circular synthetic jets. The separated turbulent flow over a two-dimensional ramp in a boundary-layer tunnel was examined by Stereo-PIV and 2D PIV. In this case the synthetic jets are operated at velocity ratios between 0.2 and 0.5. The frequency was varied independently from 20 to 150 Hz. The application of synthetic jets was found effective in modifying the recirculation region over the ramp. The explanation of this interaction is attributed to the momentum redistribution associated

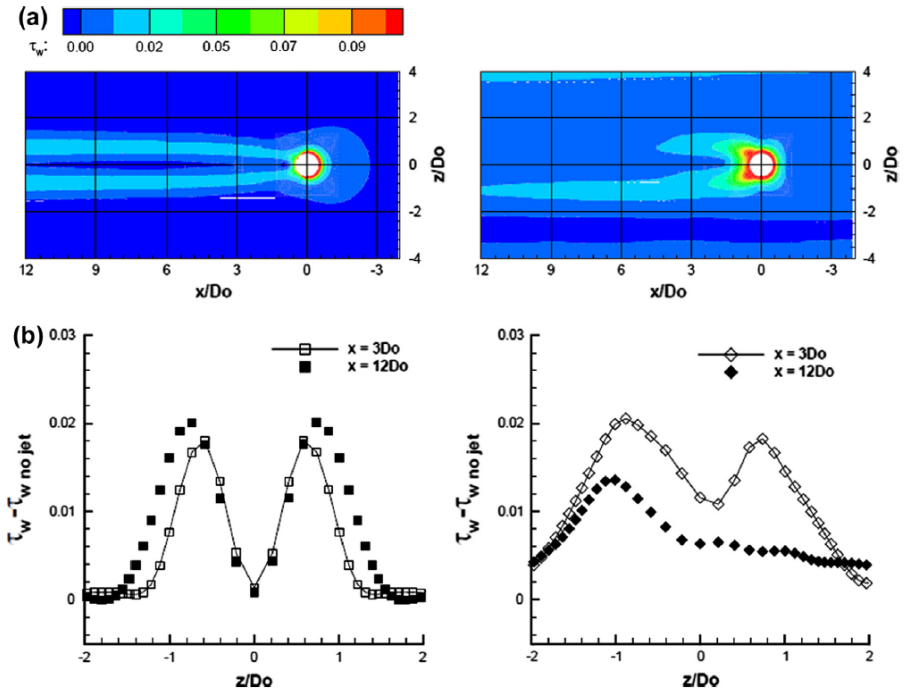

Figure 2.46: Time averaged excess wall shear stress. (a) contour maps at the wall (b) distribution in spanwise direction downstream of the jet at $x = 3D_0$ and at $x = 12D_0$. The laminar boundary layer case is shown to the left, the turbulent boundary layer case is shown to the right (figure taken from [158])

with the down-wash of the secondary streamwise vortices that form underneath the hairpin vortices (see Figure 2.47) which entrains more energetic fluid in the near-wall region. Indeed, these vortices are found to be quite persistent downstream of the syn-

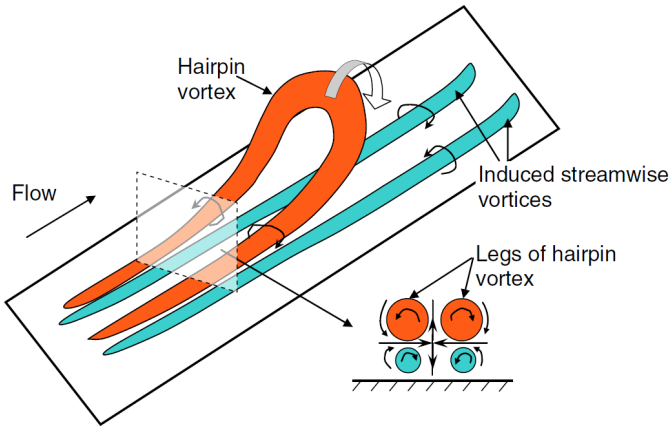

Figure 2.47: Schematic of the hairpin vortices generated by synthetic jets on a ramp in a turbulent boundary layer (figure taken from [171])

thetic jet orifices. For higher velocity ratios also the head of the hairpin vortices plays an important role in bringing more energetic fluid down to the wall and acts in combination with the secondary streamwise vortices. The effect increases with velocity ratio, as the hairpin vortices gain strength and have a longer streamwise extent. The shape difference of the hairpin vortices and of the secondary structures underneath the hairpin vortices outlined by Tang is also confirmed in these experiments.

Chapter 3

Experimental Set-up and Measurement Techniques

In this chapter the experimental methods used in this work are presented, as well as the set-up of for all the experiments. Section 3.1 contains a description of the water flume in which the experiments are performed. Section 3.2 introduces the measurement techniques employed in this thesis. Sections 3.3, 3.4, 3.5 and 3.6 contain a description of the experimental set-up for all the experiments.

3.1 The Water Flume

The water flume used for all the experimental activities is an open-surface channel 3.64 meters long. The cross-sectional dimensions are 0.305 m x 0.305 m. The test section is located at approximately 1.9 m from the flume entrance. The side walls are made of glass, this is to enable the positioning of probes for measurements on the side and underneath the flume. The test section has also a glass floor 0.8 m long, which provides visible access for experiments which require a view of the flow from underneath.

A schematic of the flume is shown in Figure 3.1, and an image of the flume in Figure 3.2. The water is set in motion by a centrifugal pump. The pump draws water from a holding tank and pushes it into a smaller entry tank. The water then enters the channel, but before reaching the test section, it passes through some straightener vanes and a honeycomb structure which both reduce the longitudinal components of turbulence or mean-velocity variation to a greater extent than the lateral components. In addition, upstream of the test section there is a series of screens, which further reduce

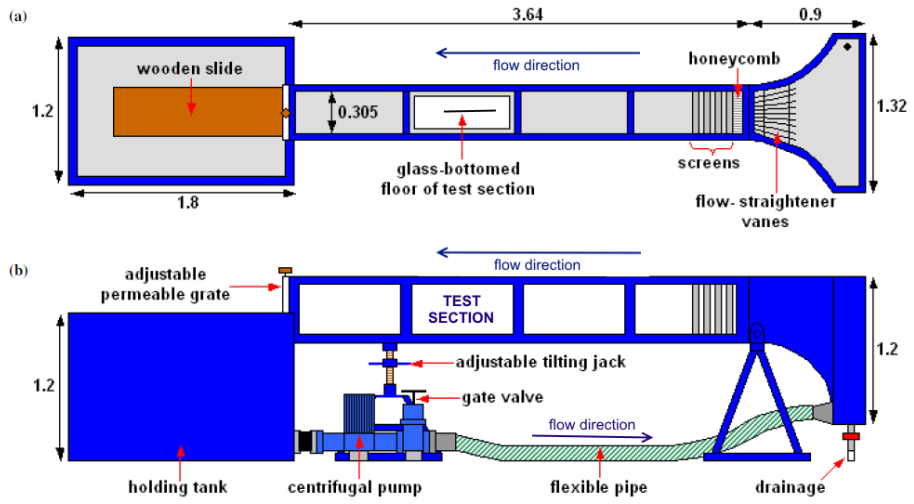

Figure 3.1: Schematic of the water flume (a) top view (b) side view (figure taken from [64])

Figure 3.2: Picture of the water flume

the level of flow turbulence. The water level and the velocity are controlled with an adjustable permeable grate, which is located at the end of the flume, and by the RPM (Revolutions Per Minute) of the centrifugal pump. This is controlled by a digital ABB inverter. Moreover, a circulating pump is also present. It is used to create a recirculation of water from the holding tank to the entry tank. Stagnant water is an incubator for bacteria and parasites. When the water tunnel is not running the recirculation pump can be activated to limit water contamination.

The highest freestream velocity achievable in the test section is about 0.4 m/s. In this thesis, experiments are all performed at a free-stream velocity of about 0.1 m/s. Some preliminary PIV experiments were carried out to estimate the turbulence intensity in the free-stream. The turbulence intensity in the streamwise component of velocity was estimated to be about 0.65% of the free-stream velocity, whereas the turbulence intensity of the wall-normal component of velocity 0.87% of the free-stream velocity. These values are in agreement with water flumes and water tunnels operating at similar free-stream velocities.

3.2 Experimental Measurement Techniques

3.2.1 Particle Image Velocimetry

Particle Image Velocimetry (PIV) is an optical method of flow measurements, with which the velocity in a certain region of the flow field can be globally measured. It is a measurement technique that was first developed in the early 1980s. In 2D PIV (also referred to as 2C-2D which means 2 components - 2 dimensional) velocity vectors are determined in a plane in the flow field.

A PIV system is composed of three fundamental elements: seeding particles in the flow, a lighting system and a camera system. These components are usually regulated by an electronic synchroniser. The fluid flow is seeded with particles which are assumed to faithfully follow the flow dynamics. This is true if the particles are sufficiently small and have a density comparable to that of the fluid. The seeded fluid is illuminated by a light sheet, generally produced by a LASER (Light Amplification by Stimulated Emission of Radiation) system. In this way, the particles moving within the light sheet are illuminated and scatter light. The particles need to be large enough to

scatter light sufficiently. By recording a pair of images of the illuminated plane with a CCD camera and by further analysing these, it is possible to estimate quantitatively the motion of the particles and to provide a velocity vector field in the plane itself. Figure 3.3 shows the typical set-up of a 2D PIV system. Though several types of laser sources

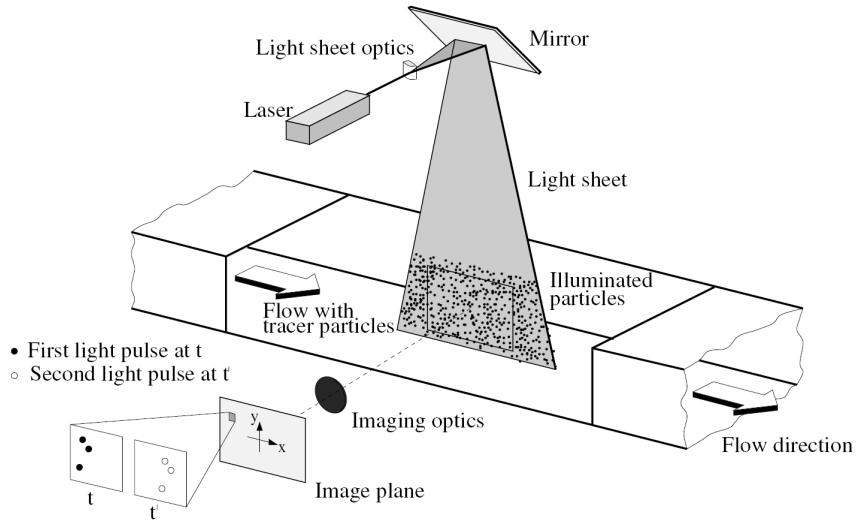

Figure 3.3: Typical PIV set-up in standard 2D PIV (figure taken from http://aim2.dlr.de)

are suitable, the most commonly used in PIV is the pulsed Neodyme-YAG (Nd:YAG) laser, doubled in frequency (532 nm). For a conventional PIV system the laser pulse duration is typically 5-10 ns, and the repetition rate is of the order of 5-10 Hz. Laser energy can reach 400 mJ/pulse. The light scattered by the particles is recorded on two separate images. For the digital evaluation of the velocity field, each image is divided into small areas, called interrogation windows. The local displacement vector (in pixels) $\vec{r}$ of the particles between the two images is determined for each interrogation window by means of a spatial statistical cross-correlation function. The process is illustrated in Figure 3.4. Given the time separation between the two laser pulses Δt, the estimated pixel displacement $\vec{r}$ and the image magnification factor M obtained from the camera calibration, the projection of the local flow velocity vector onto the plane of the light sheet, attributed to the centre of the interrogation window, can be computed as

$$\vec{v} = \frac{M\vec{r}}{\Delta t}. \tag{3.1}$$

Neighbouring interrogation windows can be partially overlapping in order to increase the spatial resolution in the resulting vector grid. Typically, a 50% overlap is used,

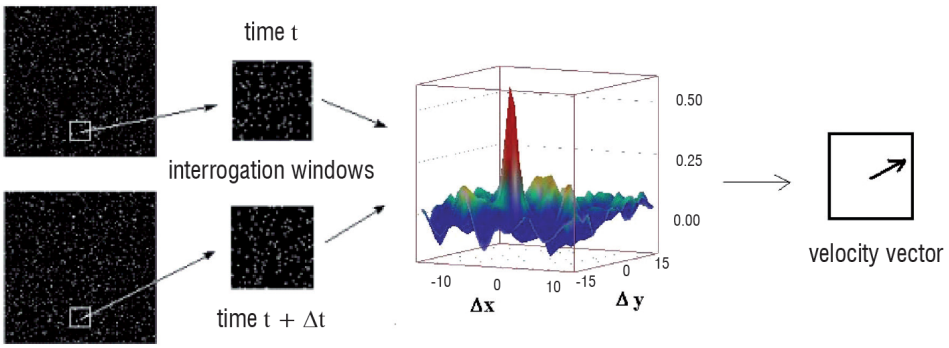

Figure 3.4: Cross-correlation of a pair of interrogation windows (figure taken from [20])

which doubles the number of vectors in each direction and thus quadruples the total number of vectors. The calculation of the cross-correlation is commonly based on Fast-Fourier Transform (FFT) algorithms. Generally the algorithms are recursive and are based on initial large interrogation windows. Large windows guarantee a high signal-to-noise ratio (SNR) due to the large amount of particles taken into account in the statistics, however the spatial resolution is low. Therefore, it is necessary to refine the spatial resolution through successive iterative steps in which the size of the interrogation windows is progressively reduced. The windows may also be shifted and deformed according to the velocity and the velocity gradient computed at the previous step. Processing algorithms nowadays are available with additional features, which increase the signal-to-noise ratio and remove spurious bad vectors.

The quality of PIV results depends on a few parameters, such as:

- the *seeding density* i.e. the number of seeding particles per unit area of an image captured, or the number of particles per unit volume of the fluid. The number of particles per unit volume needs to be sufficiently high to ensure enough particles in an interrogation window and so a good performance of the cross-correlation algorithm.

- the *size of the initial interrogation window*, chosen as a compromise between the desired spatial resolution and the minimum number of particles required for obtaining reliable velocity vectors.

- the *time separation* Δt between the two images captured, which has to be chosen

along with the size of the initial interrogation window. In fact, a sufficient number of the same particles has to be present in both images. A common rule of thumb is that the maximum particle displacement allowed between the two images must not be more than 25% of the size of the initial interrogation window.

In a single PIV test typically a certain number of image pairs is acquired. A vector field is then computed from each single image pair and finally an averaged vector field is obtained.

Uncertainty Associated with PIV Measurements

The uncertainty in the velocity obtained using PIV provides a range in which the error between the estimated and the true (unknown) value of the velocity vector at each node lies, with a certain confidence level. This depends on several factors, such as the way in which the laser system is set-up, the camera settings, the seeding particle characteristics and density, the image quality (presence of a certain level of background noise), the type of processing algorithm etc. Therefore, a straightforward method to determine the uncertainty is difficult to devise. A few advanced methods have been developed to estimate the uncertainty in the velocity components [116, 18, 103, 135, 54]. The application of such advanced methods is however beyond the scope of this work.

A simple approach, derived from considerations made in [91, 116, 64, 152] is adopted. The u-velocity (streamwise) component is determined through Equation (3.1), namely

$$u = \frac{M\Delta x}{\Delta t} \tag{3.2}$$

The uncertainty in u at a given point in space, indicated as δu is propagated from the uncertainty in the magnification factor M i.e. δM, the uncertainty in the pixel displacement Δx i.e. $\delta\Delta x$ and that in Δt i.e. $\delta\Delta t$. It can be assumed that $\delta\Delta t$ is negligible, due to the high stability of the PIV system, which is reported by the manufacturer. The value of M is determined by comparing the length of an object on a target place at the exact location of the light sheet. If L is the physical length in m, l_{pixels} is the correspondent length in pixels evaluated in the image, the uncertainty δM can be determined as:

$$\frac{\delta M}{M} = \sqrt{\left(\frac{\delta L}{L}\right)^2 + \left(\frac{\delta l_{pixels}}{l_{pixels}}\right)^2}. \tag{3.3}$$

The uncertainty in the pixel length is assumed negligible, therefore:

$$\frac{\delta M}{M} = \frac{\delta L}{L}. \tag{3.4}$$

The uncertainty on the instantaneous velocity u derived using PIV at a certain time instant can be expressed as

$$\frac{\delta u}{u} = \sqrt{\left(\frac{\delta M}{M}\right)^2 + \left(\frac{\delta \Delta x}{\Delta x}\right)^2}. \tag{3.5}$$

As mentioned above, typically all the vector fields calculated in a single PIV experiment are averaged to produce an ensemble-averaged vector field, the components of which are indicated with $\bar{u}$ and $\bar{v}$. The uncertainty δM depends on the PIV calibration and we can assume that it is the same in all the instantaneous streamwise components u_i derived in the experiment. In other words, δM can be regarded as a systematic uncertainty. On the other hand, $\delta \Delta x$ can be considered as a random uncertainty because the value of Δx may vary in each PIV evaluation due to a series of factors such as the particle density in that interrogation window at that instant, the background noise of the images, velocity gradients across the interrogation window, out-of-plane motion of the particles etc. [116]. This value is typically about 0.05 pixels but increases in regions where velocity gradients or the background noise, for example, are high. The uncertainty $\delta \Delta x$ is reduced in the averaged value $\bar{u}$ by a factor $1/\sqrt{N}$, where N is the total number of observations [152]. Therefore, the uncertainty $\delta \bar{u}$ can be calculated as:

$$\frac{\delta \bar{u}}{\bar{u}} = \sqrt{\left(\frac{\delta M}{M}\right)^2 + \frac{1}{N}\left(\frac{\delta \Delta x}{\Delta x}\right)^2}. \tag{3.6}$$

Similarly, the uncertainty in the v-component of velocity (instantaneous and averaged value) can be estimated as:

$$\frac{\delta v}{v} = \sqrt{\left(\frac{\delta M}{M}\right)^2 + \left(\frac{\delta \Delta y}{\Delta y}\right)^2} \qquad \frac{\delta \bar{v}}{\bar{v}} = \sqrt{\left(\frac{\delta M}{M}\right)^2 + \frac{1}{N}\left(\frac{\delta \Delta y}{\Delta y}\right)^2}. \tag{3.7}$$

Typically also other statistical variables are of interest, such as the root-mean-square value of the velocity components and the averaged Reynolds stress. The uncertainty in all these variables can be computed by using the uncertainty propagation formulas, see [152, 86]. Table 3.1 summarises the relationships used for the estimation on such

variables and the expression for their uncertainty. In this case N is the total number of images considered when computing the different statistical quantities.

3.2.2 Liquid Crystal Thermography

Liquid Crystal Thermography is a measurement technique that is based on the sensitivity to temperature of liquid crystals. The technique was initially only employed as a flow visualisation tool. With the advance of digital image processing technologies the technique of using thermocromic liquid crystals has evolved into a well established full surface temperature measurement tool, i.e. Liquid Crystal Thermography, from the 1980s. Comprehensive reviews of the application of this technique can be found in [72, 75, 13, 12, 60, 61, 137].

Liquid Crystals Materials

Liquid Crystal Thermography exploits the properties of liquid crystals deliberately employed in a thermodynamic anisotropic phase between their pure solid and pure liquid phase. Liquid crystals in this transitional phase exhibit the mechanical properties of a solid, whilst showing the optical properties of liquids. In particular, these properties vary according to a series of factors, the most important of which is temperature.

As also reported by Jones et. al [71], liquid crystals with increasing temperature pass through the following phases in succession: solid - smectic - nematic (cholesteric) - liquid. When liquid crystals are in the liquid phase, their behaviour is isotropic. The smectic and nematic phase instead are transitional phases in which the liquid crystal behaviour is strongly anisotropic. In the smectic phase (see Figure 3.5) liquid crystals show properties similar to solids, however their molecular disposition is not completely ordered. Molecules are arranged in layers. The longitudinal axis in adjacent layers are aligned. The typical molecule of a liquid crystal is 30 angstroms long and 3 angstroms thick. With increasing temperature, the liquid crystal assumes the nematic phase, less ordered than the solid one but not as disordered as the liquid one. In the nematic phase the distribution of molecules in planes is lost. The molecular forces however are still able to maintain an alignment of the single molecule axis. Both the smectic and the nematic phase are optically inactive in the sense that if light hits the surface of the liquid crystal, all the wavelengths pass through and are not reflected. In between the smectic and the nematic phase, thermocromic liquid crystals undergo a transient phase

statistics	estimator	uncertainty
u_{RMS}	$\sqrt{\frac{1}{N}\sum_{i=1}^{N}(u_i-\bar{u})^2}$	$\frac{1}{N u_{RMS}}\sum_{i=1}^{N}\lvert u_i-\bar{u}\rvert\,(\delta u+\delta\bar{u})$
v_{RMS}	$\sqrt{\frac{1}{N}\sum_{i=1}^{N}(v_i-\bar{v})^2}$	$\frac{1}{N v_{RMS}}\sum_{i=1}^{N}\lvert v_i-\bar{v}\rvert\,(\delta v+\delta\bar{v})$
$\overline{u'v'}$	$\frac{1}{N}\sum_{i=1}^{N}(u_i-\bar{u})(v_i-\bar{v})$	$\frac{1}{N}\sum_{i=1}^{N}\lvert v_i-\bar{v}\rvert\,(\delta u+\delta\bar{u})+\frac{1}{N}\sum_{i=1}^{N}\lvert u_i-\bar{u}\rvert\,(\delta v+\delta\bar{v})$

Table 3.1: Statistical variable estimation and related uncertainties

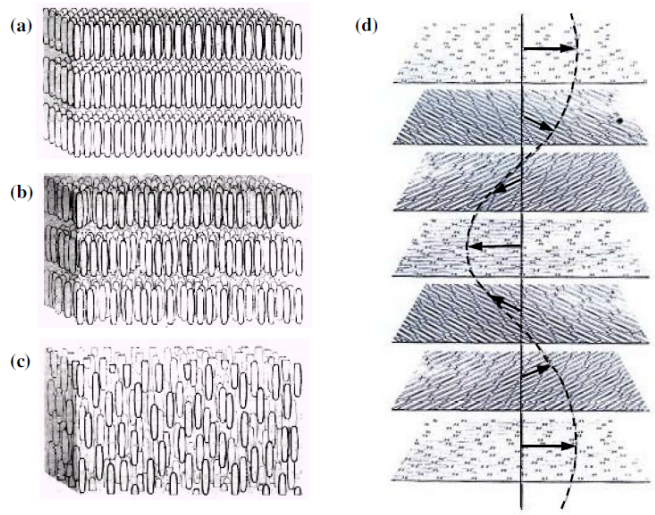

Figure 3.5: Molecular arrangement in the different liquid crystal phases:(a) solid, (b) smectic (c) nematic (d) chiral-nematic (figure taken from [64])

also referred to as cholesteric or chiral-nematic. This is the phase in which they are optically active. The molecular disposition in molecular planes is still preserved, just like the smectic phase. However the director of two adjacent planes[1] is rotated by a certain fixed angle. This means that the molecules naturally form a twisted-helical structure. When light hits this molecular structure, all its composing wavelengths pass through except the wavelength equal to the helical pitch, which is instead reflected. This phenomenon is also called selective reflection (see Figure 3.6). The reflected

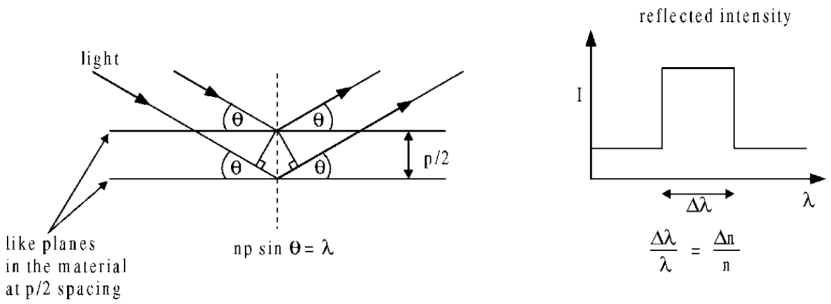

Figure 3.6: A simplified diagram for selective reflection (figure taken from [61])

light wavelength arises from the constructive interference of the reflected light rays and can be estimated by the Bragg diffraction law, which reads:

$$\lambda = n\,p\,sin\theta \tag{3.8}$$

where λ is the reflected wavelength, n is the refractive index (which depends on the liquid crystal material), θ is the light incidence angle and p is the pitch of the helicoidal structure. In order to provide the desired effects, p has to be of the order of the visible light wavelength. The incident angle of light θ also plays an important role, because the refractive index n is a function of it (in other words $n = f(\theta)$). p changes according to a number of parameters, but it has a strong dependence on temperature, more precisely it decreases with increasing temperature. Given that, liquid crystals can be calibrated in a way that a specific wavelength of reflected light is associated with a well-precise temperature. This is the working principle of *Liquid Crystal Thermography*, also illustrated in Figure 3.7. The temperature at which liquid crystals starts to reflect light in the visible range is commonly referred to as the activation temperature or red-start temperature, whereas the value at which the reflected colour is violet and

[1] the director of a molecular plane is the direction of alignment of the molecules within the plane

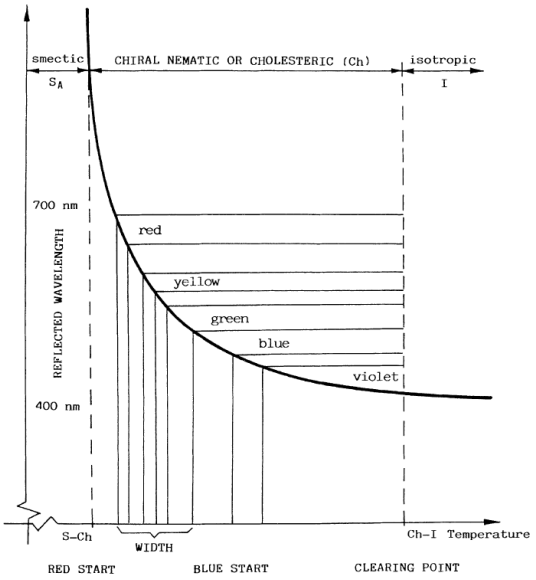

Figure 3.7: Typical reflected wavelength (colour) temperature response of a liquid crystal mixture (figure taken from [157])

therefore the other end of the visible range, is referred to as the clearing-point temperature. The reflected light is circularly polarized.

Liquid crystals in most cases are provided in encapsulated form, which means that they are enclosed in tiny capsules of gelatine material. The dimension of the capsules is of the order of 10-20 μm. The encapsulation is needed for the liquid crystals to preserve their mechanical and optical properties against external chemical and mechanical influences. Usually liquid crystal encapsulated particles are mixed with a polymeric binder to form a liquid crystal mixture. The testing surface is usually coated with this.

Liquid Crystal Calibration

The process of calibration associates a certain colour of the reflected light to a certain temperature. If the liquid crystal coating is uniform, it is possible to calibrate a small portion of it and use the obtained calibration law for the whole surface. After being calibrated, a liquid crystal coating is able to provide a non-intrusive field-wise measurement of the surface temperature on the whole coated area. The possibility of calibration has been made possible particularly in the last two decades by the advances in digital image acquisition and processing techniques. The digitised image can be stored as a triple matrix. Each colour pixel can be uniquely identified by three scalars,

commonly identified as the Red-Green-Blue values (RGB), which are related to the red, green and blue components of the reflected light. Usually the calibration technique for Liquid Crystal Thermography is not based on the RGB colour space, but on another equivalent representation known as Hue-Saturation-Value (HSV). The RGB - HSV colour space transformation is a one-to-one correspondence: it is schematically illustrated in Figure 3.8. In particular, calibration techniques of liquid crystal are usu-

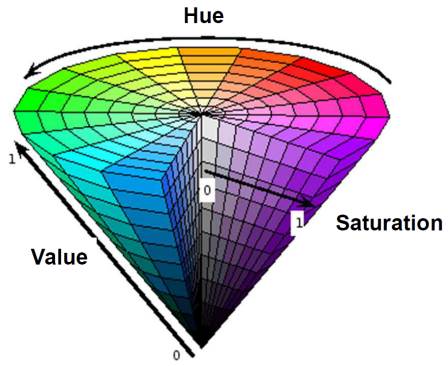

Figure 3.8: Relation between RGB and HSV value

ally based on the hue value, as hue is strongly correlated with the dominant wavelength of the light reflected by the coating. Using the HSV space instead of the RGB space also reduces the uncertainty due to the variation of the brightness of the image [137]. In fact, the hue value does not depend on the brightness. The conversion between the HSV and the RGB colour spaces can be performed in MATLAB©. The algorithm used for the conversion is illustrated in [136].

A simple calibration can be obtained by varying the temperature of the liquid crystal surface and recording simultaneously both the temperature at a point in the surface and the average value of hue over an area around that point. The time histories of temperature and hue are then transformed into a *hue-temperature map*, an example of which is shown in Figure 3.9. The area of interest is the portion in which the liquid crystal is active, between the activation and the clearing-point temperature. The relationship hue-temperature is non-linear. Usually a polynomial regression of a degree between 5 and 8 is acceptable.

The calibration procedure is related to the whole liquid crystal rig, including the lighting system and the camera. Since the viewing angle and the lighting angle strongly

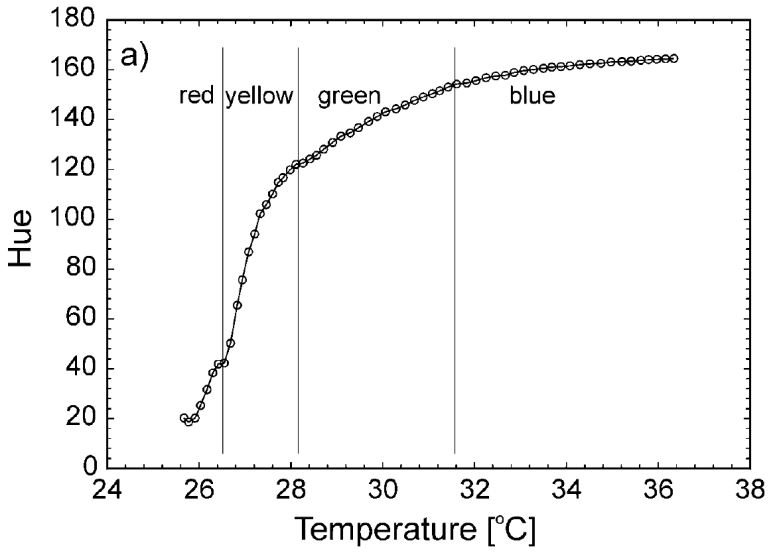

Figure 3.9: Typical calibration curve (hue-temperature) curve for a thermocromic liquid crystal (figure taken from [137])

affect the calibration, it is strongly recommended that the calibration is carried out in-situ and that the same lighting configurations and positions are maintained during the experiments.

Heat Transfer Measurements and Reynolds Analogy

Liquid Crystal Thermography can also provide the convective heat transfer coefficient at the wall, provided that the temperature of the wall is different from the temperature of the flow, i.e. there is a wall heat flux and a thermal boundary layer forms, as shown in Figure 3.10. The ***convective heat transfer coefficient*** is defined as:

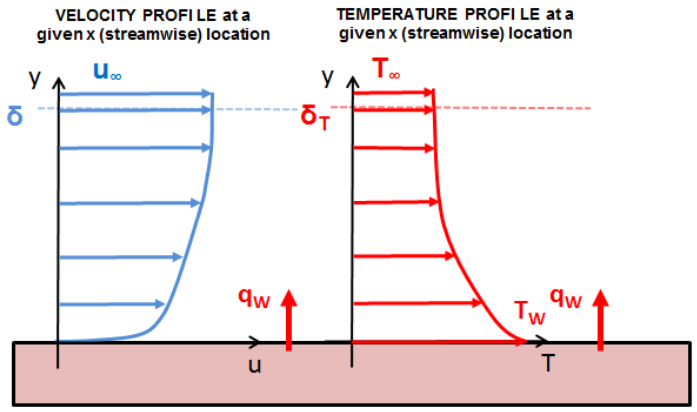

Figure 3.10: Kinematic and thermal boundary layers

$$h \doteq \frac{q_w}{T_w - T_\infty} \tag{3.9}$$

where q_w is the wall heat flux, T_w is the wall temperature and T_∞ is the freestream temperature of the flow. In a two-dimensional (laminar) boundary layer h can be obtained from analytical solutions as a function of other non-dimensional parameters such as the Reynolds number, the Nusselt number or the Prandtl number. In three-dimensional flows an analytical expression for h does not exist. However, h can be measured indirectly using equation (3.9). For example, T_∞ can be measured with a temperature sensor in the freestream, T_w can be measured using wall thermocouples or Liquid Crystal Thermography and q_W at the wall can be estimated using the Fourier conduction heat transfer theory.

In addition, in two-dimensional boundary layers, the heat transfer coefficient is related to the kinematic properties of the flow using the *Reynolds analogy*, which relates the wall heat transfer coefficient and the wall shear stress, see [15, 132]. It is also possible to extend the Reynolds analogy to turbulent boundary layers, considering the mean values of the wall heat transfer and of the skin friction coefficient. In general, for a three-dimensional flow the Reynolds analogy is not valid instantaneously, but a good degree of correlation between the streamwise component of the wall shear stress and the heat transfer coefficient at the wall is expected.

Application of Liquid Crystal Thermography

Liquid Crystal Thermography has been widely used by several researchers to obtain wall temperature and the wall heat transfer coefficient in steady flows [71]. Successful attempts to study unsteady flow events have also been made. For example, Sabatino and Smith [129], Zhong et al [168] used a liquid crystal coated surface to visualise the thermal footprints and deduce the convection velocities of turbulent spots propagating in a laminar boundary layer. Zhong et. al [167] used Liquid Crystal Thermography to visualise the formation and development of wake-induced transition events and gather information about the location of formation and the formation rate. In addition, observations of thermal footprint of streaks using thermocromic liquid crystals are also documented in [150, 106, 5], where the authors investigated the heat transfer and flow features downstream of surface-mounted rectangular and trapezoidal ribs.

3.2.3 Constant Temperature Anemometry (Hot-Films)

Constant Temperature Anemometry (CTA) is a measurement technique of primarily velocity and wall shear stress in a fluid flow. Constant Temperature Anemometry provides a high frequency response, but the simultaneous measurement points are generally limited. Therefore, it is recommended for the measurement of flows for which a large spatial resolution is not required. For a detailed description Constant Temperature Anemometry, the reader is referred to Bruun [21].
The working principle of Constant Temperature Anemometry is the cooling effect of the flow on a heated body. The heated element is usually a wire or a film, which is heated and placed in the flow at the measurement point. The convective heat transfer Q from the heated element is a function of the velocity of the incident flow U, of the over-temperature $T_w - T_0$, where T_w is the temperature of the heated element and T_0 is the temperature of the element when not heated (which is equal to the fluid temperature) and of the physical properties of the fluid. The basic relation between Q and U was suggested by L.V. King (1914) and in its simplest form reads:

$$Q = (T_w - T_0) A_w h = A + B U^n \tag{3.10}$$

where A_w is the wire surface area and h the heat transfer coefficient, and A and B are two calibration constants. In CTA, the wire is connected to an arm of a Wheatstone bridge and heated by an electrical current. The performance of the hot-wire is commonly related to the overheat ratio OR=R_w/R_0, which is the ratio of the electrical resistance of the hot wire when it is operating and the resistance of the wire when it is not heated, R_0. A servo-amplifier keeps the bridge in balance by controlling the current to the sensor so that the resistance (and hence temperature) is kept constant, independently from the cooling imposed by the fluid. The electrical power of the current flowing in the heated element is $E = I^2 R_w$. E is equal to the heat transfer Q for the conservation of energy. It is possible therefore to show (see [21]) that in practice the bridge voltage $E = I R_w$ can be related to the velocity and a calibration law similar to equation (3.10) can be derived. The combination of the low thermal inertia of the sensor and of the high gain of the servo loop amplifier results in a very fast response to fluctuations in the flow. Figure 3.11, provided by Dantec©, briefly summarises the measurement chain of Constant Temperature Anemometry. For all the questions related to the directional sensitivity, frequency response , as well as temperature sensitivity, the reader should refer to [21].

CTA probes typically have tungsten wire sensors, 1 mm long and 5 μm in diame-

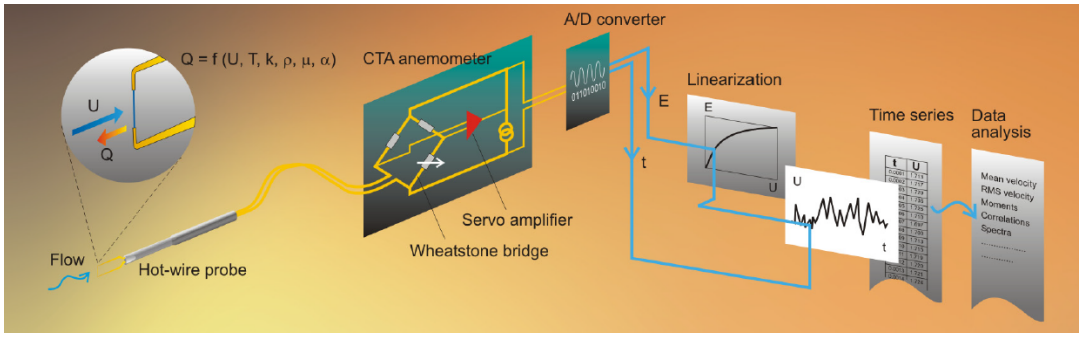

Figure 3.11: Measurement chain of Constant Temperature Anemometry (figure taken Dantec Dynamics© website)

ter, mounted on two needle-shaped prongs. They are available with 1, 2 and 3 wires differently oriented if more than one velocity component has to be measured. Film probes with thin-film sensors are recommended for liquid flows. They are usually made of a substrate of quartz, on which nickel is deposited. The films are protected by a final sputtered quartz coating for use in water. In general their diameter is larger than hot-wires. Hot film are more resistant than hot-wires and they are less sensitive to dirt or particulate in the flow. However, due to their larger dimensions, they provide a lower frequency response.

3.3 Experimental Set-Up: Interaction Cylinder and Synthetic Jet (Chapter 4)

The objectives of these experiments are to assess the capability of a single synthetic jet actuator to control streamwise vortices and streaks downstream of a circular cylinder place vertically within a laminar boundary layer and to determine the operating conditions at which the control effects are strongest. These experiments are similar to those carried out by Jacobson and Reynolds [67], described in Section 2.3. The experimental results are discussed in Chapter 4.

In this case, the type of flow actuator employed is a synthetic jet actuator with a circular orifice instead of a cantilever-beam actuator. The experiments are performed in a laminar boundary layer, which develops over a flat plate at a free-stream velocity

of about 0.1 m/s. The synthetic jet orifice diameter is 5 mm. To ensure a certain growth of the boundary layer, necessary for correct operation of the synthetic jet, the orifice is located 0.71 m from the flat plate leading edge. Side-wall contamination effects also reduce the region of operation so that it is not possible to place the orifice too far downstream. The position of the orifice is therefore a compromise between these two requirements. After some preliminary experiments, it was observed that the hairpin structures generated by the synthetic jets create flow disturbances that extend far downstream, whereas the cylindrical disturbances do not extend far downstream. It was decided that a better way to achieve the interaction was to invert the position of the SJA and the rod with respect to the experiments carried out by Jacobson and Reynolds [67]. Therefore, the cylinder is placed downstream of the SJA. This should establish more directly whether the synthetic jet may possibly modify the flow field immediately downstream of the cylinder or whether the effect of the synthetic jet is visible only in the far-field downstream, as it was in the experiments of Jacobson and Reynolds. The configuration of the experiments in this chapter is illustrated in Figure 3.12. The cylinder is 30 mm downstream of the synthetic jet orifice and its diameter is

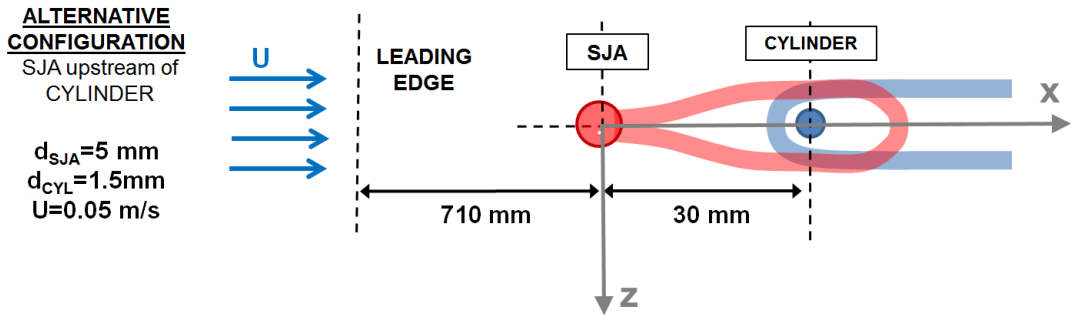

Figure 3.12: Position of the cylinder and of the SJA in the PIV experiments

2 mm.

3.3.1 Flat Plate

Experiments are carried out using Particle Image Velocimetry. The rig used in this work for Particle Image Velocimetry is a metallic flat plate 1.2 m long and 0.3 m wide. The flat plate perfectly fits the test section of the water flume. A picture of the flat plate is shown in Figure 3.13. During all the experiments the flat plate is mounted upside down in the water flume at a distance of 20 cm from the bottom. The level of water is

Figure 3.13: Flat plate used during the PIV measurements

25 cm, so the flat plate is submerged 5 cm. As can be seen in Figure 3.13, the region of investigation is also painted with a fluorescent paint (FP R6G) which, when excited with green light at 532 nm wavelength, emits light in a spectral range shifted to orange with a maximum emission of 625 nm. The emitted light can then be filtered out using an optical filter (at 532nm), placed on the camera, to eliminate undesirable reflections. At measurement location a circular insert is built, to easily mount the equipment necessary for the experiments. The insert can also be rotated in case a certain angle with respect with the free-stream flow has to be set. The insert is used to properly align the cylinder and the synthetic jet orifice with the free-stream direction.

The circular cylinder is installed by drilling a hole on the surface of the insert. The synthetic jet cavity is round and is glued to the opposite part of the insert with silicone sealant. The insert contains a single hole, with diameter 5 mm. This is the orifice of the synthetic jet actuator and is located at the centre of the round cavity.

3.3.2 Single Synthetic Jet Actuator

The synthetic jet actuator (see also Section 2.4) was manufactured in the workshop of the School of Mechanical, Aerospace and Civil Engineering of the University of

Manchester. The synthetic jet is mounted on a round cavity. A drawing of the synthetic jet cavity is provided in Figure 3.14. In part (a) the exploded view of the cavity

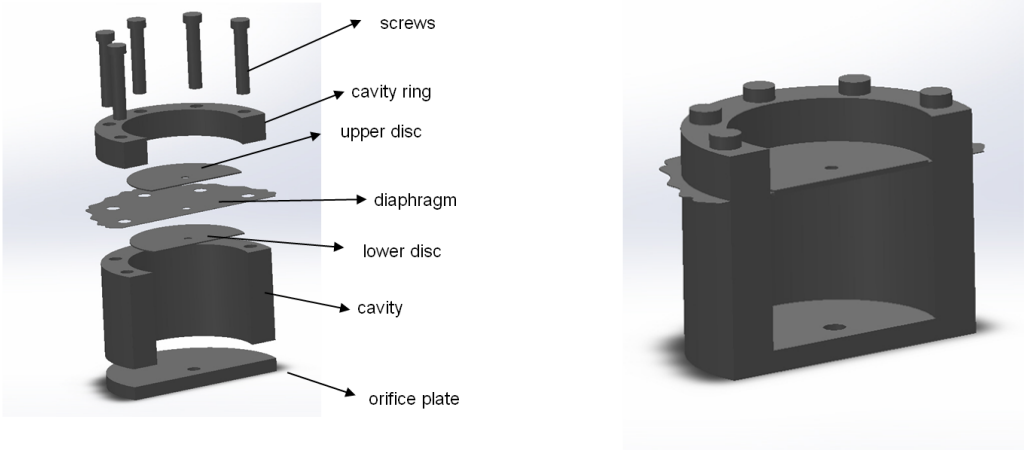

(a) Exploded View (b) Assembly

Figure 3.14: Technical drawing of the single synthetic jet mounted on a round cavity

is shown, in part (b) the assembled cavity is shown. The internal diameter of the cavity is 45 mm. The orifice diameter is 5 mm and the orifice neck height is also 5 mm. The diaphragm is made from a special rubber and is clamped onto the cavity with a cavity ring, which fixes the diaphragm in place with screws and keeps it in slight tension. In order to enable the rigid motion of the diaphragm, two discs are mounted in a "sandwich-like" configuration. The diameter of each disc is 2 mm lower than the internal diameter of the cavity, which creates a 1 mm clearance all around the border. The discs are made from Aluminium and are fixed by a bolt connection to a driving rod, which is firmly connected to a shaker, as shown in Figure 3.15. The displacement of the diaphragm is measured by a Monitron eddy current displacement sensor, which measures accurately displacements between 0 and 2 mm. The sensor operates together with a metallic target, which is fixed to the driving rod, inserted into a small Perspex disc. The sensor is aligned to the metallic target and is placed at a small distance from it. The metallic target moves with the diaphragm. The sensor is fixed to the shaker support and does not move with the diaphragm (see Figure 3.15). The calibration of the displacement sensor (voltage-displacement) is linear and is provided by the manufacturing company. The eddy current generated by the sensor passes the sensor displacement driver and finally is acquired by the DAQ card.

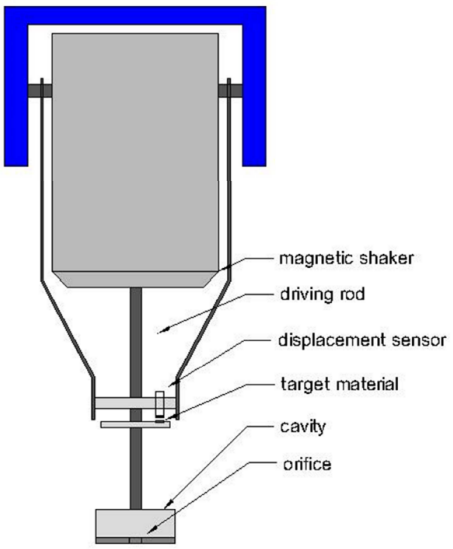

Figure 3.15: Magnetic shaker set-up and displacement sensor (figure adapted from [64])

The shaker is driven by a voltage signal generated by a DAQ card installed in a personal computer. A schematic of signal routes and component integration for the actuation of the synthetic jet is shown in Figure 3.16. The personal computer controls all the sub-

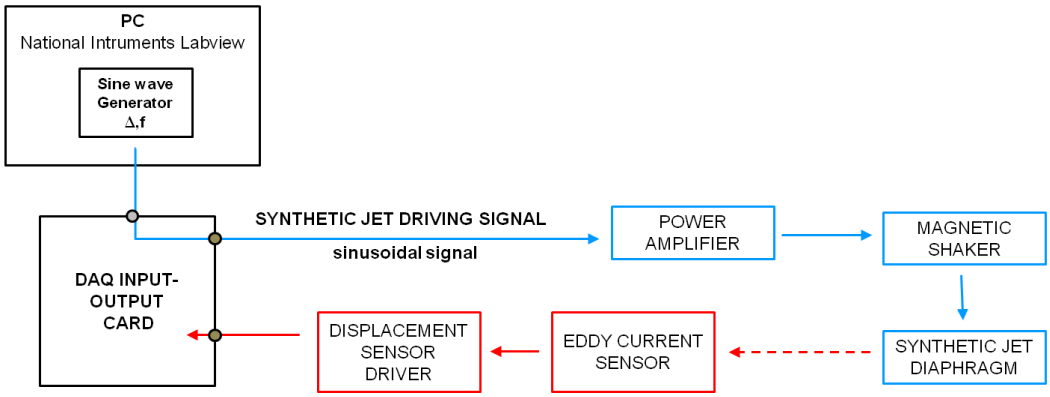

Figure 3.16: Signal routes and component integration for the actuation of the synthetic jet

systems in a virtual environment designed with the software National Instruments© Labview. The DAQ card is able to both generate and acquire voltage signals. Within the Labview code, a sine-wave generator is implemented, which generates the signal

that drives the shaker. The shaker is connected to a driving rod that moves the synthetic jet diaphragm. The amplitude and frequency of the sine-wave can be set independently. The sine-wave is converted into a voltage signal by the DAQ card, is fed into a power amplifier and finally reaches the shaker. The amplifier increases the power of the signal, because the power required by the shaker itself is much higher than what the DAQ card is able to generate.

The dimensionless number related to the synthetic jet performance can be computed as described in Section 2.4. In particular, referring to Figure 3.17 the volume displaced

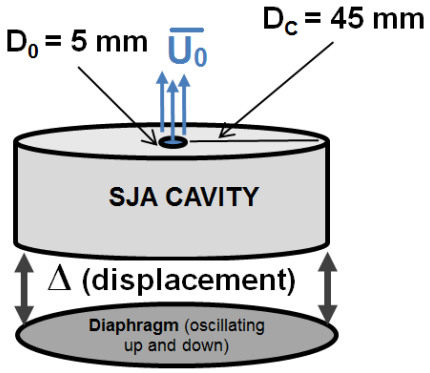

Figure 3.17: Schematic of the single synthetic jet mounted on a round cavity

by the diaphragm during an actuation cycle can be computed as

$$V = \pi D_c^2/4\,\Delta \tag{3.11}$$

where Δ is the peak-to-peak oscillation amplitude and D_c is the (internal) diameter of the cavity. If the fluid motion within the cavity can be represented by an incompressible flow model, the volumetric flow rate through the synthetic jet orifice can be computed as

$$Q_0 = V\,f = \Delta\pi D_c^2/4 \tag{3.12}$$

where f is the actuation frequency. The averaged jet velocity $\overline{U_0}$ over the blowing stroke can be calculated as

$$\overline{U_0} = \frac{Q_0}{\pi D_0^2/4} = \frac{\pi D_c^2/4}{\pi D_0^2/4}\Delta f = \alpha_S \Delta f \tag{3.13}$$

where D_0 is the diameter of the orifice and α_S can defined as

$$\alpha_S \doteq \left(\frac{D_c}{D_0}\right)^2. \tag{3.14}$$

In this case, being D_0 = 5 mm and D_C = 45 mm then α_S=81. Given that, the velocity ratio and the dimensionless stroke length can be computed as

$$\mathrm{VR} = \frac{\overline{U_0}}{u_\infty} = \frac{\alpha_S \Delta f}{u_\infty} \qquad \mathrm{L} = \frac{\overline{U_0}}{f D_0} = \frac{\alpha_S \Delta}{d_0}. \tag{3.15}$$

The cavity height in this model does not play any role in the performance of the synthetic jet.

3.3.3 PIV Set-Up

The PIV system used is a commercial system assembled by TSI: it is composed of a laser system, a laser pulse synchroniser an a CCD camera. The LASER system is a SOLO-PIV 120, developed by New Wave Research. It consists of a 120 Nd:YAG pulse laser which is capable of releasing two laser pluses in rapid succession with a maximum power of 135 mJ, and a pulse width of 3-5 ns at a repetition rate up to 15 Hz. The light wavelength is approximately 532 nm (green light). The laser systems are both connected to an ultra ICE (Integrated Cooler and Electronics) unit. The CCD camera has a maximum available resolution of 2048x2048 pixels, 12-bit intensity dynamic range and a frame rate of up to 16Hz. The laser head is installed on an appropriate optical bench. The light beam produced by the laser system, after exiting the head, is guided to the desired location using an optical arm. The optical arm is connected to a light sheet generator (containing a close-packed combination of lenses), which is mounted on a traverse system. The laser beam can be set parallel to the wall or normal to it. The flow is seeded with hollow glass particle with a mean diameter of 10 μm and a density of about 1100 kg/m^3.

The investigation plane, and so the light sheet, is parallel to the wall. The PIV set-up is shown in Figure 3.18. The laser sheet generator is installed on an optical orientation system, which is in turn fixed to the optical bench. The optical orientation system enables a fine alignment of the laser sheet with the flat plate surface. A fine alignment is crucial in near-wall studies within a boundary layer, because the velocity

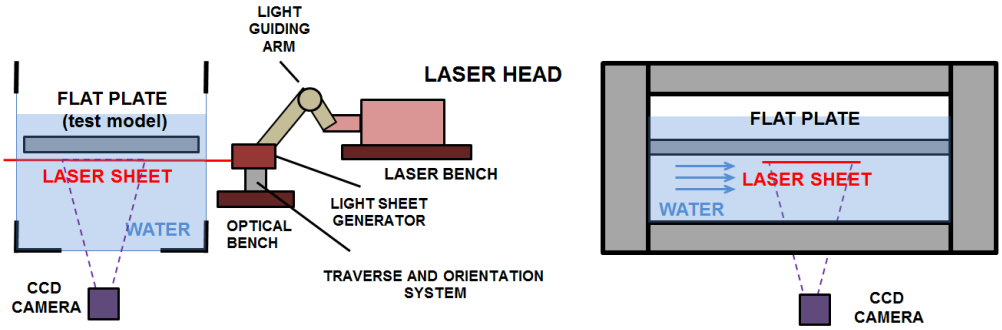

Figure 3.18: PIV set-up with light sheet parallel to the flat plate

gradient is high and so dis-uniformities in the velocity fields appear if there is an imperfect alignment. The laser beam outside the water flume is properly enclosed by a plastic made-to-measure box. The beam passes through the test section of the water flume, which is delimited by two glass windows. After the test section and the second window, the beam impinges onto a metallic, and therefore non-flammable, stainless steel plate, painted black. The camera is placed underneath the water flume, framing upwards through the window at the bottom of the test section. The field of view is 55 mm by 55 mm. The area of investigation is located at a distance of approximately 0.7 m from the leading edge of the flat plate.

The set-up of the PIV system (laser and camera) is performed using Insight 3G, a software provided by TSI. With this software, it is possible to set up the parameters of the acquisition, such as the separation time between the two images of the pair, the camera exposure time, the laser pulse repetition rate, the power of the laser pulses etc. The program also contains a real-time PIV processor. It is recommended to process sample image pairs during the system set-up, to choose optimal values for the acquisition parameters. All the parameters of the image processing can be set in the program, such as the processing algorithm, the size of the initial interrogation window, the size of the windows of the refinement steps etc. The laser pulse is operated at a frequency of 2.5 Hz. 150 image pairs are acquired in each test condition. The time separation between any two images of the pairs is set in a manner to produce a maximum displacement of about a quarter of the size of the initial interrogation window. Based on trial and error adjustments, the final value of $\Delta t = 1500 \mu s$ is chosen.

The acquired images are in grey scale. Each pixel can be identified by a certain value of the intensity within a bit depth of 12 bits, which gives 2^{12} levels, from 1 to 4096. In order to improve the contrast, a pre-processing technique of background correction, implemented in Insight 3G, is adopted. All the images of a single test are loaded. A background image is generated, in which each pixel intensity is the minimum intensity of all the correspondent pixels in the series of loaded images. In this way, all the moving particles disappear in the generated background and the stationary features of the single images are kept: these may be spurious light reflections in the near-wall region (caused by the light sheet directly impinging on the flat plate) stains in the glass window, damaged pixels in the CCD sensor etc. Subtracting this generated background from all the images removes the effect of these imprecisions and increases slightly the image contrast.

After the pre-processing, the images are analysed with a cross-correlation algorithm. The chosen algorithm uses a recursive Nyquist grid, in which the image pairs are processed in two passes, with a 50% window overlap. The initial interrogation window size is 96x32 pixels, with the longest side of the window oriented in the streamwise direction. The final interrogation window size is 32x32 pixels. The particle displacement in each interrogation window is estimated with sub-pixel accuracy by fitting a Gaussian curve to the highest pixel and its four nearest neighbours. For every image pair a vector field is calculated. A SNR (Signal-to-Noise ratio) validation is performed after the processing. The position of the highest peak in the cross-correlation map is used to estimate the local pixel displacement and the local velocity vector, see equation (3.21). The second highest peak in the map is associated with noise, caused by the random pairing of images from different particles. The ratio of the value of the highest peak to the value of the second peak indicates how much “signal” stands out above “noise”. If this ratio is greater than 1.4 the local velocity vector is considered valid, otherwise the vector is labelled as a bad vector and is discarded. Most bad vectors lie in the near-wall region, where the significant correlation peak is low due the very low velocity and also to a non complete elimination of light reflection at the wall. To improve the processing quality, the Rohaly-Hart analysis is also used, which recovers part of the bad vectors. Indeed, if a vector does not pass the above mentioned SNR test, the Rohaly-Hart processor adds the correlation maps of the nearest spots on top of the correlation map of the current spot, in order to get a good correlation peak. It proceeds in three steps, first using a 3x3 stencil, then 5x5 and finally 7x7 until a valid vector is

found. The Rohaly-Hart method is widely used, especially for the analysis of turbulent flows [110], in which the signal-to-noise ratio is high. After processing, all the vector fields acquired in a single run are then averaged to produce an averaged vector field. A vector validation is performed on each single vector field, before computing the average. The vectors whose magnitude lies out of an expected velocity range are discarded along with the vectors which have a standard deviation larger than 4 σ from the local mean value, where σ is local standard deviation.

Uncertainty Considerations

The uncertainty in the averaged velocity field is determined using the method outlined in Section 3.2.1. As far as the u component of velocity is concerned, the uncertainty is composed of a systematic uncertainty, due to a possible non perfect calibration, and of a random uncertainty, mainly related to the pixel displacement error, related to the PIV processing algorithm for each image pair. The pixel displacement error is estimated around 0.1 pixels, according to [116].

Given that, the relative uncertainty on the instantaneous observations of u i.e. $\delta u/u$ = 5.2% whereas the relative uncertainty on the ensemble average value $\bar{u}$ is $\delta\bar{u}/\bar{u}$ = 1.7%. As far as the w-component of velocity is concerned, the relative uncertainty on the instantaneous observations is $\delta w/w$ = 50%, whereas the relative uncertainty on the ensemble average value $\delta\bar{w}/\bar{w}$ is reduced to 4.4%.

3.4 Experimantal Set-up: Liquid Crystal Study of a Turbulent Boundary Layer (Chapter 5)

The objective of these experiments is to characterise the coherent structures developing in a zero-pressure-gradient turbulent boundary layer developing on a flat plate at a free-stream velocity of about 0.1 m/s, using Liquid Crystal Thermography. The experimental results are discussed in Chapter 5. To the best knowledge of the author, it is the first time that Liquid Crystal Thermography is used for this purpose. Liquid Crystal Thermography, has previously been used to study turbulent boundary layers only in a limited number of cases. Iritani et al. [62] used a thermocromic liquid crystal layer at the wall and the hydrogen-bubble visualisation method in the flow simultaneously to investigate the characteristics of the sublayer streaks in the turbulent boundary layer

in water flow, but their study was only qualitative. On the other hand, the quantitative study carried out by Zhong et. al [167] and Sabatino and Smith [130] focused on the heat transfer characterisation of turbulent spots and of the turbulent boundary layer as a whole, and not the substructures in it. The use of surface measurement techniques is advantageous for this purpose, because the near-wall region is very thin. With flush-mounted hot-films on the wall, for example, a high frequency response of the order of kHz can be achieved. However spatial resolution is often comprised, as the sensors themselves have finite dimensions and with the current technology, only a limited number of sensors can be operated simultaneously. With Liquid crystal Thermography a wider picture of the motion of the near-wall coherent structures can be obtained, with a sufficient spatial and temporal resolution.

3.4.1 Flat Plate

The flat plate made of Perspex, 1.2 m long and 0.3 m wide and fits perfectly the size of the water flume. A picture of the flat plate is provided in Figure 3.19. The flat plate

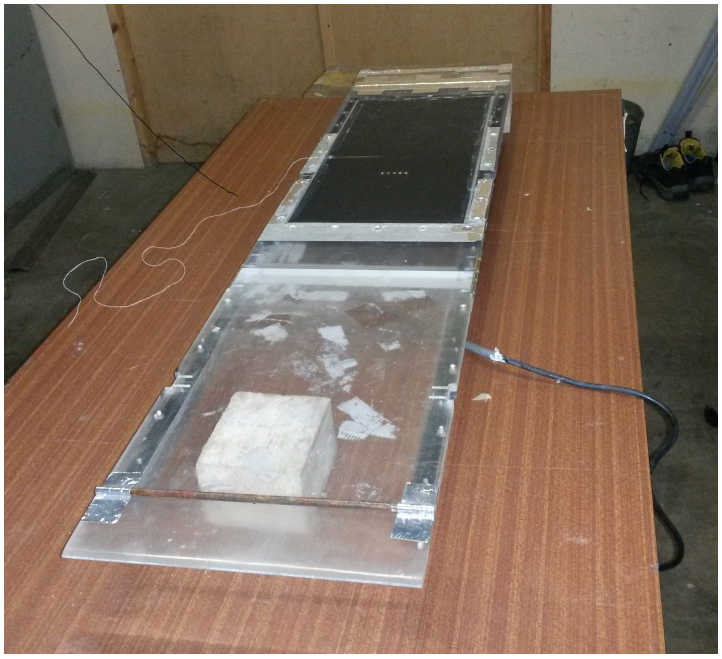

Figure 3.19: Flat plate used in Liquid Crystal Thermography experiments

has a super-elliptic leading edge, which makes the flow less sensitive to an inclination angle. It also has a flap at its trailing edge, which can be conveniently regulated to move the stagnation point at the leading edge. In this way it is possible to avoid flow

separation on the testing side of the plate downstream of the leading edge itself, which can cause unsteadiness in the flow and a premature transition of the boundary layer. To create a turbulent boundary layer, a cylindrical tripping rod of 7 mm in diameter is installed at a distance of 70 mm from the leading edge. At a location of 0.6 m from the leading edge a liquid crystal composite plate is mounted in a cavity properly designed. The composite plate is composed of a series of layers. The composite plate is in contact with water on one side and with an air cavity on the other side. The air cavity is closed by Perspex lid, which is screwed to the flat plate and properly sealed by means of a gasket and silicone sealant. The flat plate during the experiments is installed upside down in the water flume, at a distance of about 20 cm from the bottom. The water level in the flume during the experiments is 25 cm, so the flat plate is submerged by 5 cm.

A sketch of the composite plate is shown in Figure 3.20. The test surface faces downwards. The composite plates is composed of a number of layers. All the different

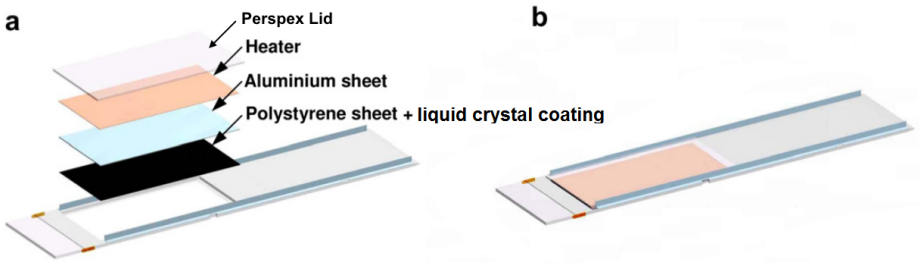

Figure 3.20: Sketch of the flat plate assembly used in LCT experiments (a) exploded view (b) assembled view

layers measure 0.25 m in width and 0.5 m in length. A description of all layers is provided hereafter.

- At the centre of composite plate there is a flexible silicone rubber heater 0.8 mm thick, which is used to produce heat by Joule effect through an electrical current flowing through its resistive wire-wound elements. The heater is capable of providing a maximum power of 15500 W/m^2.
- An Aluminium alloy sheet 2 mm thick is fixed to one side the heater surface so as to smooth out any local temperature variations generated by the wire-wound elements of the heater.

- A polystyrene sheet 0.5 mm thick is glued to to the aluminium sheet. The function of the polystyrene sheet is to retain the localised thermal variation generated by a flow feature propagating along the test surface, which otherwise would vanish due to the high thermal conductivity of the aluminium sheet. The polystyrene sheet is black. This provides a surface with the right contrast to visualize the thermal colour variation of the liquid crystal coating.

- The liquid crystals used in this experiment have a 5°C colour play, showing red at 22°C and blue at 27°C. The liquid crystal solution is provided by LCR Hallcrest© and is sprayed onto the polystyrene sheet with an airbrush. The thickness of the layer is estimated to be about 30 μm.

- In order to reduce the heat losses from back of the heater, an air cavity with a depth of 10 mm is created by attaching a Perspex lid to the Perspex frame behind the heater.

3.4.2 Other Instrumentation

The liquid crystal calibration requires a temperature measurement to be compared with the colour of the coated surface. For this purpose, it is convenient to use foil thermocouple sensors, which are very thin and, once glued to the surface, provide a very accurate temperature measurement without disturbing the flow. A Cement-On thermocouple, manufactured by Omega Engineering© is employed. The thermocouple needs to be insulated to prevent current dispersion using an appropriate insulating adhesive. The thermocouple used are of K-type, which employ a Chromel-Alumel junction. The voltage output from the thermocouple is provided to a A FLYDE© FE 362-TC thermocouple conditioner, which combines a high performance amplifier, an input protection filter, a common mode rejection and cold-junction compensation unit. In its standards form simple linearisation is also included for K-type thermocouples. The factory guarantees a $\pm 1^{\circ}$ error for 25 ° C change of ambient temperature, between 5 ° C and 45 ° C. The thermocouple is calibrated using a specific thermocouple calibrator.

Images are captured using a Basler© A201bc colour digital camera. The camera is equipped with an Interline Transfer Progressive Scan CCD Sensor. Its maximum resolution is 1008 x 1008 pixels, and the maximum attainable frame rate is 30 fps (frames per second). The exposure time and the frame rate can be controlled by means of an

internal clock or by means of an external trigger signal. Gain and offset can be programmed from the computer and saved into the camera internal memory via a serial link.

The camera is directly connected to a computer by means of a frame grabber, which is a NI PCIe-1429 image acquisition board for base-, medium-, and full-configuration Camera Link cameras. The base configuration uses three 8-bit taps, or input channels, to acquire up to 24 bits of data at a rate of 340 MB/s. The full configuration offers eight taps and can acquire images up to 680 MB/s.

Once the connection between the camera and the computer is made, the camera itself is controlled using National Instrument© Labview. Images are saved in uncompressed BMP (bitmap) format and are successively processed using MATLAB©. The camera is triggered using a Feedback Instruments© FG600 function generator, which generates a square wave a 10 Hz.

3.4.3 Uncertainty of the Imaging Technique

Liquid Crystal Thermography has been used to provide only some information about the spatial and temporal characteristics of the near-wall coherent structures in a turbulent boundary layer. In this work, this technique is not used to measure the wall temperature or the heat transfer coefficient. Therefore, uncertainty considerations are only limited to the spatial and temporal information that can be derived from the cross-correlations or from visual inspection.

Images are calibrated by measuring a fixed distance in pixels between two points in a sample image and comparing it with the number of pixels between the two points. The value of magnification factor is M=0.25 mm/pixel. An uncertainty of $\pm$ 1 mm is assumed in the calibration distance, which corresponds to an uncertainty in the magnification factor of δM=0.0035 mm/pixels at a confidence level of 95%. Given that, the uncertainty in each measured distance $s = \mathrm{M}\ s_{\mathrm{pixel}}$ from the images can be computed using the relationship:

$$\delta s = \delta \mathrm{M}\, s_{\mathrm{pixel}}. \tag{3.16}$$

In fact, the distance in pixel between two points can be measured with no error in MATLAB©. Considering that the maximum measurable length in pixel is the size of

the investigation area, which is 1008 pixels, the maximum uncertainty is about 3.5 mm, which corresponds to about 20 L_τ.

The capture frame rate is set by the FG600 function generator. It is assumed an uncertainty of 5% of the full scale in the frame rate, which corresponds to an uncertainty of 0.0064 s in the time interval between two consecutive images. The nominal value for this time interval is the inverse of 10 Hz i.e. 0.1 seconds.

3.5 Experimental Set-Up: Turbulent Boundary Layer Forcing Using a Synthetic Jet Array (Chapter 6)

The objectives of these experiments is to examine the forcing effect of an array of circular synthetic jets on the near-wall region of a turbulent boundary layer and to identify the operating conditions that yield skin friction drag reduction. The experimental results are discussed in Chapter 6

3.5.1 Flat Plate

The metallic flat plate used in these experiment is the same as that described in Section 3.3.1. In this case, the boundary layer is tripped using a circular rod placed 100 mm downstream of the leading edge. The synthetic jet array is located at 0.71 m from the leading edge of the plate. Assuming that a turbulent boundary layer develops from the leading edge of the flat plate and using the correlations (2.19) and (2.22), it is possible to provide a first estimation of a few important parameters related to the turbulent boundary layer itself as a function of the free-stream velocity. These parameter are Re_δ, Re_θ, Re_τ and θ at a distance of 0.72 m downstream of the leading edge of the flat plate. They are included in Table 3.2.

u_∞ [m/s]	**0.05**	**0.1**	**0.2**	**0.3**	**0.4**
θ [mm]	3.2	2.8	2.4	2.2	2.1
$\mathbf{Re}_\delta$	1660	2890	5040	6970	8770
$\mathbf{Re}_\theta$	160	280	490	680	850
$\mathbf{Re}_\tau$	100	160	260	350	430

Table 3.2: Parameters of the flat plate boundary layer in the test section at different free-stream velocities

3.5.2 Synthetic Jet Array Actuator

The synthetic jet array consists of 5 circular orifices, which communicate with the same rectangular cavity. The diameter of each orifice is 5 mm, the orifice neck is 5 mm deep and the spacing between two adjacent orifices is 9 mm, i.e. 50 L_τ. This value corresponds to half of the spanwise spacing the streamwise streaks in the turbulent boundary layer. Given this geometry, the synthetic jet array is expected to produce coherent structures of the same spatial scale as the near-wall coherent structures which populate the turbulent boundary layer. The rectangular synthetic jet cavity is glued on the insert again with silicone sealant. The driving system of the synthetic jet actuator is the same as that described in Section 3.3.

A technical drawing of the cavity assembly is shown in Figure 3.21. A schematic

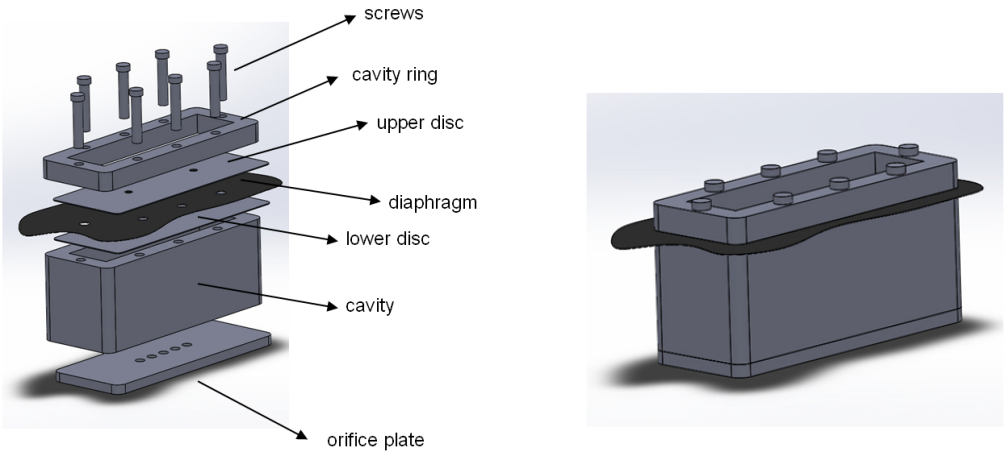

(a) Exploded View (b) Assembly

Figure 3.21: Technical drawing of the synthetic jet array mounted on a rectangular cavity

of the actuator is shown in Figure 3.22. In this case, the volume displaced by the diaphragm during an actuation cycle can be computed as:

$$V = W H \Delta \tag{3.17}$$

where W and H are the width and length of the diaphragm respectively. If we suppose that the synthetic jet fluid motion within the cavity can be represented by an incompressible flow model, then the volumetric flow rate through the synthetic jet orifices

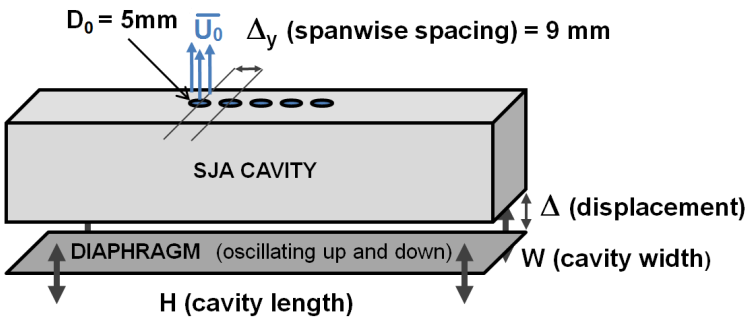

Figure 3.22: Schematic of the synthetic jet array mounted on a rectangular cavity

can be computed as

$$Q_0 = \frac{V f}{N_{or}} = \frac{W H \Delta f}{N_{or}} \tag{3.18}$$

where N_{or} is the number of orifices, 5 in this case. The averaged jet velocity over the blowing stroke is then

$$\overline{U_0} = \frac{Q_0}{\pi D_0^2/4} = \frac{W H}{5/4\pi D_0^2} \Delta f = \alpha_A \Delta f \tag{3.19}$$

where in this case α_A can be defined as

$$\alpha_A \doteq \frac{W H}{5/4\pi D_0^2}. \tag{3.20}$$

Being W=25 mm and H=100 mm and D_0= 5mm, then $\alpha_A \approx 25.5$. In this case it is possible to compute the velocity ratio and the dimensionless stroke length according to the relationships

$$\mathrm{VR} = \frac{\overline{U_0}}{u_\infty} = \frac{\alpha_A \Delta f}{u_\infty} \qquad \mathrm{L} = \frac{\overline{U_0}}{f D_0} = \frac{\alpha_A \Delta}{D_0}. \tag{3.21}$$

The computation of all these parameters is performed real-time and with National Instruments© Labview.

3.5.3 PIV Set-Up

The PIV system used is the same as that described in Section 3.3.3. In this case, the investigation plane, and so the light sheet, is normal to the flat plate and aligned to the streamwise direction, as shown in Figure 3.23. The field of view is 55 mm by 55 mm

and is approximately located at about 0.7 m from the leading edge of the flat plate. The camera is located at the side of the water flume and frames the flow through one of the lateral glass windows of the test section. The node spacing in the velocity vector grid is determined by half the final size of the interrogation window , given the 50% overlap of the recursive Nyquist grid. This corresponds to 16 pixels i.e. 0.510 mm both in the x and y direction.

Long-time averaged PIV measurements and Phase-Locked PIV measurements are

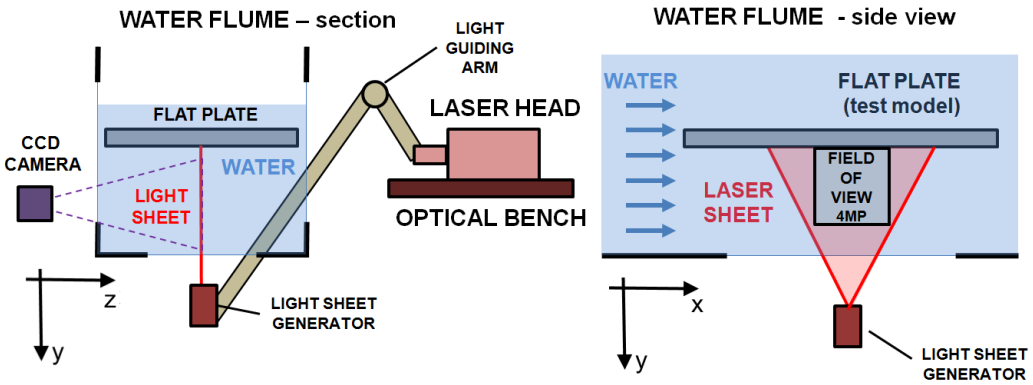

Figure 3.23: PIV set-up with light sheet normal to the flat plate

carried out. For long-time PIV measurements no synchronisation between the camera and the shaker is needed. For phase-locked 2D PIV measurements, instead, the camera and laser have to be synchronised to the oscillation of the synthetic jet diaphragm. To do that, it is necessary to trigger the camera with a TTL (Transistor-Transistor Logic) signal, which has to be provided to the synchroniser. The TTL signal is a square-wave of amplitude 0-5 volts, with the same frequency as the synthetic jet diaphragm oscillation. The modified signal routes and component integration for the synthetic jet actuation and synchronised phase-locked PIV is shown in Figure 3.24. The PC detects the phase of the diaphragm oscillation from the signal measured by the eddy current sensor. In each run the TTL signal is shifted by a certain phase delay Φ, set manually by the user. In this way the peak rise of the TTL sine wave is always delayed by Φ with respect to the diaphragm oscillation.

The PIV acquisition settings are the same as those described in Section 3.3 and also the post-processing method employed is the same. The camera magnification factor, i.e. the physical measure of a pixel size in m, is $31.87 \cdot 10^{-6}$ m/pixel so the field of

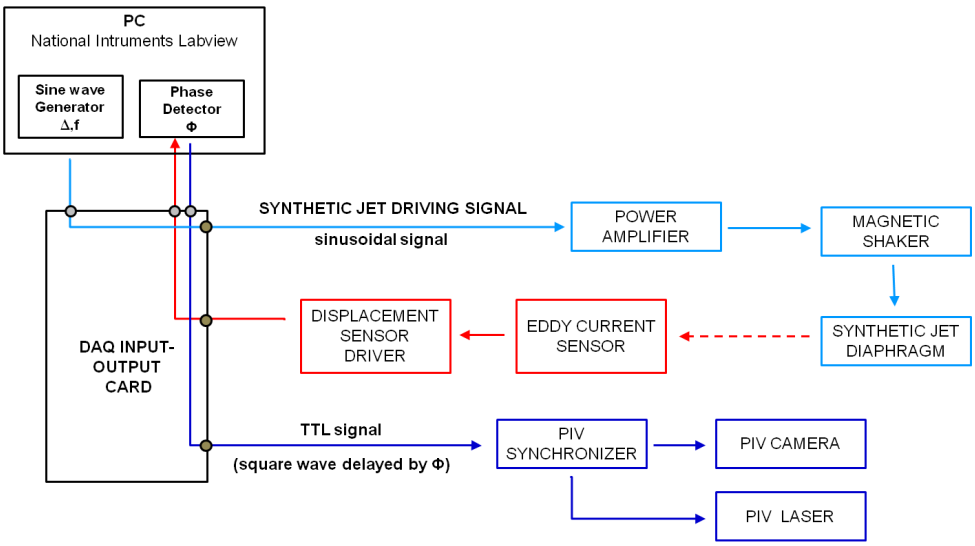

Figure 3.24: Signal routes and component integration for the actuation of the synthetic jet and synchronised Phase-Locked PIV

view is about 65 mm by 65 mm. The laser pulse is operated at a frequency of 2.5 Hz. A minimum of 500 image pairs are acquired in each test condition. The time separation between any two images of the pairs is set in a manner to produce a maximum displacement of about a quarter of the size of the initial interrogation window. Based on trial and error adjustments, the final value of $\Delta t = 5000\mu s$ is chosen.

Uncertainty Considerations

The uncertainty in the velocity vectors is calculated following the procedure described in Section 3.2.1. In particular, the uncertainty in the u-component of velocity is mainly related to the uncertainty in the pixel displacement $\delta\Delta x$, determined using PIV. It is assumed that in a turbulent boundary layer this is mainly due to the u-velocity gradients, which are high especially in the near-wall region. A velocity gradient across a single interrogation window is observed to increase the uncertainty in the determination of the pixel displacement using the typical sub-pixel interpolation schemes, implemented in all the PIV processing algorithms [116]. Considering the case of the unforced turbulent boundary layer, the uncertainty in u resulting from the contribution of the velocity gradient and of the systematic error due to the uncertainty in the magnification factor is estimated using Equations (3.5) and (3.6) for the instantaneous u-component and for the averaged $\bar{u}$-component respectively. Results are plotted in Figure 3.25. It is evident that the relative uncertainty in u is higher in the region close to the wall (about 5%), due

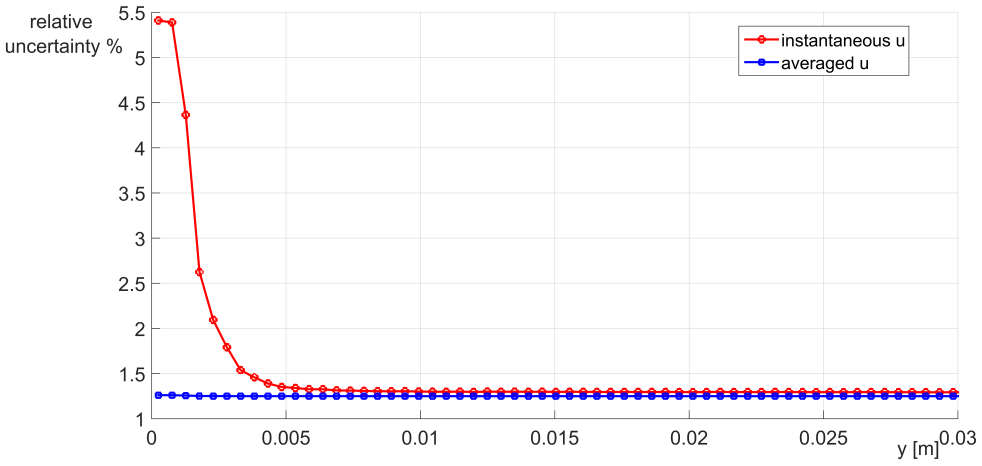

Figure 3.25: Relative uncertainty profiles assumed for u and $\bar{u}$ in the case of an unforced turbulent boundary layer

to the presence of high gradients and this tends to reach a constant value of about 1.3% away from the wall. The uncertainty in the averaged velocity $\bar{u}$ is reduced to about 1.26% in the near-wall region and reaches a value of 1.25% away from the wall. Given these considerations, an averaged u^+ profile obtained with PIV, plotted with error bars related to the uncertainty in u^+, is shown in Figure 3.26. The $\bar{u}$-velocity values are all scaled in wall units. It is assumed that the relative uncertainty in the calculation of u_τ is 5%. The uncertainty in u_τ is accordingly propagated to evaluate the uncertainty in u^+. The relative uncertainty in the v-component of velocity is estimated using Equation

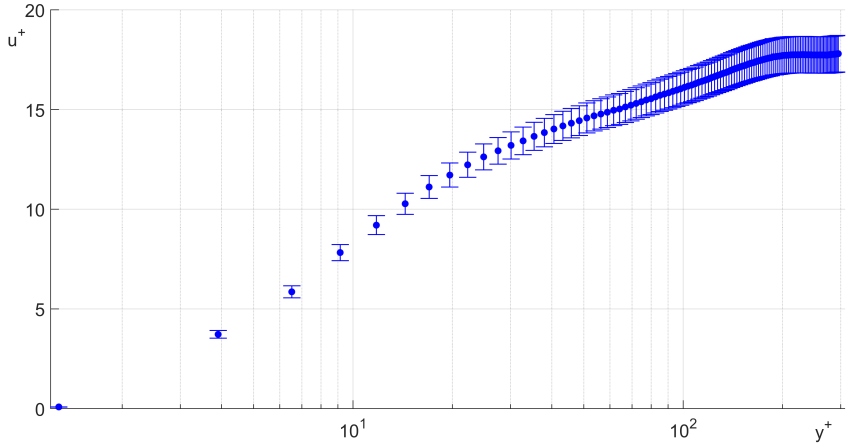

Figure 3.26: u^+-velocity profile with error bars associated to the uncertainty

.

(3.7). Gradients of v are considered negligible across the height of each interrogation

window, however the magnitude of v is much smaller than u. Therefore the relative uncertainty in v is estimated to be about 50% both in the near-wall region and away from the wall, which is reduced to 2% for the averaged $\bar{v}$-component.

Finally, using the equations shown in Table 3.1 the uncertainties in u_{RMS}, v_{RMS} and $\overline{u'v'}$ are computed and plotted using error bars about their nominal values in Figure 3.27. These values are all scaled in wall units. It is again assumed that the relative uncertainty in the calculation of u_τ is 5% which is accordingly propagated to evaluate the uncertainty of the scaled statistics.

In the case of forced turbulent boundary layers the uncertainties in all the statistical quantities estimated above are observed to have the same order of magnitude as in the case of the unforced turbulent boundary layer.

3.5.4 Extraction of Velocity Profiles and Estimation of the Skin Friction Coefficient

An example of an image pair captured is shown in Figure 3.28. By visual inspection, the wall position can be estimated with an uncertainty of about 3 pixels because the presence of light reflection on the wall prevents the position of the wall from being accurately determined. Once the averaged velocity vector field has been calculated, mean velocity profiles can be extracted at specific streamwise x locations. Consequently, the wall shear stress and the skin friction coefficient can be estimated from the velocity profiles. It has to be stressed that this is only a rough estimation of skin friction and cannot be considered as accurate as a direct method of skin friction measurement. The skin friction coefficient (and the wall shear stress) estimation is carried out through a best fit of the measured velocity data points to a boundary layer model profile in the near-wall region. The method is similar to that described by Kendall and Koochesfahani [76]. Velocity data point very close to the wall are not considered accurate enough for the estimation of skin friction, essentially because of the presence of light reflection at the wall. Therefore, only points at $y^+ > 3$ are taken into account. An upper limit for y^+ also has to be considered, based on the validity of a boundary layer model.

Two boundary layer model profiles are considered:

- the relationship $u^+ = y^+$, in the viscous sublayer. According to [57, 9] a linear

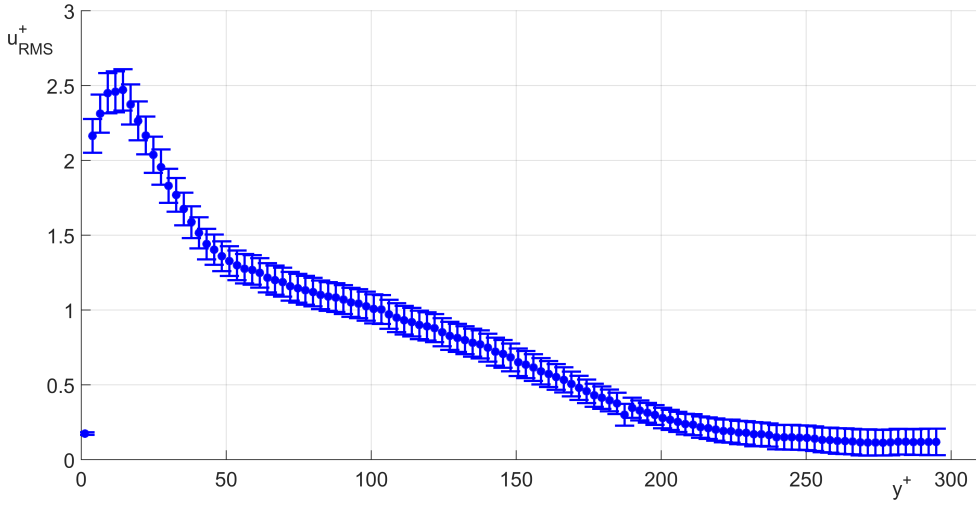

(a) u^+_{RMS} profile

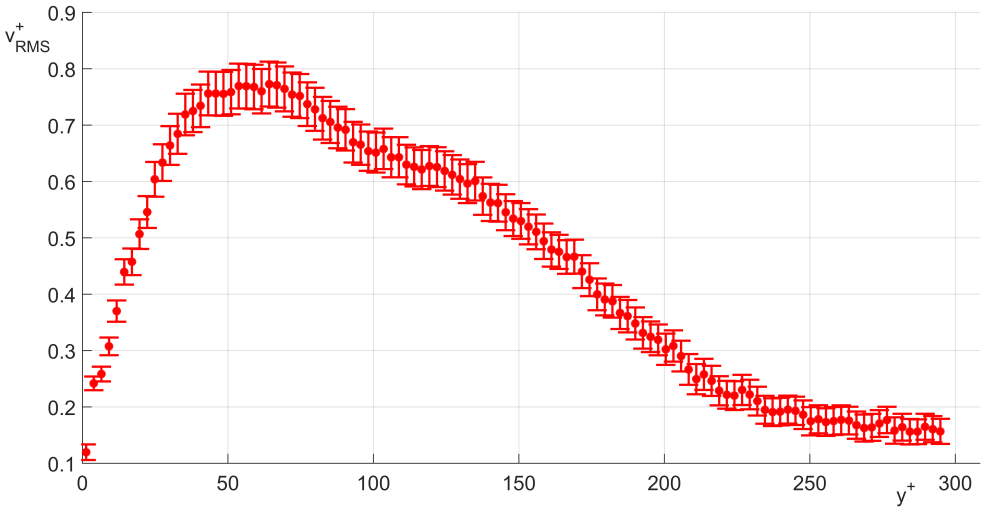

(b) v^+_{RMS} profile

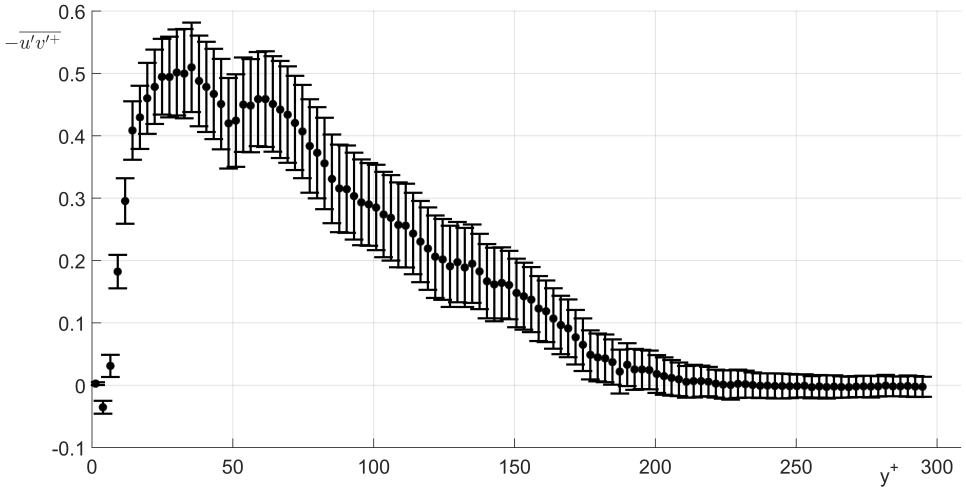

(c) $\overline{u'v'}^+$ profile

Figure 3.27: u^+_{RMS}, v^+_{RMS} and $\overline{u'v'}^+$ profiles in the unforced turbulent boundary layer with error bars

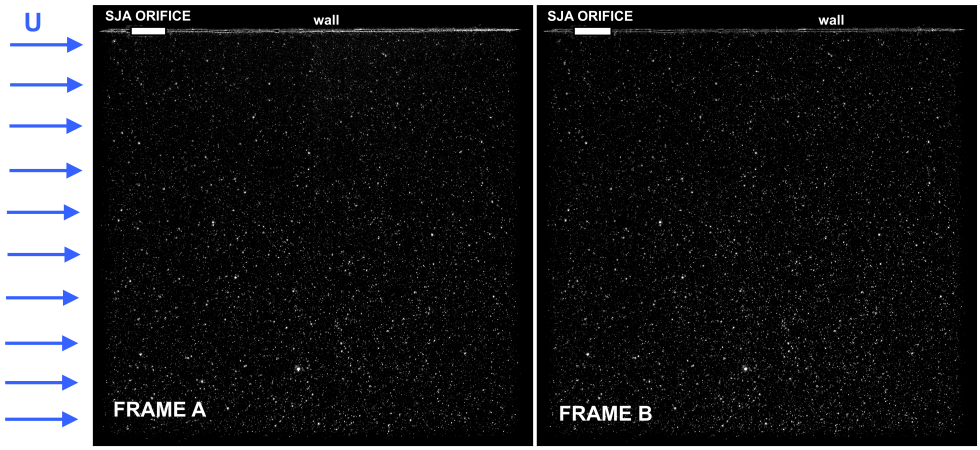

Figure 3.28: Example of a captured PIV image pair: the flow is from left to right, the wall is on the top

sublayer is assumed to be present for flows with moderate three-dimensionality, pressure gradient and surface roughness, therefore it is assumed to exist also in a boundary layer forced by synthetic jets.

- also the law of the wall derived by White, equation (2.28) can be used. In this case, it is also possible to include velocity points in the buffer layer and in the logarithmic layer, as long as the shape of the velocity profile tends to follow that of the boundary layer model. Therefore, the application of this boundary layer model is believed to be appropriate only for an unforced turbulent boundary layer, as the synthetic jet forcing is observed to modify the velocity profile in the near-wall region, especially in the buffer layer and in the logarithmic layer.

In both cases the estimation is carried out using an optimisation routine implemented in MATLAB©, which is based on the Nelder-Mead simplex search method of Lagarias et al. [89]. The method is sketched in figure 3.29. The optimisation routine objective is to estimate first the value of u_τ. In order to do this, an initial value has to be provided. This is derived from the empirical relationship for the skin friction coefficient C_{fx0} in a zero-pressure gradient turbulent boundary layer at that exact x location, see equations (2.19). Given C_{fx0}, $u_{\tau 0} = u_\infty \sqrt{\frac{C_{fx0}}{2}}$. The experimental data points are then considered and the value of u_τ that minimises the residual functional Ψ defined as

$$\Psi \doteq \frac{1}{N} \sum_{i=1}^{N} \left[u_i^+ - u_{mod}^+(y_i^+) \right]^2 \tag{3.22}$$

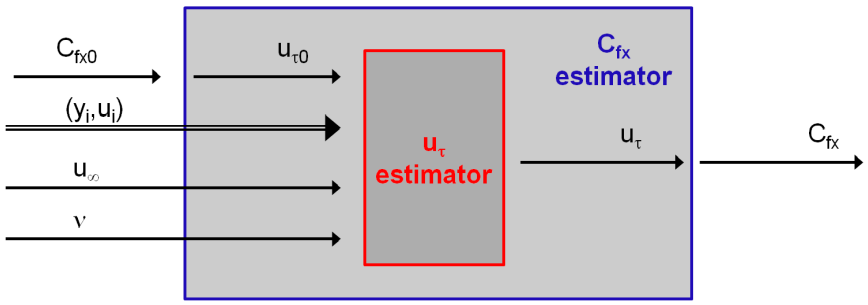

Figure 3.29: Schematic of the estimation method of u_τ and C_{fx}

is determined, where (y_i, u_i) are the data points in the experimental velocity profiles derived with PIV and u_{mod} is the boundary layer model assumed. Once u_τ has been estimated, the skin friction and the wall shear stress are respectively calculated as

$$C_{fx} = 2\,\frac{u_\tau^2}{u_\infty^2} \qquad \tau_w = \rho\, u_\tau^2. \tag{3.23}$$

To validate the method, u_τ and C_{fx} are estimated considering the experimental points between $y^+ = 3$ and $y^+ = 7$ and a fitting to the viscous sublayer law of the wall $u^+ = y^+$, where initially it is assumed that $y^+ = \frac{y u_{\tau 0}}{\nu}$. The calculation is performed also for the forced turbulent boundary layer profiles. Once the value of u_τ is estimated, the scaled velocity profiles are plotted along with the law of the wall $u^+ = y^+$ and the White law of the wall. The results are shown in figure 3.30, 3.31 and 3.32 for forcing frequencies of 2 Hz, 3 Hz, and 4 Hz respectively. Observing these figures, it seems appropriate to conclude that:

- in the case of unforced turbulent boundary layer, the scaling to the White law of the wall seems to hold quite well, at least up to $y^+ = 50$. Using the fitting to the White law of the wall, as a larger number of data points is available for the fitting, the estimation of the friction velocity, and consequently of the skin friction coefficient, is considered more accurate.

- for forced turbulent boundary layers a velocity fitting to the scaling $u^+ = y^+$ in the range $3 < y^+ < 7$ seems to hold in all cases. The viscous sublayer hypothesis is not believed to hold for $y^+ > 5$ (see also Section 2.1.3). However, in these cases it is assumed valid up to $y^+ = 7$, so that the skin friction velocity estimation is performed with at least an additional data point. A good fitting is visually observed in all the analysed cases, except at VR=0.2 and f=4Hz. The fitting to

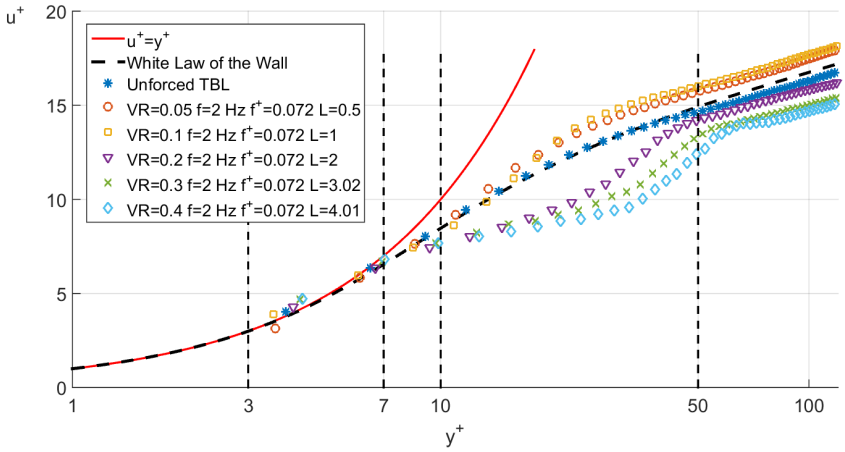

Figure 3.30: Scaled velocity profiles with the correspondent values of u_τ, for the unforced turbulent boundary layer case and the cases with synthetic jet forcing at f=2Hz

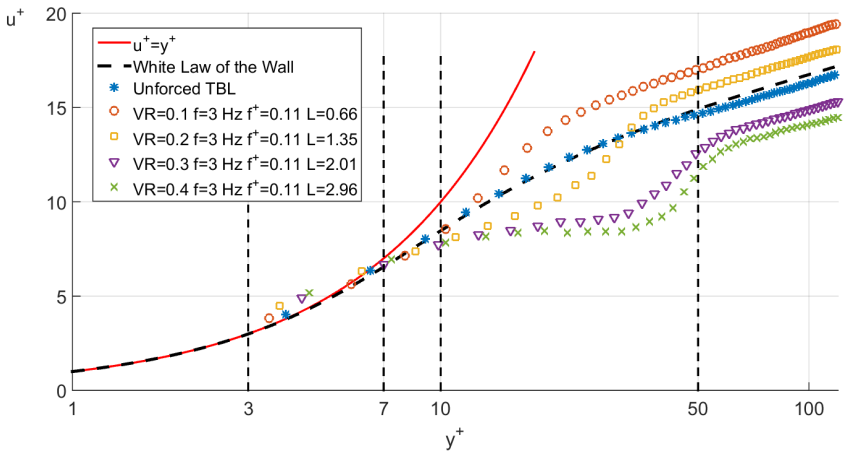

Figure 3.31: Scaled velocity profiles with the correspondent values of u_τ, for the unforced turbulent boundary layer case and the cases with synthetic jet forcing at f=3Hz

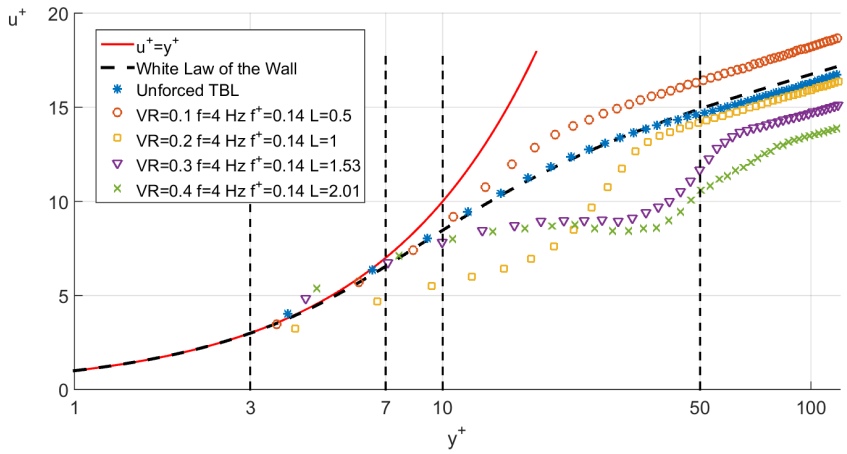

Figure 3.32: Scaled velocity profiles with the correspondent values of u_τ, for the unforced turbulent boundary layer case and the cases with synthetic jet forcing at f=4Hz

the White law of the wall does not seem to be appropriate for $y^+ > 10$.

In summary, it is concluded that the best way to estimate skin friction is to use a fitting of the velocity profile to the viscous sublayer law in the range $3 < y^+ < 7$. Therefore, this is the method of skin friction estimation used in Chapter 6.

To validate the method, it is possible to compare the estimated skin friction coefficients, using both the fitting laws, in the case of an unforced turbulent boundary layer over a range of x locations. The results can also be compared with the empirical relationship for the skin friction coefficient provided in Equation (2.19), as shown in figure 3.33. The comparison shows good agreement between the values of the skin friction coefficients determined with the two methods and with the empirical correlation. In this case $\Delta x^+ = \frac{(x-x_{SJA})\,u_\tau}{\nu}$ represents the scaled streamwise distance in wall-units from the synthetic jet array. The estimation with the viscous sublayer fitting between $y^+ = 3$ and 7 provides values very close to both the empirical relationship and the estimation using the White law of the wall. A certain discrepancy is observed around the position of the jet, because the presence of the orifice locally perturbs the flow. A small deviation starting from Δx^+=170 is also noticed, probably due to a lack of PIV image quality quality in that region.

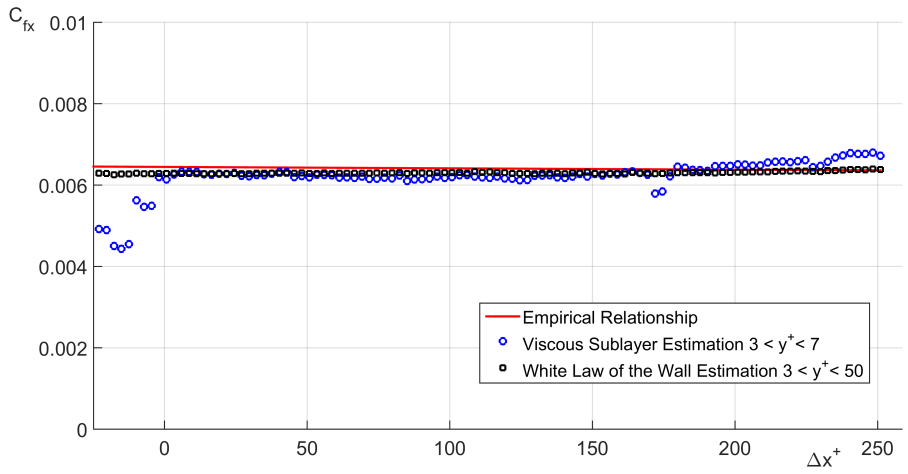

Figure 3.33: Comparison of the different methods of C_{fx} estimation in an unforced turbulent boundary layer as a function of x

Uncertainty and Sensitivity Analysis on the Estimation of the Skin Friction Coefficient

The determination of the skin friction coefficient involves a complex and non-linear method, which includes an optimisation routine. The estimation can be seen as the output of a function which relates some input variables to an estimate of C_{fx}, see again Figure 3.29. Therefore, it is not straightforward to carry out a simple uncertainty propagation analysis. It is more convenient to run a simple Monte Carlo simulation. The Monte Carlo simulation is run in MATLAB© and assumes a Gaussian (or normal) distribution in which the mean value is the nominal value used for the C_{fx} estimation and the standard deviation that depends on the variable uncertainties. At every step of the simulation, each input variable is sampled from the assumed distribution and a value of C_{fx} is estimated. A total number of 500,000 samples is considered for each variable. The output of the simulation is a distribution of values of C_{fx}. From this distribution it is possible to easily compute a value of the uncertainty in C_{fx} at a certain confidence level. In particular, it is assumed that:

- The uncertainty in the free-stream velocity is assumed to be $\delta u_\infty = 1.25\%$ of u_∞.
- The uncertainty in the velocity profile points (y_i, u_i) is split into the uncertainty in y_i, which represent the uncertainty in the determination of the wall location y_0 and into an uncertainty in the u_i values. The uncertainty in the wall position y_0 is assumed to be of 3 pixels, as stated in Section 3.5.4. This means that the

normal distribution is assumed to have a standard deviation of 1.5 pixels. The uncertainty in the velocity in the near-wall region $3 < y^+ < 7$ is higher than in the free-stream. To be conservative, an uncertainty of 3.0% of the value of the local velocity is assumed.

- The uncertainty in the value of kinematic viscosity is based on the uncertainty in the measurement of the water temperature. In fact, the kinematic viscosity ν is derived using Sutherland's law. The water temperature is measured with a thermometer, the resolution of which is 0.2° C. Therefore, it is conservative to assume an uncertainty of 0.1° C. This results in an uncertainty in ν of about 1% of its nominal value.

- The initial estimation of the skin friction coefficient can also affect the outcome of the estimation. This value is derived according to empirical correlations for a turbulent boundary layer. To be conservative, an uncertainty of about 10% is assumed.

The results for the Monte Carlo simulation in the case of an unforced turbulent boundary layer are shown in Figure 3.34. In part (a) the histograms of the principal input variables are shown, whereas in part (b) the histogram of the output variable i.e. the skin friction coefficient C_{fx} is shown. The distribution of the skin friction coefficient also assumes a shape similar to a Gaussian distribution.

This study shows that the value of the uncertainty in C_{fx} is about 9.3% of the nominal expected value, with a confidence level of about 94.5%. The value of the uncertainty in C_{fx} is surely significant. However, this is expected, since it has already been stated that this method of estimation of the skin friction coefficient is not the most accurate, it only guarantees a first estimation.

The uncertainty in C_{fx} in the case of a forced turbulent boundary layer has also been estimated and it is found to be of the same order of magnitude as that of an unforced turbulent boundary layer.

A sensitivity analysis is also recommended because it helps to identify the input variables that affect most significantly the estimate of C_{fx} i.e. the output variable. In this case, sensitivity analysis is carried out using a variance-based method, in particular the FAST (Fourier Amplitude Sensitivity Test) algorithm, implemented in MATLAB©. A

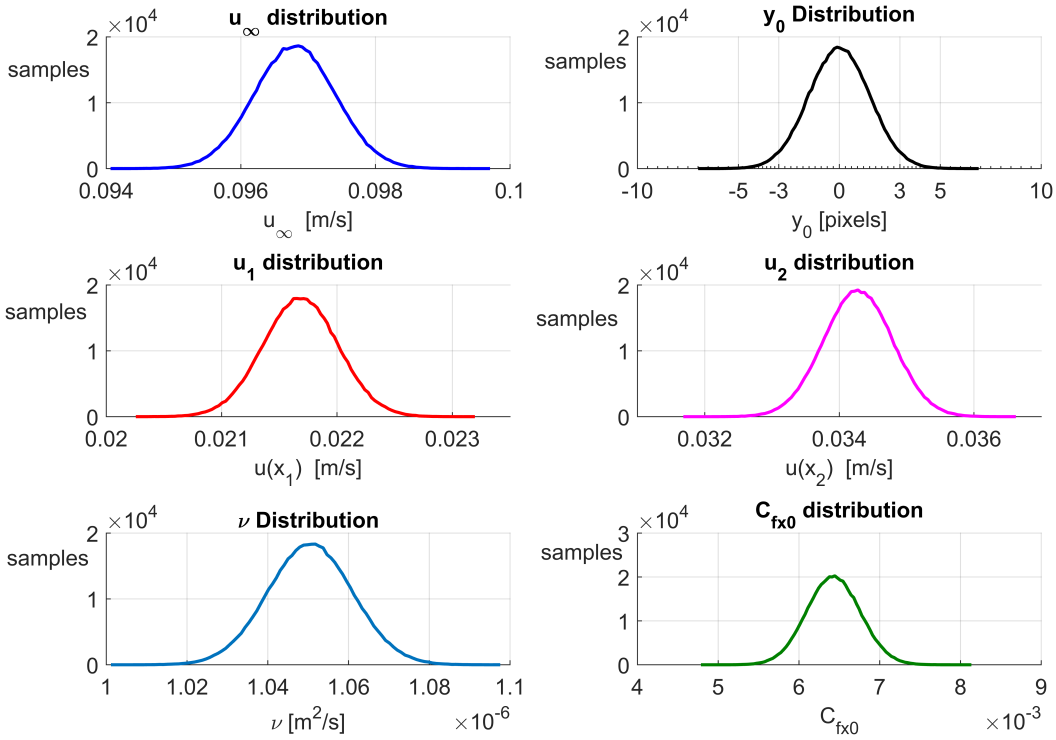

(a) Histograms of the sampled input variables: u_∞, y_0, u_1 or $u(x_1)$ i.e. the mean u-velocity of the first point from the wall, u_2 or $u(x_2)$ i.e. the mean u-velocity of the second point from the wall, ν and C_{fx0}

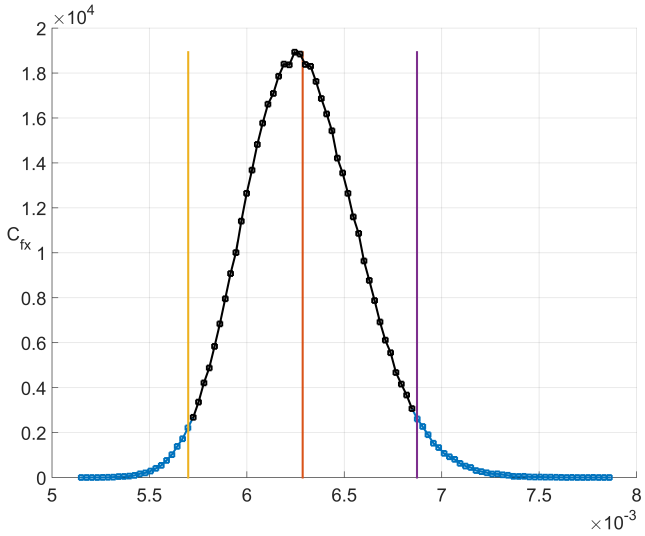

(b) C_{fx} histogram (output variable)

Figure 3.34: Inputs/Outputs of the Monte Carlo simulation in the case of an unforced turbulent boundary layer

detailed description of the method is given in [25, 140]. For each variable a first-order sensitivity coefficient S_i is determined, which measures the contribution of the variance of i-th variable to the variance of the output i.e. C_{fx}, neglecting the interactions with the other input variables. The coefficients are normalised and therefore their value is from 0 to 1. The method is applied to the case of the unforced turbulent layer, using the viscous sublayer fitting. The obtained coefficients S_i are reported in Table 3.3. The

variable i	S_i
y_0	0.84
$u(x_1)$	0.0072
$u(x_2)$	0.049
ν	0.041
C_{fx0}	0.0000024
u_∞	0.064

Table 3.3: First-order sensitivity coefficients for all the input variables

results show that the estimation of C_{fx} is, as expected, very sensitive to the determination of the wall position y_0 and is practically insensitive to the initial value C_{fx0}. The sensitivity to the other variables is approximately the same, even if it is found that the second velocity point from the wall has a stronger importance with respect to the first one. Results in the case of a forced turbulent boundary layer are similar to the case of an unforced turbulent boundary layer.

The accuracy of the method of estimation of the skin friction coefficient could be improved by zooming in the region of interest. In fact, this will increase the number of data points available in the viscous sublayer. In addition, the zoom should also enable a more accurate location of the wall, which is seen to be the variable the estimation is most sensitive to. It is also recommended to compare the performance of the method with other skin friction measurement techniques, even if they are all quite challenging to apply in the case of a turbulent flow.

3.5.5 Triple Decomposition

When a turbulent flow is periodically forced, the triple decomposition of the velocity field can be used to extract the periodic disturbance imposed by the actuator and the random fluctuations superimposed onto it. The reader is referred to [56] for a complete description of this procedure. Following this discussion, the generic time series of the

variable g at a point (x,y) can be decomposed as[2]

$$g(x,y,t) = \bar{g}(x,y) + \tilde{g}(x,y,t) + g'(x,y,t). \tag{3.24}$$

where $\bar{g}$ is the time average, $\tilde{g}$ is the periodic part and g' is the random fluctuating part. Indeed, the flow is perturbed by a periodic disturbance at any given point, which has approximately the same frequency f of the imposed sinusoidal perturbation i.e. the oscillation frequency of the synthetic jet diaphragm. In Figure 3.35 the decomposition process is shown. The decomposition requires the definition of a reference wave,

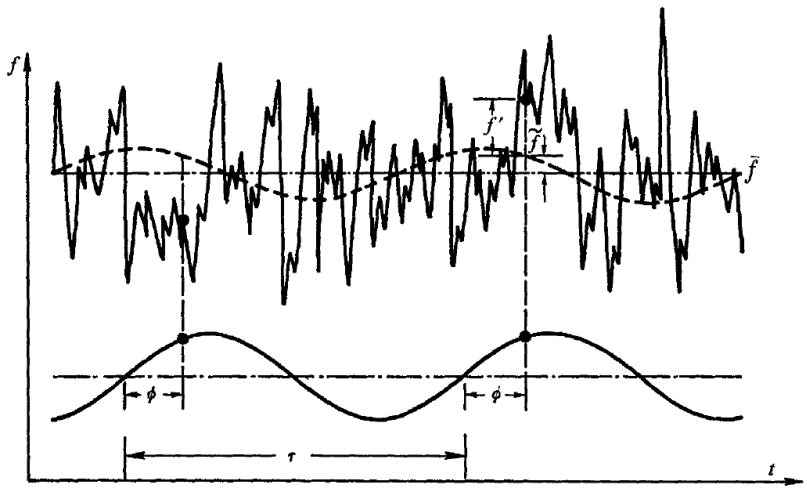

Figure 3.35: Process of triple decomposition (figure taken from [56])

which we can assume to be the sinusoidal oscillation of the diaphragm.

Given that, the time average can be defined as:

$$\bar{g}(x,y) \doteq \lim_{T_{obs}\to\infty} \frac{1}{T_{obs}} \int_0^{T_{obs}} g(x,y,t)\,dt. \tag{3.25}$$

where T_{obs} is the observation time interval.

The periodic part is defined at any given point as:

$$\tilde{g}(x,y,t) \doteq < g > (x,y,t) - \bar{g}(x,y) \tag{3.26}$$

[2]The dependence on z is omitted, considering only the PIV flow field on a plane at constant z.

where

$$< g > (x,y,t) \doteq \lim_{N\to\infty} \frac{1}{N} \sum_{n=0}^{N} g(x,y,t+nT), \tag{3.27}$$

where T is the period of the reference wave. The quantities $< g >$ and $\tilde{g}$ are periodic with period T, which means $< g > (x,y,t+nT) =< g > (x,y,t)$ and $\tilde{g}(x,y,t+nT) = \tilde{g}(x,y,t)$.
Finally, the random fluctuating part can be computed as

$$g'(x,y,t) = g(x,y,t) - \bar{g}(x,y) - \tilde{g}(x,y,t) = g(x,y,t) - < g > (x,y,t). \tag{3.28}$$

It represents the random fluctuating field which is superimposed onto the periodic disturbance. This field is supposed to be uncorrelated with the periodic part.

The triple decomposition is applied to the velocity fields obtained with PIV. The generic instantaneous components obtained for a single image pair are indicated as $u_i(x,y)$ and $v_i(x,y)$. For each test condition, the mean components $\bar{u}(x,y)$ and $\bar{v}(x,y)$ of the velocity field can be obtained by averaging the 1000 $u_i(x,y)$ and $v_i(x,y)$ fields, with $i = 1,2,...1000$, obtained in the PIV tests in which the image capturing is not phase-locked with the shaker/diaphragm oscillation. On the other hand, the periodic components of the vector fields are obtained from each phase-locked test. Initially the phase-locked average velocity components are computed from the 500 velocity fields obtained at each phase. These components are also functions of the phase itself and are indicated as $< u > (x,y,\Phi)$ and $< v > (x,y,\Phi)$. Then the periodic components are estimated by calculating the differences:

$$\tilde{u}(x,y,\Phi) =< u > (x,y,\Phi) - \bar{u}(x,y) \qquad \tilde{v}(x,y,\Phi) =< v > (x,y,\Phi) - \bar{v}(x,y). \tag{3.29}$$

The random components $u_i'(x,y,\Phi)$ and $v_i'(x,y,\Phi)$ can be finally obtained as:

$$u_i'(x,y,\Phi) = u_i(x,y) - < u > (x,y,\Phi) \qquad v_i'(x,y,\Phi,t) = v_i(x,y) - < v > (x,y,\Phi) \tag{3.30}$$

with $i = 1,2,...500$. The random velocity components are only available for the eight phases considered. In order to compute the statistics, like u_{RMS}, v_{RMS} and $\overline{u'v'}$ all the

random components for all the eight phases have to be considered altogether. Therefore, they are estimated as:

$$u_{RMS}(x,y) = \sqrt{\frac{1}{N * N_\Phi} \sum_{j}^{N_\Phi} \sum_{i}^{N} \left(u_i'(x,y,\Phi)\right)^2} \tag{3.31}$$

$$v_{RMS}(x,y) = \sqrt{\frac{1}{N * N_\Phi} \sum_{j}^{N_\Phi} \sum_{i}^{N} \left(v_i'(x,y,\Phi)\right)^2} \tag{3.32}$$

$$\overline{u'v'}(x,y) = \frac{1}{N * N_\Phi} \sum_{j}^{N_\Phi} \sum_{i}^{N} \left(u_i'(x,y,\Phi)\, v_i'(x,y,\Phi)\right) \tag{3.33}$$

where N is the number of velocity vectors available at each phase (500 in our case) and N_Φ is the total number of phases considered (8 in our case). If the statistics are computed in this way, only the contribution of the random fluctuations is taken into account, whereas the contribution of the periodic components of velocity is not.

3.6 Experimental Set-up: Design of A Feed-Forward Predictor for Turbulent Boundary Later Control (Chapter 7)

The objective of these experiments is to lay the basis for the design of a feed-forward control system of a turbulent boundary layer based on wall-sensors and on an array of circular synthetic jets. The motivation of the study and the experimental results are described in detail in Chapter 7.

3.6.1 Flat Plate for Liquid Crystal Experiments

The experimental set-up for the Liquid Crystal Thermography experiments is the same as that described in Section 3.4.

3.6.2 Flat Plate for CTA Experiments

The rig used for Constant Temperature Anemometry is the same metallic flat plate used for Particle Image Velocimetry measurements, see Sections 3.3 and 3.5. However, in order to carry out these measurement, the flat plate is slightly modified. First of all, to

install the support of the hot-film probe, the plate has to placed in the upright position in the water flume, unlike in the Particle Image Velocimetry experiments. In addition, in order to limit the heat transfer to the substrate, a polystyrene sheet 0.5 mm thick is glued onto the surface of the flat plate using a suitable double-sided tape.

The wall hot-film 55R47 probes are then individually glued to the polystyrene substrate. Thin copper wires are soldered to the metallic ends of the probes using a proper seal. The wires are then soldered to a BNC cable which is connected to the anemometer. In order to prevent oxidisation, the probes are covered with a layer of varnish. For liquid grounding a brass electrode is placed in the flow, sufficiently downstream of all the probes. The hot-film 55R15 probe is mounted instead on a traverse system which allows an accurate positioning in the flow.

3.6.3 Hot-film Probes

Two types of probes are used in the present work: the Dantec 55R47 wall glue-on probe and a Dantec 55R15 hot-film probe.

The Dantec 55R47 glue-on sensor is a nickel film deposited on a 0.05 mm thick polyimide foil carrying 0.5 μm quartz coating. The sensor is large 0.9x0.1 mm and is connected to gold-plated lead areas. A drawing of the sensor with its dimension in mm is shown in Figure 3.36. The sensor has to be glued directly onto the wall at the mea-

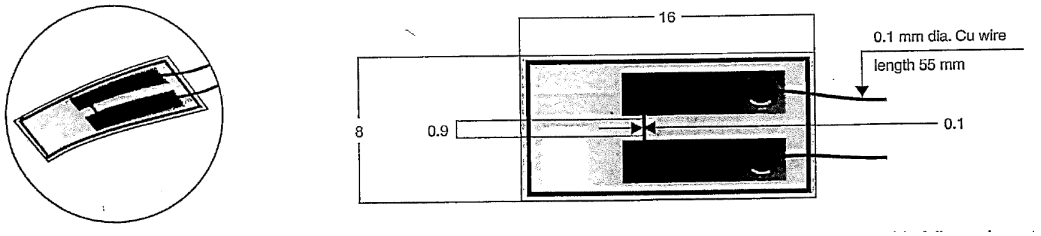

Figure 3.36: Dantec 55R47 probe

surement point. Copper wires soldered to the leads represent an electrical connection between probe cable and probe. If the probe is used for quantitative measurements it must be calibrated in-situ, as it normally cannot be removed when first glued in place. The probe is sensitive to the component of wall shear stress normal to the sensor: if the flow direction is normal to the film, the probe is mainly sensitive to the streamwise component of wall shear stress. The 55R47 glue-on probe is originally for use in air,

but a version for water use also exists, in which the protective quartz coating is 2 μm thick, instead of 0.5 μm. With a few precautions, it is possible to extend the use of the air probes also for water. The first measure to adopt is to cover the sensor with a layer of special varnish, which insulates the sensor element from the water. Secondly, the probe needs to be grounded to the water by connecting a wire to the anemometer ground terminal. The grounding wire is soldered to a small brass electrode plate, which is immersed in the flow and is located as close as possible to the glue-on probe. In this way the potential difference between the probe and the water is always kept at a low level, avoiding the corrosion of the probe.

When measuring the wall shear stress the *loss of heat transfer to the substrate* needs to be taken into account. Indeed, since the sensor is in direct contact to the wall, heat is transferred to the fluid by convection, but also to the substrate by conduction. The heat transfer to the substrate can be interpreted as an increased thermal inertia of the film. Therefore, the frequency response of the hot-film glued to the wall is reduced compared with the case in which the film is only immersed in the fluid. The problem depends on the material of the film, on the type of fluid and on the material of the substrate. Tardu [148] addressed this problem with accurate numerical simulations, see Figure 3.37. The conclusion of this study is that for high values of the conductivity ratio k_S/k_F,

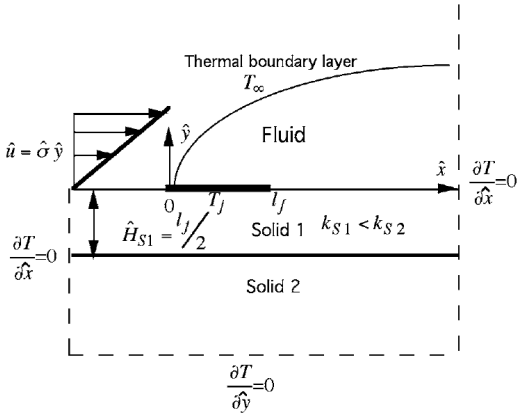

Figure 3.37: Heat transfer through a wall hot-film probe in a boundary layer (figure taken from [148])

where k_S is the thermal conductivity of the substrate and k_F is the thermal conductivity of the fluid, the heat transfer from the film to the substrate is considerably larger than the direct transfer to the fluid. The importance of heat transfer to the substrate increases

if the velocity decreases. A thin layer of material with low conductivity inserted between the film and the substrate attenuates this effect. The solution proposed by Breuer of creating a vacuum cavity directly below the sensor greatly increases the frequency response of the probe [119]. If the substrate is made from polystyrene and the fluid is water, the conductivity ratios is about 0.05. However, if the fluid was air, this value would be much higher, about 1.3. Therefore, the attenuation of the frequency response is not expected to be significant for water flows, as also reported in Colella and Keith [33]. To have a confirmation of that, simple experiments are preliminarily carried out in a desktop water flume. A water flow is established and a 55R47 probe is installed, provided by liquid grounding. The probe is operated at an overheat ratio of 1.1 and driven by a TSI IFA 300 system. Upstream of the probe a disc is inserted in the flow. The disc is moved by a shaker at different oscillation frequencies, as shown in Figure 3.38. The signals from the anemometer are digitally acquired at a sampling frequency

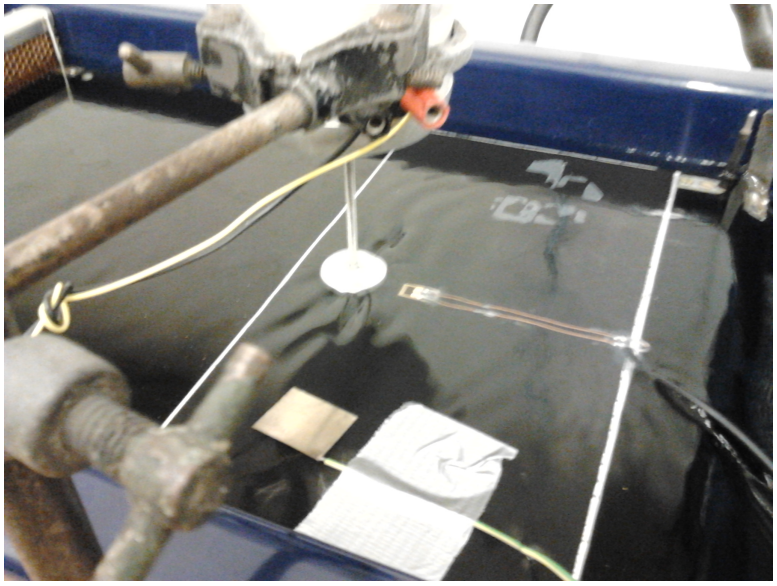

Figure 3.38: Set-up of the experiments for the frequency response analysis of a 55R47 hot-film probe in water

of 250 Hz sampling after being analogically filtered at 100 Hz to prevent aliasing. A power spectral density plot is computed and shown in Figure 3.39. The sensor appears to picks up very well oscillations at low frequencies, up to 10 Hz. For higher frequencies the peak in the power spectral density is still detectable, but is weakened. This is however due do the reduction in amplitude of the oscillations generated by the shaker for increasing frequencies. In any case, it is also possible to pick up partially an oscillation of 100 Hz, confirming an acceptable frequency response of the probe in water.

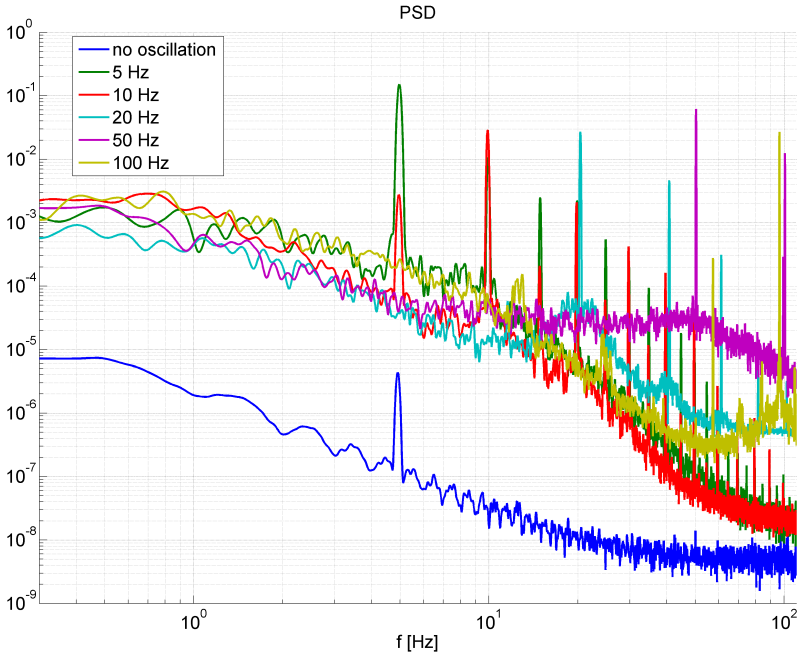

Figure 3.39: Power spectral density of CTA voltage output signals at different frequencies of oscillation of the disc

The Dantec 55R15 hot-film probes are instead shown in Figure 3.40 . They are nickel

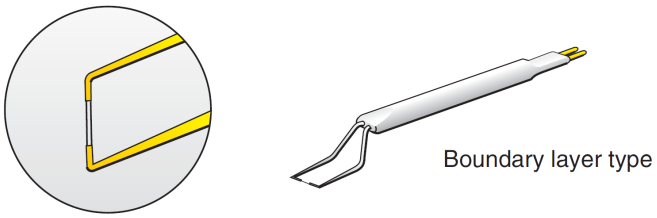

Figure 3.40: Dantec 55R15 probe and boundary layer mount

film deposited on 70 μm diameter quartz fibre. The overall length is 3 mm, whereas the sensitive length is 1.25 mm. The film is protected by quartz coating of approximately 2 μm in thickness. These sensors are designed to be used in conducting liquids covering velocities up to 10 m/s. The probe is installed in a special mount, also shown in Figure 3.40, which reduces the intrusiveness in boundary layer measurements. The mount is then fixed to a right angle mounting tube and fixed to a manual traverse system.

3.6.4 CTA Systems

The two CTA systems used in the present experiments are the TSI IFA 300 and the Dantec mini-CTA system.

The TSI IFA 300 is a fully-integrated, thermal anemometer-based system that measures mean and fluctuating velocity components in air, water, and other fluids. The system has three channels, but it is further expandable up to sixteen channels. It provides up to 300 kHz frequency response, depending on the sensor used. Each module is designed with a built-in thermocouple circuit for measuring fluid temperature and for making temperature corrections. The system consists essentially of a bridge and amplifier circuit. As the fluid flow passes over the heated sensor, the amplifier senses the bridge off-balance and adjusts the voltage to the top of the bridge, keeping it in balance. The bridge voltage is also sensitive to temperature, therefore the built-in thermocouple circuit can be employed to correct the results and to minimise the effects of a temperature drift. Each channel of anemometry contains a single bridge circuit and signal conditioner. The bridge circuit employs the so-called SMARTTUNE technology, which automatically optimises the frequency response. The back panel includes an input BNC connector for each channel labelled "Channel x Prob" and another BNC connector labelled "Output Voltage". The front panel LEDs indicate the configuration and status of each sensor. The signal conditioners in the IFA 300 also provide settings for filtering and increasing the bridge voltage gain to use the entire $\pm$5V signal range.

The ***Dantec mini-CTA 54T42*** system is a versatile anemometer that can be used with Dantec Dynamics© standard hot-wire and hot-film probes. The Dantec mini-CTA 54T42 is especially suitable for basic flow diagnostics and its small size facilitates its installation close to the probe. The anemometer is mounted on a small box equipped with BNC connectors and it is operated with a 12 VDC power adapter. It can be used for measurements both in air and in water flows. The operational resistance range is 4-20 Ω, but depending on the set-up it can also be used to operate probes whose cold resistance is higher than 20 Ω at moderate overheat ratios. Overheat adjustment, signal conditioning and cable compensation are performed via DIP-switches and jumpers inside the box. The overheat adjustment is assisted by an Excel spreadsheet, which can be downloaded from the Dantec Dynamics© website. The box also contains the socket for liquid grounding, necessary in water flows.

Chapter 4

Control of Streamwise Streaks Downstream of a Circular Cylinder in a Laminar Boundary Layer

The results of this chapter are presented in [144] Spinosa E., Zhong S. - *Control of streamwise vortices using synthetic jets*, The 4th International Conference on Experimental Fluid mechanics, Beijing (China), 2014

4.1 Introduction

In this chapter a flow control strategy based on the principle of suppressing the streamwise disturbances that naturally form in a turbulent boundary by creating ad-hoc complementary streamwise disturbances with synthetic jet actuators is developed. The first logical step towards this is to evaluate the capability of this type of flow actuator in controlling artificially created streamwise disturbances in a laminar environment. The objective of this series of experiments is to operate a single round synthetic jet actuator so as to control the streamwise disturbances, and in particular the streamwise vortices, generated by a circular cylinder mounted vertically across a laminar boundary layer.

A schematic of the experimental rig and of the reference system used in the following discussion is shown in figure 4.1. The diameter of the cylinder d_{CYL} is 2 mm, the synthetic jet orifice diameter D_0 is 5 mm, therefore the ratio d_{CYL}/D_0 is 0.4. The origin of the reference system used for the description of the results is located at the wall at

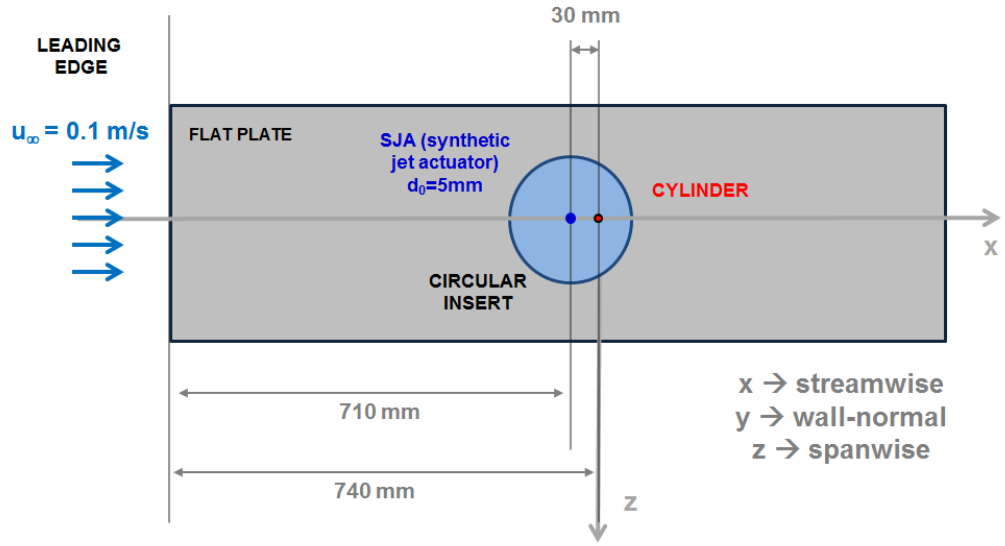

Figure 4.1: Schematic of the rig for the study of the synthetic jet - cylinder interaction (top view, not in scale)

the centre of the cylinder. The streamwise coordinate x points downstream, the wall-normal coordinate y is orientated away from the wall and the spanwise coordinate is orientated as shown in Figure 3.12. In this system, the synthetic jet orifice is therefore located at x=-30 mm i.e. $x/D_0 = -6$.

Base Flow PIV experiments to derive the base flow are performed immediately after the PIV measurements on the plane parallel to the test plate. The same configuration of the water flume is kept and the same RPM value of the centrifugal pump is used, therefore the experimental conditions are approximately the same as in the previous experiments. In this case, PIV measurements are carried out in the longitudinal plane i.e. plane $x-y$. The experimental set-up is that illustrated in Figure 3.23. The profile is extracted at x=10 mm i.e. $x/D_0 = 2$, upstream of the cylinder and downstream of the synthetic jet orifice, with the synthetic jet switched off. The velocity profile is shown in Figure 4.2. The free-stream velocity is about 0.128 m/s. The velocity profile derived from the Blasius solution for a laminar boundary layer, taken from the tabulated data reported in [159], is also plotted for comparison. There is a good agreement between the experimental and the Blasius velocity profile. This also shows that the synthetic jet orifice does not perturb significantly the flow downstream when the synthetic jet is switched off.

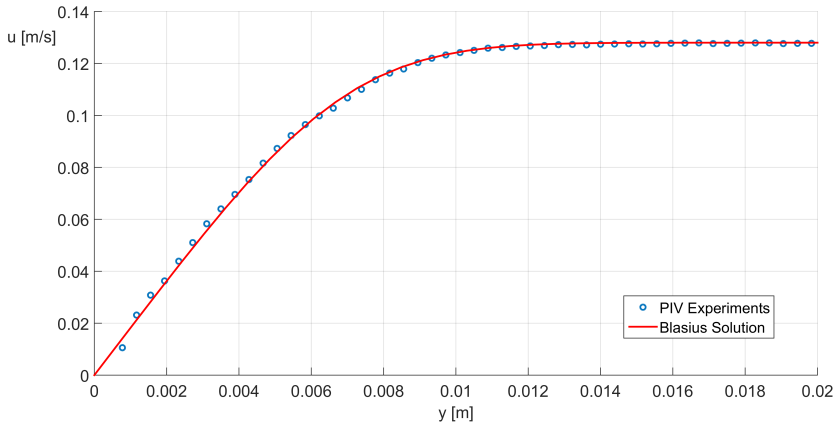

Figure 4.2: Velocity profile $u(y)$ across the laminar boundary layer

At that location the boundary layer thickness is approximately $\delta = 11.6$ mm. The ratio of the synthetic jet diameter to the boundary layer thickness is about 0.43. Being this parameter lower than 1, it is possible to assume that the synthetic jet penetrates the boundary layer without being affected by the shear. The length of the column of fluid that is pushed out of the synthetic jet orifice during the blowing stroke is represented by the dimensional stroke length L_0. The ratio of the largest column length to the boundary layer thickness during this series of experiments is 0.59. Also in this case, the ratio is lower than 1, therefore the disturbance to the boundary layer should not be significant and non-linear effects can be considered irrelevant.

The momentum thickness θ is 1.6 mm, therefore the Reynolds number based on the momentum thickness is 210.

4.2 Test Conditions

A number of operating conditions are tested by altering the actuation frequency f and the diaphragm displacement Δ independently. As explained in Section 3.3.2, the types of structures produced by the jet depends on two dimensionless parameters, such as the velocity ratio VR and the dimensionless stroke length L. The operating conditions span part of the area in the parametric map in which hairpin vortices are formed. All test conditions are reported in Table 4.1. It is convenient to use a non-dimensional frequency i.e. the Strouhal number St, which is defined as $St = f D_0/u_\infty$. As suggested in [169] the use of u_∞ in the definition of the Strouhal number instead of the averaged

test	VR	L	St	f (Hz)	Δ (mm)
test01	0.07	0.57	0.12	3.1	0.035
test02	0.10	0.79	0.12	3.1	0.049
test03	0.13	1.02	0.12	3.1	0.063
test04	0.16	1.28	0.12	3.1	0.079
test05	0.10	1.25	0.082	2.1	0.077
test06	0.077	0.94	0.082	2.1	0.058
test07	0.065	0.78	0.082	2.1	0.048
test08	0.048	0.62	0.082	2.1	0.038
test09	0.10	0.62	0.16	4.1	0.038
test10	0.13	0.84	0.16	4.1	0.052
test11	0.16	1.05	0.16	4.1	0.065
test12	0.21	1.3	0.043	1.1	0.08
test13	0.027	0.63	0.043	1.1	0.039
test14	0.035	0.83	0.043	1.1	0.051
test15	0.044	0.99	0.043	1.1	0.061
test16	0.056	1.3	0.043	1.1	0.08
test17	0.12	1.44	0.082	2.1	0.089
test18	0.24	1.22	0.20	5.1	0.075
test19	0.20	0.99	0.20	5.1	0.061
test20	0.16	0.81	0.20	5.1	0.050
test21	0.12	0.62	0.20	5.1	0.038
test22	0.18	1.43	0.12	3.1	0.088
test23	0.23	1.41	0.16	4.1	0.087
test24	0.061	1.41	0.043	1.1	0.087
test25	0.28	1.43	0.20	5.1	0.088

Table 4.1: Test conditions for the interaction cylinder and synthetic jet actuator experiments

jet velocity over the blowing stroke $\overline{U_0}$ is more appropriate for a boundary layer flow with respect to a quiescent flow.

4.3 Principle of the Flow Control Technique

The principle of the flow control technique is that synthetic jets produce a near-wall disturbance field which is complementary to that of the cylinder if the diameter of the cylinder and that of the synthetic jet are chosen appropriately. A number of preliminary tests were carried out in order to choose the final size of the cylinder diameter and of the synthetic jet orifice. The principle of operation is illustrated in the diagram of Figure 4.3. To obtain a complementary flow field, the synthetic jet must be operated so as to produce hairpin vortices. Part (a) of Figure 4.3 shows a diagram of the three-dimensional interaction between the hairpin vortices and the cylinder. In part (b) the interaction is shown from the top. The synthetic jet produces hairpin vortices and counter-rotating secondary streamwise vortices that induce a lower speed streak (with respect to an undisturbed case) in the middle and two higher streamwise streaks at the side. The cylinder instead produces two streamwise counter-rotating vortices that induce a higher speed streak in the middle and lower speed streaks at each side. If the distance between the streaks downstream of the cylinder and the distance between the streaks downstream of the jet orifice are the same, then the distance between the hairpin vortex legs and the distance between the streamwise vortices downstream of the cylinder should be the same too. Different diameters were tested until this was achieved. The distance of the two sets of vortices from the wall remains unknown, but it is expected that it should be approximately the same. Future studies in the $y-z$ plane will be able to provide more details on this point.

Given that, three conditions can be achieved, according to the relative intensity of the vortices produced:

- if the the vortices produced by the synthetic jet have the same intensity as the streamwise vortices downstream of the cylinder, a total cancellation of the vortices downstream the cylinder is achieve. This is the ideal flow control condition that can be obtained and in this case the flow field at a certain distance downstream the cylinder should resemble that of an undisturbed boundary layer.

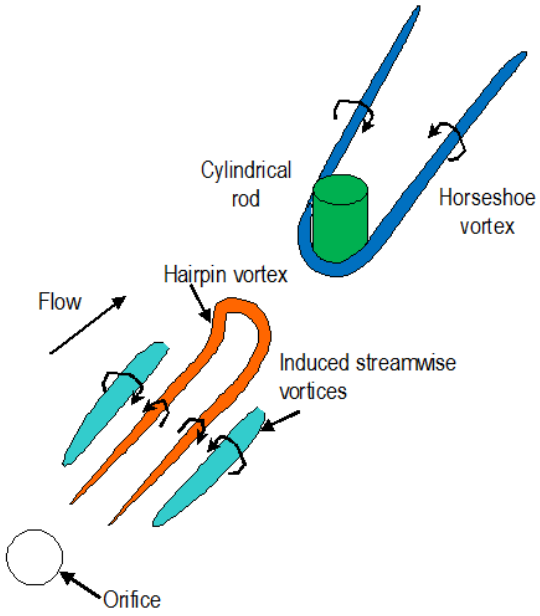

(a) 3D diagram of the interaction

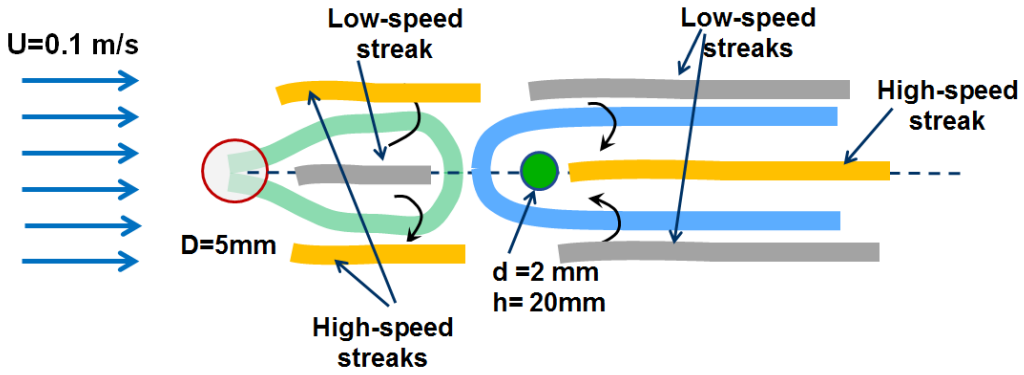

(b) Streak cancellation

Figure 4.3: Schematic of the ideal interaction between synthetic jet flow and cylinder near-wall flow

- if the vortices produced by the synthetic jet are weaker than the vortices downstream the cylinder, only a partial cancellation is achieved and the streaks and vortices downstream of the cylinder remain present, but weaker.
- if the vortices produced by the synthetic jet are stronger than the vortices downstream the cylinder, there is an overwhelming effect, and the hairpin vortices produced by the synthetic jets remain downstream of the cylinder.

The objective of the experiments are:

- to investigate the interaction between the vortical structures produced by the round synthetic jet actuator and the circular cylinder.
- to identify the synthetic jet operating conditions at which a nearly complete cancellation of the streamwise vortices produced by the circular cylinder is achieved.

4.4 Interaction Synthetic Jet and Streamwise Vortices

4.4.1 Uncontrolled Flow Field

The uncontrolled flow field is the flow field obtained without the synthetic jet, in other words it is the flow field around the circular cylinder alone. The velocity field in the plane parallel to the wall, about 2 mm above it, is shown in figure 4.4. This distance is established with a hand ruler and is not very accurate. Looking at the velocity profile of the undisturbed flow in Figure 4.2, in fact, it seems that the actual distance is slightly lower, about 1.5 mm.

The velocity contour maps shown in this chapter refer to the ensemble-averaged velocity obtained from the 150 velocity vector fields determined at each test condition.

In part (a) a contour map of the streamwise velocity divided by the free-stream velocity u/u_∞ is shown; in part (b) a contour map of the spanwise velocity divided by the free-stream velocity w/u_∞ is shown along with streamlines of the flow field. The flow comes from the bottom to the top of the figure. As mentioned above, the cylinder is located at the origin of the coordinate system, whereas the synthetic jet is aligned with the flow but located upstream, at $x/D_0 = -6$. In the u/u_∞-contour map just downstream of the cylinder, it is possible to observe a streak of higher velocity compared to

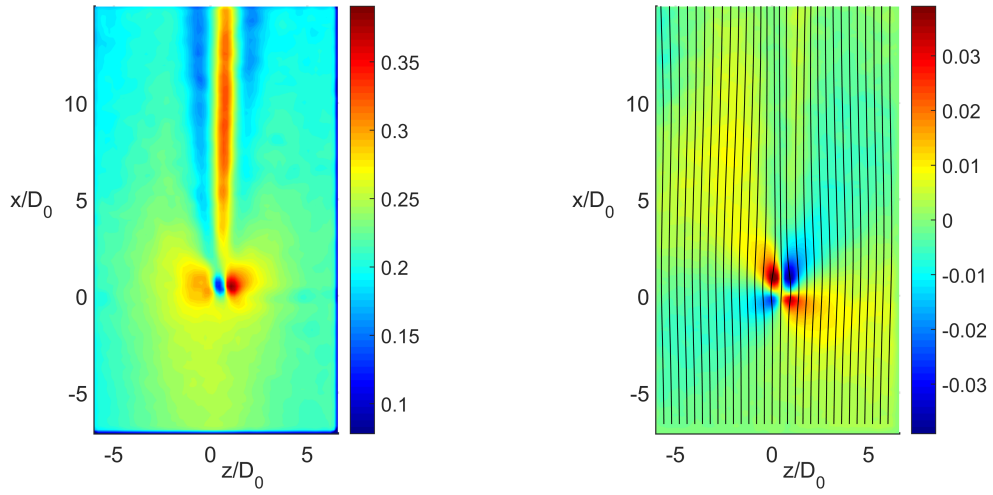

(a) u/u_∞-velocity (b) w/u_∞-velocity

Figure 4.4: Contour maps of u/u_∞ and w_∞ at about y=2 mm in the uncontrolled flow field

the undisturbed flow in between two streaks of lower velocity. This flow field is compatible with the presence of two counter rotating vortices which produce an up-wash in the central region and a down-wash at each side. An up-wash brings upwards the low momentum fluid present in the near-wall region of the boundary layer. In a boundary layer there is strong velocity gradient in y direction and so low momentum fluid is located in the near-wall region and higher momentum fluid is located in the region farther way from the wall. The up-wash generates a region of lower velocity and lower shear stress, because the velocity gradient at the wall is decreased. The opposite situation occurs with a down-wash, yielding an increase in skin friction. The lower velocity streaks tends to spread while moving downstream. Their spacing reaches a constant value of about x/D_0=4 (about 10 d_{CYL}) at a distance of x/D_0=12 downstream of the cylinder. These streaks also tend to diffuse and become wider downstream. The slight asymmetry present in the flow field is probably caused by a non-perfect alignment of the light sheet with the wall. Upstream of the cylinder there is a region of negative w/u_∞ to the left of the cylinder and a region of positive w/u_∞ to the right. This pattern is due to the fact that the fluid moves laterally around the cylinder. Downstream of the cylinder the opposite spanwise motion is observed, since the flow tends to recover the original trajectory. This feature can also be observed in the streamlines.

4.4.2 Effect of Dimensionless Stroke Length

The impact of the synthetic jet on the flow field is now studied. Two parameters are chosen to characterise the behaviour of the synthetic jet: the dimensionless stroke length L and the Strouhal number, which can be controlled by varying the frequency and amplitude of the diaphragm oscillation. The effect of the variation of the dimensionless stroke length L is shown in figure 4.5. In figure 4.5 four streamwise velocity

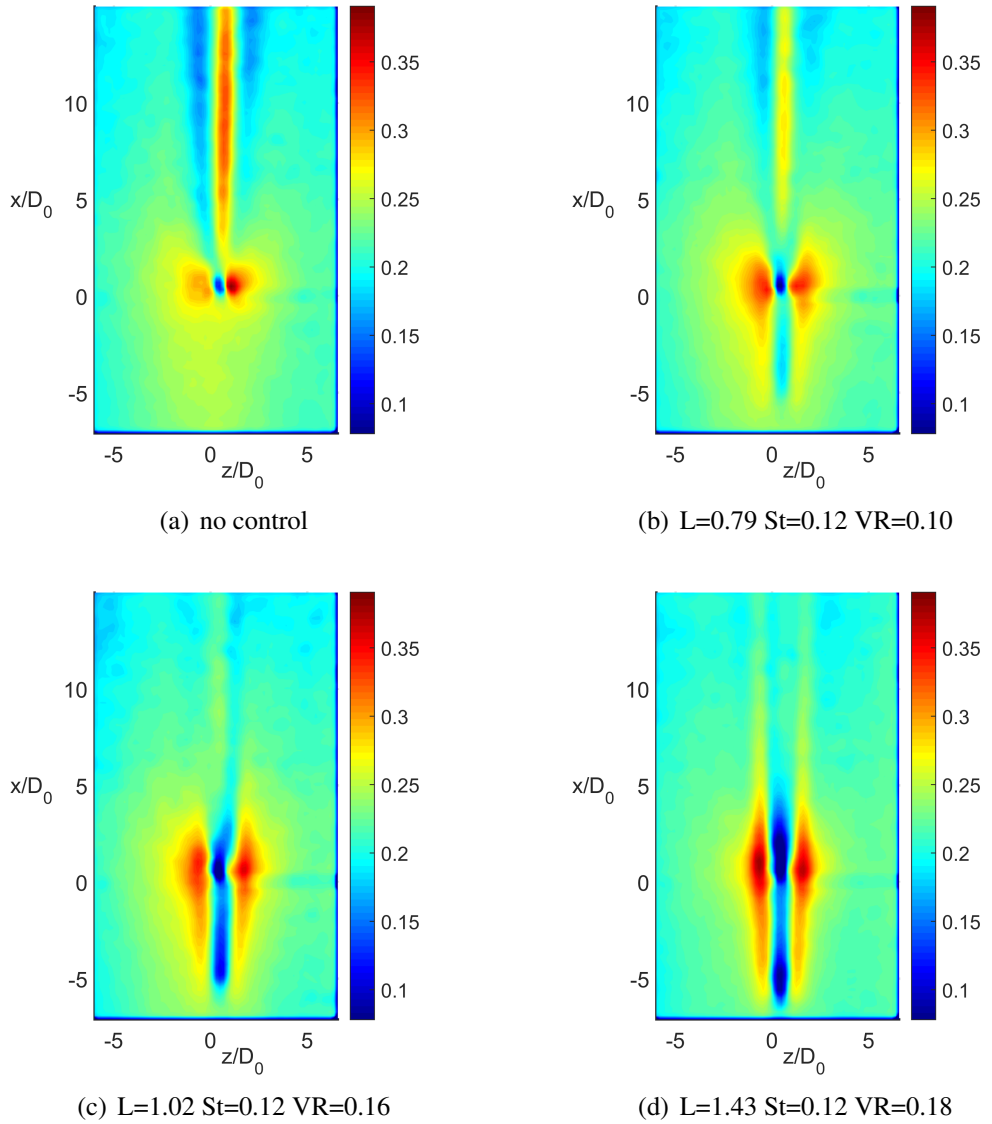

(a) no control

(b) L=0.79 St=0.12 VR=0.10

(c) L=1.02 St=0.12 VR=0.16

(d) L=1.43 St=0.12 VR=0.18

Figure 4.5: Contour maps of u/u_∞ for cases at the same Strohual number (St=0.12) and different dimensionless stroke lengths

contour maps are shown. The first one, (a), is the base flow, with no synthetic jet. In

the other three cases the synthetic jet is operated at the same Strouhal number of 0.12 (and therefore at the frequency of 3.1 Hz), but with different oscillation amplitudes, yielding different dimensionless stroke lengths.

Downstream of the synthetic jet a streak pattern is produced with a streak of lower velocity in the centre with two streaks of higher velocity on each side. This is opposite in sign to that produced the cylinder. This can be observed when the synthetic jet is switched on in the region upstream the cylinder ($x/D_0 < 0$), for example in part (b), (c) and (d). This pattern is due to the passage of the hairpin vortices, which form at the synthetic jet orifice. If L (or VR) increases, the strength of the hairpin vortices increases and the intensity of the velocity deficit/increase in the streaks is higher. Downstream of the cylinder the interaction process between the two sets of vortical structures occurs. According to the value of L, all three conditions described in Section 4.3 are observed. In case (b), in which the synthetic jet is operated at L=0.79 St=0.12 VR=0.10, weak control is achieved. The streaks downstream the cylinder are weakened, but remain visible. In case (c), in which the synthetic jet is operated at L=1.02 St=0.12 VR=0.16, an almost complete cancellation of the streaks is observed. In this case the streaks downstream of the cylinder have almost disappeared and the flow field looks uniform. Finally in case (d) over-control is achieved: the same streak pattern which occurs downstream of the synthetic jet is also observed downstream the cylinder, with a central region of lower velocity and two lateral regions of higher velocity. This case is not desirable. In fact, the flow field downstream the cylinder is still disturbed and the objective of the control strategy, which is to remove the streaks in that region is not achieved. It can be observed in all cases shown in figure 4.5 that the interaction between the two sets of vortical structures occurs just downstream of the cylinder. This is because the velocity field changes in this region when the synthetic jet is switched on. The region in which the flow control seems to be more effective begins at $x/D_0 = 6-8$ and extends indefinitely downstream within the area of examination. This is observed especially in the the cases in which the cancellation of the streaks downstream of the cylinder is achieved.

In figure 4.6 spanwise w/u_∞-velocity contour maps corresponding to the same cases shown in figure 4.5 are shown. The streamlines are plotted over the contour maps. Downstream of the synthetic jet orifice there is pair of regions of negative and positive

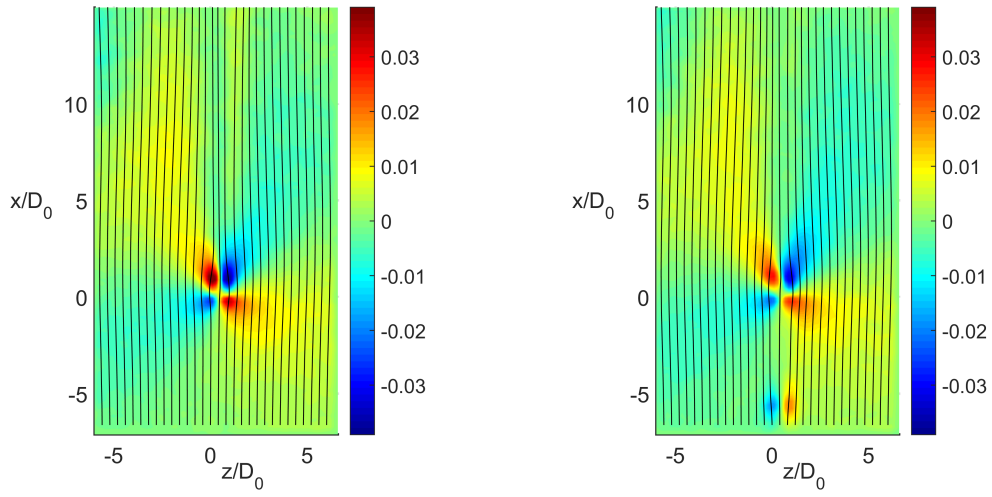

(a) no control

(b) L=0.79 St=0.12 VR=0.10

(c) L=1.02 St=0.12 VR=0.16

(d) L=1.43 St=0.12 VR=0.18

Figure 4.6: Contour maps of w/u_∞ in four cases at the same Strohual number (St=0.12) and different dimensionless stroke lengths

velocity (from left to right) similar to those observed near the cylinder in the undisturbed case. This pattern is due to the flow disturbance generated by the jet itself. Indeed, when the fluid goes out of the orifice jet, fluid is expelled in all directions, causing divergence of the streamlines. Downstream of the orifice the flow tends to recover the original streamwise direction, therefore an opposite pair of regions of positive and negative velocity is observed. The intensity and the size of these regions are proportional to VR and L. If L increases, these regions become larger and the velocity increase/decrease becomes larger. This can be observed looking at the streamlines. As in the base flow, upstream of the cylinder there is a region of negative w/u_∞ to the left of the cylinder and a region of positive w/u_∞ to the right. Downstream of the cylinder the opposite pattern is observed. The interaction slightly modifies the intensity and the shape of these regions, especially those downstream of the cylinder. In all cases the regions appear to be weaker and tend to assume a U shape. The least intense regions are observed in the case where an almost full cancellation of the streamwise velocity streaks downstream of the cylinder is achieved, which is in case (c). In case (d) the regions appear to be slightly stronger than case (c), even if they still preserve a well defined U shape. Looking at the streamlines, it is possible to notice that the interaction of the two sets of vortical structures makes the flow downstream of the cylinder less perturbed.

4.4.3 Effect of Strouhal Number

In figure 4.7 the effect of the variation of the Strohual number, and consequently of actuation frequency of the synthetic jet, on the velocity field is shown. Part (a) in figure 4.7 shows the streamwise velocity contour map with the synthetic jet off. In the other three cases the synthetic jet is operated at approximately the same dimensionless stroke length L=1.4, but at different Strouhal numbers, yielding different velocity ratios. With increasing Strouhal number, and so with increasing velocity ratio, the interaction between the two sets of vortical structures becomes more significant. In case (b), in which the synthetic jet is operated at St=0.043 and VR=0.061, the streak pattern downstream the cylinder is similar to that of the uncontrolled case. However, the streaks look slightly weakened. In case (c), St=0.12 L=1.43 VR=0.18, the streak pattern is almost completely absent. In case (d), St=0.16 L=1.41 VR=0.23, an overcontrol is achieved and the streak pattern downstream the cylinder is similar to the streak pattern downstream of a synthetic jet producing hairpin vortices. Therefore, the frequency (and the velocity ratio) seems to have a similar effect to the dimensionless

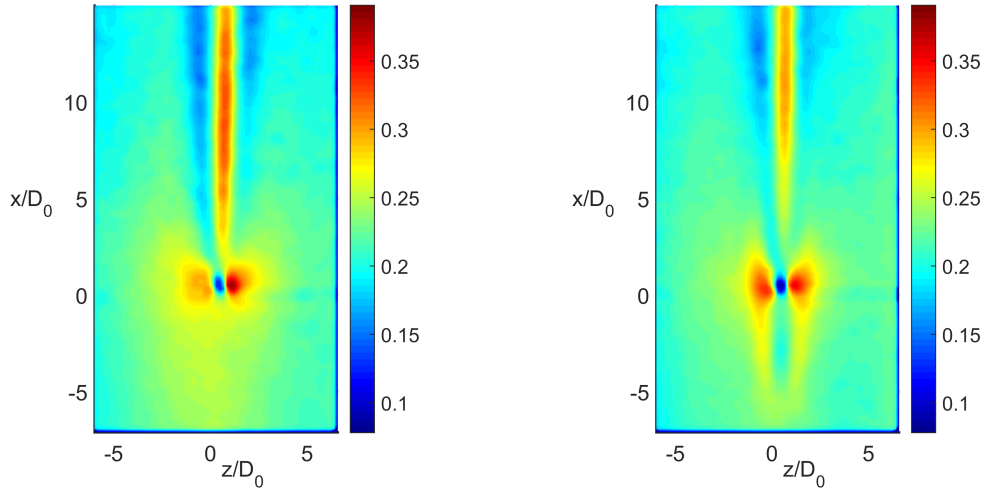

(a) no control

(b) St=0.043 L=1.41 VR=0.061

(c) St=0.12 L=1.43 VR=0.18

(d) St=0.16 L=1.41 VR=0.23

Figure 4.7: Contour maps of u/u_∞ in four cases at the same dimensionless stroke length (L=1.4) and different Strouhal numbers

stroke length.

In figure 4.8 the spanwise w/u_∞ velocity contour maps are presented for the same cases as figure 4.5. Similar observations to those related to effect of the dimensionless

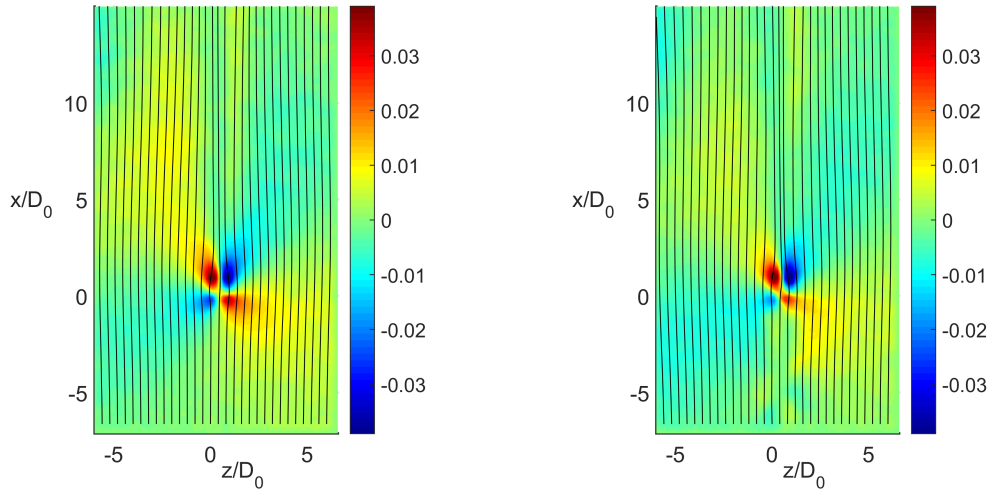

(a) no control

(b) St=0.043 L=1.41 VR=0.061

(c) St=0.12 L=1.43 VR=0.18

(d) St=0.16 L=1.41 VR=0.23

Figure 4.8: Contour maps of w/u_∞ in four cases at the same dimensionless stroke length (L=1.4) and different Strouhal numbers

stroke length on the spanwise contour maps can be made. In particular, the regions of higher and lower velocity downstream the cylinder appear to be weakened by the passage of the hairpin vortices produced by the synthetic jet and their shape tends to assume that of a U shape, symmetric about the centreline. In case (c), in which the

best control effect is achieved, these regions appear more extended in the streamwise direction and seem to be substantially weaker compared to the uncontrolled case. In case (d), in which an over-control is attained, these regions appear to be more intense than case (c), even if they preserve the U shape.

4.5 Control Performance Analysis

4.5.1 Definition of the Control Indicator

All of the 25 cases reported in Table 4.1 are tested. In order to evaluate the performance of the synthetic jet in terms of control effect, a control effectiveness indicator can be defined. This control indicator varies as a function of the synthetic jet operating conditions. Since the control effect is observed mainly in the streamwise velocity field, the objective of the control indicator is to compare the u velocity profile as a function of z i.e. $u(z)$ with and without jet actuation at a certain location x downstream of the cylinder. The control indicator evaluates how different $u(z)$ is from the optimal controlled case, in which $u(z)$ is constant and equal to u_0, where u_0 is the local velocity in the case neither the cylinder nor the synthetic jet are present i.e. in an undisturbed laminar boundary layer at that x location.

The possible velocity profiles that can be observed at a certain distance downstream of the cylinder are illustrated in figure 4.9. The velocity profile $u(z)/u_\infty$ when the

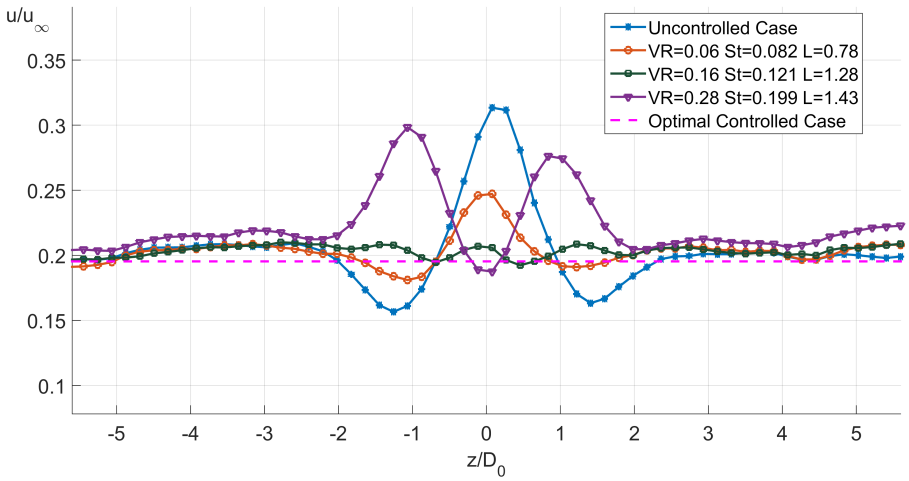

Figure 4.9: The velocity profiles that can be observed downstream of the cylinder

synthetic jet is off is plotted in blue, is indicated with $u_1(z)$ and is referred to as the

uncontrolled case. In this case, the velocity is maximum in the middle, where the higher velocity streak is present, and presents two local minima symmetrically at each side, which is where the two lower speed streaks are located. The velocity at the far end tends to recover the value of the local velocity u_0 . The optimal controlled case is plotted in magenta with a dash line: this is a uniform velocity profile, in which the velocity is equal to u_0. The case with VR=0.16 St=0.12 and L=1.28 is very close to an optimal controlled case. The case with VR=0.065 St=0.082 L=0.78 is a case in which weak control is achieved: in this case both the central higher velocity streak and the lateral lower velocity streaks are attenuated with respect to $u_1(z)$. The case with VR=0.28 St=0.20 and L=1.43 is a case in which over control is achieved: in this case there are two lateral higher speed streaks and a central lower speed streak, resembling the velocity profile attained if only the synthetic jet was present in the flow field with no cylinder inserted.

The value R_O, which represents the integral "distance" in the least squares sense between the uncontrolled velocity profile and the optimal control profile can be defined as

$$R_0 \doteq \int_{z_{min}}^{z_{max}} [u_0 - u_1(z)]^2 \, dz. \tag{4.1}$$

The value R, which represents the integral "distance" in the least squares sense between the generic controlled velocity profile $u(z)$, with the synthetic jet on, and the uncontrolled spanwise profile $u_1(z)$ can be defined as

$$R_0 \doteq \int_{z_{min}}^{z_{max}} [u(z) - u_1(z)]^2 \, dz. \tag{4.2}$$

Following these definitions, the control indicator I_{eff} is defined as:

$$I_{\text{eff}} \doteq \frac{R_0 - R}{R_0} \tag{4.3}$$

It is possible to see that:

- if $I_{\text{eff}} > 0$ weak control has been achieved and the control improves as I_{eff} tends to 0;
- if $I_{\text{eff}} = 0$ the control performance is optimal as the spanwise profile is uniform and the streaks are cancelled;
- if $I_{\text{eff}} < 0$ over control has been achieved and the control performance is poorer

if I_{eff} decreases.

Therefore, the best control performance is obtained if $I_{\text{eff}} = 0$. If the velocity profile coincides with that of the uncontrolled flow then $I_{\text{eff}} = 1$.

The velocity profiles $u(z)/u_\infty$ extracted from the PIV velocity fields, corresponding to the test conditions examined in Section 4.4.2 are plotted in figure 4.10. In these cases the dimensionless stroke length is varied and the Strouhal number is kept constant. The profiles are extracted at $x/D_0 = 12$ downstream the cylinder. The case

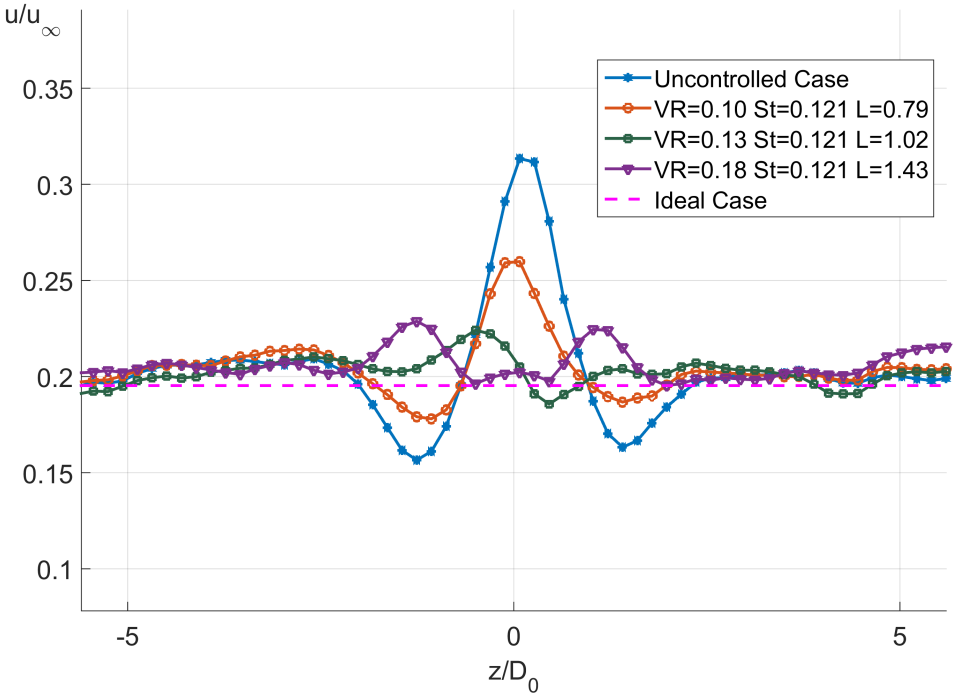

Figure 4.10: Velocity profiles $u(z)$ at the same Strouhal number (St=0.12) and different dimensionless stroke lengths, extracted at x/D_0=12

with L=0.79 and VR=0.10 is a case of weak control, in which the velocity profile $u(z)$ presents the same qualitative shape as that of the velocity profile $u_0(z)$. However, in this case the lateral velocity peaks are lower and so is the central velocity peak. In this case I_{eff}=0.72. In the case with L=1.02 and VR=0.13 the profile seems to be almost uniform in the z direction, therefore this situation can be considered close to optimal control. I_{eff} is estimated to be 0.043, which is close to zero. For the case with L=1.43 and VR=0.18 over control is attained and two lateral high speed streaks appear. In this case I_{eff} is negative and equal to -0.19.

Similar considerations apply if the velocity profiles for the cases analysed in Section 4.4.3 are considered. In these cases the dimensionless stroke length is constant and the frequency and the velocity ratio are varied. The profiles are plotted in figure 4.11. In the case St=0.043 and VR=0.061 the control effect is very weak and therefore the

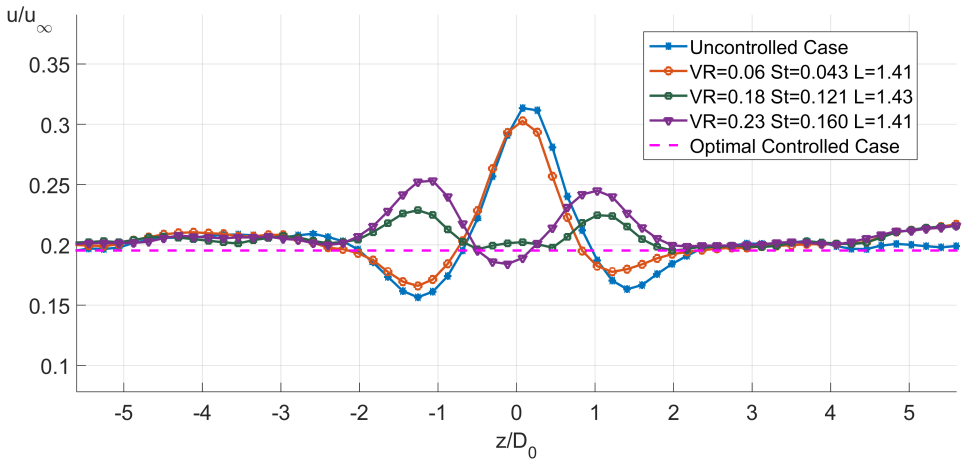

Figure 4.11: Velocity profiles $u(z)$ at the same dimensionless stroke length (L=1.4) and different frequencies and velocity ratios, extracted at x/D_0=12

spanwise velocity profile is close to that of the uncontrolled case, yielding $I_{\text{eff}} = 0.93$, very close to 1. In the case with St=0.12 and VR=0.18 a slight over control effect appears, with I_{eff}=-0.19, whereas in the case with St=0.16 and VR=0.23 the over control effect is more evident and I_{eff}=-0.63.

These two examples show that the control indicator I_{eff}, defined in equation (4.3), is suitable to evaluate the performance of the flow control with the synthetic jet.

4.5.2 Control Scatter Plot

The control indicator is computed for all the cases reported in table 4.1, using velocity profiles extracted at $x/D_0 = 12$ downstream of the cylinder. It is possible to build a scatter plot with circles located in the L-St plane and the colour of which is proportional to the control indicator value associated to each test condition. This plot is shown in figure 4.12. Lines at constant velocity ratio VR are also plotted in the graph, to help the interpretation of the data. The analysis of this plot helps to identify the parametric region where the best control effect is achieved. Observing the scatter plot,

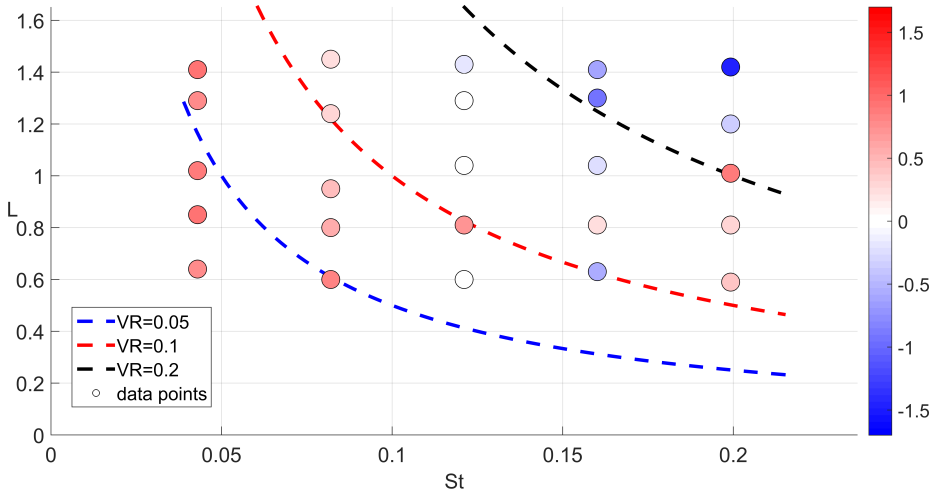

Figure 4.12: Scatter plot of test conditions coloured with the control indicator intensity in the L-St plane, at $x/D_0 = 12$

it seems that the control indicator assumes values close to 0 (which implies a streak cancellation) for values of St between 0.1 and 0.15 and for L between 1 and 1.2. This is due to a combination of favourable location and strength of the hairpin vortices produced by the synthetic jet. In the scatter plot it is possible to see that this combination of parameters corresponds to values of VR between 0.1 and 0.2. It is believed that if $VR < 0.1$ the trajectory of the hairpin vortices is close to the wall, but their strength is too weak. Therefore, the streaks downstream of the cylinder are reduced, but not cancelled. For $VR > 0.2$ the strength of the hairpin vortices becomes progressively too strong and an over control effect is obtained.

The results are consistent with each other for $L \geq 0.8$, whereas a not clear trend is observed at $L = 0.6$. In fact, care must be taken when analysing results at low dimensionless stroke length because the structures produced by the synthetic jet could either be too weak or they might not have the expected shape.

4.6 Summary of Findings and Future Work

In this chapter the interaction of a round synthetic jet and the near-wall streamwise vortices developing downstream of a circular cylinder mounted vertically across a laminar boundary layer is examined. It is shown that it is possible to achieve an almost complete cancellation of the lower and higher speed streaks downstream of the cylinder

induced by the vortical structures generated by the cylinder itself. A series of operating conditions are tested, spanning the parametric region in terms of velocity ratio, Strouhal number and dimensionless stroke length where it is expected that a round synthetic jet produces hairpin vortices. In fact, this is the region where a positive control effect can be achieved, because the expected near-wall disturbance field downstream of the synthetic jet is complementary to that downstream of the cylinder, making possible the cancellation of the streaks downstream of the cylinder at the right operating conditions. For a cylinder of diameter 2 mm, mounted at a distance of 0.71 m from the leading edge of a flat plate immersed in a uniform stream of u=0.128 m/s, it is shown that optimal control effects are attained if the round synthetic jet is operated at about L=1, VR=0.1 and St=0.1.

The study could be completed with additional analyses to understand in more detail the mechanism of interaction between the two sets of vortical structures described above. In particular, it would be interesting to perform a velocity analysis on the spanwise plane $y-z$, normal to the wall, but oriented transversally. With this analysis the vertical position of the vortices could be observed and it would be possible to see directly what the effect of vortex superposition is. Stereo-PIV could be used for this purpose, as it would provide all three components of the velocity field in the investigation plane. In addition more experiments can be performed in the region where the flow control effect is best, in order to refine the parametric control effectiveness plot shown in figure 4.12.

Chapter 5

Characterisation of a Turbulent Boundary Layer using Liquid Crystal Thermography

The results of this chapter are published in [146]: Spinosa E., Zhong S. - *Application of Liquid Crystal Thermography for the Investigation of the Near-Wall Coherent Structures in a Turbulent Boundary Layer*, Sensors and Actuators:Physical, Vol 233, pp. 207-216, 2015.

5.1 Introduction

The objective of the work presented in this chapter is to perform a characterisation of the coherent structures present in the near-wall region of a turbulent boundary later at a low Reynolds number using Liquid Crystal Thermography.

Experiments are carried out at a free-stream velocity of approximately 0.12 m/s. The experimental methods and set-up are described in section 3.4. A schematic of the flat plate is shown in Figure 5.1. The origin of the reference system is at the leading edge of the flat plate. The x axis points downstream in the streamwise direction, the y axis is wall-normal and the z axis is oriented as shown in Figure 5.1. The liquid crystal coating is located at x=0.6 m, the area of investigation at $x \approx$0.8 m.

Base Flow The experiments to derive the base flow were carried out immediately after the liquid crystal experiments, keeping the same configuration of the water flume

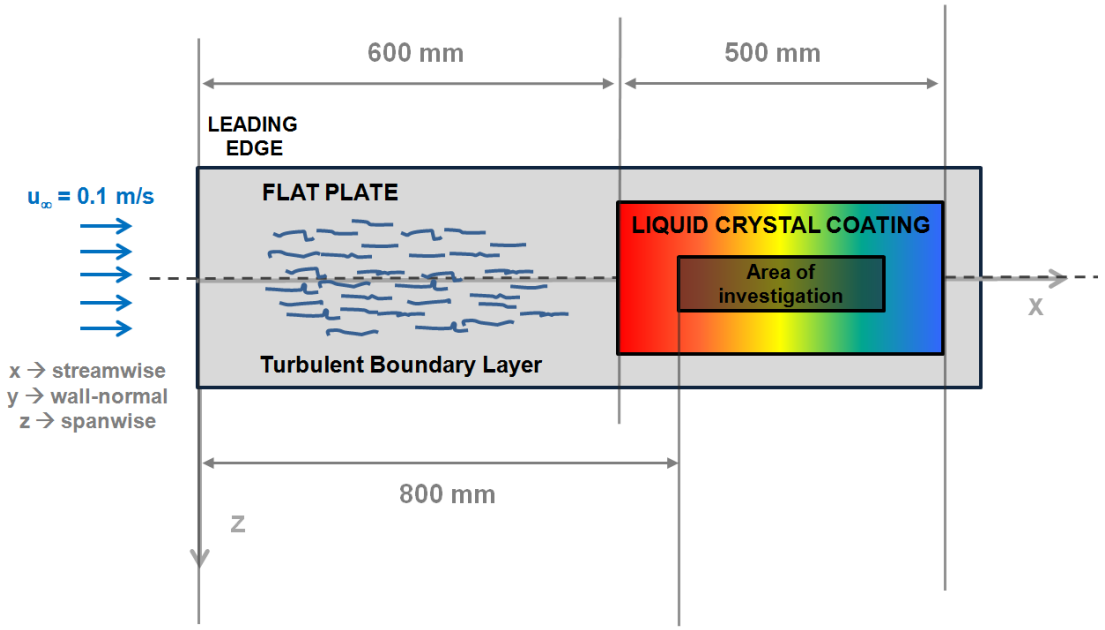

Figure 5.1: Schematic of the liquid crystal rig (top view, not in scale)

and using the same RPM value of the centrifugal pump, therefore the experimental conditions are approximately the same as in the liquid crystal experiments. The velocity measurements are carried out using Particle Image Velocimetry (see Section 3.4 and Figure 3.23 for details on the experimental set-up). Figure 5.2 shows the time-averaged velocity profile across the turbulent boundary layer at x=0.75. At this location it is estimated that $\theta \approx 2.8$ mm. $\mathrm{Re}_\theta = \frac{\theta u_\infty}{\nu}$ is approximately 310. The velocity profile obtained from a DNS simulation performed by Spalart [141] in similar flow conditions are also included for comparison. Also the law of the wall provided by White [159] is plotted. By fitting the velocity profile up to $y^+ = 50$ to the White law of the wall skin friction velocity is estimated to be $u_\tau = 0.0064$ m/s. From this value the inverse value of the viscous time length ν/u_τ^2, i.e. the highest frequency present in the flow, is estimated to be about 40 Hz. Re_τ, defined as $\frac{u_\tau \delta}{\nu}$, is approximately 170.

The agreement between the measured profile and that obtained by DNS is good in the near-wall region. However a deviation from the DNS profile at the end of the logarithmic region is observed, for $y^+ > 50$. The reason why the velocity profile deviates from the numerical results is not clear. It also seems that the Coles' wake in the outer part of the boundary layer is not as evident as in the profile obtained from the DNS by Spalart. Three possible reasons are proposed to explain this discrepancy:

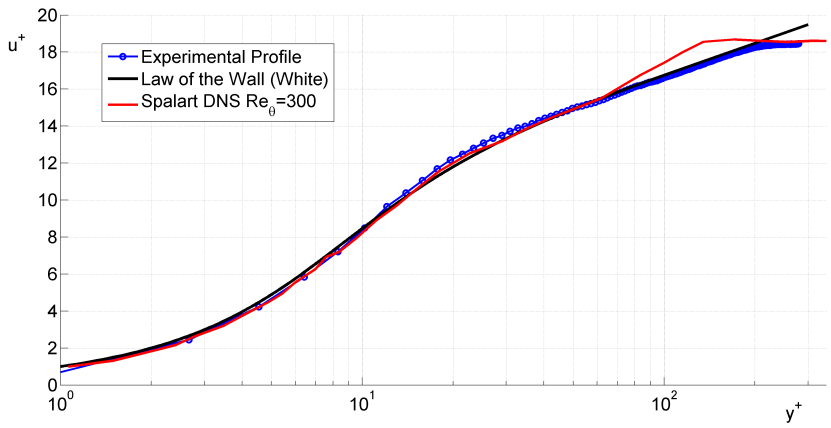

Figure 5.2: Velocity profile measured with PIV. $u^+ = \bar{u}/u_\tau$ and $y^+ = y u_\tau/\nu$

- the first is that the pressure gradient in the water flume is not zero, but probably slightly negative i.e. $dp/dx < 0$. This is due to the blockage effect of the flat plate in the test section and to the presence of a thick turbulent boundary layer at the bottom of the flume, which reduces the mass flow in the test section of a quantity equal to the sum of the displacement thicknkesses of the boundary layers on both sides [22, 159, 132] multiplied by ρ. As also reported in [51], a negative pressure gradient causes a modification of the velocity profile especially in the outer region of the turbulent boundary layer and, in particular, reduces the intensity of the Coles' wake.

- The tripping rod used to trip the boundary layer may be too large and may create large scale fluctuations that do not decay at the measurement location, especially in the outer part of the boundary layer.

- there may be three-dimensional disturbances that originate from the side walls of the flume and that propagate downstream, also perturbing the velocity profile at the centre.

No final answer has been found and some experiments are being carried out to clarify this point. It is believed that the most likely reason of the discrepancy is the presence of a slightly favourable pressure gradient. However, since the scaled velocity profile in wall units is not significantly modified by that, it is believed that the characteristics of the flow in the near-wall region of the boundary layer will not be significantly different from a ZPG turbulent boundary layer. The other possible explanations of the discrepancy are also believed to affect more significantly the outer region of the boundary

layer. To summarise, although it is desirable to understand and fix the issues related to the flow quality, the considerations on the flow field near the wall are believed to be, to a certain extent, meaningful.

It is known that the logarithmic region is not very extended at low Reynolds numbers. It is possible to identify a logarithmic region by visual inspection in Figure 5.2, however it is not easy to distinguish between the logarithmic region and the wake region, as mentioned by Spalart [141]. In fact, Spalart talks about 'apparent' log region. The diagnostic function $\Xi = y^+ du^+/dy^+$ can be used to identify the presence and the extent of the logarithmic region. In fact, the logarithmic region appears as a region in which Ξ is constant. The diagnostic function is calculated for the unforced TBL velocity profile obtained with PIV, the Spalart DNS profile at Re_θ=300 and the White law of the wall i.e. Equation (2.28). Results are shown in Figure 5.3. As expected, it is

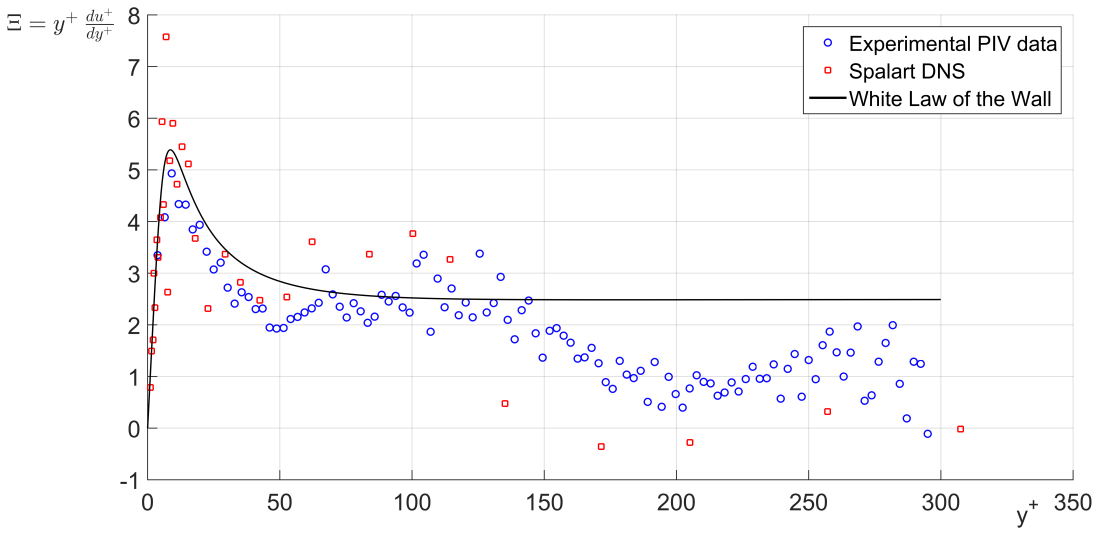

Figure 5.3: Diagnostic functions of the White law of the wall, of the experimental TBL velocity profile and of the velocity profile obtained by Spalart at Re_θ=300

difficult to identify a clear logarithmic region in the experimental velocity profile, i.e. a region of constancy of the diagnostic function, although the data between y^+=75 and 145 fall reasonably well on the line. In any case, the existence and the extent of the logarithmic region do not change the conclusions of the experimental work presented in this chapter and in the following ones. The estimation of the skin friction coefficient described in Section 3.5.4 is based on a fitting of the velocity profile in the viscous sublayer or on a fitting to the White law of the wall up to $y^+ = 50$. A good match is

observed up to that value of y^+.

5.2 Investigation of Near-wall Coherent Structures in a Turbulent Boundary Layer

5.2.1 Visual Identification of the Streamwise Streaks

Figure 5.4 shows the liquid crystal colour images taken at six consecutive instants. The flow is from the bottom to top of the images. The streamwise streak footprints are clearly visible as they appear as regions of higher and lower surface temperature, arranged in an alternating pattern. A lower temperature streak is associated with a region of higher heat transfer at the wall and by the Reynolds analogy to a region of higher wall shear stress, whereas a higher temperature streak is associated with a region of lower heat transfer or wall shear stress at the wall. Although the appearance

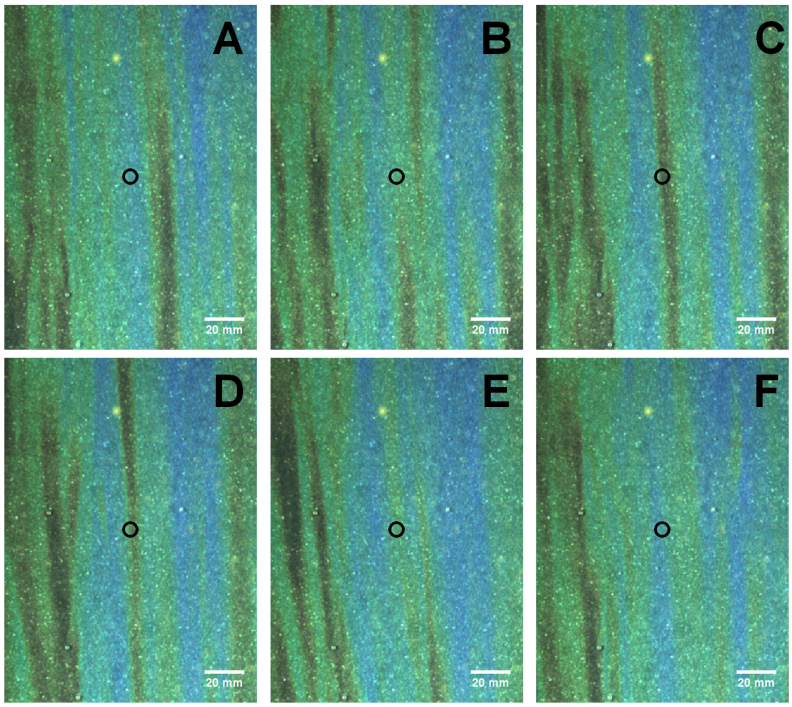

Figure 5.4: Liquid crystal colour maps extracted at six consecutive time instants. 20 mm correspond to about 120 L_τ

of the streaks is random in space and time, a low-temperature streak is often flanked

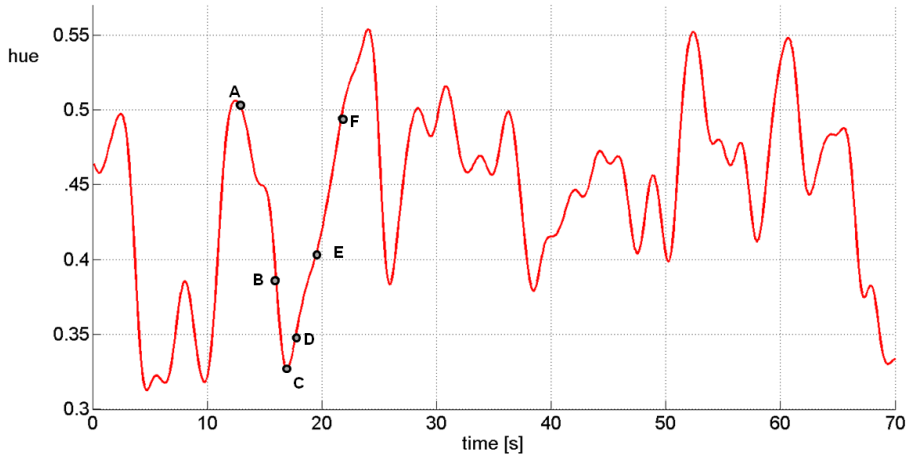

Figure 5.5: Time history of hue extracted at the mid-point of each image and correspondent time instant

by a high-temperature streak and the spacing between the streaks seems to be regular. The sublayer streaks are believed to create a spanwise modulation of the velocity in the near-wall region, and consequently of the wall shear stress . From Figure 5.4 the spanwise modulation wavelength is estimated to be about 20 mm, corresponding to $\Delta z^+ \approx 110$ - 120 (where $\Delta z^+ = \Delta z u_\tau/\nu$). This value is in agreement with that reported in the literature [26, 35, 128, 83]. Following the considerations in Section 3.4.3, the uncertainty in the spanwise streak spacing is about 0.9 mm, which corresponds to 5 L_τ. A more precise estimation of the spanwise spacing is described below in Section 5.2.3 using spatial cross-correlation functions.

By following the images in Figure 5.4 frame by frame, the arrival and passage of an individual streak at the same physical location marked by a circle can be visualised. In Frame A, the region around the point of interest appears in blue and clear of streaks. In Frame B, a low temperature streak can be seen coming from upstream. In Frame B and D, this low temperature streak appears to persist over the region of interest as it convects downstream. It becomes weakened in Frame E and eventually disappears in Frame F. In Figure 5.5 the time history of hue acquired over 70 seconds (about 2600 T_τ) at the marked point in Figure 5.4 is shown. The corresponding time instants for each frame shown in Figure 5.4 are indicated with their frame number. Figure 5.5 shows that the hue (temperature) value at that point fluctuates correspondingly as the low temperature streak passes.

5.2.2 Analysis of Frequency Response

As Liquid Crystal Thermography is applied to provide temporal information about the turbulent flow in the near-wall region, it is important to establish its frequency response. The frequency response is related to the time scale of turbulent structures that the technique itself is capable of capturing. The frequency response of Liquid Crystal Thermography is presented in terms of the power spectral density. For this purpose, the raw hue signals extracted at some pixels located at fixed and specified positions in space are analysed, as only the fluctuations around the mean value are of interest.

Figure 5.6 presents the power spectral density of hue extracted at a point 0.83 m (about 5000 L_τ) downstream of the leading edge of the plate. The sampling rate of the extracted hue time series is 10 Hz (about 0.25 f_τ) and its length is 250 seconds (about 9500 T_τ). In this plot, the power spectral density is normalised to have a unit area and the frequency is normalised in wall units, i.e. $f^+ = f\nu/u_\tau^2$. The power spectral density curves obtained from both a surface glue-on hot-film probe and a thermocouple are also shown for comparison. In addition, two sets of results available in the literature are also included.

- Firstly, the wall shear stress spectrum of a turbulent channel flow at $\mathrm{Re}_\tau = 180$ obtained from the numerical simulations by Jeon et al.[68]. Although in this case the results are not from a zero-pressure gradient turbulent boundary layer, the behaviour of the flow in the near-wall region is expected to be quite similar.

- Secondly, the wall shear stress spectrum obtained in Colella and Keith [33], who used similar Dantec glue-on probes at a higher Reynolds number of Re_θ=2160 in a turbulent boundary layer flow.

The power spectral density curve obtained from the glue-on hot-film sensor from our experiment exhibits a steady reduction from a level of 10^2 at f^+ = 0.001 to 10^{-4} at f^+ = 0.3. As f^+ increases further, the level of power spectral density reduces below 10^{-5} indicating negligible power content beyond f^+ = 0.3. The trend of the power spectral density curve of Colella and Keith [33]) and of Jeon [68]) is also similar except that no data is available beyond f^+ = 0.2. The power spectral density of the surface thermocouple seems to follow that of the glue-on hot-film sensor up to f^+ = 0.005, above which its magnitude begins to fall below that of the glue-on hot-film sensor. At f^+ = 0.1, its magnitude remains constant at about 10^{-3}. In comparison, the power spectral density plot of Liquid Crystal Thermography follows closely that of the surface

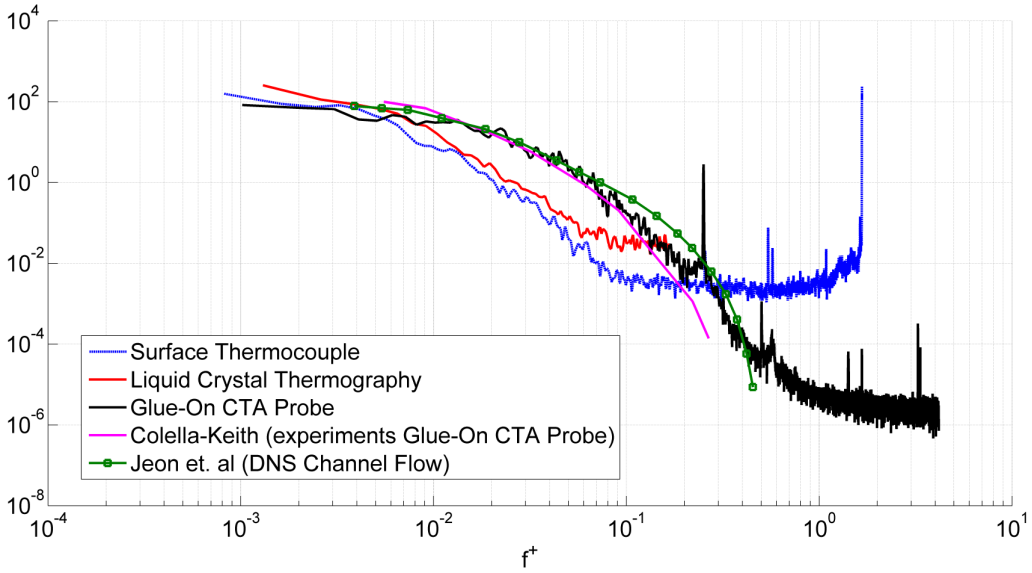

Figure 5.6: Comparison of normalised power spectral density in wall units

thermocouple until $f^+ = 0.07$, before it begins to level out at a slightly higher density level. To summarise, the comparison indicates that the frequency response of the glue-on hot-film sensor is superior to that of both the surface thermocouple and the liquid crystal coating, whereas the response of the liquid crystal coating is of similar order as that of the surface thermocouple.

The differences in response between these three different surface sensors are attributed to the fact that both the thermocouple and the liquid crystal coating are open-loop measurement systems, whereas the CTA system is a closed loop measurement systems. In fact, the glue-on hot-film sensor forms an arm of a highly sensitive Wheatstone bridge with a feed-back loop, which greatly enhances its dynamic performance. It is possible to conclude that there is a quite good agreement between the power spectral density obtained using different techniques below $f^+ = 0.01$, which corresponds to about 0.4 - 0.5 Hz, and this confirms the validity of the liquid crystal technique in sensing at least the large scale turbulence structures in the near-wall region. If we assume that the characteristic length of the wall streaks as 1000 L_τ and their convection velocity as 10 - 15 u_τ, the characteristic frequency of the flow fluctuations associated with the passage of a single streak is estimated to be about $f^+ = 0.01$ - 0.015 (the correspondent period of streak passage is the inverse of this value i.e. $T^+ = 65 - 100$), which is a value at which the power spectral density has sufficiently high energy content. This confirms the possibility of using this technique for the study of the streamwise streaks at this Reynolds

number. Finally it is also worth mentioning that, even if Liquid Crystal Thermography has a lower frequency response than Constant Temperature Anemometry, if the shape of the real power spectral density is available, by using measurement techniques with a higher frequency response, it is possible to reconstruct the actual shape of the variable fluctuations using established spectrum-based correction techniques, as described in references [93] and [97].

5.2.3 Determination of Space-Time Cross Correlations

Given the capability of Liquid Crystal Thermography to capture the motion of the large turbulent structures, it is possible to use this technique to derive the main characteristics of near-wall coherent structures, especially the streamwise streaks. Also in this case, since it is the fluctuations of the flow variables which are of interest, the hue signals extracted from the liquid crystal images are not converted into temperature signals.

The space-time cross-correlation function obtained at two points on the wall with coordinates $P_1 = (x, 0, z)$ and $P_2 = (x + \Delta x, 0, z + \Delta z)$, is defined as:

$$F_{hh}(\Delta x, \Delta z, \tau) \doteq \frac{1}{T} \int_0^T h(x, z, t)\, h(x + \Delta x, z + \Delta z, t + \tau)\, dt \tag{5.1}$$

where t is time, τ is the time-lag and $(0, T)$ is the observation time interval. The cross-correlation function is then normalised to obtain the so called cross-correlation coefficient by dividing it by the value of the cross-correlation function at zero time-lag

$$C_{hh}(\Delta x, \Delta z, \tau) \doteq \frac{F_{hh}(\Delta x, \Delta z, \tau)}{F_{hh}(\Delta x, \Delta z, 0)}. \tag{5.2}$$

At first, it is possible to estimate the streamwise cross-correlation coefficient $C_{hh}(\Delta x, 0, \tau)$, which is a function of only the streamwise separation distance Δx. Figure 5.7 shows the shape of the streamwise cross-correlation coefficient as a function of the time-lag for different values of the streamwise spatial separation Δx^+. To improve the smoothness of the curves, the streamwise cross-correlation coefficient is obtained by averaging all the cross-correlation coefficients obtained across the span at x_0 = 0.83 m (about 5000 L_τ). Furthermore, the computational time T of about 200 seconds (about 7500 T_τ) is divided into a number of overlapping sub-intervals and the cross-correlation coefficients are also averaged over them. It can be observed, as expected, that with the increasing streamwise separation, the maximum value of the cross correlation coefficients drops

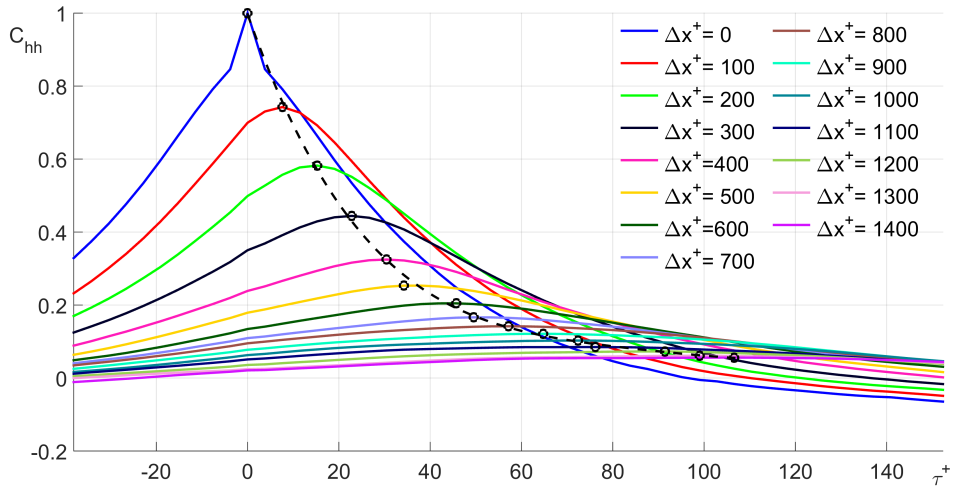

Figure 5.7: Space-Time streamwise cross-correlation coefficients as a function of time lag for different streamwise separation distances

and the time-lag at which the maximum occurs increases.

The maximum value of the cross-correlation coefficient as a function of the streamwise separation distance is plotted in figure 5.8. The value of the maximum decreases from

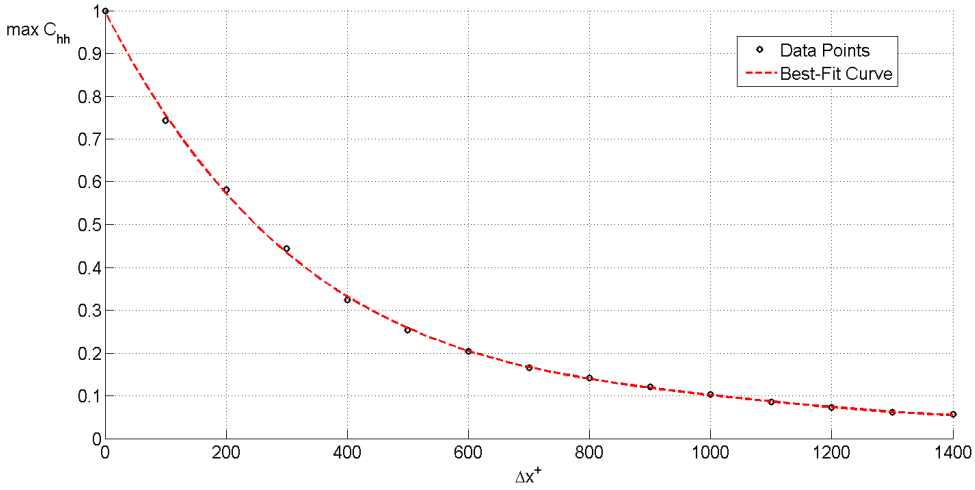

Figure 5.8: Value of the maximum of the cross-correlation coefficient as a function of the streamwise separation distance Δx^+

1 to about 0.1 within $\Delta x^+ \approx 750 - 800$: thus, it can be concluded that the streamwise streaks create a modulation of near-wall velocity field with a streamwise wavelength which is twice this size, i.e. 1500-1600 viscous length units. This value is slightly

higher than the most frequently quoted value for the streamwise extent of the sublayer streamwise streaks in the literature, i.e. 1000 viscous lengths. The reason for this discrepancy probably lies in the thermal inertia of the heater composite plate, which is probably slightly lower than needed and for this reason slows down the recovery of the surface temperature to its initial value, even after the streaks passage over a fixed point.

The convection velocity of the streaks can be estimated from the streamwise cross-correlation function as:

$$U_c \doteq \frac{\Delta x}{t_{max}} \tag{5.3}$$

where Δx is the spatial separation between the two points and t_{max} is the time lag corresponding to the maximum value of the correlation function. The calculations are repeated for a range of separation distances Δx and the computed values are shown in figure 5.9. In the plot the convection velocity is normalised in wall units, $U_c^+ = U_c/u_\tau$.

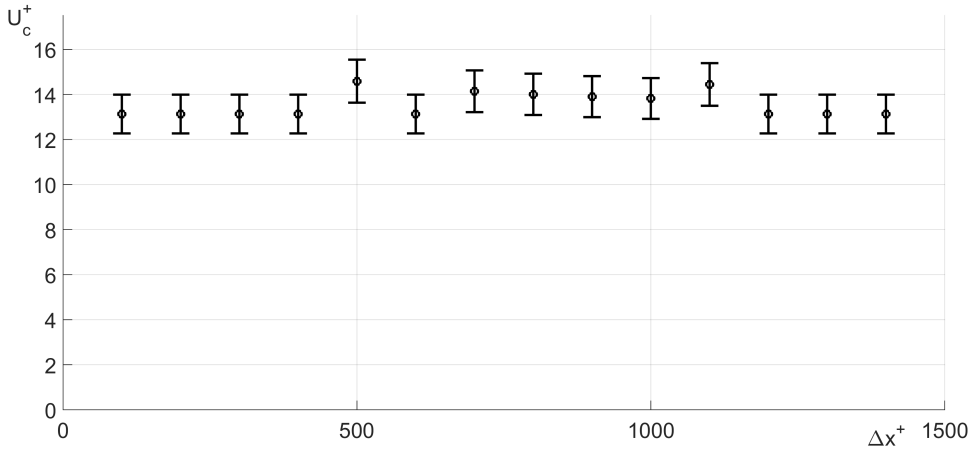

Figure 5.9: Estimation of the convection velocity at $x_0 \approx 0.83$ (about 5000 L_τ) as a function of the streamwise separation

The estimated value of the convection velocity is found to be 0.084 m/s, equivalent to 13-14 u_τ. This value is in agreement with the results obtained by Osterlund and Jeon [105, 68], whereas it results slightly higher than that obtained by Quadrio and Luchini [112], presumably because they considered a confined channel flow and not a developing turbulent boundary layer. The uncertainty on the convection velocity can be derived using a classical uncertainty propagation approach and is equal to:

$$\frac{\delta U_c}{U_c} = \sqrt{\frac{\delta M^2}{M^2} + \frac{\delta t_{max}^2}{t_{max}^2}} \tag{5.4}$$

where M is the magnification factor (the physical size of a pixel). It is assumed that the separation in pixel is determined with no error in MATLAB©. The uncertainty on M is 0.0035 mm/pixel and the uncertainty on t_{max} is 0.0064 seconds every 0.1 seconds, as mentioned in Section 3.4.3. Error bars are also shown in Figure 5.9. The maximum uncertainty is about 0.0061 m/s, about 0.96 u_τ.

In order to establish the spanwise spacing of the streaks in a more rigorous manner, the spanwise space-time cross-correlation coefficient, i.e. $C_{hh}(\Delta x, 0, \tau)$, which is a function of Δz, is also computed and is shown in figure 5.10. In this graph, the time lag

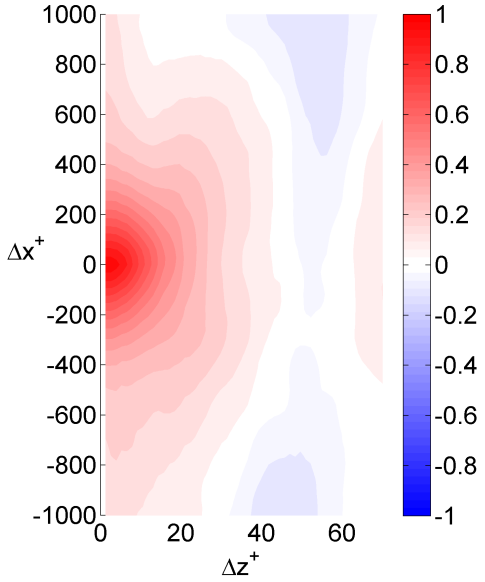

Figure 5.10: Spanwise space-time cross correlation map

τ is converted into a length scale Δx by using Taylor's hypothesis and the streamwise convection velocity computed above. The red area in the graph represents a region in which the hue is highly correlated with itself, indicating the shape of the average coherent structure in the near-wall region. From this graph, the length of the structure is estimated to be $1400 - 1500 L_\tau$, in agreement with results reported above. The uncertainty in the streamwise length of the structure depends both on the uncertainties in the temporal and spatial separations, because Taylor's hypothesis is used. A classical uncertainty propagation approach is used and the uncertainty in the streamwise length is determined to be around 100 L_τ. The spanwise spacing of the streaks has the expected value of $100 L_\tau$, as the spanwise correlation coefficient drops to about zero in $50 L_\tau$, which corresponds to a half of the total spanwise modulation wavelength. The

uncertainty in the spanwise spacing is estimated to be about 5 L_τ.

The variations of the zero-lag value of the spatial temporal spanwise cross-correlation function, which corresponds therefore to a pure spatial cross-correlation i.e. $C_{hh}(\Delta z, 0)$, with the spanwise separation is shown in figure 5.11. The curve obtained with Liquid

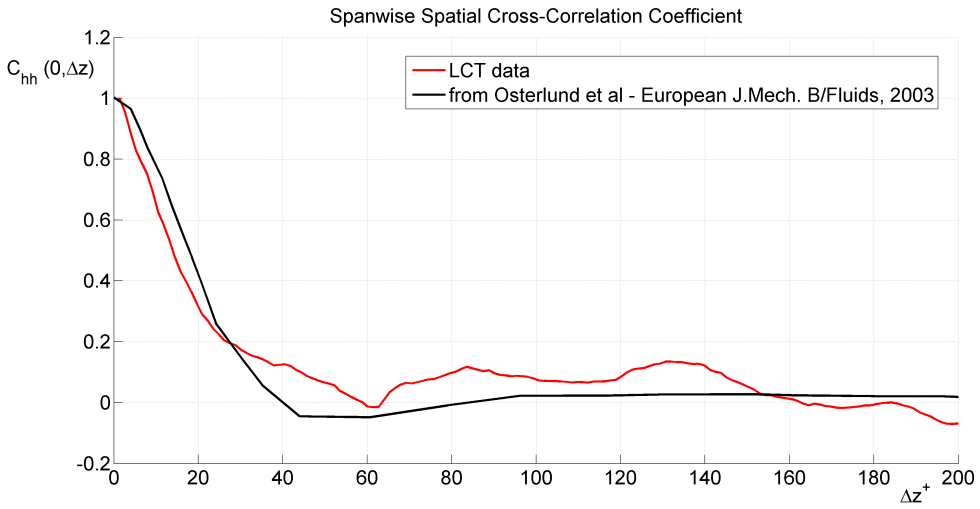

Figure 5.11: Spanwise cross-correlation function compared with that obtained by Osterlund et al. [105]

Crystal Thermography is in reasonable agreement with the results obtained by Osterlund et al. [105] at $Re_\tau = 2300$, which are also plotted in figure 5.11 for comparison.

5.2.4 Examination of Taylor's Hypothesis

As Liquid Crystal thermography provides surface flow data available over a substantial length and for a sufficient time interval, the so-called Taylor's hypothesis can also be examined. In Taylor's hypothesis, first introduced by G.I. Taylor in [151], the turbulent eddies are considered "frozen" as they propagate downstream, i.e. their shape does not change in time. The use of Taylor's hypothesis enables the statistical properties of the spatial development of convecting eddies to be established from the temporal information obtained with a single probe fixed in space, such as a hot-wire probe. In some cases, using Taylor's hypothesis is the only way to derive spatial information on the turbulent eddies because in some experiments it is not possible to obtain simultaneous measurement in space at several points and with a sufficient spatial resolution. In mathematical terms, when Taylor hypothesis is applied to a "scalar" flow variable Φ,

it can be expressed as

$$\Phi(x+\Delta x, y, z, t) = \Phi(x, y, z, t+\Delta x/U_c) \tag{5.5}$$

where U_c is the convection velocity in the streamwise direction.

To verify the validity of Taylor's hypothesis from the current experiments, the time history of hue is first extracted at all the points along a line oriented in the spanwise direction z. The temporal variations are then converted into spatial variations using the relationship $\Delta x = U_c t$. In this case, the convection velocity deduced from figure 5.9 is used, which is $U_c = 14\,u_\tau$. In figure 5.12 (a) the spatial map reconstructed using the time series obtained at a spanwise array of measurement points using Taylor's hypothesis is shown. In figure 5.12 (b) the actual spatial map obtained at the time instant corresponding to the mid-point of the time series shown in figure 5.12 is illustrated for a qualitative comparison. Between figure 5.12(a) and 5.12(b), a clear resemblance ap-

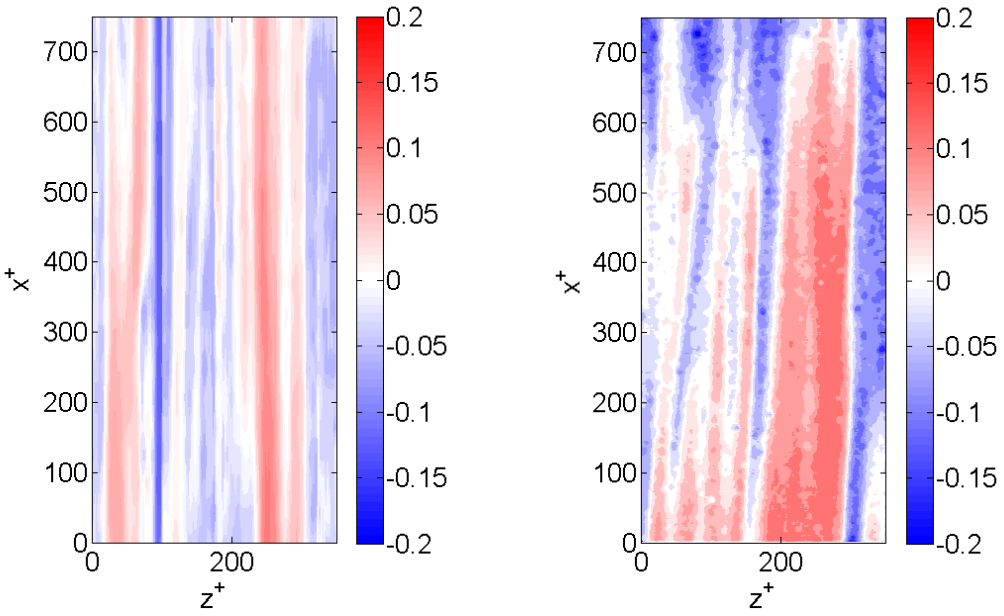

(a) Reconstructed hue map using Taylor's Hypothesis (scaled in wall units)

(b) Observed spatial hue map, extracted from the liquid crystal test (scaled in wall units)

Figure 5.12: Comparison of hue maps for Taylor's hypothesis verification

pears to exists, as far as the largest structures are concerned. The reconstructed streaks, however, are essentially parallel to the streamwise direction. This is expected, as Taylor's hypothesis assumes that the convection velocity has a zero spanwise component

and therefore the spanwise wandering of the streaks, which is apparent in the actual flow field, cannot be reconstructed. The overall resemblance of these two graphs, lends support to the use of Taylor's hypothesis in determining for example the global spatial statistical information on the near-wall coherent structures from temporal measurement at a fixed location at the wall.

A quantitative study on the validity of Taylor's hypothesis can be also carried out using the liquid crystal data. According to Taylor's hypothesis, as turbulent eddies are frozen, the fluctuations in hue induced at the wall at two points separated by a distance Δx in the streamwise direction, are related to each other by the following relationship:

$$h(x+\Delta x,z,t) = h(x,z,t+\Delta x/U_c) \tag{5.6}$$

Hence, it is possible to estimate the fluctuations of the hue signals at the wall at the position $(x+\Delta x,z)$ given the fluctuations measured at the point (x,z) at an earlier time instant. In other words, if Taylor's hypothesis is perfectly valid, the cross-correlation coefficient (computed according to the definitions given in equations (5.1) and (5.2) between the actual hue time series obtained at $(x+\Delta x,z)$, $h(x+\Delta x,z,t)$, and the signals reconstructed using the time series obtained at (x,z), $h(x,z,t+\Delta x/U_c)$ should be 1. As Liquid Crystal Thermography provides a time series at any point in space, the validity of the above equation can be checked. To do so, values of a series of Δt are firstly chosen as multiples of the sampling period of $T_s = 0.1$ s, from which the correspondent $\Delta x = U_c \Delta t$ is worked out in the liquid crystal map. The cross-correlation coefficient between the actual and reconstructed time series for a given Δx is then computed. The variation of this cross-correlation coefficient with Δx^+ is shown in figure 5.13. It is possible to see that the coefficient decreases quite rapidly with the increasing Δx^+: this implies that Taylor's hypothesis can be considered valid only for a short separation distance. This is expected as the coherent structures will continue to wander and to evolve. In addition, other structures may enter the line of travel, making the estimation of the fluctuations at a downstream position $(x+\Delta x,z)$ from those recorded at a point upstream (x,z) less accurate. According to Belmonte et al. [14], the evolution length is the streamwise separation distance at which the spatial cross-correlation coefficient drops from 1 to 0.5: in this case the evolution length is about 300 L_τ. The integral length scale, which corresponds more or less to the largest scale structures present in

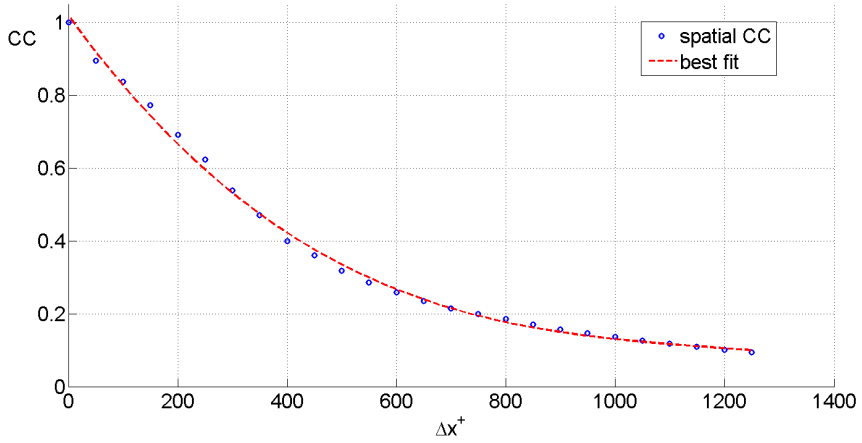

Figure 5.13: Cross-correlation coefficients for the verification of Taylor's hypothesis

the turbulent flow, is defined as [14]

$$l_0 \doteq \int_0^\infty C_{hh}(\Delta x) d\Delta x \tag{5.7}$$

where C_{hh} is the spatial cross-correlation coefficient. According to Belmonte et al. [14] Taylor's hypothesis is expected to work satisfactorily when the evolution length is much larger than the integral length scale. In our case, $l_0 \approx 0.075$ m, equivalent to about 450 L_τ. Hence the evolution length is 50% less than the integral length scale, indicating a rapid evolution of the turbulent structures and a limited validity of Taylor's hypothesis.

In essence, Taylor's hypothesis allows a very simple"predictive" filter to be built, which is able to estimate the hue signal at the point $(x+\Delta x, z)$ (output of the filter), given the hue signal at the point (x,z) (input of he filter). The filter designed with the aid of Taylor's hypothesis only introduces a phase delay between the input and output signals. If one wishes to design a feed-forward controller consisting of an upstream sensor and a downstream actuator using a simple predictive filter based on Taylor's hypothesis, according to the findings of our study, it is not recommended to install the actuator more than 300 L_τ downstream of the sensor. A more complex filter, which is able to account for the evolution of the shape of the structures, their wandering and the entrance of new structures in the line of travel, would be surely more desirable. An adaptive filter, which is designed based on simultaneous measurements of the wall flow variables at several upstream locations, has been shown to be effective for this purpose

[119, 19] . Details on the design on these types of filter and on their application to a turbulent boundary layer flow are reported in more detail in Chapter 7.

5.3 Summary of Findings and Future Work

In this chapter the application of Liquid Crystal Thermography for the investigation of near-wall coherent structures in a turbulent boundary layer is presented. The boundary layer under examination is developing on a similar flat plate and at the same freestream velocity as the following studies reported in Chapter 6 and 7. The free-stream velocity is 0.12 m/s, Re_θ=310 and Re_τ=170 in the area of investigation. The purpose of this study is to analyse the behaviour of the near-wall coherent structures to be controlled. In addition, the extension of Liquid crystal Thermography for the investigation of the coherent structures in a turbulent boundary layer is proposed.

The main results obtained during this investigation are the following:

- the technique is capable of revealing the presence of the streamwise streaks and their footprints at the wall. Comparing the power spectral density of different techniques that measure the fluctuations of the flow variable at the wall, the frequency response of the present liquid crystal thermography rig is estimated around $f^+ = 0.01$, which corresponds to about 0.4 Hz. The frequency response is sufficiently high to follow the motion of the streamwise streaks and to capture the large scale motions in the near-wall region at low Reynolds number, however it is found to be lower than wall hot-film probes driven by Constant Temperature Anemometry.

- Spatial-temporal cross correlation over a wide investigation area and with a high spatial resolution allowed the main properties of the streamwise streaks to be studied. It is observed that the streamwise spacing, extent and their convection velocity present values very close to those reported in literature.

- Taylor's hypothesis is also examined. A comparison between the reconstructed streamwise streaks using the temporal variations of hue signals extracted along a spanwise array of points with the aid of Taylor's hypothesis and the actual hue map obtained on the test surface in real time lends support to the use of Taylor's hypothesis, but only up to a spatial streamwise separation of 300 L_τ.

It is concluded that Liquid Crystal Thermography is suitable for the visualisation and for the study of the behaviour of large-scale structures in a turbulent boundary layer at low Reynolds number. However, it is possible to further improve the rig, especially the liquid crystal composite plate, to obtained better results in terms of frequency response and spatial resolution. For instance, an improved performance in terms of frequency response can be obtained by reducing the thermal inertia of the heater composite via the use of a thinner polystyrene layer. This should also result in a higher spatial resolution. Also the use of high-speed cameras is recommended in order to improve the overall frequency response of the technique.

Chapter 6

Turbulent Boundary Layer Forcing using a Synthetic Jet Array

The results of this chapter are presented in:

- [143] Spinosa E., Zhang S., Zhong S. *Control of Near-Wall Coherent Structures in a Turbulent Boundary Layer Using Synthetic Jets*, European Drag Reduction and Flow Control Meeting 2015, Cambridge (UK), 2015

- [145] Spinosa E., Zhong S. - *Synthetic Jet Actuator Experiments for Turbulence Control* DIPART 2014 (The Airbus Flight Physics Distributed R&T Partnership) Bristol (UK), 2014

6.1 Introduction

In this chapter an extensive investigation of the turbulent boundary layer forcing with a synthetic jet array is performed mainly using Particle Image Velocimetry (PIV). In Section 6.7 some preliminary flow visualisations of the forcing effect at the wall, using Liquid Crystal Thermography (LCT) are also presented.

The experimental set-up for these experiments is described in Section 3.5. A schematic of the rig is shown in Figure 6.1. As indicated in this figure, the origin of the reference system is at the leading edge of the flat plate, in the middle. The streamwise coordinate x points downstream, the wall normal coordinate y is zero at the wall and points out of the wall, the spanwise cooordinate z is oriented as shown in Figure 6.1. The measurements are carried out in the longitudinal plane, normal to the wall i.e. plane

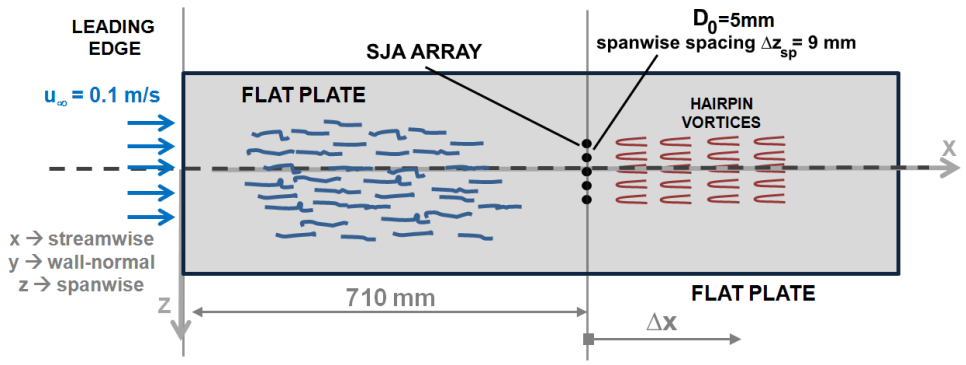

Figure 6.1: Schematic of the rig for turbulent boundary layer forcing using a SJA array (top view, not in scale)

x-y. The experimental setup is shown in Figure 3.23 and described in Section 3.5.3. The centre-plane is the plane $x-y$, the off-centred planes are parallel to it.

Base Flow The properties of the base flow are computed from the mean velocity profile of the unforced turbulent boundary layer, scaled and plotted in Figure 6.6 together with the White law of the wall and the DNS profile obtained by Spalart [141] at Re_θ=300. The profile is extracted at about x=0.72. The free-stream velocity is u_∞

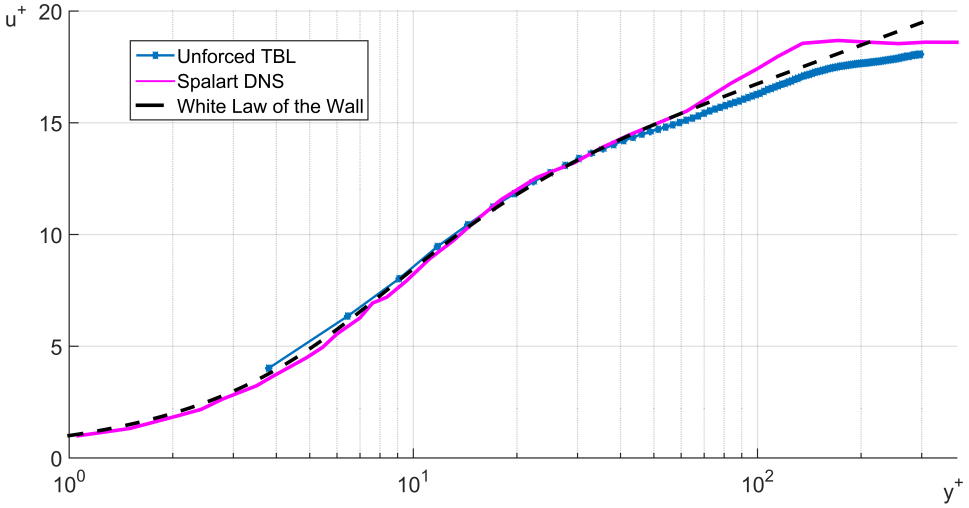

Figure 6.2: Scaled velocity profile measured with PIV together with the White law of the wall and the DNS profile obtained in [141]

= 0.097 m/s. At that location it is estimated that $\theta \approx 4.0$ mm and Re_θ=370. From the profile, the friction velocity is derived using a fitting to the White law of the wall in the range $0 < y^+ < 50$, as described in Section 3.5.4. In this way it is estimated

that $u_{\tau 0} = 0.054$ m/s, $L_{\tau 0} = 1.94 \cdot 10^{-4} m$, $T_{\tau 0} = 0.036$ s and $f_{\tau 0} = 27.9$ Hz. The skin friction coefficient is C_{fx0}=0.00627.

6.2 Test Conditions

On the centre-plane a number of different conditions are tested. For each condition 1000 image pairs are acquired. The frequency of acquisition is f_s=2.5 Hz ($f_s^+ = 0.090$). This value corresponds to a sampling period of T_s=0.4 s, T_s^+=11. The characteristic period of streak passage estimated in Section 5.2.2 is about $T^+ = 65 - 100$. The sampling frequency therefore can be considered high enough (and so the sampling period small enough) to capture the motion the near-wall coherent structures.

All test conditions, reported in Table 6.1, are chosen in order for the synthetic jet actuators to produce hairpin vortices. Previous studies in a laminar boundary layer showed that this occurs if VR=$\overline{U_0}/u_\infty$ is lower than 0.4 or if L=L_0/D_0 is lower than 1.5, see Figure 2.41. These conditions are considered as a starting point to produce similar coherent structures in a turbulent boundary layer. The averaged jet velocity $\overline{U_0}$ can also be scaled using the friction velocity. The correspondent dimensionless parameter is $\mathrm{VR}^+ \doteq \overline{U_0}/u_{\tau 0} = \mathrm{VR}\sqrt{\frac{2}{C_{fx0}}} \approx 18$ VR in the present case. The stroke length can also be scaled using the viscous length scale, defining the parameter $L_0^+ \doteq L_0/L_{\tau 0}$. In the present case the ratio of the synthetic jet diameter to the viscous length scale is $D_0/L_{\tau 0} = 25.8$, therefore $L_0^+ = LD_0/L_{\tau 0} \approx 25.8L$. The actuation frequency f is scaled using the viscous frequency, $f^+ = f/f\tau 0$.

Measurements are also performed on a few off-centred planes. In this case only the test conditions in which the synthetic jets are operated at a frequency of 2 Hz ($f^+ = 0.072$) are considered. In all off-centred plane measurements, 1000 image pairs are acquired, still at a sampling frequency of 2.5 Hz. All the test conditions are reported in Table 6.2. The off-set of the planes from the centre-plane can be scaled with the distance between two adjacent synthetic jet orifices Δz_{sp}=9 mm or scaled in wall units $\Delta z^+ \doteq \Delta z/L_{\tau 0}$.

Finally phase-locked PIV measurements are also carried out. Eight phases within the period of oscillation are analysed: namely 0° , 45°, 90°, 135°, 180°, 225°, 270°, 315°.

test	VR	VR^+	L	L_0^+	f (Hz)	f^+	Δ(mm)
test01	0.05	0.9	1.0	26.0	1.0	0.036	0.20
test02	0.10	1.9	2.0	51.0	1.0	0.036	0.39
test03	0.05	0.9	0.50	12.8	2.0	0.072	0.098
test04	0.10	1.8	0.99	25.2	2.0	0.072	0.19
test05	0.20	3.6	2.0	51.0	2.0	0.072	0.39
test06	0.30	5.4	3.0	77.0	2.0	0.072	0.59
test07	0.40	7.2	4.0	102	2.0	0.072	0.79
test08	0.10	1.8	0.066	1.70	3.0	0.11	0.13
test09	0.20	3.7	1.4	34.4	3.0	0.11	0.27
test10	0.30	5.4	2.0	51.3	3.0	0.11	0.39
test11	0.40	7.3	2.7	68.6	3.0	0.11	0.53
test12	0.10	1.8	0.50	12.8	4.0	0.14	0.10
test13	0.20	3.6	1.0	25.5	4.0	0.14	0.20
test14	0.30	5.5	1.5	39.0	4.0	0.14	0.30
test15	0.40	7.3	2.0	51.3	4.0	0.14	0.40

Table 6.1: Test conditions: Long-Time Averaged PIV analysis in the centre-plane

test	VR	VR^+	L	L_0^+	f (Hz)	f^+	Δ(mm)	Δz(mm)	$\frac{\Delta z}{z_{sp}}$	Δz^+
test01	0.10	1.8	1.0	25.8	2.0	0.072	0.20	0.0	0.0	0.0
test02	0.20	3.6	2.0	51.0	2.0	0.072	0.39	0.0	0.0	0.0
test03	0.30	5.4	3.0	76.8	2.0	0.072	0.59	0.0	0.0	0.0
test04	0.10	1.8	1.0	25.5	2.0	0.072	0.20	2.0	0.22	10.4
test05	0.20	3.6	2.0	51.3	2.0	0.072	0.39	2.0	0.22	10.4
test06	0.30	5.4	3.0	77.3	2.0	0.072	0.59	2.0	0.22	10.4
test07	0.10	1.9	1.0	26.3	2.0	0.072	0.20	4.5	0.50	23.4
test08	0.20	3.6	2.0	51.3	2.0	0.072	0.39	4.5	0.50	23.4
test09	0.30	5.4	3.0	77.0	2.0	0.072	0.59	4.5	0.50	23.4
test10	0.10	1.8	1.0	25.8	2.0	0.072	0.20	9.0	1.00	46.9
test11	0.20	3.6	2.0	51.3	2.0	0.072	0.39	9.0	1.00	46.9
test12	0.30	5.4	3.0	77.0	2.0	0.072	0.59	9.0	1.00	46.9

Table 6.2: Test conditions: Long-Time Averaged PIV analysis in the off-centred planes

The oscillation cycle starts with the upward movement of the diaphragm, which corresponds to the suction part of the cycle (the synthetic jets are installed in the flat plate mounted upside down). Therefore, the maximum suction occurs at $\Phi = 90°$. After that, the diaphragm starts to move in the opposite direction and the maximum blowing occurs at $\Phi = 270°$. At each phase 500 image pairs are acquired at the correspondent frequency of oscillation of the diaphragm . All the test conditions are reported in Table 6.3.

In the following discussion, the synthetic jet operating conditions are described mainly

case	**VR**	**VR$^+$**	**L**	L_0^+	**f (Hz)**	f^+	**Δ(mm)**
case01	0.10	1.8	1.0	26.1	2.0	0.072	0.20
case02	0.20	3.6	2.0	50.8	2.0	0.072	0.39
case03	0.30	5.4	2.9	76.1	2.0	0.072	0.58

Table 6.3: Test conditions - Phase-Locked Averaged PIV Analysis

as functions of three non-dimensional parameters: VR, L and f$^+$.

6.3 Long-Time Averaged PIV Analysis in the Centre-Plane

6.3.1 Mean Velocity Contours

This section reports a study of the long-time averaged $\bar{u}$-contour maps in the centre-plane, plane x,y at $z = 0$. The averaged vector field is obtained by averaging in time 1000 vector fields. In order to avoid any phase-locking, the samples are taken randomly within the period of oscillation of the synthetic jet diaphragm. The mean streamwise velocity field $\bar{u}$ measured in the unforced turbulent boundary layer, without synthetic jets, is shown in Figure 6.3. The x and y coordinates are normalised in wall units, using the friction velocity $u_{\tau 0}$ of the unforced turbulent boundary layer at $x = 0.72m$, see Section 6.1. The variable Δx is zero at the location of the synthetic jet orifice and increases in the downstream direction, see Figure 6.1. Results are only shown up to $y^+ = 100$.

Effect of Velocity Ratio In Figure 6.4 the mean velocity field obtained with PIV are shown for five cases, in which the synthetic jets are operated at a frequency of f=2 Hz

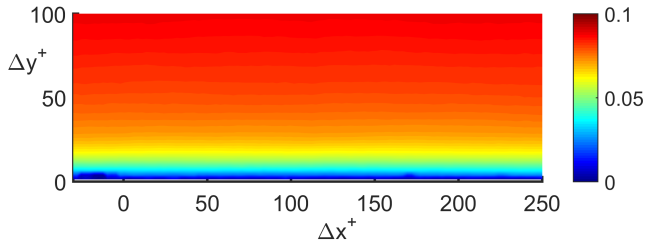

Figure 6.3: $\bar{u}$ velocity field in an unforced turbulent boundary layer

i.e. f^+=0.072. Different value of VR and L are obtained by varying the amplitude of the diaphragm oscillation (see Section 3.5.2). Each row in Figure 6.4 corresponds to a single test condition. The mean velocity fields $\bar{u}$ are shown in the left column of the figure. The $\bar{u}$-field of the unforced turbulent boundary layer is subtracted from the $\bar{u}$-fields of the forced turbulent boundary layer cases and the resulting velocity fields, indicated with $\bar{u}_{SUB}$, are shown in the column on the right. In this case, the red-blue colour map allows an immediate visualisation of the regions where the velocity is higher (red) or lower (blue) than in the unforced case. The velocity field appears to change with the velocity ratio (and hence with the dimensionless stroke length L). As VR increases the effect of the synthetic jets on the mean field becomes more evident. In particular, a bulge of lower velocity compared to the unforced turbulent boundary layer appears in the region downstream the synthetic jet orifice. If VR < 0.1 the effect of the synthetic jets seems confined to the inner region of the boundary layer, up to $y^+ = 20$. In case of VR >0.2, the synthetic jets have an impact also on the outer region of the boundary layer.

The comparison with the unforced turbulent boundary layer case is better shown in the $\bar{u}_{SUB}$ fields. A region of lower velocity (blue) compared to the unforced turbulent boundary layer appears in all cases. At VR=0.05 and VR=0.1 the region is attached to the to the wall, at least up to $\Delta x^+ = 200$. In correspondence of this region a lower wall shear stress is expected because the velocity gradient at the wall decreases. For VR higher than 0.2, the lower velocity region detaches from the wall at $\Delta x^+ = 50$ and remains detached downstream. The lower velocity region extends approximately from y^+=20 to y^+=50, and below it a higher velocity region appears, which extends down to the wall and seems persistent downstream. In correspondence of this region a higher wall shear stress is expected because the velocity gradient at the wall increases.

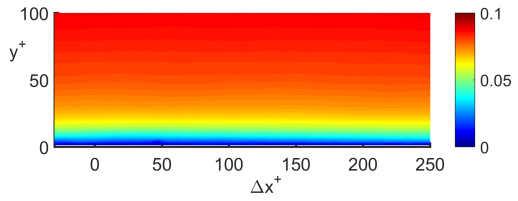

(a) $\bar{u}$ VR=0.05, f^+=0.072, L=0.50

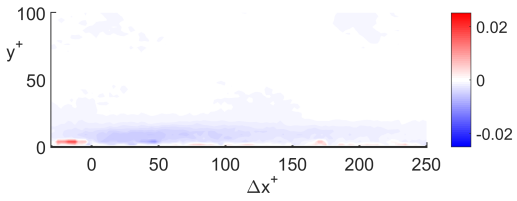

(b) $\bar{u}_{SUB}$ VR=0.05, f^+=0.072, L=0.50

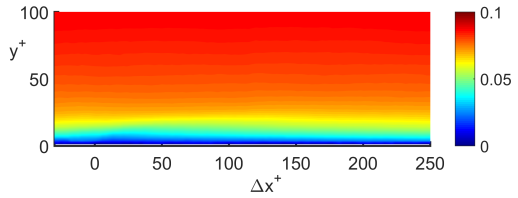

(c) $\bar{u}$ VR=0.10, f^+=0.072, L=1.00

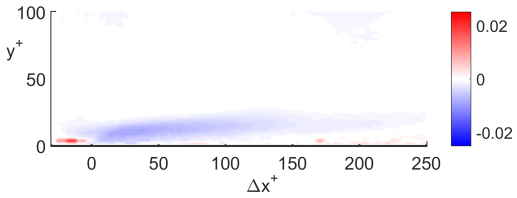

(d) $\bar{u}_{SUB}$ VR=0.10, f^+=0.072, L=1.0

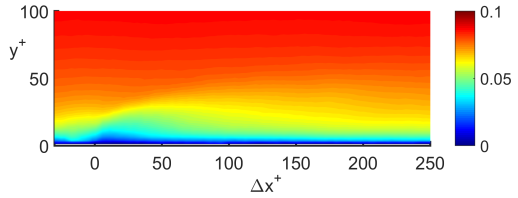

(e) $\bar{u}$ VR=0.20, f^+=0.072, L=2.0

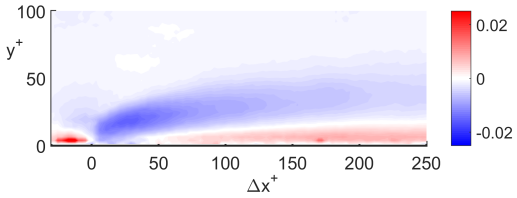

(f) $\bar{u}_{SUB}$ VR=0.20, f^+=0.072, L=2.0

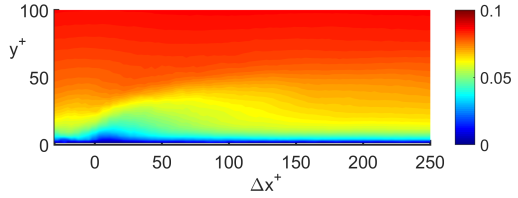

(g) $\bar{u}$ VR=0.30, f^+=0.072, L=3.0

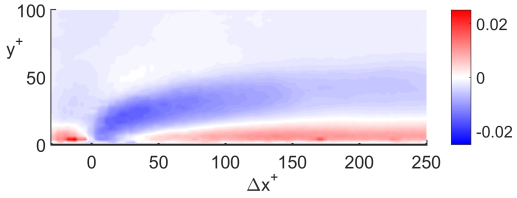

(h) $\bar{u}_{SUB}$ VR=0.30, f^+=0.072, L=3.0

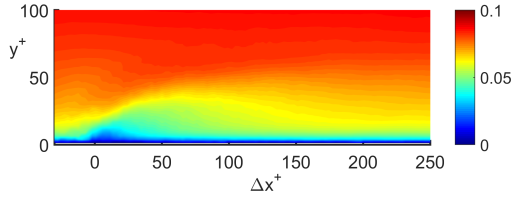

(i) $\bar{u}$ VR=0.40, f^+=0.072, L=4.0

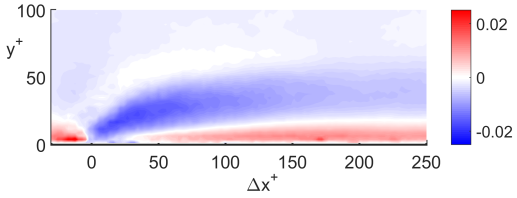

(j) $\bar{u}_{SUB}$ VR=0.40, f^+=0.072, L=4.0

Figure 6.4: $\bar{u}$ and $\bar{u}_{SUB}$ contour maps in the centre-plane with synthetic jets operated at f^+=0.072 (f^+=0.072) and at different VR

Effect of frequency In Figure 6.5 three forced turbulent boundary layer cases are shown, in which the synthetic jets are operated at VR=0.2 and f is varied. The effect of

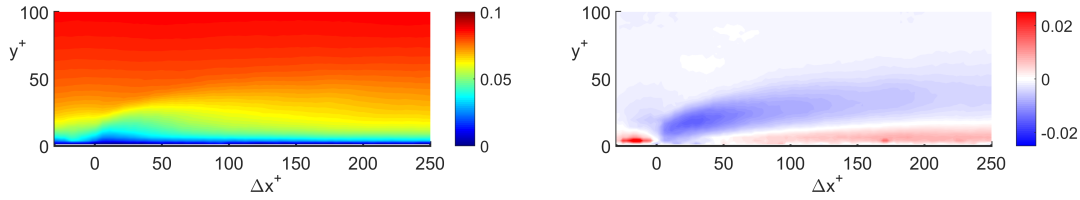

(a) $\bar{u}$ VR=0.20, f^+=0.072, L=2.0 (b) $\bar{u}_{SUB}$VR=0.20, f^+=0.072 L=2.0

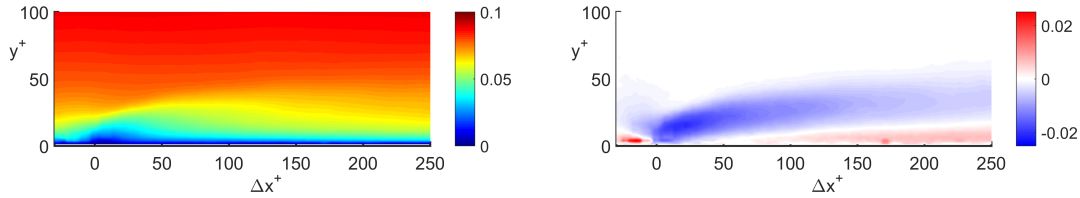

(c) $\bar{u}$ VR=0.20, f^+=0.11, L=1.4 (d) $\bar{u}_{SUB}$ VR=0.20, f^+=0.11, L=1.4

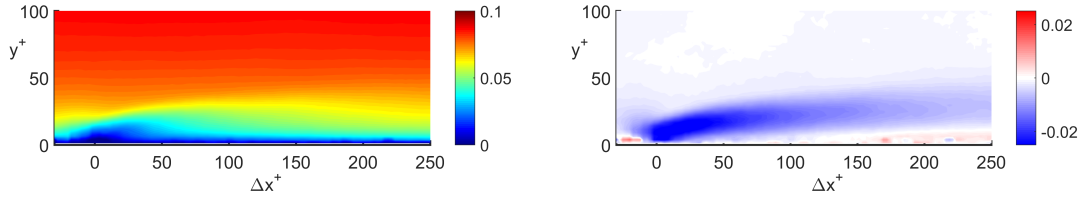

(e) $\bar{u}$ VR=0.20, f^+=0.14, L=1.0 (f) $\bar{u}_{SUB}$ VR=0.20, f^+=0.14, L=1.0

Figure 6.5: $\bar{u}$ and $\bar{u}_{SUB}$ contour maps in the centre-plane with synthetic jest operated at VR=0.2 and at different frequencies

frequency on the flow field is less significant than VR and the velocity field does not seem affected particularly by a frequency increase, at least up to f=4Hz i.e. f^+=0.14.

6.3.2 Mean Velocity Profiles

Effect of Velocity Ratio Velocity profiles can be extracted from the measured vector fields at a given x location. In Figure 6.6 velocity profiles of forced turbulent boundary layer cases with synthetic jet operating at a f=2 Hz (f^+=0.072) and at $\Delta x^+ = 50$ are shown. In this graph all variables are normalised in wall units, using the friction velocity of the unforced turbulent boundary layer. The velocity profile presents a different shape at different values of VR. Indeed, at VR ≤ 0.1 in the near-wall region the velocity is lower than the correspondent velocity in the unforced turbulent boundary layer. In these cases, a lower wall shear stress and a lower skin friction coefficient are

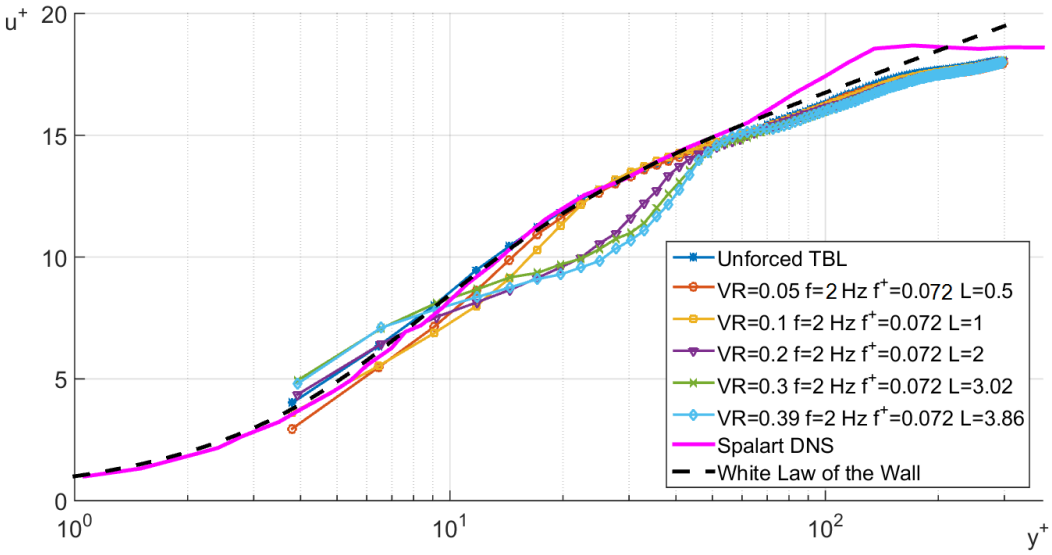

Figure 6.6: Velocity profiles at f^+=0.072, different VR, $\Delta x^+ = 50$ downstream of the SJA array: wall units of unforced TBL

expected, as the velocity gradient at the wall is lower. If VR $\geq$ 0.2 the velocity in the near-wall region is higher than in the unforced boundary layer case. Therefore, a wall shear stress increase is expected. In addition at VR $\geq$ 0.2 the increase of velocity in the near-wall region is accompanied by a region of velocity deficit in the buffer layer and in the log-layer, between y^+ = 10 and 50. In all cases, for $y^+ > 60$ the profile recovers the shape of that of the unforced turbulent boundary layer.

It is also possible to normalise the velocity profiles in wall units by using the friction velocity of the specific forced case, using a fitting to the viscous sublayer law, as described in Section 3.5.4. These velocity profiles are shown in Figure 6.7. In case of drag reduction, i.e. at VR=0.05 and VR=0.1 the velocity profile presents the same slope as in the logarithmic layer, but the intercept is higher: in the literature this is referred to as an *upward shift* of the log-layer and is a typical feature of drag reducing turbulent boundary layers. The opposite trend occurs in drag increasing cases, i.e. VR $>$ 0.2. In these case the intercept is lower and a *downward shift* is achieved. The amount of upward shift or downward shift is proportional to the skin friction drag reduction or increase respectively, as can be seen in Figure 6.7. The upward shift of the velocity profile has been extensively reported in literature. For example, it was observed in turbulent flows controlled using riblets [53, 29], LEBUs [10, 104] and long-chain polymers [95, 154]. The upward shift can be related to an increase of the thickness of the viscous sublayer and to an increase of the smallest scales of the turbulent flow,

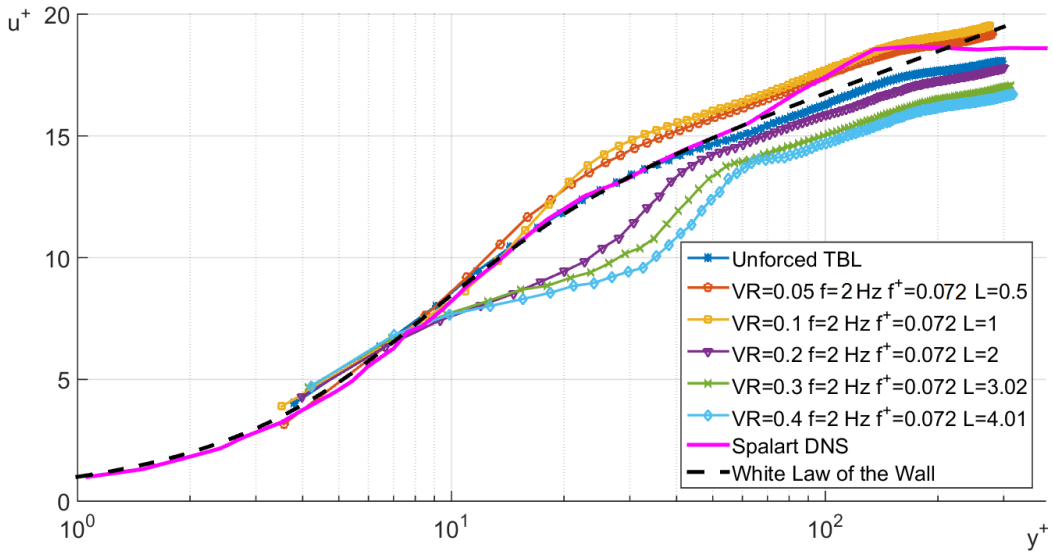

Figure 6.7: Velocity profiles at f^+=0.072, different VR, $\Delta x^+ = 50$ downstream of the SJA array: wall units of forced TBL

towards which the turbulent energy cascade process evolves (see also Section 2.1.1). In other words, the upward shift is related to a decrease of turbulent energy production in the near-wall region and hence to a local skin friction drag reduction.

Effect of Frequency As mentioned above, the effect of frequency on the velocity field seems to be less significant than that of velocity ratio. In Figure 6.8 the velocity profile in the cases where the synthetic jets are operated at fixed VR=0.1 but at different frequencies are shown. The profiles are all extracted at $\Delta x^+ = 50$ and are normalised using the friction velocity of the unforced turbulent boundary layer. At VR=0.1 the velocity profiles do not show a definite trend with increasing frequency. Below y^+=20 the velocity deficit is approximately the same, and all the profiles tend to recover the shape of the unforced turbulent boundary layer profile for $y^+ > 20$.
The correspondent cases at VR=0.3 are shown in Figure 6.9. Also in this case the profiles do not show a definite trend with increasing frequency in the near-wall region. In the region between $y^+ = 10$ and 60 it seems that the velocity deficit increases as frequency increases. This is probably because, as the frequency increases, the coherent structures are produced more frequently by the synthetic jets and therefore their impact on the long time-averaged velocity profile is more relevant. The effect is not however significant.

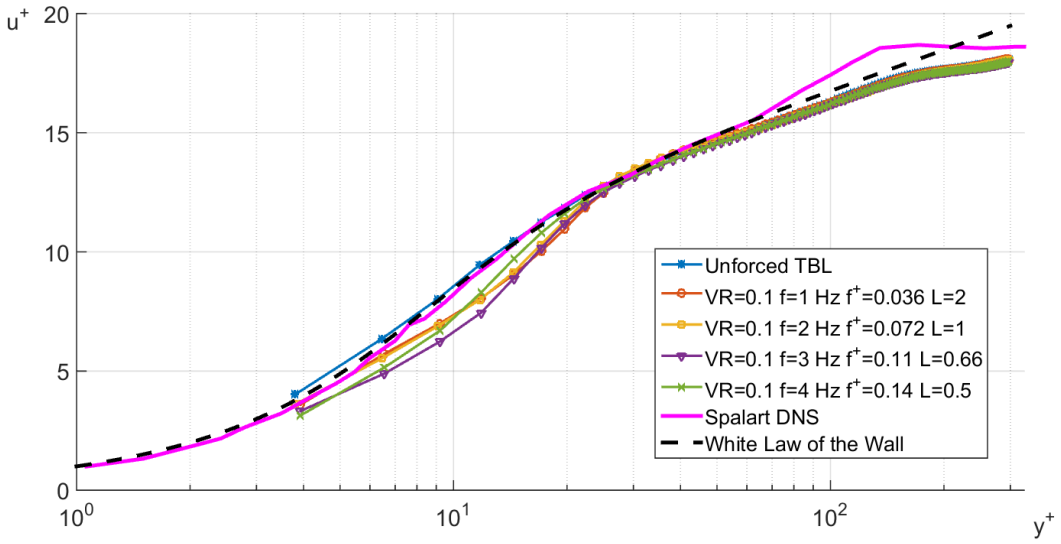

Figure 6.8: Velocity profiles at VR=0.10, different f, $\Delta x^+ = 50$ downstream of the SJA array

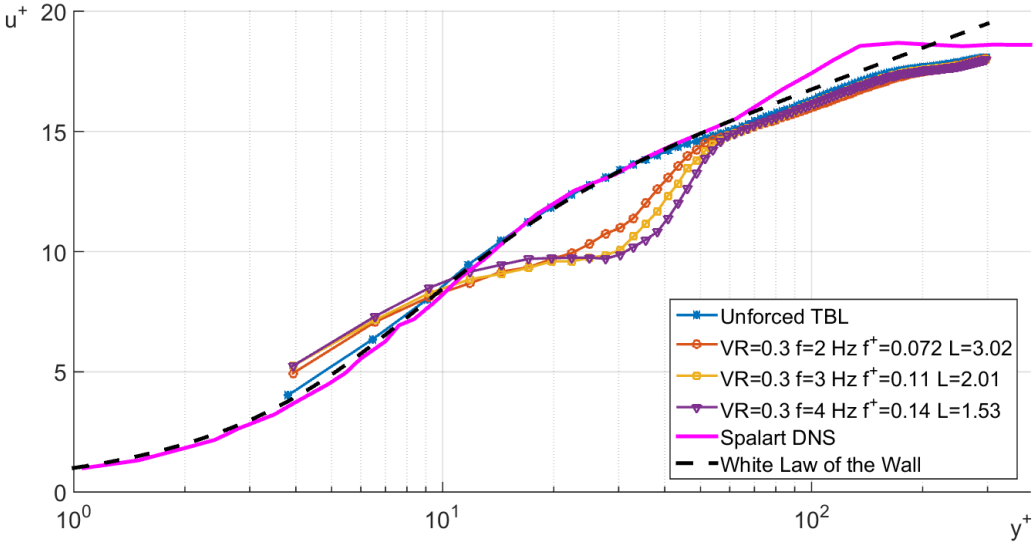

Figure 6.9: Velocity profiles at VR=0.30, different f, $\Delta x^+ = 50$ downstream of the SJA array

Mean velocity Profiles at Different Δx It is also interesting to see how the velocity profiles varies at fixed synthetic jet operating conditions at different Δx^+. The variation of the velocity profile at f^+=0.072 and VR=0.1 is shown in Figure 6.10. The distance Δx^+ is normalised in wall units using the friction velocity of the unforced turbulent boundary layer. The velocity deficit in the near-wall region at low values of Δx^+ tends

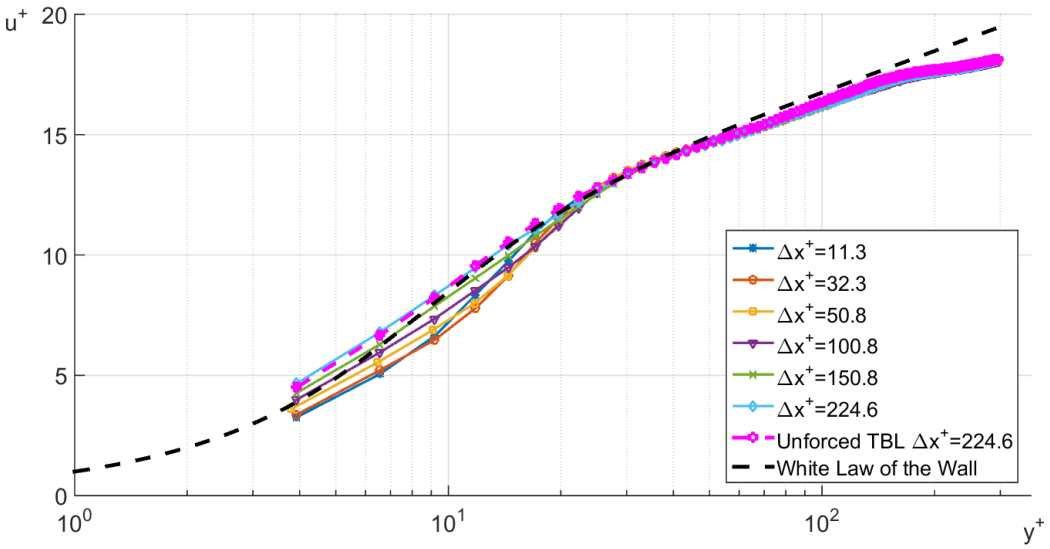

Figure 6.10: Velocity profiles at VR=0.10, f^+=0.072, at different Δx^+ downstream of the SJA array

to decrease downstream until the shape of the unforced turbulent boundary layer profile is recovered, as expected. This occurs at $\Delta x^+ \approx 225$.

The variation of the velocity profile at f^+=0.072 and VR=0.3 is shown in Figure 6.11. In this case the velocity profile shows a velocity deficit in the near-wall region only immediately downstream of the synthetic jet orifices. Further downstream, the velocity in the near-wall region becomes higher than the correspondent velocity in the unforced turbulent boundary layer, yielding a skin friction drag increase, which is quite persistent downstream. It is possible to see that the profile has not recovered the shape of the velocity profile of the unforced turbulent boundary layer at $\Delta x^+ \approx 225$.

6.3.3 Skin friction Streamwise Variation

In the following discussion the estimation of the skin friction coefficient, using a fitting to the viscous sublayer law, as described in Section 3.5.4, is systematically carried out

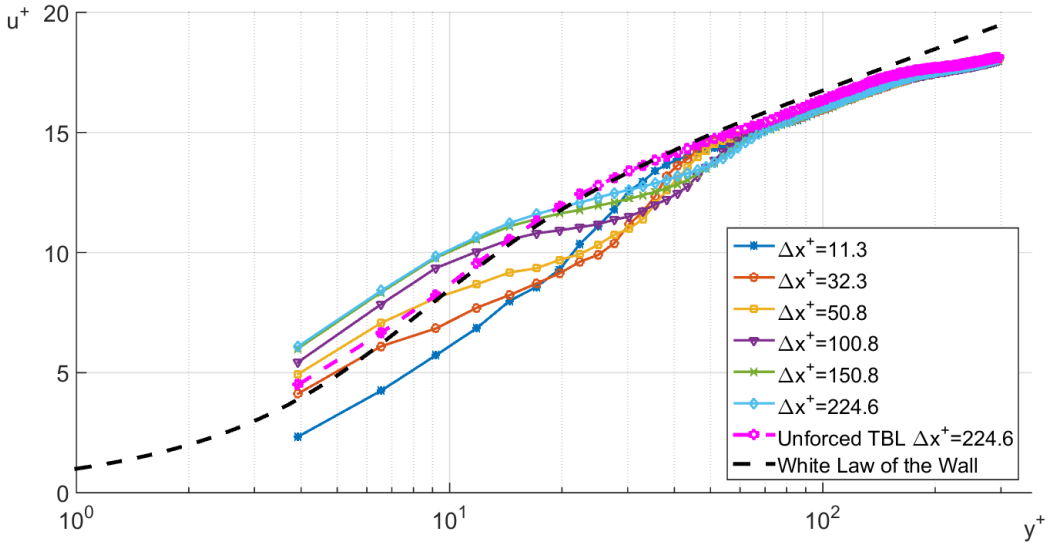

Figure 6.11: Velocity profiles at VR=0.30, f^+=0.072, at different Δx^+ downstream of the SJA array

at several x locations in the centre-plane. The skin friction coefficient is related to the streamwise velocity field in the near-wall region. This is shown shown in Figure 6.12. In part (a) the variation of the skin friction coefficient as function of Δx^+ for two forced cases is shown, namely the case at VR=0.1 f^+=0.072 L=1.0 and the case with VR=0.3 f^+=0.072 L=3.0. Also the skin friction variation in the case of unforced turbulent boundary layer is plotted for comparison. Part (b) and part (c) show the $\bar{u}_{SUB}$-contour maps for the same forced cases. When the streamwise velocity in the near-wall region is locally higher than the velocity in the unforced turbulent boundary layer, the skin friction is higher. When the velocity is lower, the skin friction coefficient is lower. For the case with VR=0.1 it is possible to notice that the region of higher velocity in the near-wall begins at Δx^+=150. In correspondence of this region an increase in the skin friction coefficient with respect to the unforced value is observed. In the case with VR=0.3 the region of higher velocity, and thus of higher skin friction, is observed from Δx^+=40.

In Figure 6.13 the skin friction variation as a function of Δx^+ is plotted for all the cases at a frequency of f^+=0.072 and different VR and L. In general, two different types of behaviour are obtained, whether $VR \leq 0.1$ or $VR \geq 0.2$. In the first case, the skin friction coefficient, as proceeding downstream, initially decreases until it reaches a minimum at $\Delta x^+ = 20 - 30$. The correspondent skin friction coefficient reduction is

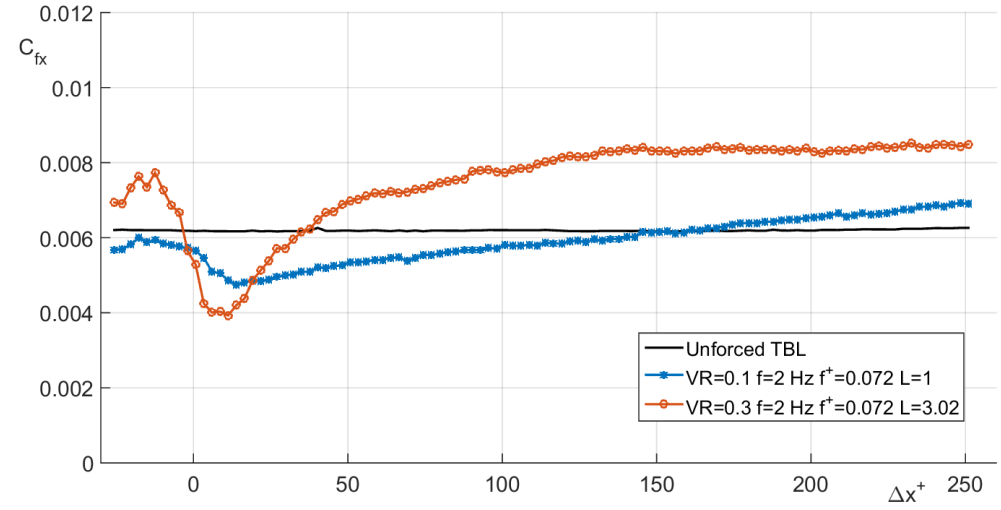

(a) Skin Friction Coefficient Varations with Δx^+

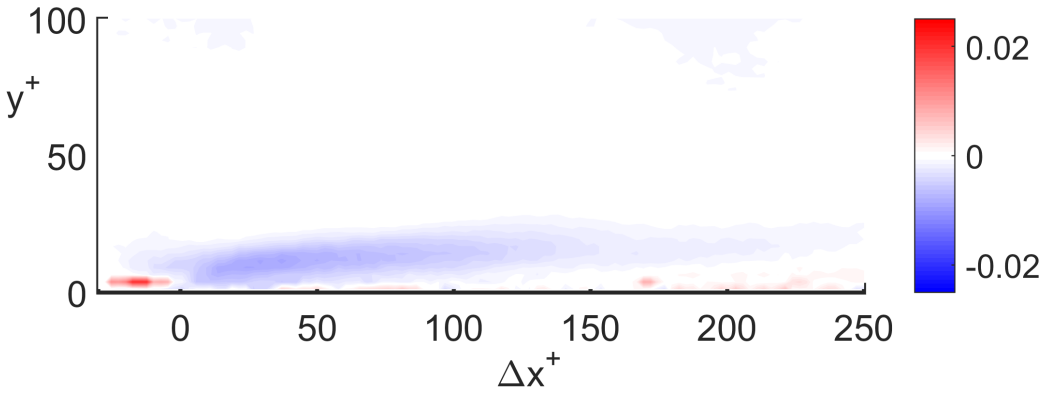

(b) $\bar{u}_{SUB}$-contour map at VR=0.10 f^+=0.072 and L=1.0

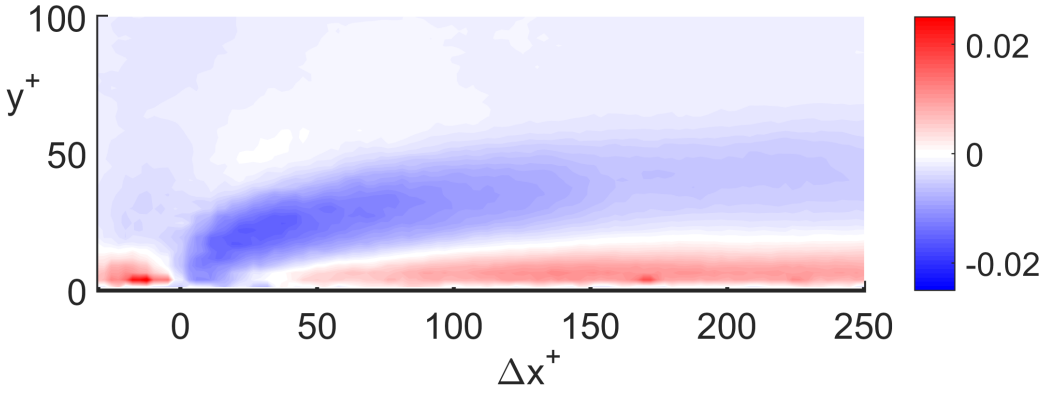

(c) $\bar{u}_{SUB}$-contour map at VR=0.30 f^+=0.072 and L=3.0

Figure 6.12: Relationship $\bar{u}_{SUB}$-velocity field and skin friction streamwise variation

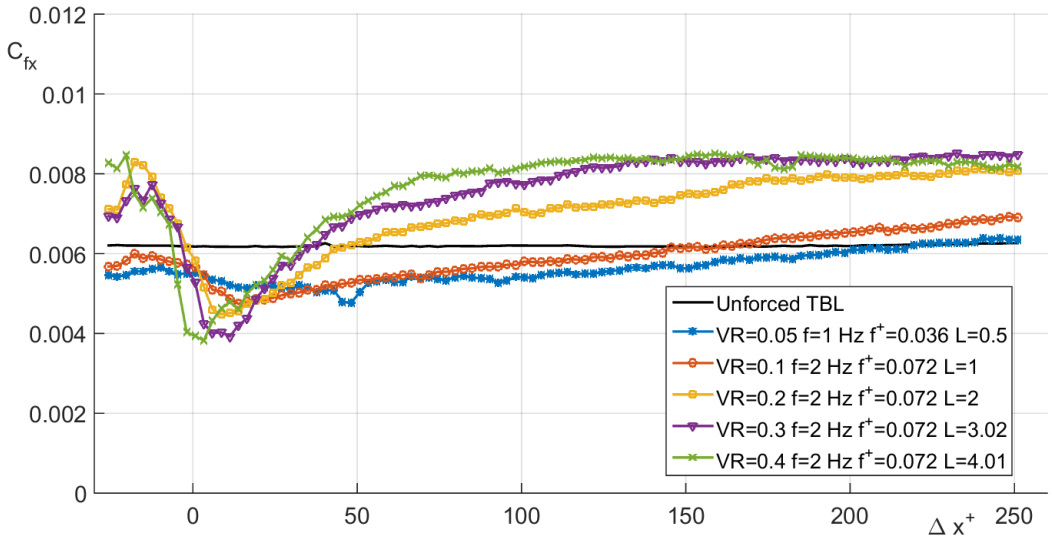

Figure 6.13: Variation of C_{fx} as a function of Δx^+: cases with f^+=0.072

about 23%. Downstream of the minimum, the skin friction coefficient increases and tends to recover the value of the unforced turbulent boundary layer. In the case with VR= 0.05 the value is recovered at $\Delta x^+ \approx 200$, while in the case with VR= 0.1 at $\Delta x^+ = 150$. In both cases with VR$\leq$ 0.1 an area of skin friction reduction is observed, which is at least $\Delta x^+ = 150$ long.

In the cases with VR $\geq$ 0.2 the skin friction coefficient is lower than that of the unforced turbulent boundary layer only in a very limited region, up to $\Delta x^+ \approx 30-40$. After that, the skin friction coefficient becomes higher than in the unforced turbulent boundary layer value. At VR=0.3 and 0.4 the increase in the skin friction coefficient is more than 30% of that of the unforced turbulent boundary layer . The skin friction coefficient does not recover the unforced turbulent boundary layer value within the investigation region. This is consistent with the shapes of the velocity profile discussed in Section 6.3.2.

The same trend also appears for the cases in which the synthetic jets are operated at 4 Hz, as shown in Figure 6.14. However in these cases, the value of VR at which the behaviour of the C_{fx} curves changes, seems to be a little bit higher and, for example, at VR=0.2 a transitional behaviour is found in which a marked region of drag reduction is observed just downstream the synthetic jet orifice. The skin friction coefficient increases again and a drag increase region is found starting from $\Delta x^+ > 150$. The cases with VR=0.3 and VR=0.4 show similar trends to the correspondent cases with

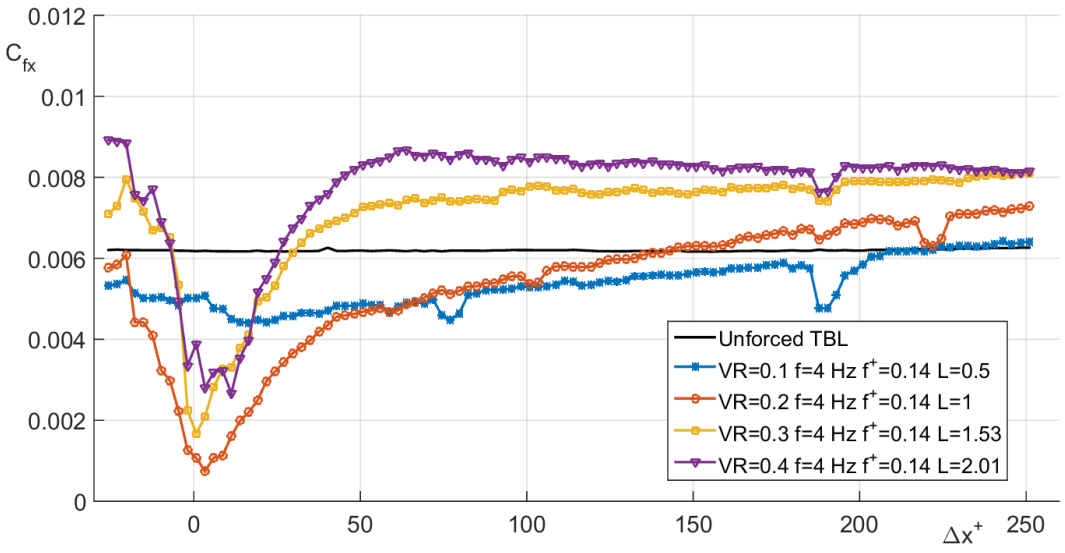

Figure 6.14: Variation of C_{fx} as a function of Δx^+: cases with $f^+ = 0.14$

f^+=0.072. In this case the drag reduction close to the synthetic jet orifice is higher, but the effect does not persist further downstream. Starting from $\Delta x^+ \approx 50-60$ a constant increase in skin friction drag of about 30-40% is observed. In this case the skin friction value also in this case does not recover the value of the unforced turbulent boundary layer within the region of investigation.

6.3.4 C_{fx} Reduction/Increase Map

It is possible to build a scatter plot of the skin friction drag reduction/increase compared to the unforced turbulent boundary layer case, considering all the test conditions and at a fixed Δx^+. The scatter plot of the ratio C_{fx}/C_{fx0} at $\Delta x^+ = 50$ is shown in Figure 6.15. C_{fx} is the skin friction coefficient estimated in the forced turbulent boundary layer case, while C_{fx0} is the skin friction coefficient estimated in the forced turbulent boundary layer case at the same Δx^+. The variables Δx^+ and f are normalised in wall units using the friction velocity of the unforced turbulent boundary layer. C_{fx}/C_{fx0} is plotted as a function of L and f^+. The choice of f^+ as a direct variable related to drag reduction is due to the fact that the forcing frequency is expected to play an important role in the interaction between the synthetic jets and the near-wall coherent structure dynamics in the turbulent boundary layer. Lines at constant VR are also plotted. It can be seen that the skin friction coefficient reduction/increase is mainly dependent on VR, although a slightly greater drag reduction is observed at higher frequencies. Drag

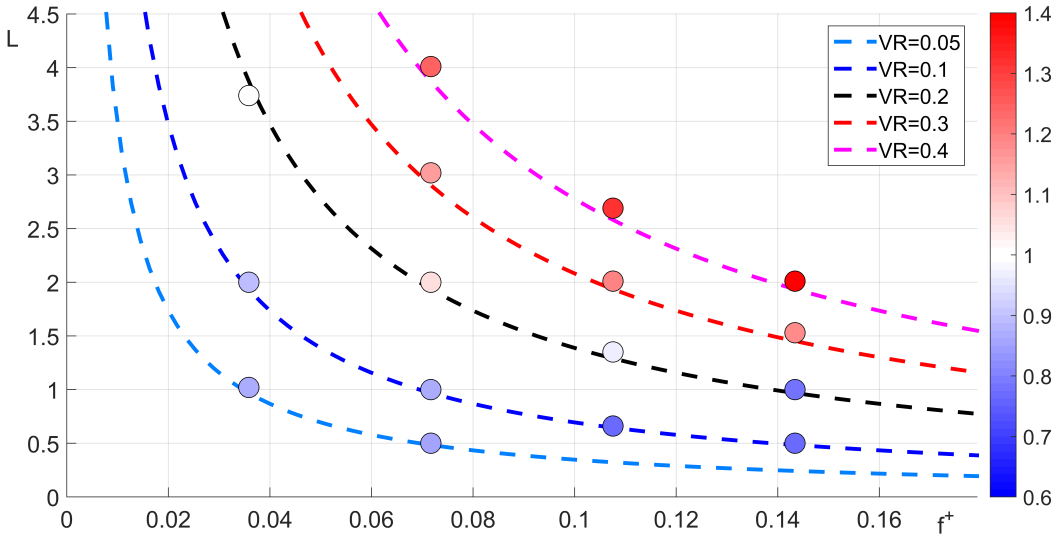

Figure 6.15: C_{fx}/C_{fx0}-contour map in the centre-plane at $\Delta x^+ = 50$

reduction is observed at VR$<$ 0.2, drag increase at VR$>$ 0.2. Overall, results are in agreement with the results reported in previous sections.

6.4 Long-Time Averaged PIV Analysis in the Off-Centred Planes

This section reports a study of the long-time averaged velocity vector fields in four off-centred planes, parallel to centre-plane. The test conditions considered are reported in Table 6.2. The displacements of the off-centred planes from the centre-plane are Δz= 0 mm, 2 mm, 4.5 mm and 9 mm . The spacing between two adjacent orifices is z_{sp}=9 mm, so the planes examined are located at $\Delta z/z_{sp}$= 0.22, 0.5 and 1. The plane at $\Delta z/z_{sp}$=1 passes through the centre of the orifice adjacent to the central one in the synthetic jet array. Therefore, due to flow periodicity, the velocity in this plane should be very similar to that in the centre-plane, at $\Delta z/z_{sp}$=0.

6.4.1 Mean Velocity Contours at Different Δz

$\bar{u}$-velocity contours can be shown in a stacked plot, to allow the flow field in different planes to be compared in the same figure. For an immediate comparison with the velocity field in the unforced case, the $\bar{u}$-velocity in the unforced case is subtracted to that of the forced cases. The resulting velocity field is referred to as $\bar{u}_{SUB}$ again. A

stacked plot with the $\bar{u}_{SUB}$-contour maps obtained when the synthetic jets are operated at f^+=0.072 and VR=0.1 is shown in Figure 6.16. The region of lower velocity com-

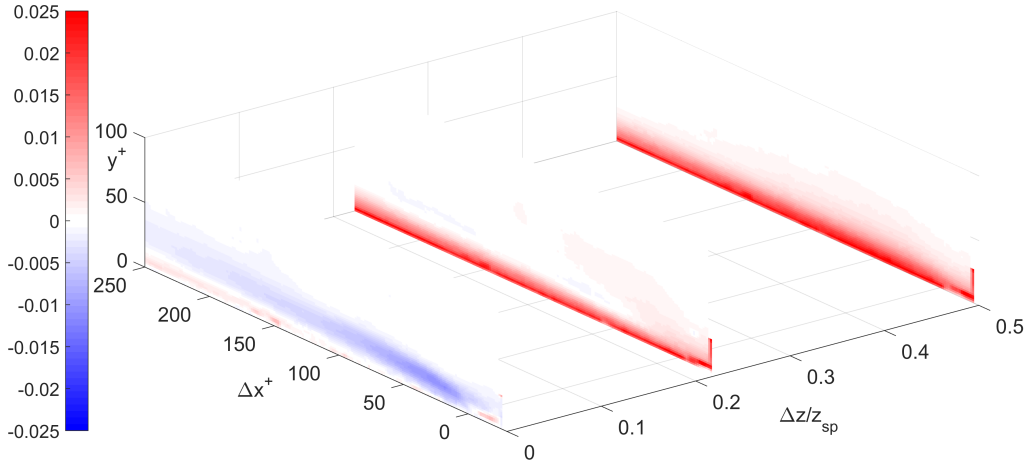

Figure 6.16: $\bar{u}_{SUB}$-contour maps at VR=0.10, f^+=0.072 and at different Δz

pared to the unforced turbulent boundary layer case appears attached to the wall only in the centre-plane, at $\Delta z/z_{sp}$=0. In the other two planes for the near-wall region an increase in velocity is observed, which is expected to cause an increase in skin friction. The region of velocity increase in the off-centred planes is quite extended and is longer than the area of investigation. The intensity of this region is highest in the plane in-between two adjacent orifices, which is at $\Delta z/z_{sp}$=0.5.

A stacked plot with the $\bar{u}_{SUB}$-contour maps obtained when the synthetic jets are operated f^+=0.072 and VR=0.2 is shown in Figure 6.17. In the centre-plane the region of lower velocity is attached to the wall only for a very limited distance downstream of the synthetic jet orifice. Downstream of it, the region of higher velocity also described in Section 6.3 appears. In the planes at $\Delta z/z_{sp}$=0.22 and $\Delta z/z_{sp}$=0.5 the region of lower velocity is lifted away from the wall everywhere in the area of investigation and in the near-wall a region of significant velocity increase appears. This region is thicker than the analogous region in the plane at $\Delta z/z_{sp}$=0 and the increase in velocity is more intense. Therefore, the skin friction coefficient is expected to be higher than in the unforced turbulent boundary layer case in all planes.

Finally, a stacked plot with the $\bar{u}_{SUB}$-contour maps obtained when the synthetic jets are operated f^+=0.072 and VR=0.3 is shown in Figure 6.18. In this case, the veloc-

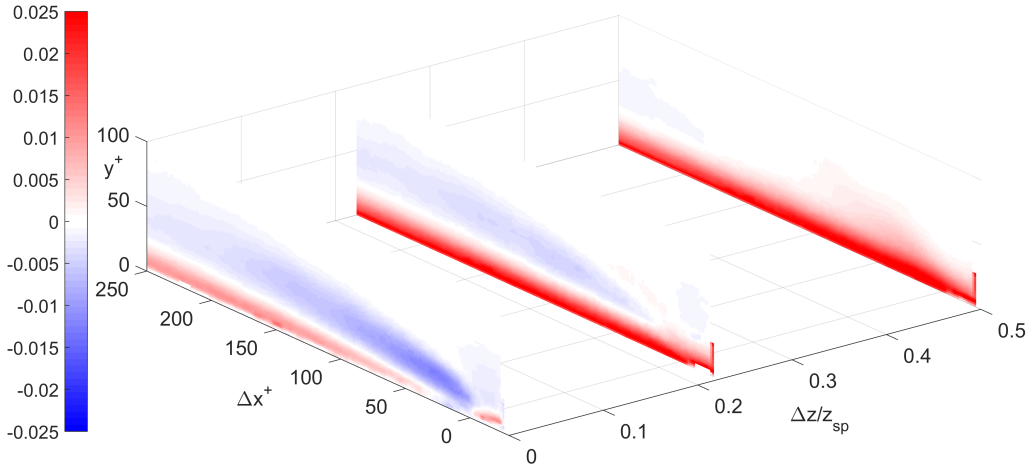

Figure 6.17: $\bar{u}_{SUB}$-contour maps at VR=0.20, f^+=0.072 and at different Δz

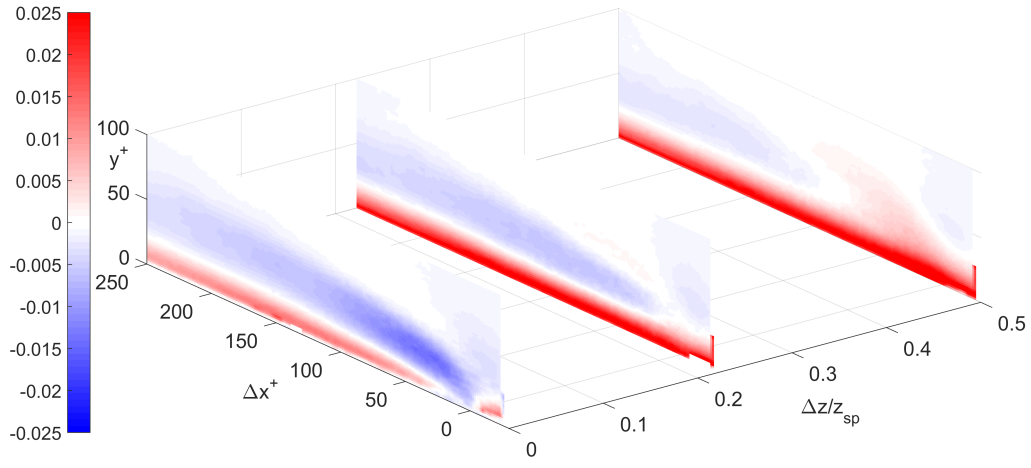

Figure 6.18: $\bar{u}_{SUB}$-contour maps at VR=0.30, f^+=0.072 and at different Δz

ity field in all planes is very similar to the case with VR=0.2 and an increase in skin friction drag is expected in all planes.

6.4.2 Mean Velocity Profiles at Different Δz

In Figure 6.19 $\bar{u}$ velocity profiles, normalised in wall units using the friction velocity of the unforced turbulent boundary layer, are shown at different Δz for the case in which the synthetic jets are operated at f^+=0.072 and VR=0.1. The profiles are extracted at Δx^+= 50; this location is the same as in Section 6.3.2. The velocity profiles extracted at

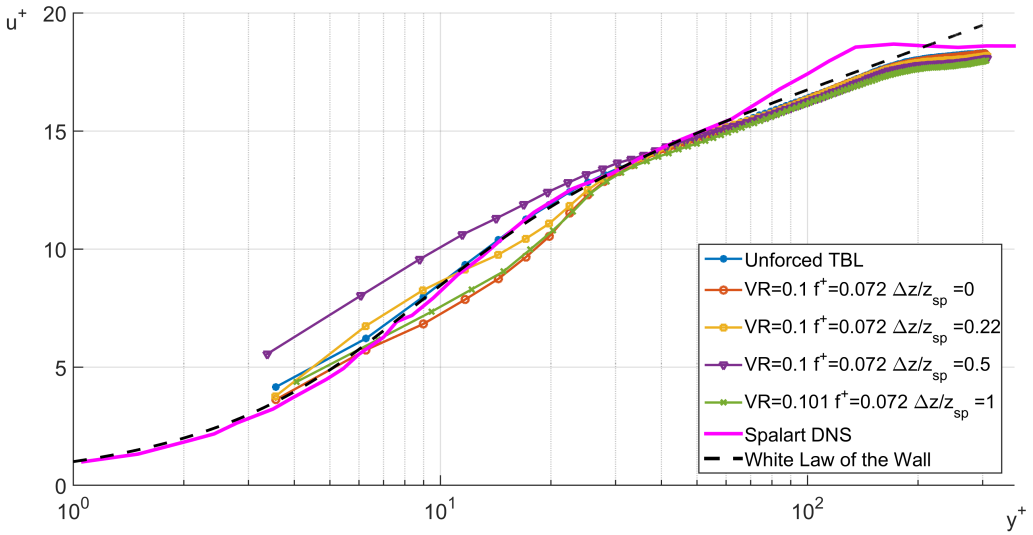

Figure 6.19: Velocity Profiles at VR=0.10, f^+=0.072, $\Delta x^+ = 50$ downstream of the SJA array, different Δz

Δz= 0 mm and $\Delta z/z_{sp}$= 1 are similar, due to flow periodicity. In the plane at $\Delta z/z_{sp}$= 0 the profile is similar to that analysed in Section 6.3.2. At $\Delta z/z_{sp}$= 0.22 the decrease in velocity in the near-wall compared to the unforced case disappears. However, between $4 < y^+ < 20$ a velocity increase is observed. At $\Delta z/z_{sp}$= 0.5 the velocity is higher than the velocity of the unforced turbulent boundary layer up to $y^+ = 30$. In all cases the profiles overlap with those of the unforced turbulent boundary layer above $y^+ = 30$. Drag reduction is only observed in the central plane. The region of drag reduction is therefore less than 4 mm wide, $\Delta z/z_{sp} <= 0.44$. For $\Delta z/z_{sp} > 0.44$ only drag increase is expected.

In Figure 6.19 $\bar{u}$ profiles are shown at different Δz in the case in which the synthetic

jets are operated at f=2 Hz and VR=0.3. Velocity profiles are again extracted at Δx^+= 50. Also in this case, the velocity profiles extracted at $\Delta z/z_{sp}$= 0 and at $\Delta z/z_{sp}$= 1

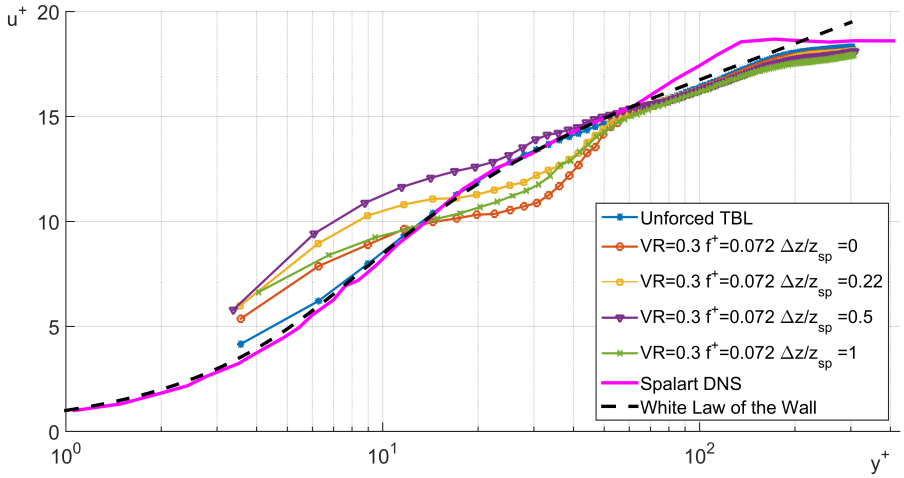

Figure 6.20: Velocity Profiles at VR=0.30, f^+=0.072, $\Delta x^+ = 50$ downstream of the SJA array, different Δz

show similar trends, due to flow periodicity. However $\bar{u}$ is higher than the unforced value across the whole boundary layer at all Δz. The decrease in velocity in the region $10 < y^+ < 40$, observed at $\Delta z/z_{sp}$= 0 and $\Delta z/z_{sp}$= 0.22, disappears at $\Delta z/z_{sp}$= 0.5.

6.4.3 Skin Friction Streamwise Variation at Different Δz

In this section the skin friction coefficient streamwise variation is computed at several values of Δz^+. The case in which the synthetic jets are operated at VR=0.1 and f^+=0.072 is shown in Figure 6.21. The skin friction coefficient related to the unforced turbulent boundary layer is also plotted for comparison. At $\Delta z/z_{sp}$= 1 the skin friction coefficient variation with Δx^+ is very similar to that at $\Delta z/z_{sp}$= 0 due to flow periodicity. Away from the centre-plane, the skin friction coefficient is higher than that in the unforced turbulent boundary layer . These results are consistent with shape of the velocity profiles shown above and confirm that the skin friction reduction region occurs only in a limited area near the centre-plane.

The case with VR=0.3 and f^+=0.072 is shown in Figure 6.22. As expected, the skin friction coefficient is increased in all planes, confirming that this operating condition does not provide any drag reduction.

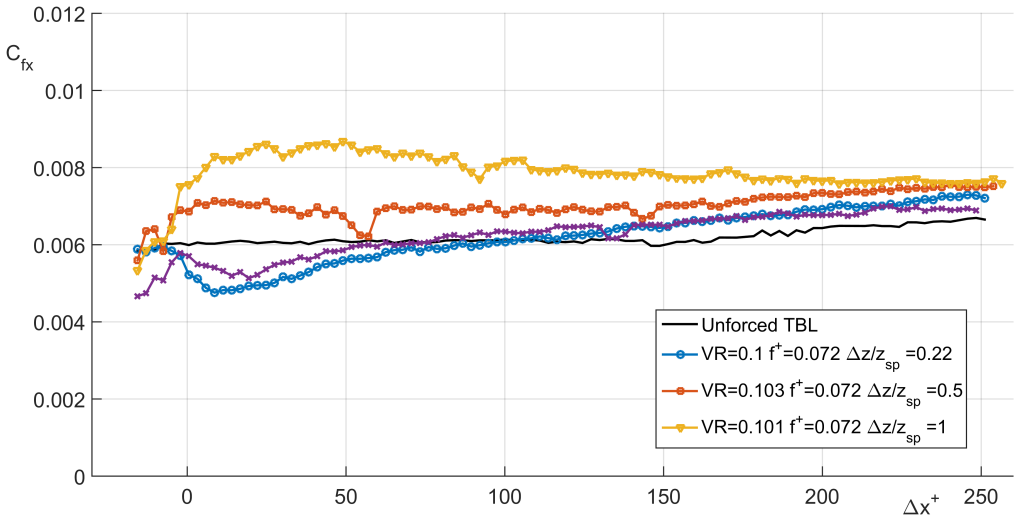

Figure 6.21: Variation of C_{fx} as a function of Δx^+ at f^+=0.072, VR=0.10 and different Δz

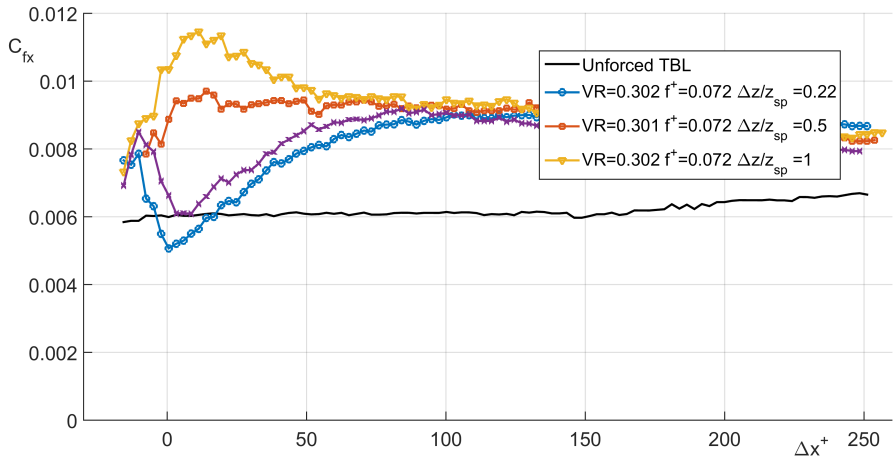

Figure 6.22: Variation of C_{fx} as a function of Δx^+ at $f^+ = 0.072$, VR=0.30 and different Δz

6.4.4 Variation of Skin Friction Drag and Power Saving Considerations

Given the skin friction variation with Δx^+ at different off-centred planes, the skin friction coefficient variation over the area indicated with A in Figure 6.23 can be determined. The area A spans $-15 < \Delta x^+ < 250$ and $-0.5 < \Delta z/z_{sp} < 0.5$. As the flow is periodic the area is representative of the performance of the whole array. A rough

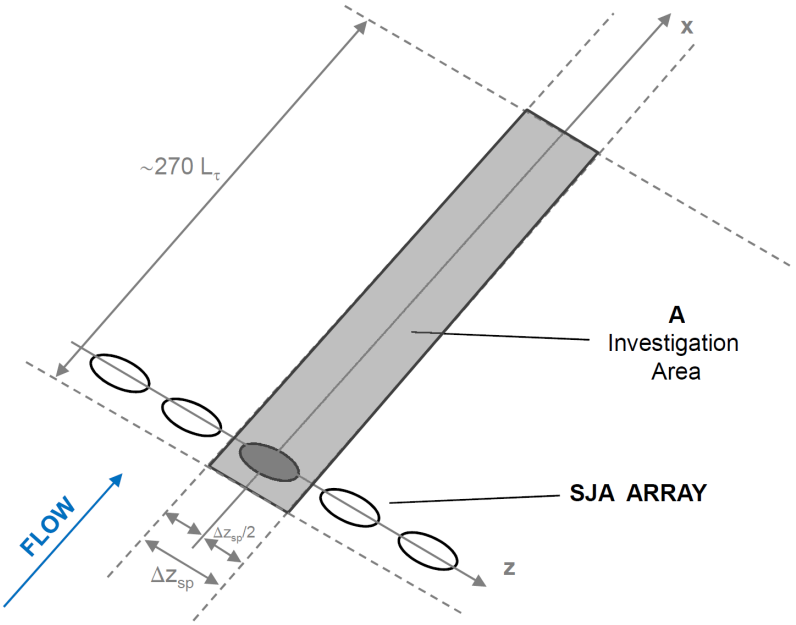

Figure 6.23: Area considered for power reduction considerations

estimate of the skin friction drag over the investigation area can be obtained. The value ΔC_{fA}, which represents the net 'averaged' variation of the skin friction coefficient over A, is computed as:

$$\Delta C_{fA} \doteq 1/A \int_A \left[C_{fx}(x,z) - C_{fx0}(x,z)\right] dxdz \tag{6.1}$$

where $C_{fx}(x,z)$ is the skin friction coefficient obtained in the forced cases and $C_{fx0}(x,z)$ is the coefficient in the unforced case.

The skin friction coefficient variation over the investigation area when the synthetic

jets are operated at VR=0.1 and f^+=0.072 is shown in Figure 6.24. The skin friction coefficient in the unforced case is subtracted to the skin friction coefficient in the forced turbulent boundary layer case. The red-blue colour map gives an immediate indication of the regions with drag reduction (blue) an the regions with drag increase (red). The reduction in skin friction appears only in a limited area near the synthetic

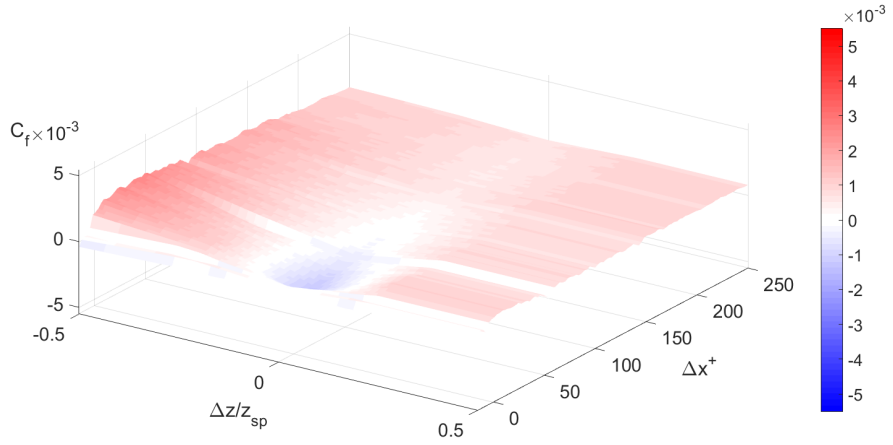

Figure 6.24: Skin friction coefficient variation (compared to the unforced turbulent boundary layer) at VR=0.10 f=2 Hz

jet orifice. This area extends for about $\Delta x^+ = 200$ downstream of the orifice and for about $\Delta z/z_{sp} = 0.2$ at each side of the orifice. The skin friction coefficient increases as Δz increases, and it is maximum in the plane in-between two orifices i.e. $\Delta z/z_{sp} = 0.5$. In this case $\Delta C_{fA} \approx 0.12$, which means the skin friction drag is about 12% higher than in the unforced turbulent boundary layer. This result is not positive. However, it is believed that this configuration can be optimised in order to achieve a negative value of ΔC_{fA}. For example, if the spacing between two adjacent orifices is increased, the drag increase in the region in between them could be mitigated and the drag reduction region in the centre-plane could be enlarged. The physical reason behind this is explained in Section 6.6.

The case with VR=0.2 and f^+=0.072 is shown in Figure 6.25. As expected the area near the synthetic jet orifice with skin friction drag reduction is very small. In addition, the drag increase in the region in-between two orifices is much greater than in the case with VR=0.1. In this case, $\Delta C_{fA} \approx 0.36$, which means that the skin friction drag is about 36% higher than in the unforced turbulent boundary layer.

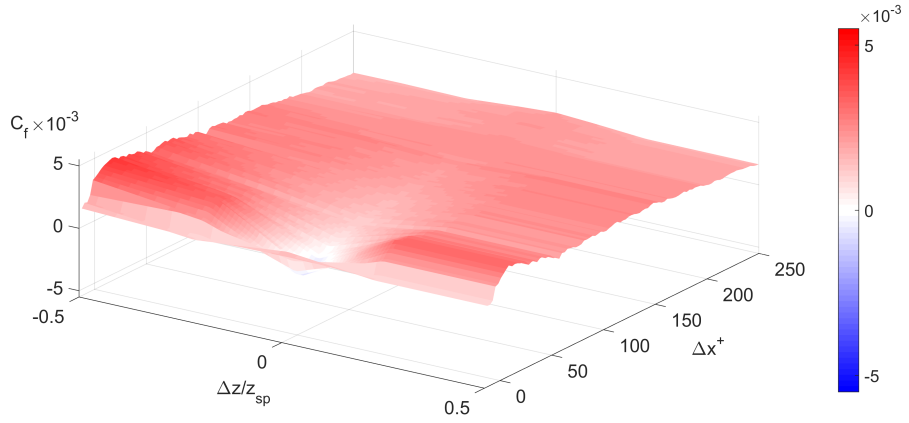

Figure 6.25: Skin friction coefficient variation (compared to the unforced turbulent boundary layer) at VR=0.20 f=2 Hz

The case with VR=0.3 and f^+=0.072 is shown in Figure 6.26.

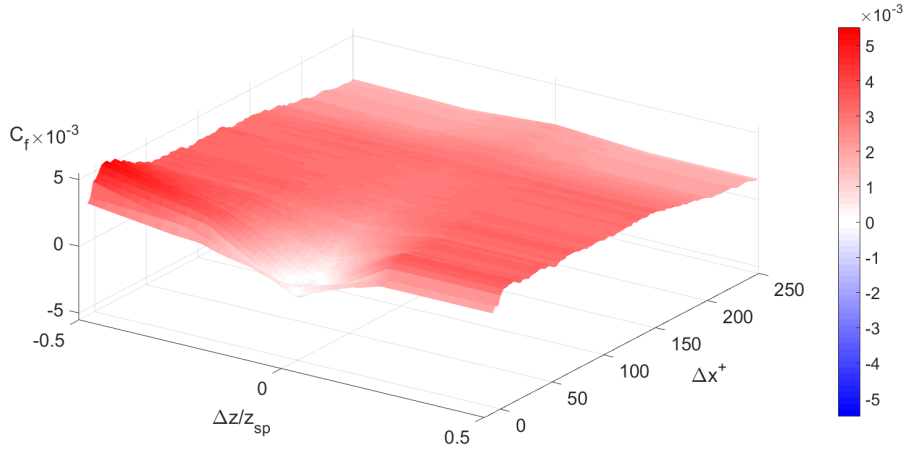

Figure 6.26: Skin friction coefficient variation (compared to the unforced turbulent boundary layer) at VR=0.30 f=2 Hz

The drag increase in this case is higher than at VR=0.2: $\Delta C_{fA} \approx 0.40$, which means that the skin friction drag is about 40% higher than in the unforced turbulent boundary layer.

In order to evaluate the efficiency of the flow control strategy, the power consumption of the synthetic jet needs to be estimated. In the case of a single synthetic jet, this value can be estimated from the ideal delivered fluid power, which can be expressed

as[63]:

$$P_{\text{jet}} = \frac{1}{2}\rho \bar{U}_0^3 \left(\frac{D_0^2\pi}{4}\right) = \frac{1}{2}\rho u_\infty^3 VR^3 \left(\frac{D_0^2\pi}{4}\right) \tag{6.2}$$

The actual power consumed by the actuation system is higher than this, because also an efficiency factor η has to be taken into accounts. This efficiency factor takes into account all the sources of power loss. Given η the power consumed by the whole actuation system is $P_{\text{SJA}} = P_{\text{jet}}/\eta$. A precise estimation of η is beyond the scope of this work and is not carried out. The value of P_{jet} has to be compared with the reduction in the power dissipated by skin friction drag over the area A, which can be expressed as:

$$P = \frac{1}{2}\rho u_\infty^3 \int_A C_{fx}(x,z)\, dxdz. \tag{6.3}$$

In the following P_{unf} represents the power dissipated in the unforced turbulent boundary layer case, P_{forced} the power dissipated in a forced turbulent boundary layer case. Power is saved in the forced turbulent boundary layer if $P_{\text{forced}} < P_{\text{unf}}$ and in this case the power saved is

$$P_{\text{saved}} = P_{\text{forced}} - P_{\text{unf}}. \tag{6.4}$$

It is assumed that the maximum power saved is obtained in the case of complete flow relaminarisation over the area A

$$P_{\text{saved}}^{\text{MAX}} = P_{\text{lam}} - P_{\text{unf}}. \tag{6.5}$$

The percentage of power saved is calculated as

$$P_{\text{saved}^{\%}} = 100 \left(\frac{P_{\text{forced}} - P_{\text{unf}}}{P_{\text{unf}}}\right). \tag{6.6}$$

Figure 6.27 shows the power consumption of a single synthetic jet actuator i.e. P_{jet} as a function of VR at a free-stream velocity of 0.1 m/s in water flow. On the right axis the level of power saved over the area A correspondent to an 'averaged' C_{fx} reduction in percentage with respect to the unforced turbulent boundary layer is indicated. The maximum drag reduction is expected in the case the boundary layer is completely relaminarised over A. The level of power saved in this case is shown in the plot and corresponds to a drag reduction of about 60%. In Figure 6.27 also the drag increase obtained when the synthetic jets are operated at f^+=0.072 and VR=0.1, 0.2 and 0.3 are included. As the drag is increased, the values of power saved are considered to be negative. The performance of the synthetic jet array in terms of skin friction drag

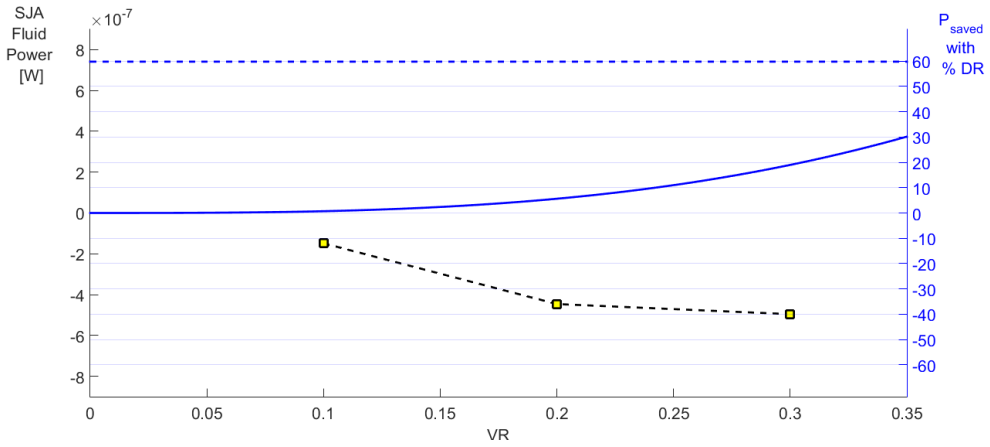

Figure 6.27: Fluid power delivered by a single synthetic jet as a a function of VR and levels of drag reduction obtained in the present experiments

reduction over A degrades with VR, so if the geometry of the array is optimised, it is believed that the power saved could be greater than the power consumed at low values of VR. Further studies are required to provide further insight on this.

It has to be stressed that this analysis only considers the power saved due to a possible lower skin friction drag over A. The introduction of hairpin vortices modifies the flow field and may lead to an increase in the total drag, even if a skin friction drag reduction is achieved. In order to obtain the total drag reduction, further measurements are required, which are strongly recommended for future work.

6.5 Phase-Locked PIV Investigation in the Centre-Plane

This section contains the results of the Phase-Locked PIV experiments. With Phase-Locked PIV a more detailed investigation on the coherent structures produced by the synthetic jet and their effect on the flow field can be obtained. In these experiments the synthetic jets are operated at three velocity ratios, VR=0.1, 0.2 and 0.3. The frequency of oscillation of the diaphragm is f= 2 Hz i.e. f^+=0.072. For each test condition a preliminary non-synchronised PIV measurement is performed, in which 1000 image pairs are acquired at a sampling frequency of 2.5 Hz. Then phase-locked PIV measurements are carried out at eight phases within the oscillation cycle of the diaphragm, namely $\Phi = 0°$, 45°, 90°, 135°, 180°, 225°, 270° and 315°.

6.5.1 Mean and Phase-Locked Averaged Velocity $< u >$

In this section the fields of the mean streamwise velocity $\bar{u}$ and the phase-locked streamwise velocity component $< u > (x, y, \Phi)$ at all phases are discussed. Only four out of the total eight phases are shown, for simplicity. In Figure 6.28 the contour maps in the case in which the synthetic jets are operated at VR=0.1 and f^+=0.072 are shown. In the first row the long-time averaged velocity field is shown. On the column on the left the $\bar{u}$-contour maps is shown. The unforced turbulent boundary layer field is subtracted from the $\bar{u}$-field of the forced turbulent boundary layer and the contour map of the resulting field, indicated as $\bar{u}_{SUB}$, is shown in the column on the right. In the successive four rows the phase-locked averaged velocity fields are shown for the phases $\Phi = 0°$, $90°$, $180°$ and $270°$. For each row, in the column on the left the $< u >$-contour maps are shown for a certain phase. The unforced mean turbulent boundary layer velocity field is subtracted from each $< u >$ field and the resulting vector field $< u_{SUB} >$ is shown in the column on the right. In this case the effect of the synthetic jet is barely visible in the $< u >$ contour maps (column on the left). Very small lower velocity bulges compared to the unforced turbulent boundary layer appear, which are in all cases confined to the near-wall region, $y^+ < 20$. The velocity difference with respect to the unforced turbulent boundary layer case is highlighted in the $< u_{SUB} >$-contour maps, in the column on the right. Between $\Delta x^+ = 0$ (the location of the synthetic jet orifice) and $\Delta x^+ = 40$, there is a region of higher or lower velocity compared to the unforced case, according to the fact that the synthetic jet blows or sucks water during the oscillation cycle. Downstream of this region several regions of lower velocity compared to the unforced turbulent layer appear. These zones become weaker as they proceed downstream.

In Figure 6.29 the contour maps in the case in which the synthetic jets are operated at VR=0.2 and f^+=0.072 are shown. In the $< u >$-contour maps in this case larger bulges of lower streamwise velocity appear, which propagate downstream within the period of actuation. In the $< u >$-contour maps, it is observed that the lower speed regions are shifted away from the wall and are more intense. Underneath them, in the near-wall region, a region of higher velocity is present in all the four phases. The edge of this region appears to be modulated by the passage of the travelling lower speed regions above it.

In Figure 6.30 the contour maps in the case in which the synthetic jets are operated

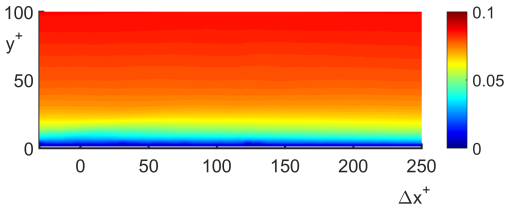

(a) $\bar{u}$ mean

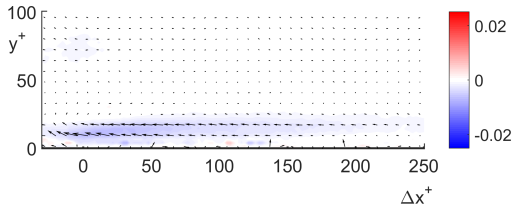

(b) $u_{\bar{SUB}}$ mean

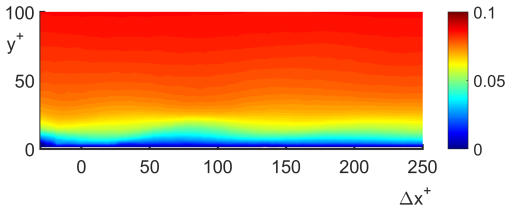

(c) $< u > \Phi = 0°$

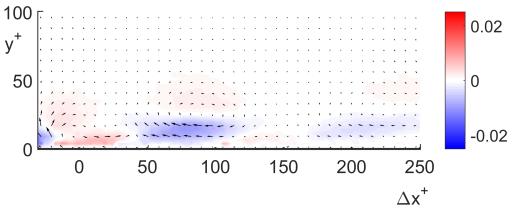

(d) $< u_{SUB} > \Phi = 0°$

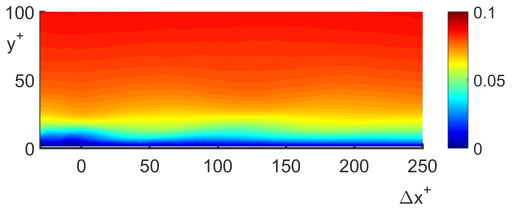

(e) $< u > \Phi = 90°$

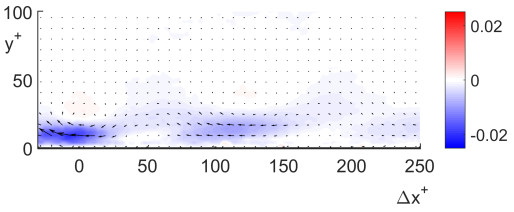

(f) $< u_{SUB} > \Phi = 90°$

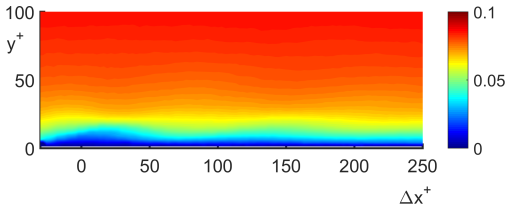

(g) $< u > \Phi = 180°$

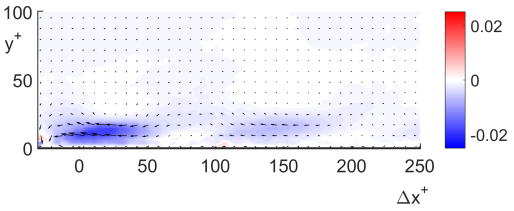

(h) $< u_{SUB} > \Phi = 180°$

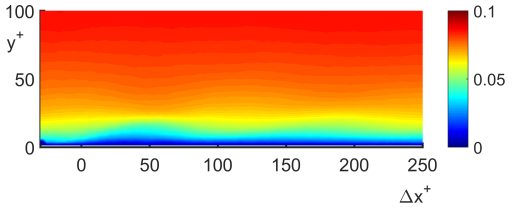

(i) $< u > \Phi = 270°$

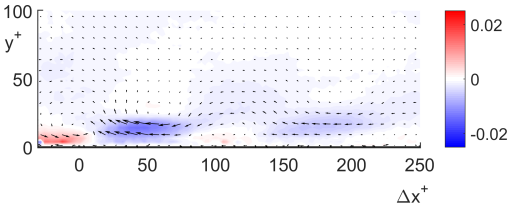

(j) $< u_{SUB} > \Phi = 270°$

Figure 6.28: Mean $\bar{u}$ and phase-locked averaged $< u >$ and $< u_{SUB} >$ contour maps at f^+=0.072 VR=0.10, different Φ

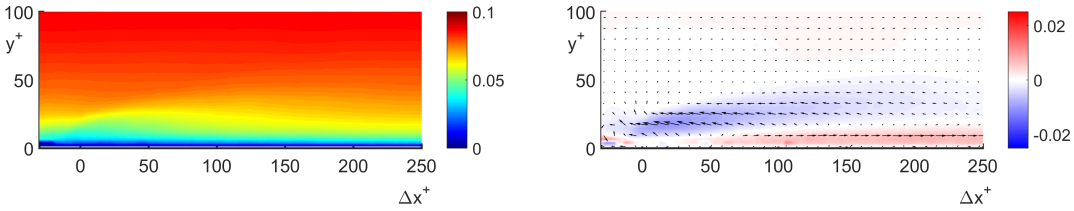

(a) $\bar{u}$ mean

(b) $u_{\bar{SUB}}$ mean

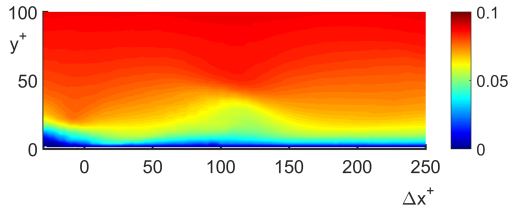

(c) $< u > \Phi = 0°$

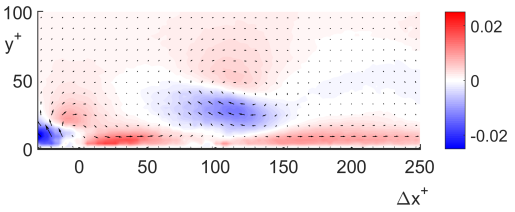

(d) $< u_{SUB} > \Phi = 0°$

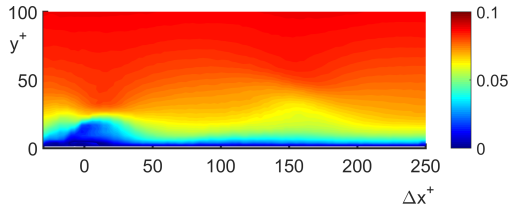

(e) $< u > \Phi = 90°$

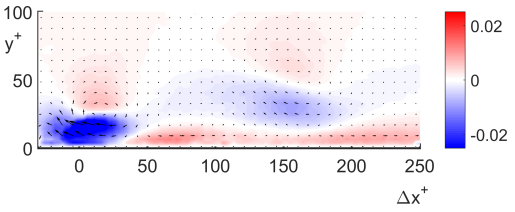

(f) $< u_{SUB} > \Phi = 90°$

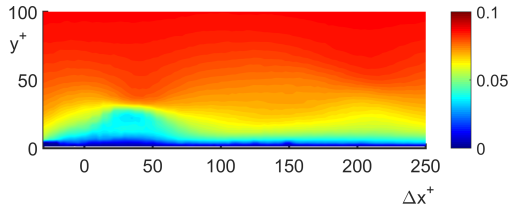

(g) $< u > \Phi = 180°$

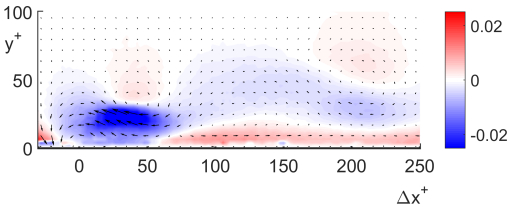

(h) $< u_{SUB} > \Phi = 180°$

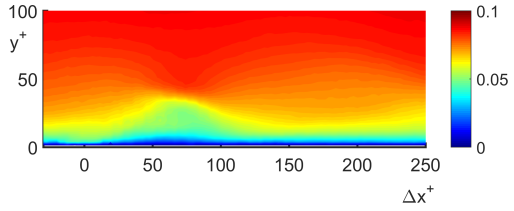

(i) $< u > \Phi = 270°$

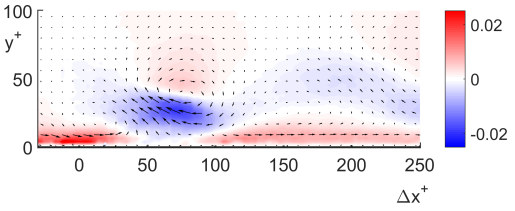

(j) $< u_{SUB} > \Phi = 270°$

Figure 6.29: Mean $\bar{u}$ and phase-locked averaged $< u >$ and $< u_{SUB} >$ contour maps at f^+=0.072 VR=0.20, different Φ

at VR=0.3 and f^+=0.072 are shown. Similar considerations to the case with VR=0.2 can be made. In this case, the regions of lower velocity are more intense as well as the region of higher velocity in the near-wall region.

6.5.2 Periodic $\tilde{u}$ and $\tilde{v}$ Velocity Components

In this section, the fields of the periodic velocity component $\tilde{u}(x,y,\Phi)$ and $\tilde{v}(x,y,\Phi)$ are presented. Also in this case, only four phases out of eight are shown, for simplicity.

In Figure 6.31 the $\tilde{u}$-contour and $\tilde{v}$ are shown maps in the case in which the synthetic jets are operated at VR=0.1 and f^+=0.072. To distinguish these contour maps from those presented in Section 6.5.1 the colour map used is a magenta-cyan colour map, instead of a red-blue one. Each row in the figure corresponds to a certain phase. In the column on the left the $\tilde{u}$-contour maps are shown, whereas in the column on the right $\tilde{v}$-contour maps are shown. Regions of positive and negative $\tilde{u}$ arranged in alternating pattern are observed near the wall. These regions extend up to y^+=20 and are long about 50 L_τ each. The magnitude of $\tilde{u}$ within these regions decreases as they move downstream. Also the $\tilde{v}$-maps present positive and negative regions. A defined anti-correlation between the $\tilde{u}$ and $\tilde{v}$ appears. In fact, a region of positive $\tilde{u}$ is correlated with a region of negative $\tilde{v}$ and vice-versa. This is consistent with the flow model of a train of hairpin vortices travelling near the wall, as explained in Section 6.6.

In Figure 6.32 the $\tilde{u}$-contour and $\tilde{v}$ maps at VR=0.2 and f^+=0.072 are shown. In this case, the regions of positive and negative $\tilde{u}$ are more extended, up to $y^+ = 80$, and tend to assume inverted C shape, with respect to the flow direction. The wall normal extent of these regions increases as they proceed downstream, whereas the magnitude of $\tilde{u}$ within the region decreases. At VR=0.2 the regions of positive and negative $\tilde{v}$ also tend to assume an inverted C shape, just like the $\tilde{u}$ regions. However, these regions appear to be more extended in the wall normal direction with respect to the case with VR=0.1. In this case an anti-correlation between $\tilde{u}$ and $\tilde{v}$ is also observed.

In Figure 6.33 the $\tilde{u}$-contour and $\tilde{v}$ maps at VR=0.3 and f^+=0.072 are shown. The $\tilde{u}$-contour maps are similar to those in the case with VR=0.2, but the magnitude of $\tilde{u}$ is greater. Note that the regions of positive and negative $\tilde{v}$ are also more intense.

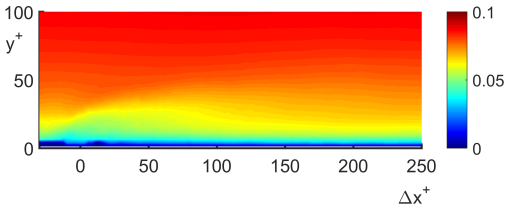

(a) $\bar{u}$ mean

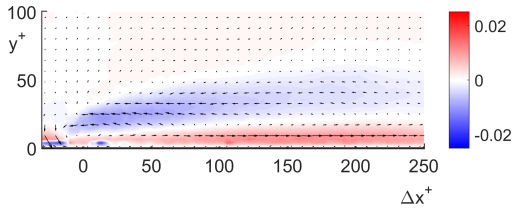

(b) $u_{\bar{SUB}}$ mean

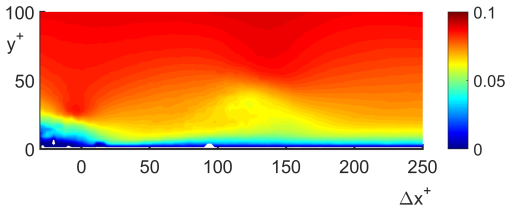

(c) $< u > \Phi = 0°$

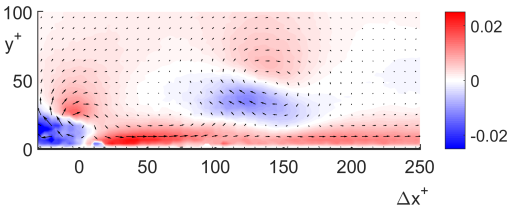

(d) $< u_{SUB} > \Phi = 0°$

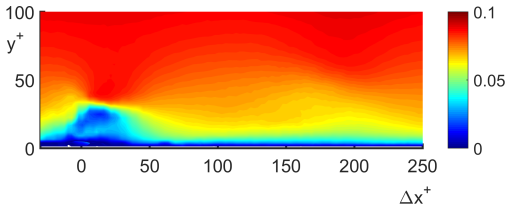

(e) $< u > \Phi = 90°$

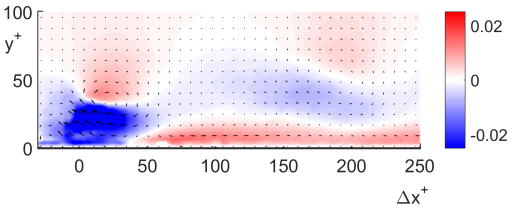

(f) $< u_{SUB} > \Phi = 90°$

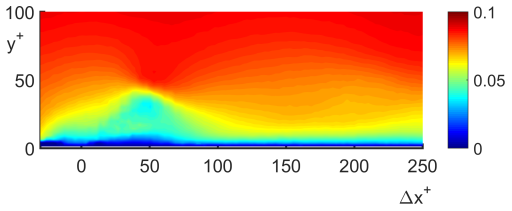

(g) $< u > \Phi = 180°$

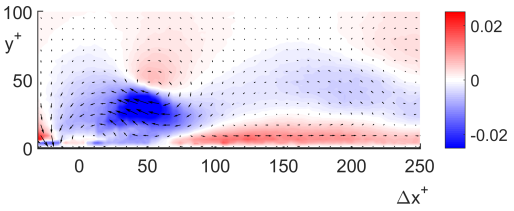

(h) $< u_{SUB} > \Phi = 180°$

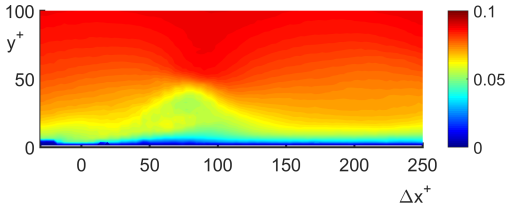

(i) $< u > \Phi = 270°$

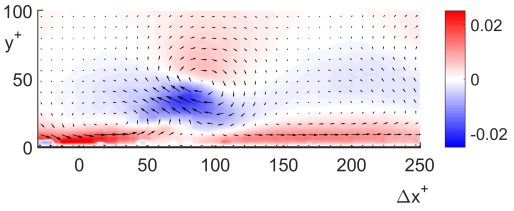

(j) $< u_{SUB} > \Phi = 270°$

Figure 6.30: Mean $\bar{u}$ and phase-locked averaged $< u >$ and $< u_{SUB} >$ contour maps at f^+=0.072 VR=0.30, different Φ

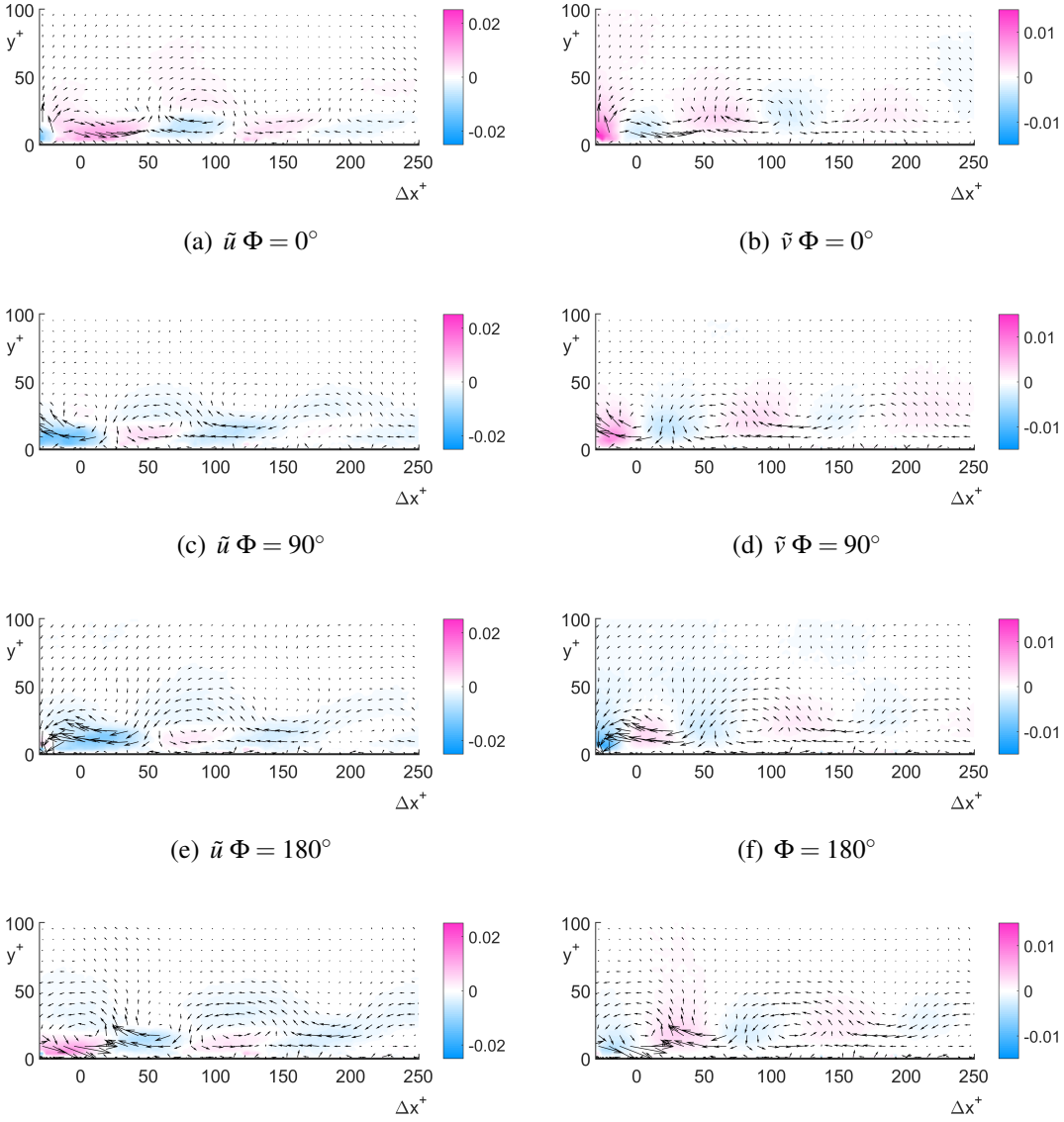

(a) $\tilde{u}$ $\Phi = 0°$ (b) $\tilde{v}$ $\Phi = 0°$

(c) $\tilde{u}$ $\Phi = 90°$ (d) $\tilde{v}$ $\Phi = 90°$

(e) $\tilde{u}$ $\Phi = 180°$ (f) $\Phi = 180°$

(g) $\tilde{u}$ $\Phi = 270°$ (h) $\tilde{v}$ $\Phi = 270°$

Figure 6.31: $\tilde{u}$ and $\tilde{v}$ contours on the centre-plane f^+=0.072 VR=0.10, different phases

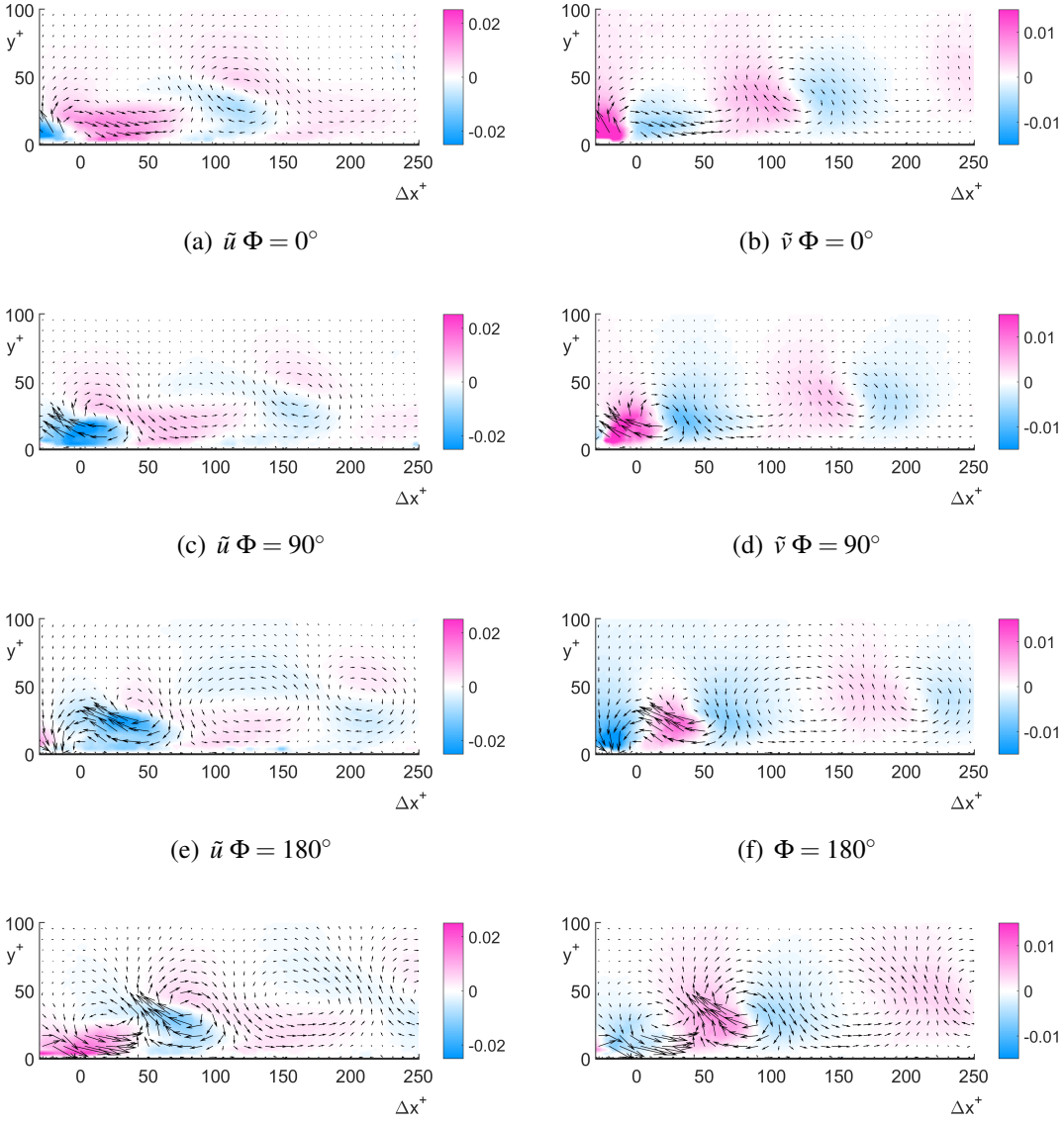

(a) $\tilde{u}$ $\Phi = 0°$ (b) $\tilde{v}$ $\Phi = 0°$

(c) $\tilde{u}$ $\Phi = 90°$ (d) $\tilde{v}$ $\Phi = 90°$

(e) $\tilde{u}$ $\Phi = 180°$ (f) $\Phi = 180°$

(g) $\tilde{u}$ $\Phi = 270°$ (h) $\tilde{v}$ $\Phi = 270°$

Figure 6.32: $\tilde{u}$ and $\tilde{v}$ contours on the centre-plane f^+=0.072 VR=0.20, different phases

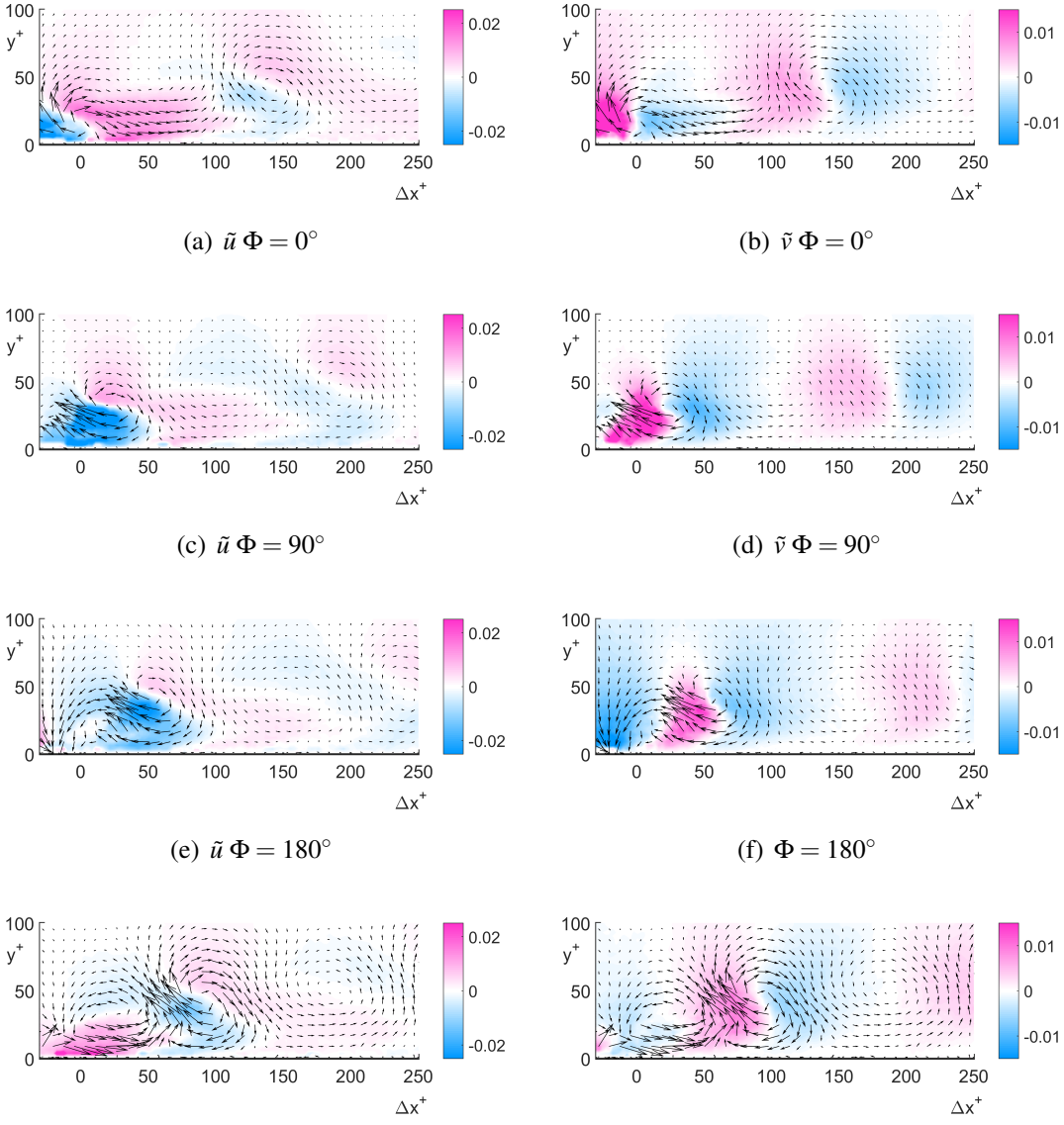

(a) $\tilde{u}$ $\Phi = 0°$ (b) $\tilde{v}$ $\Phi = 0°$

(c) $\tilde{u}$ $\Phi = 90°$ (d) $\tilde{v}$ $\Phi = 90°$

(e) $\tilde{u}$ $\Phi = 180°$ (f) $\Phi = 180°$

(g) $\tilde{u}$ $\Phi = 270°$ (h) $\tilde{v}$ $\Phi = 270°$

Figure 6.33: $\tilde{u}$ and $\tilde{v}$ contours on the centre-plane f^+=0.072 VR=0.30, different phases

6.5.3 Skin Friction Streamwise Variation at Different Phases

The variation of skin friction coefficient with Δx^+ is calculated using the viscous sublayer estimation method described in Section 3.5.4 at different phases. The results for the case in which the synthetic jets are operated at f^+=0.072 and VR=0.1 are shown in Figure 6.34. The skin friction coefficient variation estimated from the mean velocity field is plotted as well as that from the unforced turbulent boundary layer case. The

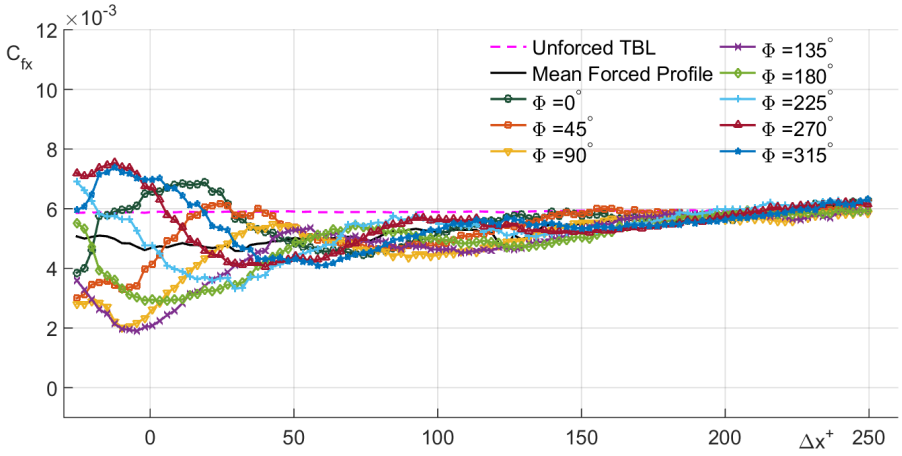

Figure 6.34: Variation of C_{fx} as a function of Δx^+ at f^+=0.072 and VR=0.10 at all phases

skin friction coefficient at each phase exhibits an oscillatory behaviour in the streamwise direction around the value of the skin friction of the mean field. The amplitude of the oscillation decreases with Δx^+ and converges at zero at $\Delta x^+ = 200$. The shape of the skin friction variation with Δx^+ is observed to vary periodically within the period of oscillation of the synthetic jet diaphragm. The phase at which the skin friction presents the minimum value is $\Phi = 135°$ and the maximum skin friction reduction occurs very close the synthetic jet orifice, at $\Delta x^+ \approx 0$. This value is different from the location of the minimum of the skin friction coefficient in mean forced profile, which is about Δx^+=40.

The case in which the synthetic jets are operated at f^+=0.072 and VR=0.3 is shown in Figure 6.35. In this case, the amplitude of the oscillation is larger than the case with VR=0.1 and extends up to $\Delta x^+ = 150$. In addition the oscillatory behaviour of the skin friction coefficient in the streamwise direction appears limited to the region upstream of Δx^+100, unlike the case with VR=0.1 in which the oscillatory behaviour is observed

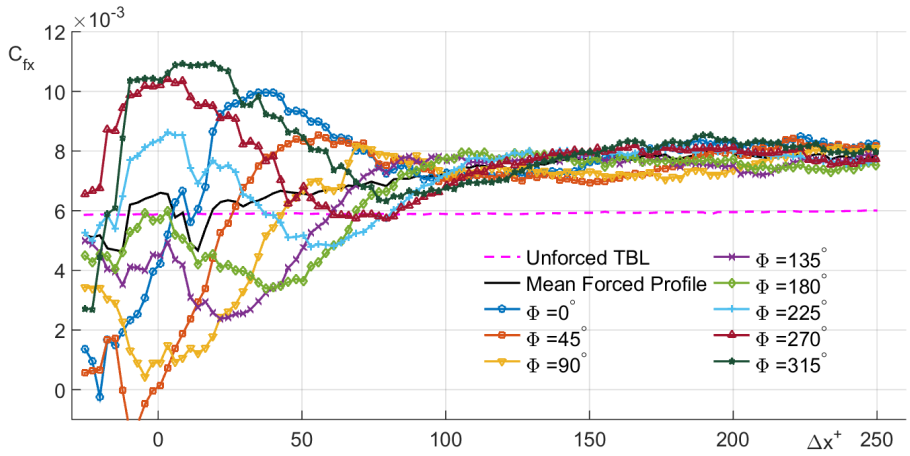

Figure 6.35: Variation of C_{fx} as a function of Δx^+ at f^+=0.072 and VR=0.30 at all phases

up to $\Delta x^+ = 200$.

The variation of skin friction with Δx at each phase can be compared to phase-locked averaged velocity field. The velocity field corresponding to the unforced turbulent boundary layer case is subtracted from each phase-locked velocity field also in this case, to highlight the difference from the unforced case.

The case in which the synthetic jets are operated at f^+=0.072 and VR=0.1 is shown in Figure 6.36. Two phases are shown, $\Phi = 0^\circ$ and $\Phi = 180^\circ$. As expected, the skin friction variation is strongly related to velocity in the near-wall region. Near the wall a series of regions of lower velocity appear and propagate downstream, when compared with the unforced case. The lower the velocity in these regions, the lower the skin friction coefficient. The skin friction becomes similar to the unforced boundary layer value in the regions where the velocity is approximately the same as in the unforced case (white regions in the contour maps). In both phases, after $\Delta x^+ = 200$ the intensity of the lower velocity regions is very low, and the skin friction value does not appear to vary any more with Δx^+, maintaining the value of the unforced turbulent boundary layer.

The case in which the synthetic jets are operated at f^+=0.072 and VR=0.3 is shown in Figure 6.37. In this case, after $\Delta x^+ = 50$ a steady regions of higher velocity compared to the unforced case is present at both phases. This results in a higher skin friction

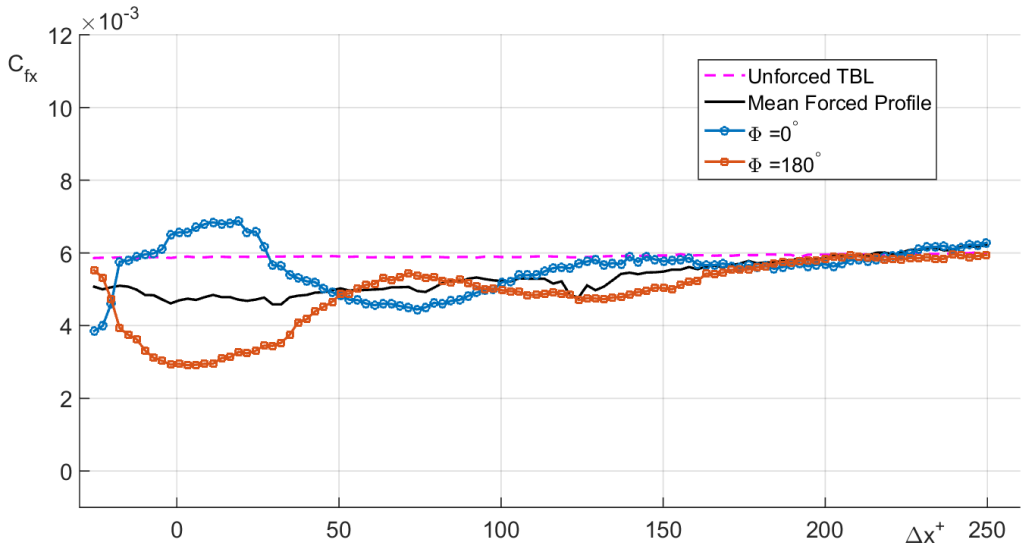

(a) Skin friction coefficient trend $\Phi = 0°$ and $\Phi = 180°$

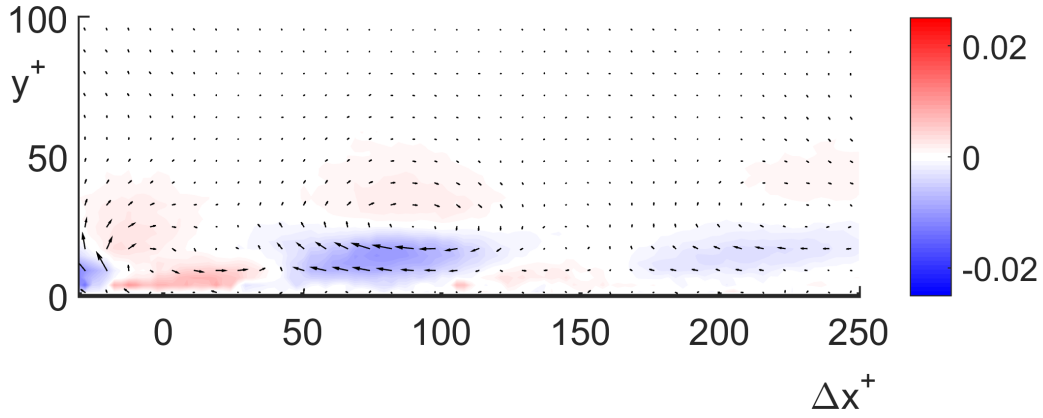

(b) $< u_{SUB} >$-contour map at $\Phi = 0°$

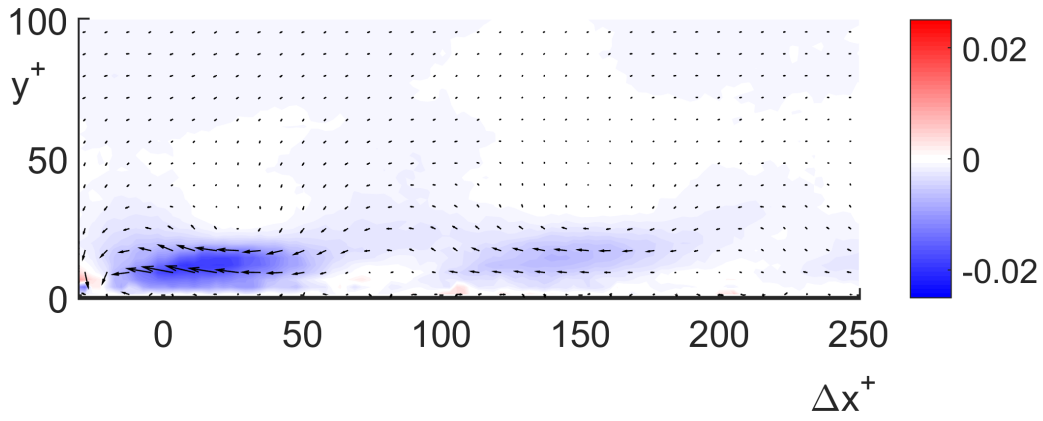

(c) $< u_{SUB} >$-contour map at $\Phi = 180°$

Figure 6.36: Comparison $< u_{SUB} >$-contour map and streamwise skin friction variation at VR=0.10 and f^+=0.072, two phases shown

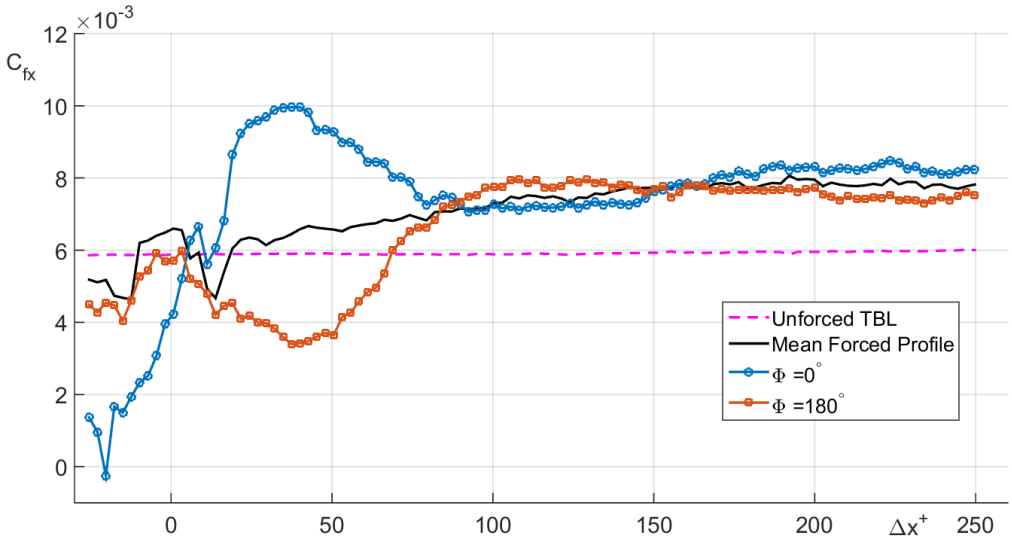

(a) Skin friction coefficient trend $\Phi = 0°$ and $\Phi = 180°$

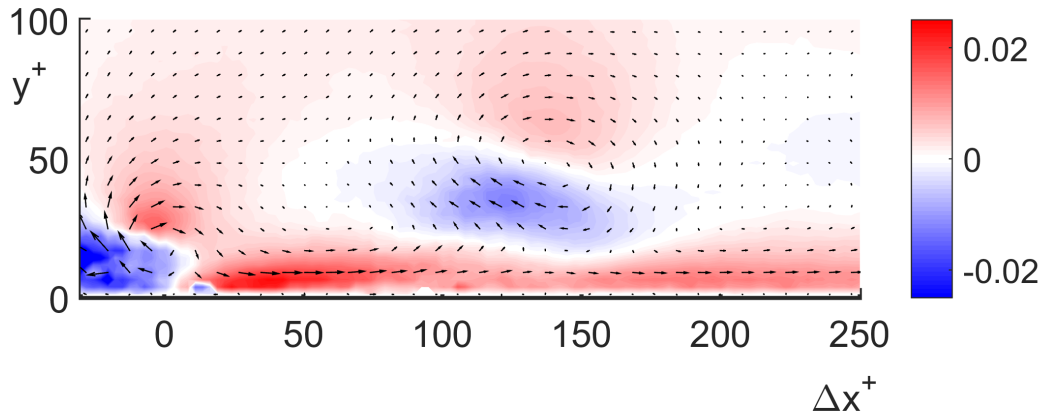

(b) $< u_{SUB} >$-contour map at $\Phi = 0°$

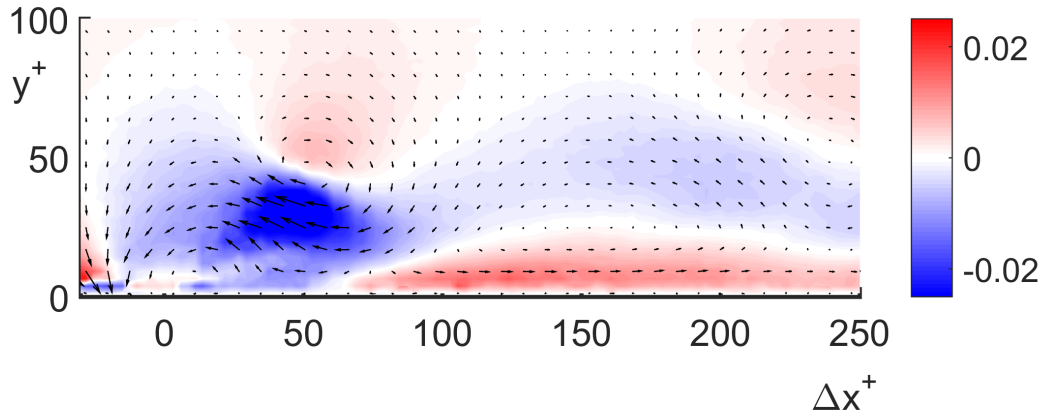

(c) $< u_{SUB} >$-contour map at $\Phi = 180°$

Figure 6.37: Comparison $< u_{SUB} >$-contour map and streamwise skin friction variation at VR=0.30 and f^+=0.072, two phases shown

coefficient then the unforced turbulent boundary layer. The oscillatory behaviour of the skin friction coefficient with Δx^+ is therefore confined to the region upstream of $\Delta x^+ = 180$. The great skin friction reduction at $\Phi = 0°$ at $0 < \Delta x^+ < 50$ is due to the corresponding intense region of lower velocity. At $\Phi = 180°$ in the same region a higher velocity and, therefore, a higher skin friction coefficient is observed.

6.5.4 Turbulence Statistics

The statistics of the velocity components and the Reynolds shear stress component can be computed from the random part of the velocity field, obtained using the triple decomposition. The u_{RMS}, v_{RMS} and $-\overline{u'v'}$ profiles, defined in Section 3.5.5, are calculated at $\Delta x^+ = 100$, i.e. inside the region of drag reduction present when the synthetic jets are operated at VR=0.1, and at $\Delta x^+ = 200$, downstream of the region of drag reduction.

u^+_{RMS} profiles at $\Delta x^+ = 100$ at VR=0.1, 0.2 and 0.3 are shown in Figure 6.38. The

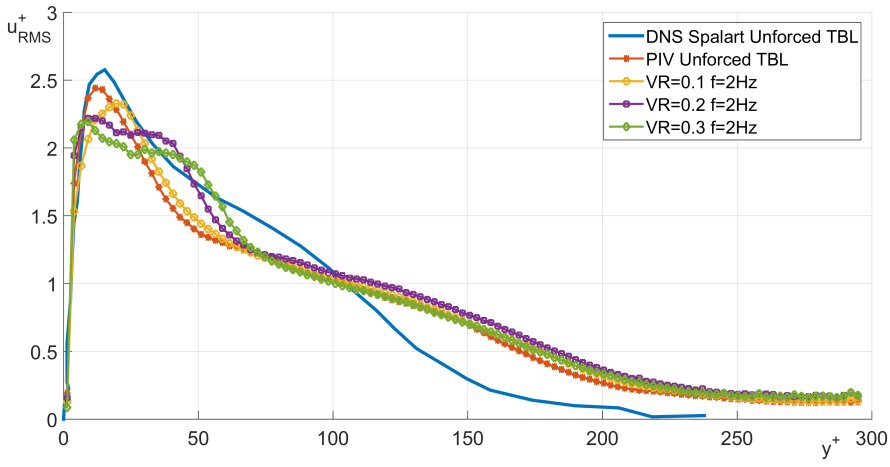

Figure 6.38: u_{RMS} profile in wall units for f^+=0.072 and $\Delta x^+ = 100$

profiles are also compared with the DNS results by Spalart [141] and the profile obtained in the unforced turbulent boundary layer. It is possible to notice a difference between the u^+_{RMS} profile obtained with PIV in the unforced turbulent boundary layer and the results of the DNS by Spalart. The reason behind this discrepancy has not been clarified yet. An explanation could be the presence of a slightly negative pressure gradient, as already outlined in Section 5.1. Observing the results of [51] in presence of a

negative pressure gradient the flow becomes slightly more 'stable' and this reduces the level of velocity fluctuations across the whole boundary layer. However, in the present case the u^+_{RMS} values result lower than the DNS profile only below y^+=100. Above that, the u^+_{RMS} profile is higher. This trend is also observed in the cases of forced turbulent boundary layer. This fact cannot be explained only by assuming the presence of a negative pressure gradient. Probably other factors play a role, such as a possible too large size of the tripping rod and the presence of three-dimensional disturbances originating from the side walls of the water flume. More detailed experiments to clarify this point are strongly recommended as future work. Observing the forced boundary layer u^+_{RMS} profiles, the typical peak present at the edge of the buffer layer at $y^+ = 12$ in the the unforced turbulent boundary layer is observed to have slightly moved away from the wall at $y^+ = 22$ in the case with VR=0.1. The value of the peak is slightly lower, u^+_{RMS}=2.3 compared to 2.45 in the unforced turbulent boundary layer. This result can be interpreted as an increase in the viscous sublayer thickness and as a slight reduction of the turbulence production in the buffer layer. However, further verifications are needed to prove this point. In the cases with VR=0.2 and VR=0.3 the u^+_{RMS} value at the peak is reduced to u^+_{RMS}=2.15, but the peak appears to be located closer to the wall, at $y^+ \approx$ 8-10. In addition, the value of the fluctuations is higher than the unforced turbulent boundary layer up to $y^+ \approx 70$ in both cases, and a secondary peak is observed at $y^+ = 40$ at VR=0.2 and $y^+ = 50$ at VR=0.3. Therefore, in these last cases the boundary layer forcing appears to enhance the velocity fluctuations especially in the region above the buffer layer.

The u^+_{RMS} profiles at $\Delta x^+ = 200$ are shown in Figure 6.39. It can be observed that at $\Delta x^+ = 200$ the peak at the edge of the buffer layer is reduced to a value of u^+_{RMS}=2.25 and is located at $y^+ = 17$ i.e. slightly farther from the wall than in the case of an unforced turbulent boundary layer. In the cases with VR=0.2 and VR=0.3 the peak value of u^+_{RMS} is further reduced in intensity down to u^+_{RMS}=2.15, but it is also closer to the wall, at $y^+ = 7-8$. The secondary peak appears at about $y^+ = 50$, but it is reduced with respect to the case at $\Delta x^+ = 100$ (u^+_{RMS}=1.7).

The v_{RMS} profiles at $\Delta x^+ = 100$ are shown in Figure 6.40. Considerations regarding the discrepancy between the present v_{RMS} and that obtained in [141] are similar to those about the u_{RMS} profile. The v_{RMS} profile shape at VR=0.1 is very similar to that of the unforced turbulent boundary layer. The profile presents a maximum value of

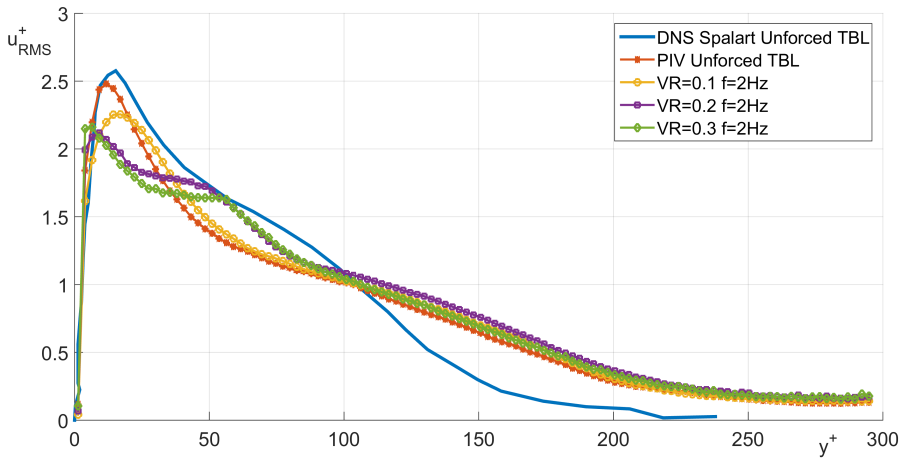

Figure 6.39: u_{RMS} profile in wall units for f^+=0.072 and $\Delta x^+ = 200$

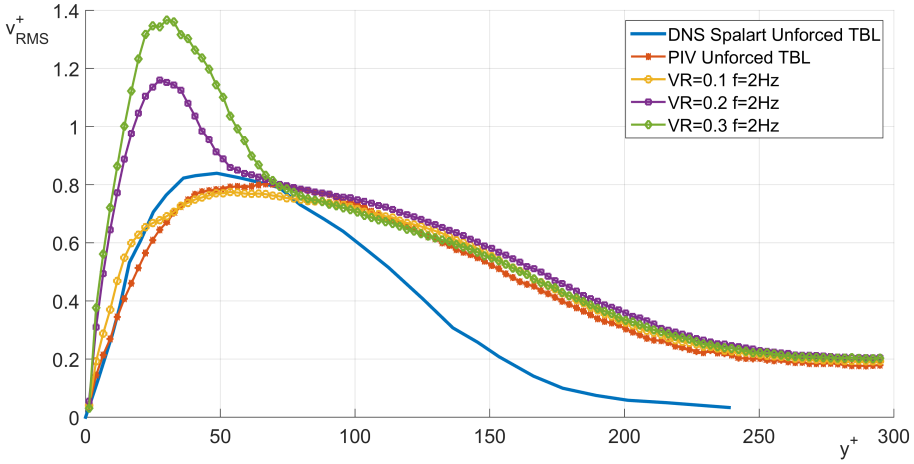

Figure 6.40: v_{RMS} profile in wall units for f^+=0.072 and $\Delta x^+ = 100$

v^+_{RMS}=0.8 for $y^+ \approx 60$. In the cases with VR=0.2 and VR=0.3 a strong fluctuation peak is observed at $y^+ \approx 30$, at which v^+_{RMS}=1.05 for VR=0.2 and v^+_{RMS}=1.35 for VR=0.3.

The v_{RMS} profiles at $\Delta x^+ = 200$ are shown in Figure 6.41. In this case the v_{RMS} pro-

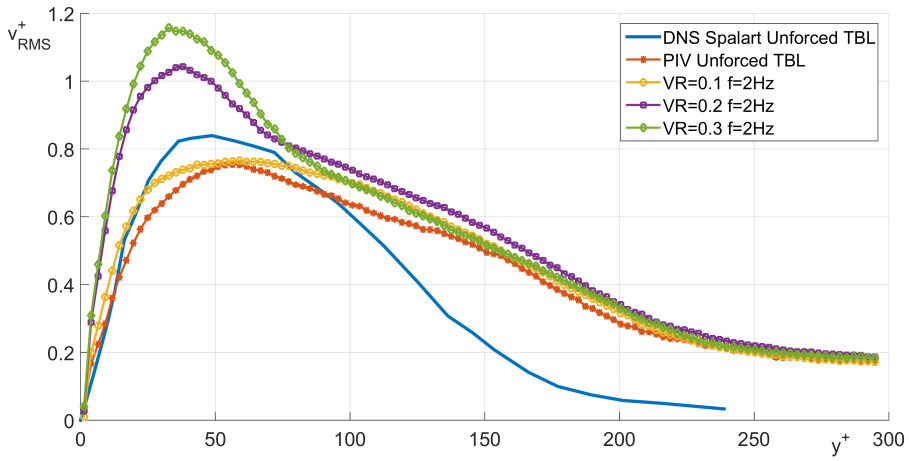

Figure 6.41: v_{RMS} profile in wall units for f^+=0.072 and $\Delta x^+ = 200$

file has substantially recovered to the shape of the unforced turbulent boundary layer profile in the case with VR=0.1. In the cases with VR=0.2 and VR=0.3 the strongest peaks at $y^+ \approx 30-40$ are still present, but they are lower than at $\Delta x^+ = 100$, their value being 1.05 and 1.15 at VR=0.2 and VR=0.3 respectively .

Finally, the mean value of Reynolds stress $-\overline{u'v'}$ is estimated. Its negative value, normalised in wall units, is shown in Figure 6.42 for the cases with f^+=0.072 and a distance $\Delta x^+ = 100$ from the synthetic jet orifice. Considerations regarding the discrepancy between the present $-\overline{u'v'}$ profile and that obtained in [141] are similar to those about the u_{RMS} and v_{RMS} profiles. At VR=0.1 a peak of $\overline{u'v'}^+ = 0.67$ at $y^+ = 23$ appears, higher then the corresponding peak observed in the $\overline{u'v'}^+$ profile of the unforced case ($\overline{u'v'}^+$=0.57). However, the area below the $\overline{u'v'}^+$ curve seems equal or slightly smaller than that under the curve in the unforced turbulent boundary layer. According to the Fukagata identity, Equation (2.39), this means that the skin friction coefficient is either equal or lower than that of the unforced turbulent boundary layer. This is in agreement with the skin friction coefficients values estimated and reported in Section 6.3.3. At VR=0.2 and VR=0.3 the peak appears to be located farther away from the wall at $y^+ \approx 35$, at which $\overline{u'v'}^+ \approx 1$. In these cases, the area under the $\overline{u'v'}^+$

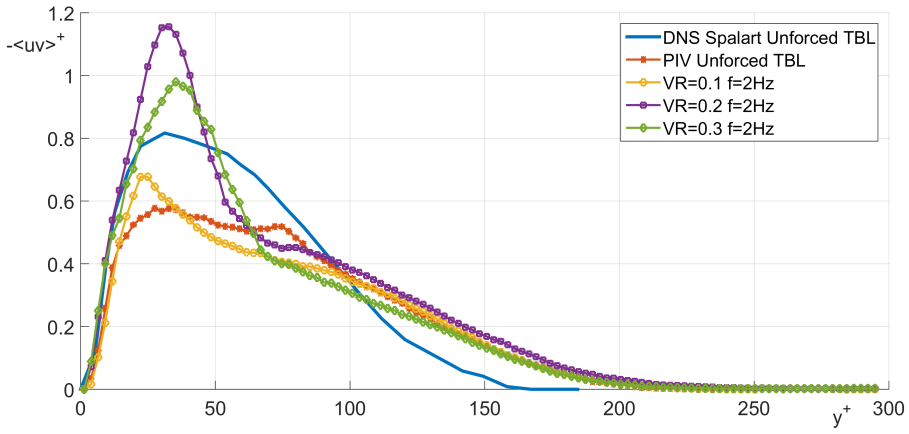

Figure 6.42: Reynolds shear stress $-\overline{u'v'}$ profile in wall units for f^+=0.072 and $\Delta x^+ = 100$

profiles is surely larger than in the case of the unforced boundary layer, so according to the Fukagata identity the skin friction coefficient is higher. Results are in agreement again with those described in Section 6.3.3.

The Reynolds shear stress at $\Delta x^+ = 200$ is shown in Figure 6.43. For all the test

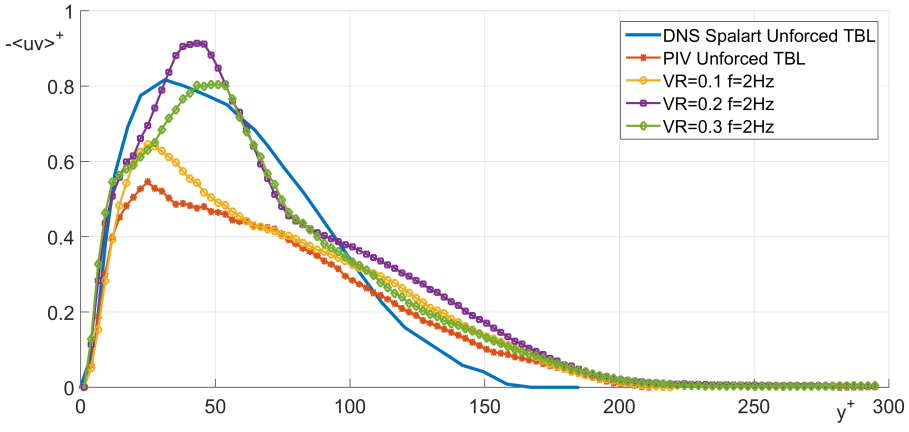

Figure 6.43: Reynolds shear stress $-\overline{u'v'}$ profile in wall units for f^+=0.072 and $\Delta x^+ = 200$

conditions here the Reynolds stress peaks observed at $\Delta x^+ = 100$ are still present, but they appear to be located farther away from the wall. Their magnitude is lower than at $\Delta x^+ = 100$. In all cases an increase in the Reynolds shear stress is observed across the whole boundary layer, so an increase in the skin friction coefficient is expected

according to the Fukagata identity. This result is again in agreement with the results described in Section 6.3.3.

6.6 Physical Explanation of Drag Reduction

Given the results presented in this chapter, it is possible to propose a physical model that is able to explain the local drag reduction or increase observed. Two typical cases will be illustrated, one representing drag reduction in the centre-plane (at VR=0.1 or lower), the other representing drag increase (at VR=0.2 or higher).

In the first case, which is achieved when the synthetic jet array is operated at at VR=0.1 or lower, a diagram reporting the coherent structures expected to be produced by the synthetic jet array is shown in Figure 6.44. The whole array of synthetic jets is drawn, but for simplicity only the coherent structures produced by the central jet and by the two adjacent ones are shown. The flow field is symmetric about the centre-plane and is periodic in the spanwise direction, up to the extend of the synthetic jet array. As

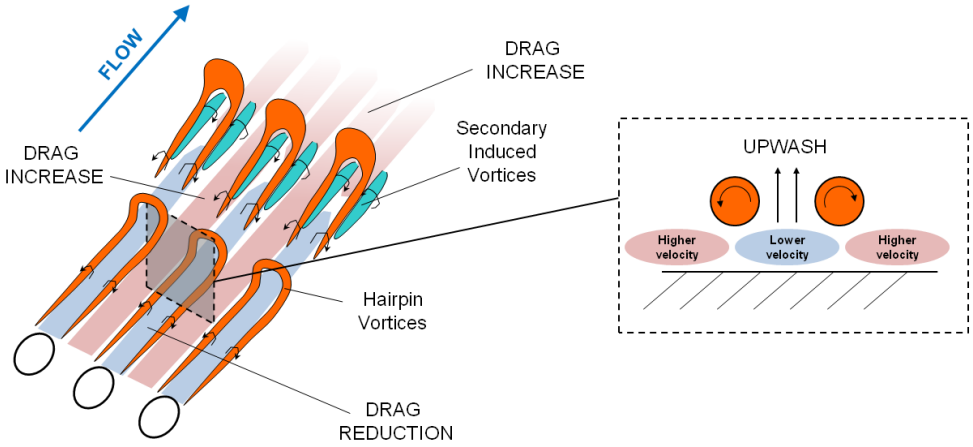

Figure 6.44: Diagram explaining drag reduction/increase effects for the cases VR=0.1 and lower

described in Section 2.4, at low velocity ratios, the synthetic jets are expected to generate hairpin vortices. The presence of hairpin vortices in the flow field is compatible with the $\tilde{u}$ and $\tilde{v}$ velocity contour maps shown in Figure 6.31. If VR=0.1 or lower and L is not significantly high, the hairpin vortices are expected to be quite weak and to travel along a trajectory very close to the wall. A hairpin vortex induces a region of

lower streamwise velocity in between its legs, with respect to the case of an unforced boundary layer. In this region the fluid experiences an up-wash, and low momentum fluid is brought upwards, giving rise to a region of reduced streamwise velocity and increased wall-normal velocity. This mechanism is also detailed in the cross-section view in Figure 6.31 on the right and explains the travelling regions of lower velocity observed in centre-plane downstream of the synthetic jet orifice and up to $\Delta x^+ = 200$, shown in in Figure 6.31. These regions are believed to be associated with the interior of the travelling hairpin vortices. An averaged reduction of lower velocity is found in the mean streamwise velocity field of the forced turbulent boundary layer cases with VR=0.1 or lower. In turbulent boundary layers, as described in Section 2.4.3, two secondary and quasi-stationary vortices are also observed near a hairpin vortex. These vortices are believed to be located just underneath the hairpin vortex legs in at turbulent flow. The presence of such vortices has also been confirmed in the numerical simulations by Tang [158] and in the experiments by Zhang and Zhong [166, 171]. At VR=0.1 the streamwise vortices do not appear to form immediately in the region just downstream of the orifice, because in this region the hairpin vortices are very close to the wall. These vortices seem to appear when the hairpin vortex has travelled a sufficient distance away from the wall. The streamwise vortices create a down-wash in the region in between them, which results in a higher streamwise velocity and lower wall-normal velocity. This region is observed in the centre-plane downstream of Δx^+=200 (see again Figure 6.31). If the streamwise velocity near the wall is lower than the value in an unforced turbulent boundary layer, a skin friction drag reduction is achieved, as the gradient of streamwise velocity is expected to be lower and the wall shear stress is expressed as $\tau_w = \mu \frac{\partial \bar{u}}{\partial y}$ (see also Section 2.1.5). On the contrary, if the streamwise velocity near the wall is higher, a skin friction drag increase is achieved, as the gradient of streamwise velocity is expected to be higher. This may explain the skin friction variation in the centre-plane with Δx^+ observed at VR=0.1 or lower.

In the region between two orifices, as shown in Figure 6.44, the hairpin vortex legs of two adjacent hairpin vortices are believed to create instead a down-wash, which causes a local increase of local streamwise velocity with respect to the unforced case. This explains the velocity increase observed in the off-centred planes at VR=0.1, described in Section 6.4. The down-wash is expected to be reduced if the spacing between of two adjacent orifice is increased. Given these two effects, downstream of Δx^+= 200 a region of drag increase appears at VR=0.1, as shown in Figure 6.24. It is expected that at a certain distance downstream, away from the investigation area, the flow recovers

the characteristics of an unforced turbulent boundary layer.

The situation in the case of higher velocity ratios, VR=0.2 or higher, is illustrated in Figure 6.45. In this case, as results of the higher VR, the hairpin vortices tend to leave

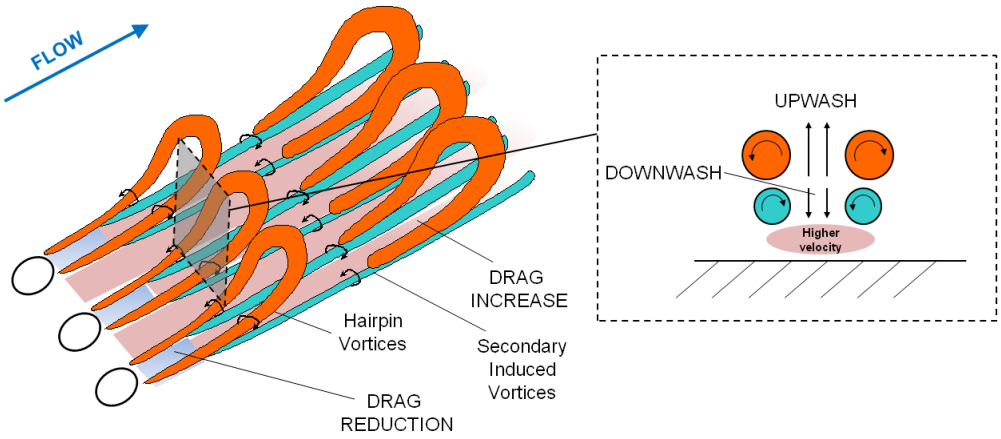

Figure 6.45: Diagram explaining drag reduction/increase effects for the cases VR=0.2 and higher

the near-wall region after a short distance downstream of the orifice. Underneath the hairpin legs almost immediately the two secondary streamwise vortices form, which appear to be intense and quite persistent downstream. These vortices are believed to be the reason for the stationary region of higher velocity observed in the centre-plane at VR=0.2 and VR=0.3 in Figure 6.32 and 6.33. The situation is also illustrated in Figure 6.45, in the cross-section on the right. In the region between two orifices, a downwash effect due to the combined effects of two adjacent streamwise vortices produced by two adjacent synthetic jets, would be expected. However, the PIV measurements in the off-centred planes report an increase of streamwise velocity with respect to the unforced case, across the whole boundary layer (see figures 6.17 and 6.18). The mechanism of interaction between the streamwise vortices produced by adjacent synthetic jets therefore does not appear to be completely understood and further experiments are required to clarify this point. It is anticipated that the increase in skin friction may be caused by the merging of the vortices.

6.7 Liquid Visualisation of Turbulent Boundary Layer Forcing with a Synthetic Jet Array

Flow visualisations using liquid crystals are also performed. The experimental rig used is the same used for the experiments in Section 3.4. Experiments are still carried out in a turbulent boundary layer developing on a flat plate at a free-stream velocity of 0.1 m/s. In this case the synthetic jet array is installed on a round cavity. The synthetic jet array is composed of five circular orifices of diameter 5 mm each, spaced 9 mm. The objective of these experiments is to assess if the synthetic jets modifies the footprints of the streamwise streaks and of the near-wall coherent structures.

In figure 6.46 a snapshot of the flow field with no synthetic jets is shown. The origin of the coordinate system is in the centre of the synthetic jet orifice in the middle. The coordinates are normalised in wall units. The flow is moving from the bottom to the top of the figure. The five synthetic jet orifices do not seem to alter the flow down-

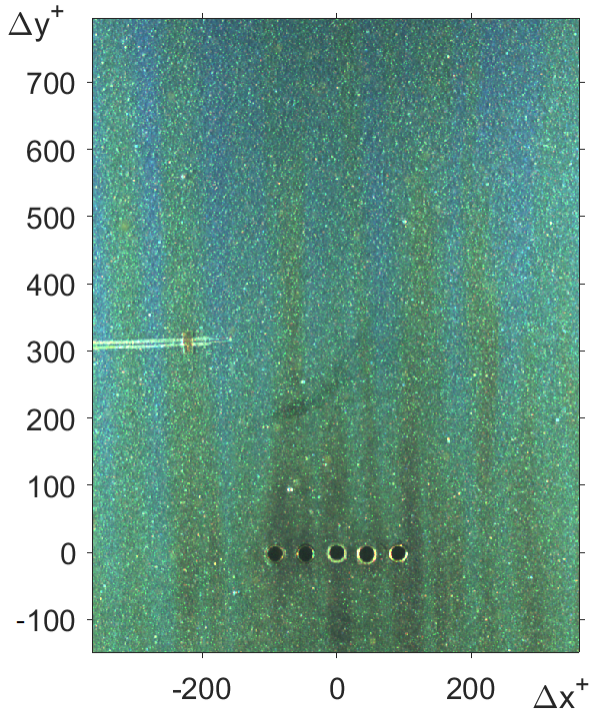

Figure 6.46: Liquid crystal image of a turbulent boundary layer, without synthetic jets

stream when switched off. The footprints of the streamwise streaks are visible in the liquid crystal coating as regions of different colours.

The PIV experimental campaign in the previous sections revealed that the velocity ratio is one of the key parameters for drag reduction. Two cases in which synthetic jets are operated at the same frequency and at different VR, namely VR=0.1 and VR=0.2 are shown in Figure 6.47. The case with VR=0.1 shows that the synthetic jets modify

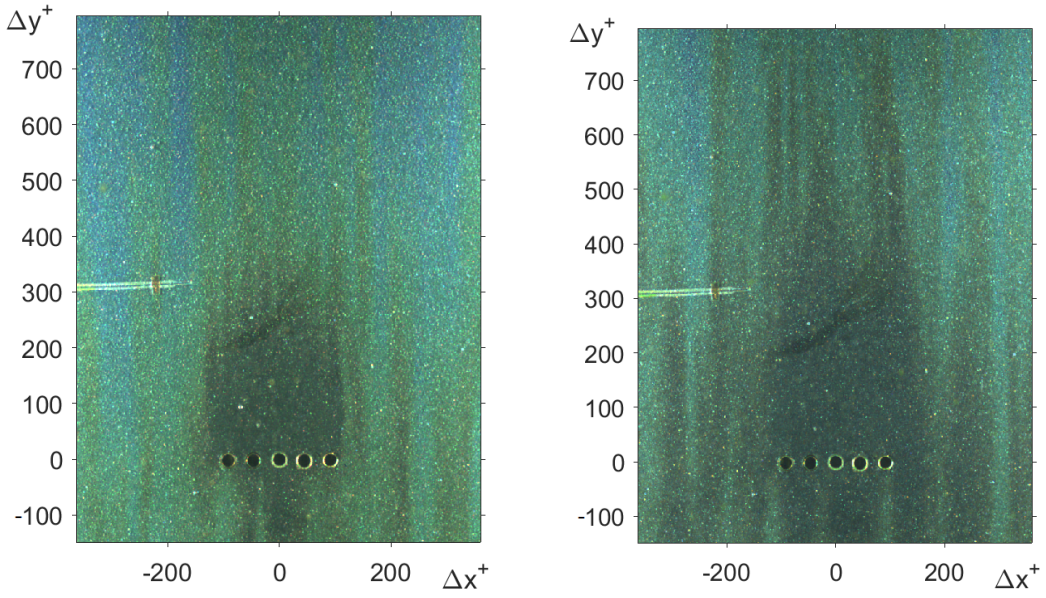

(a) VR=0.10 f^+=0.072 L=1.1 (b) VR=0.20 f^+=0.072 L=1.7

Figure 6.47: Liquid crystal colour maps with synthetic jets operating at f^+=0.072 and VR=0.10 and 0.20

the flow field for a region as far away as Δx^+=300 downstream of the synthetic jet array. Then the effects of the forcing appears to disappear and the streaky pattern recovers the characteristics of an unforced turbulent boundary layer. This is in agreement with the results obtained with the PIV experiments. In the case in which the synthetic jets are operated at VR=0.2 the disturbance seems to be more extended in the streamwise direction, at least up to Δx^+=500. This is also in agreement with results of the PIV experiments, where it is observed that for VR $>$ 0.2 the flow does not recover the characteristics of an unforced turbulent boundary layer within the streamwise extent of the investigation area, which is Δx^+=250.

The presence of an area in which the liquid crystal colour is closer to the red part of the colour spectrum suggests that the local temperature in the region downstream of the synthetic jet array is lower, and so the heat transfer coefficient and, for Reynolds

analogy, the skin friction coefficient are higher. This is visible in both the cases with VR=0.1 and VR=0.2. The overall increase in the skin friction coefficient is also in agreement with the results obtained with Particle Image Velocimetry at different planes. The increase in temperature and in skin friction seems higher in the case with VR=0.2. The regions of lower skin friction in the regions just downstream of the single synthetic jet orifices do not appear clearly in the liquid crystal map at VR=0.1. The reason for this is believed to be the low spatial resolution of the liquid crystal map, which is not able to capture too narrow and localised temperature variations.

If one wants to visualise the presence of those regions region, the liquid crystal rig needs to be improved. A thinner polystyrene and Aluminium sheet are expected to decrease the overall thermal inertia of the liquid crystal plate, hence they should also allow the visualisation of narrow regions of temperature changes.

6.8 Summary of Findings and Future Work

In this chapter the effects of forcing a turbulent boundary layer with a synthetic jet actuator is analysed by Particle Image Velocimetry (PIV). The synthetic jet array is designed to produce artificial coherent structures (in particular, hairpin vortices) of the same scale as the natural near-wall coherent structures present in the near-wall region of the turbulent boundary layer. It is found that the forcing creates regions of alternate higher and lower velocity within the boundary layer, with respect to the unforced case. In the regions where a lower velocity is observed in the near-wall region, a skin friction drag reduction compared to the case of an unforced turbulent boundary layer is found, whereas in the regions of higher velocity, a skin friction drag increase is found.

The analysis of the flow in the centre-plane, passing through the centre of the central orifice of the array, revealed that the the most important parameter which determines the capability of synthetic jet to produce regions of skin friction drag reduction is the velocity ratio VR. If the synthetic jets are operated at VR=0.1 or lower, a skin friction drag reduction regions is observed in the region downstream of the synthetic jet orifice, as a result of the appearance of a lower mean velocity region in the near-wall. This region is believed to be induced by the legs of a train of hairpin vortices generated by the synthetic jets, which remain very close to the wall for a significant distance downstream of the orifice, about Δx^+=200.

This is also confirmed by the observation of the phase-locked averaged velocity fields, which show a series of regions of lower velocity near the wall. These regions are observed to travel downstream at different phases analysed within the period of oscillation of the diaphragm. The regions are believed to be induced by the legs of the hairpin vortices, while they travel downstream and away from the wall.
In correspondence of these regions the analysis of the velocity fluctuations u_{RMS}, v_{RMS} and of the Reynolds shear stress $\overline{u'v'}$ suggests a possible reduction of the turbulence production activities as well as a slight increase of the viscous sublayer thickness. However not enough evidence is reached to conclude this. Further measurements, involving probes with higher frequency response could help to clarify this point.

If the synthetic jets are operated at VR=0.2 or higher, the regions of lower velocity in the mean velocity field are shifted away from the wall. In the near-wall region a region of higher mean velocity is observed, which corresponds to a region of skin friction drag increase.
The analysis of the phase-locked averaged velocity fields revealed that the region of higher velocity in the near-wall is steady at $\Delta x^+ > 50$, whereas the region of lower mean velocity is caused by a series of lower velocity regions which are observed to travel above it within the period of oscillation. This pattern is due to the fact that the hairpin vortices tend to leave the near-wall region immediately. In addition, two counter-rotating streamwise vortices form just underneath them, which produce a down-wash in centre-plane, and therefore an increase in the streamwise velocity.
Statistical analyses reveal that all the statistics, including mean velocity, fluctuating velocity and Reynolds shear stresses increase near the wall.

The analysis of the flow in off-centred planes, in between two adjacent orifices in the array, revealed the presence of a region of higher velocity and of increased skin friction compared to the unforced case. It is believed that this region could be caused by the merging of two adjacent hairpins or two adjacent induced streamwise vortices, but further analyses are required to conclude this.
The analysis of the flow field with PIV at different planes allowed an estimation of the total skin friction drag in the area in-between two adjacent orifices. It is found that in no case, even at VR=0.1, a total skin friction drag reduction is achieved. In the best case, which is at VR=0.1, a drag increase of about 12% with respect to the unforced turbulent boundary layer is estimated. It is believed that an overall skin friction drag

reduction can be achieved with a slight modification of the array geometry. For example, if the spacing of two adjacent orifices is increased, the drag increase in the region in-between the orifices could be mitigated, as the merging of two adjacent streamwise vortices could be reduced. Also the use of inclined or skewed synthetic jets could provide benefits, as the hairpin vortices in this case are expected to travel close to the wall for a longer distance downstream. This should extend the regions of skin friction drag reduction.

Preliminary flow visualisation on a liquid crystal coating reveal the presence of a large region of higher temperature downstream of the synthetic jet array. In this region the heat transfer coefficient is higher along with the wall shear stress for Reynolds analogy. This is in agreement with the findings in the PIV experiments. At VR=0.1 the region extends up to Δx^+=300 downstream of the synthetic jet array. At VR=0.2 the region extends up to Δx^+=500. However, the spatial resolution of the technique is not sufficient to show the narrow regions of local lower or higher skin friction inside this large region.

Overall, this study shows the capability of a synthetic jet array (producing vortices at the same scale as the near-wall coherent structures in a turbulent boundary layer) to generate skin friction drag reduction regions. As future work, the author recommends first to investigate the wide design space for the synthetic jet array (involving, for example, the orifice diameter, the spacing between two adjacent orifices, the inclination angle of the jets etc.) by means of a quick flow visualisation technique or by numerical simulations, which should allow the analysis of several configurations in a shorter time than an experimental campaign for low Reynolds number turbulent boundary layers. When the optimal configuration is found, experimental studies can be continued, to investigate the detailed physics of flow and the mechanism by which the drag reduction is achieved. For this purpose the use of Stereo-PIV is surely recommended, given the three-dimensional nature of the flow and the possibility of analysing in detail transversal planes, normal to the flow and to the stream direction.

Chapter 7

Towards the Design of a Feed-Forward Control Strategy of a Turbulent Boundary Layer

7.1 Feed-Forward Control of a Turbulent Boundary Layer

Predetermined flow control in the case of a turbulent boundary layer might not always yield a good performance. This is because it requires the knowledge of the flow properties a priori and thus it is not a very flexible strategy. In general, it is more indicated to use a reactive method, which employs also a few sensors to gather some information on the flow field to be controlled. In this chapter the design of a reactive method using feed-forward control is initiated.

The advantage of feed-forward control is the simplicity of the control strategy. Typically, feed-forward control is preferred to feed-back control in the cases where the behaviour of the system and of the control variable is well understood or can be modelled in a relatively simple way, by means of system identification or a self-learning procedure. This is in contrast with the model of a complicated system such as a turbulent boundary layer, which has to be necessarily approximated to build a relatively simple control procedure. Nevertheless, the results reported in this chapter reveal that sufficiently good results could be achieved even only with one sensor. This is due to a good understanding of the dynamics of a turbulent boundary layer in the near-wall region, as reported in Chapter 2. On the other hand, the disadvantage of feed-forward control is the sensitivity to external disturbances, which is higher than in a feedback

approach.

7.1.1 Principle of Operation

The study presented in this chapter is based on the work of Rathnasingham and Breuer [119, 118, 19, 6] and Knobloch [84]. The control unit they used is shown in Figure 7.1. In this simple configuration, the control system consists of an array of sensors

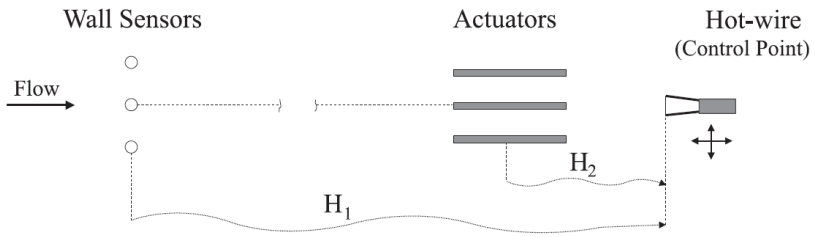

Figure 7.1: Simple schematic of a feed-forward control unit for a turbulent boundary layer (figure taken from [84])

located at a certain location at the wall in a turbulent boundary layer. The points at which the sensors are located are referred to as "sensor points" hereafter. At a certain distance downstream of the sensor array an array of actuators is placed. The "control point" (in which the desired control effects need to be achieved) is located at a certain distance downstream of the actuators, as the actuator disturbances need a certain space to properly develop and also to produce the desired control effects on the flow. The objective of the feed-forward control unit is to achieve a well-defined control objective at the control point. For instance, in the case of the turbulent boundary layer the objective could be to minimise the fluctuations of the velocity or of the wall shear stress at the control point. It is possible to set several control points, in order to provide control benefits over a larger portion of the flow field.

In a feed-forward strategy a self-learning control strategy based on a *system identification* approach is typically used. In the design phase, signals at the sensor points and at the control points are acquired and used to build a system model. In the control phase, however, only the signals at the sensor points are needed. These signals are time series measurements of a flow variable at the sensor points (velocity, wall shear stress etc.). They are used to estimate a certain flow variable at the same time at the control points. This variable does not necessarily have to be of the same type of the variable measured at the sensor points. For example, wall shear stress sensors at the

sensor points can be used to minimise the velocity fluctuations away from the wall at the control points, or vice-versa. The most important requirement to achieve this estimation is to have a certain degree of correlation between the sensor signals and the signals measured at the control point. As shown in Chapter 2, a certain degree of correlation is present between flow variables in a turbulent boundary layer, due to the strong convective character of the near-wall disturbances. Being the position of the control points downstream of the actuators, it is obvious that the signals measured at the control point are affected by the exerted forcing. Therefore in a feed-forward control strategy it is not possible to use the signal at the control points to regulate the actuators. The actuators must be regulated using the estimated signals at the control point in the uncontrolled flow. This information has to be derived only using the information from the signals acquired by the sensors upstream. In this way, for instance, the actuator could produce a complementary disturbance that can suppress or weaken the flow disturbance at the control points and achieve a reduction of the flow variable fluctuation. In a feed-back system applied to the same control unit only the information acquired at the control points is used to regulate the actuators. In this case, no system model needs to be built. The feedback algorithm observes the observed signal change at the control point and uses it to regulate the actuator until the control objective is reached. Consequently the sensors upstream are not needed. In feed-forward control, on the contrary, the signals at the control points downstream are not strictly needed apart from the design phase. However they can be utilised to evaluate the efficiency of the control procedure a posteriori.

Figure 7.1 also indicates that the design of a feed-forward control strategy can be divided into two separate phases: the development of the feed-forward predictor (H_1) and the characterisation of the forcing effect produced by the actuator (H_2):

- the *development of the feed-forward predictor* is the design of an algorithm which is able to estimate, in real-time, the instantaneous value of the signal at the control point based on the instantaneous value of the signals at the sensor points. The term predictor is not entirely appropriate because the output of the routine is not the prediction of the signal in a future instant, rather it is the estimation of the flow variable at the same instant at a point downstream. However, as the fluid moves from upstream to downstream, the term predictor seems to represent well the logic of the process. This step is equivalent to determining the "transfer function" H_1 between the sensor and the control point signals in an unforced

turbulent boundary layer. A conventional approach to achieve this is by using a Wiener filter. However, nowadays other adaptive filters which provide faster performances are also available: one of the most commonly used is the Least Mean Squares (LMS) filter;

- the *impact of the actuator at the control point* has also to be determined. This provides a relationship between the driving voltage of the actuator and the fluctuation of the measured flow variable (velocity, wall shear stress, etc.) at the control point. This step is equivalent to determining the "transfer function" H_2.

The known transfer functions H_1 and H_2 can be combined to derive the driving voltage of the actuators that is able to cancel/weaken the fluctuations of the measured flow variable at the control point.

To summarise, the upstream sensor signals are fed to the feed-forward predictor H_1 which estimates the instantaneous flow variable at some downstream control point in an undisturbed turbulent boundary layer. The output of the feed-forward predictor represents an approximation of the signal at the control point in an uncontrolled boundary layer. This estimated signal is multiplied by the inverse of the transfer function H_2^{-1} to derive the driving voltage to be input to the actuator to produce the opposite of the estimated fluctuation at the control point. This may result in a cancellation, or at least in a weakening, of the fluctuation of the flow variable at the control point, which is in fact the objective of the control.

7.2 Development of the Feed-Forward Predictor

Motivated by the prevalent convective nature of the disturbances in the turbulent boundary layer, Rathnasingham and Breuer [119, 118] developed a feed-forward predictor able to estimate the evolution of a flow variable at a certain point in a flow, only based on measurements performed at one or more points upstream of it. Amonlirdviman and Breuer [6] performed a detailed parametric study to assess the optimal positioning for the sensors in a turbulent boundary layer, using direct numerical simulations. The design of the feedforward predictor was also revisited by Knobloch [84].

It is assumed that the disturbance detected by the sensor in the upstream position moves downstream with the flow. Therefore the flow variable measured downstream should

retain a high degree of correlation with the flow variable measured upstream. A simple feed-forward predictor installed a turbulent boundary layer, with only a sensor point and a control point is shown in Figure 7.2. The objective of the predictor is to recon-

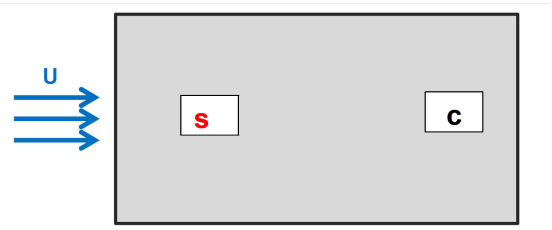

Figure 7.2: Configuration of a SISO feed-forward predictor

struct the instantaneous wall shear stress variation at point C, given the instantaneous the wall shear stress variation at point S. The wall shear stress is influenced, for example, by the passage of a high speed sublayer streak, as shown in Figure 7.3. The passage

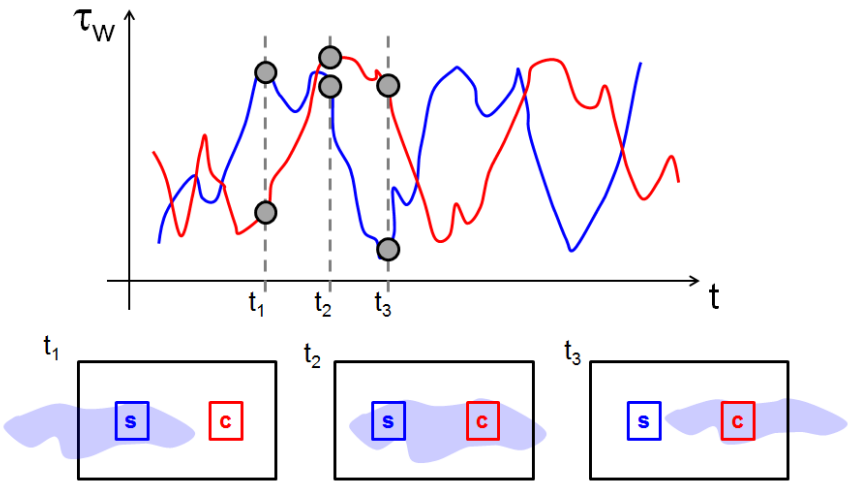

Figure 7.3: Passage of a streak and correspondent variation of wall shear stress at the sensor and at the control point

of the high speed streak creates an increase in the streamwise wall shear stress, which is first detected at point S at time t_1. As the streaks convects downstream, at instant t_2 the increase in wall shear stress is detected at both points S and C. Finally at time t_3 the streak leaves the region over point S and a higher shear stress is only detected at point C. This simple situation ideally occurs when the streak travels exactly along the streamwise direction. In reality, however, streaks also deviate from this trajectory. In addition, the shape of the streak is not frozen and evolves in space and time. To

take this into account, the prediction of the flow variable at point C can be improved if signals at more sensor points are used. This leads, for example, to a multiple input - single output (MISO) model, such as that illustrated in the left side of Figure 7.4. If one wants to achieve control effects in more than one control point, then the prediction can be extended to more points downstream. In this case a multiple input - multiple output (MIMO) model can be designed, as shown in the right side of Figure 7.4.

In particular, Rathnasingham and Breuer focused on predictive linear models, by

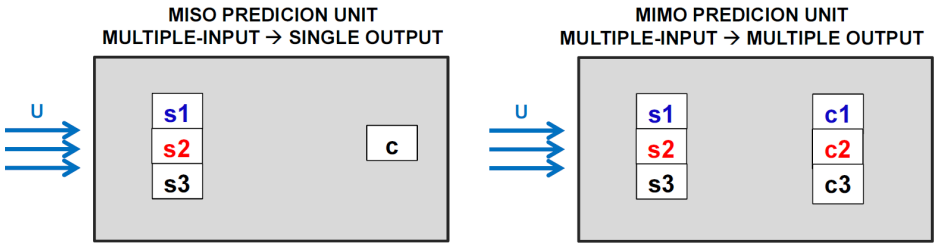

Figure 7.4: Comparison between a MISO and MIMO feed-forward sensing unit

assuming that the evolution of flow variables in the near-wall region can be modelled for a short time by dynamical equations which are linear with respect to the mean flow. In fact, the strong mean shear in the near-wall dominates the short-time evolution of small perturbation, in agreement with the Landahl model [90] and with Rapid Distortion Theory [55]. The linearity assumption has to hold only for the short time that it takes a structure to advect from location S to location C in Figure 7.2) and does not imply that the turbulence production process as a whole is governed by a linear mechanism [119]. Given that, an ad-hoc linear model can be built by interrogating the specific flow field to be controlled. This strategy is also known as *system identification* and the system model can be built using an adpative filter. In this chapter, two linear approaches are examined: the Wiener filter, which is the most conventional adaptive filter, and the Least Mean Squares filter (LMS), developed more recently. The design of these filters is briefly outlined in the following sections.

7.2.1 Wiener Filter

The Wiener filter is a classical linear adaptive filter. In this section the design of a digital Finite Impluse Response (FIR) Wiener filter is presented. In this case, the

application of the filter is performed on discrete time signals, acquired by a DAQ card. Every signal $x(n), y(n), ...$ is sampled in time at a certain number of instants. All the signals are supposed to be sampled at the same sampling frequency f_s. n is the index that indicates the generic data point and N is the total number of samples available. A FIR filter of order M is a linear system that transforms the input $x(n)$ into the output $y(n)$ and analyses M points at a time, according to the following equation:

$$y(n) = \sum_{k=0}^{M-1} H(k)x(n-k) \tag{7.1}$$

where $H(k)$ for $k = 0...M-1$ are the weights or coefficients of the filter and are determined during the design of the filter itself. The output at the current instant n is a function of only of the current and the past data points, i.e. the filter is causal.

To describe the design of a Wiener filter, firstly the SISO case is considered for simplicity, see Figure 7.5. The objective of the filter is to estimate the flow variable measured

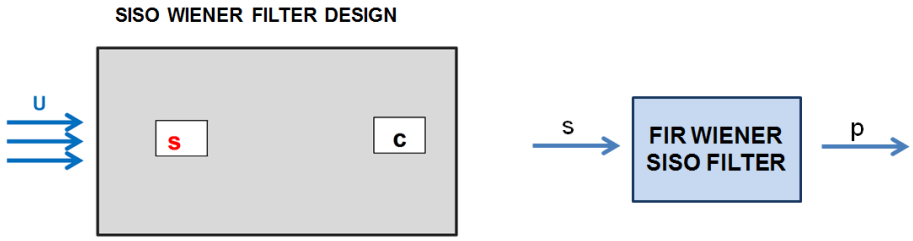

Figure 7.5: Schematic of a SISO Wiener filter

at location C, whose signal acquired and sampled is indicated as $c(n)$. The input signal is the flow variable measured at location S, whose signal acquired and samples is indicated as $s(n)$. Both signals are assumed to be statistically stationary, which is a necessary condition for the design and the application of the Wiener filter. A FIR Wiener filter of order M can be expressed in the same way as a generic FIR filter, as

$$p(n) = \sum_{k=0}^{M-1} H(k)s(n-k) \tag{7.2}$$

where $s(n)$ is the input of the filter, $p(n)$ is the output (the predicted signal) and $H(k)$ are the weights to be determined within the filter design procedure. The error $e(n)$ is

defined as

$$e(n) = c(n) - p(n). \tag{7.3}$$

A criterion for the determination of the weights is the minimisation of the mean squared error E, defined as

$$E = \sum_{n=1}^{N} [e(n)]^2 = \sum_{n=1}^{N} [c(n) - p(n)]^2 \tag{7.4}$$

Substituting equation (7.2) into equation (7.4) and developing the summation, the following expression for the mean squared error is obtained:

$$E = \sum_{n=1}^{N} c^2(n) - 2H(k) \sum_{k=0}^{M-1} \sum_{n=1}^{N} c(n)\, s(n-k) + \sum_{k=0}^{M-1} \sum_{l=0}^{M-1} H(k)\, H(l) \sum_{n=1}^{N} s(n-k)\, s(n-l). \tag{7.5}$$

Last equation can be rewritten as:

$$E = \sum_{n=1}^{N} c^2(n) - 2H(k) \sum_{k=0}^{M-1} R_c(k) + \sum_{k=0}^{M-1} \sum_{l=0}^{M-1} H(k)\, H(l)\, R_a(k-l) \tag{7.6}$$

where $R_c(k) \doteq \sum_{n=1}^{N} c(n)\, s(n-k)$ and $R_a(k-l) = \sum_{n=1}^{N} s(n-k)\, s(n-l)$ are the cross-correlation between the $s(n)$ and $c(n)$ and the autocorrelation of the signal $s(n)$ respectively. The minimisation of this equation is obtained by differentiating last expression with respect to the single coefficients and setting the value of the derivative equal to zero:

$$\frac{\partial E}{\partial H(k)} = 0 \qquad k = 0, 1, ..., M-1. \tag{7.7}$$

This leads to the solution of the linear system:

$$\sum_{k=0}^{M-1} H(k)\, R_a(k-l) = R_c(k) \qquad k = 0, 1, ..., M-1. \tag{7.8}$$

The system can also be written in matrix form as

$$R = H \cdot C. \tag{7.9}$$

Equation (7.9) is better known as the Wiener-Hopf equation. In (7.9) R is defined as

$$R = \begin{bmatrix} R_a(0) & R_a(-1) & ... & R_a(-M) \\ R_a(1) & R_a(0) & ... & R_a(1-M) \\ & & ... & \\ R_a(M) & R_a(M-1) & ... & R_a(1) \end{bmatrix} \tag{7.10}$$

and C and H are defined as

$$C = \begin{bmatrix} R_c(0) \\ R_c(1) \\ ... \\ R_c(M) \end{bmatrix} \qquad H = \begin{bmatrix} H(0) \\ H(1) \\ ... \\ H(M) \end{bmatrix} \tag{7.11}$$

R is the *MxM* autocorrelation matrix of the signal $s(n)$. It is a symmetric matrix, known as a Topelitz matrix. C is the cross-correlation vector and H is the weight vector, which represents the unknown of the system of equations. Signal $s(n)$ and $c(n)$ can be simultaneously acquired in experimental tests, followed by the calculation of the auto-correlation and cross-correlation functions $R_a(k-l)$ and $R_c(k)$. These values, subsequently, form the matrices C and R in equation (7.9). Finally the Wiener filter coefficients can be computed. The solution of the linear system, as R is a Toeplitz matrix, can be improved using a special recursive solving algorithm, known as Levinson-Durbin recursion (see [52] for more details). The solution of the system can be easily implemented in MATLAB©.

As stated before, a MISO FIR Wiener filter is expected to yield a better performance. The filter design in this case is more complicated, so it will be only briefly outlined hereafter. More detailed information is given in [52]. The schematic of a MISO Wiener filter with three inputs and one output is illustrated in Figure 7.6. In this case the objective of the filter is to predict the flow variable measured at location C, whose signal acquired and sampled is indicated as $c(n)$. The input signals are $s_1(n), s_2(n), s_3(n)$ acquired at three locations upstream. All the signals are again assumed to be statistically stationary. The output of the filter $p(n)$, is a weighted linear combination of data points from all three signals acquired upstream:

$$p(n) = \sum_{k=0}^{M-1} H(k)\, s_1(n-k) + \sum_{k=M}^{2M-1} H(k)\, s_2(n-k) + \sum_{k=2M}^{3M-1} H(k)\, s_3(n-k). \tag{7.12}$$

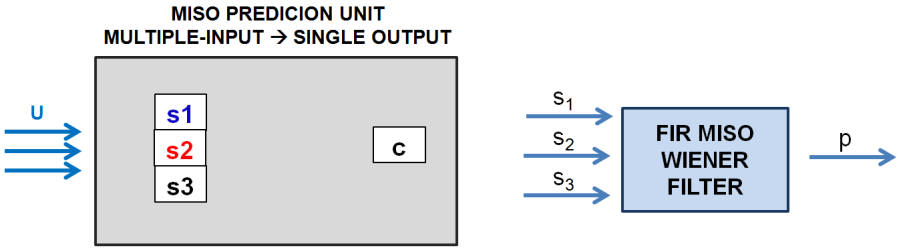

Figure 7.6: Schematic of a MISO Wiener filter

It is possible to derive a discrete Wiener-Hopf equation similar to equation (7.9) by repeating analogous mathematical elaborations. The difference, however, is that the structure of the matrices, R, C and H is the following

$$R = \begin{bmatrix} R_{11} & R_{12} & R_{13} \\ R_{21} & R_{22} & R_{23} \\ R_{31} & R_{32} & R_{33} \end{bmatrix} \qquad C = \begin{bmatrix} R_c(0) \\ R_c(1) \\ \dots \\ R_c(3M-1) \end{bmatrix} \qquad H = \begin{bmatrix} H(0) \\ H(1) \\ \dots \\ H(3M-1). \end{bmatrix} \tag{7.13}$$

In particular the R matrix so constructed is a block matrix, consisting of nine sub-matrices. Each single sub-matrix has the same structure of matrix R in equation (7.10) when the indices of the sub-matrix are equal (i.e. R_{11}, R_{22} and so on). For different sub-indexes (i.e. R_{12}, R_{13} and so on), the sub-matrix is built through cross-correlations between the correspondent input signals, instead of auto-correlation. In other words, the structure of the generic sub-matrix is

$$R_{ij} = \begin{bmatrix} cc_{ij}(0) & cc_{ij}(-1) & \dots & cc_{ij}(-M) \\ cc_{ij}(1) & cc_{ij}(0) & \dots & cc_{ij}(1-M) \\ & & \dots & \\ cc_{ij}(M) & cc_{ij}(M-1) & \dots & cc_{ij}(1) \end{bmatrix} \tag{7.14}$$

where $cc_{ij}(k-l)$ is defined for a discrete-time signal as

$$cc_{ij}(k-l) \doteq \sum_{n=1}^{N} s_i(n-k)\, s_j(n-l). \tag{7.15}$$

Clearly the matrix is the same as R in equation (7.10) when $i = j$. The solution of the linear system can be improved using the block matrix version of the Levinson-Durbin

recursion algorithm. This solution is also implementable in MATLAB©.

7.2.2 LMS Filter

A feed-forward predictor based on the FIR Wiener filter is the most accurate. However, as stated earlier, it is only applicable to statistically stationary signals. This means that the performance of a flow control technique based on this type of filter is quite vulnerable to environmental changes, such as small variations of the free-stream velocity, sensor drifts etc. In addition, the design of the filter itself typically requires the inversion of large matrices. This makes the filter design computationally very expensive. To improve the efficiency of the filter and extend its applicability also to non-stationary signals, digital adaptive filters can be used, the most popular of which is the Least Mean Squares filter (LMS). The introduction of the LMS filter is more recent than the Wiener filter.

Also in this case it is convenient to first illustrate the design method for a SISO case. The schematic of a LMS filter is the same as a Wiener filter and is shown in Figure 7.7. The objective of the filter is to estimate the flow variable measured at location C, correspondent to the sampled signal indicated as $c(n)$ The input signal is the flow variable measured at location S, correspondent to the sampled signal indicated as $s(n)$. The predicted signal is indicated as $p(n)$. In the case of the SISO FIR Wiener filter the

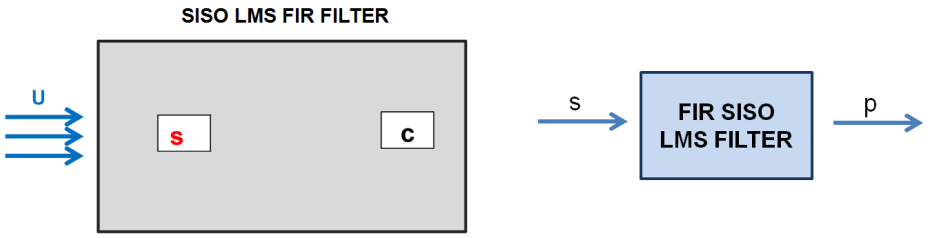

Figure 7.7: Schematic of a SISO LMS filter

error to be minimised is defined globally, which means considering all the data points acquired and sampled during the whole observation time:

$$E = \sum_{n=1}^{N} [c(n) - p(n)]^2 .$$

This implies that the error estimation can be performed only after all the N samples of the signals $s(n)$ and $c(n)$ are acquired and stored. In the case of the LMS filter the definition of error is relaxed to:

$$E(n) = [e(n)]^2 = [c(n) - p(n)]^2 . \tag{7.16}$$

It is worth noticing that that in this case the error is a function of time (and so of n), therefore the error estimation is performed during the observation of the signals themselves. The LMS design is an iterative process in which the error and the filter coefficients are continuously updated until a certain performance goal is reached, as shown in Figure 7.8. The generic LMS filter can be expressed in the form of equation

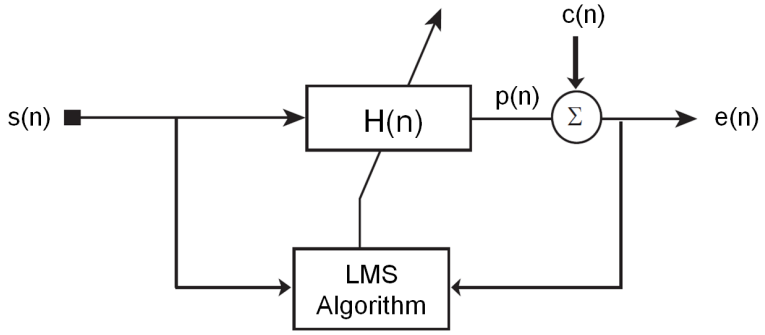

Figure 7.8: Schematic of an LMS algorithm (taken from [48])

(7.1), as:

$$p(n) = \sum_{k=0}^{M-1} H(k)\, s(n-k). \tag{7.17}$$

The squared error can be re-written as:

$$E(n) = \left[c(n) - \sum_{k=0}^{M-1} H(k)\, s(n-k) \right]^2 . \tag{7.18}$$

The derivative of the squared error with respect to a single coefficient can be computed as:

$$\frac{\partial E(n)}{\partial (H(k))} = 2\,[c(n) - p(n)]\; s(n-k) = 2\, e(n)\, s(n-k) \tag{7.19}$$

from which it is possible to derive an update equation for the coefficients

$$H(n+1,k) = H(n,k) + 2\mu e(n)\, s(n-k) \tag{7.20}$$

where μ is the step of the coefficient update. If the error $e(n)$ is zero, the coefficients will not be modified by the algorithm. However, if it is not zero, each coefficient is modified by adding to it a fraction of the error signal multiplied by $s(n-k)$. As $p(n) = \sum_{k=0}^{M-1} H(k)\, s(n-k)$. An increase in $H(k)$ results in an increase of $p(n)$ and thus in a decrease of $e(n)$ since $e(n) = d(n) - y(n)$. As a result, if the rate of convergence is too fast, the algorithm will over-shoot and become unstable. To ensure stability the following condition on μ has to be verified

$$0 < \mu < \frac{1}{10 M P_s} \tag{7.21}$$

where M is again the filter order and $P_s \doteq 1/N \sum_i^N s^2(n)$ is the average power of the input signal. Although it is not the fastest adaptive filter routine for a given filter order M, the LMS algorithm is widely used due to its simplicity and stability, as long as the condition (7.21) is respected. In addition, it can be also applied to signals which are not strictly statistically stationary, if their statistics in time, however, do not vary too much.

The MISO case for the LMS filter is shown in Figure 7.9. The objective of the fil-

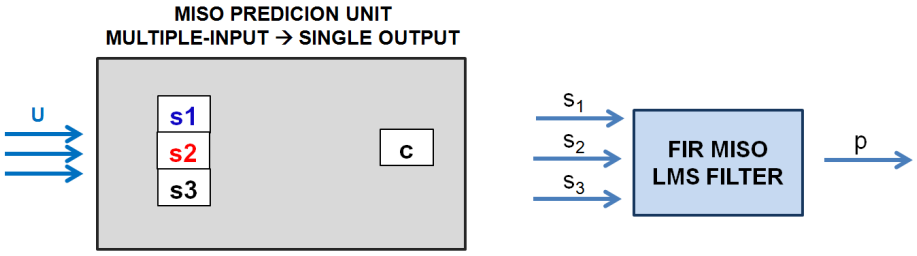

Figure 7.9: Schematic of a MISO LMS filter

ter is to predict the signal $c(n)$ from the input signals $s_1(n), s_2(n), s_3(n)$. The output of the filter $p(n)$ is given by:

$$p(n) = \sum_{k=0}^{M-1} H(k)\, s_1(n-k) + \sum_{k=M}^{2M-1} H(k)\, s_2(n-k) + \sum_{k=2M}^{3M-1} H(k)\, s_3(n-k). \tag{7.22}$$

Similarly the error can be defined as:

$$E(n) = [e(n)]^2 = [c(n) - p(n)]^2 . \tag{7.23}$$

In these case, following the same procedure outlined for the SISO case, the three sets of coefficients named $H_1(k)$ for $k = 0 \ldots M-1$, $H_2(k)$ for $k = M \ldots 2M-1$ and $H_3(k)$ for $k = 2M \ldots 3M-1$ can be updated independently according to coefficient update equations:

$$H_1(n+1,k) = H_1(n,k) + 2\mu e_1(n) s_1(n-k) \tag{7.24}$$

$$H_2(n+1,k) = H_2(n,k) + 2\mu e_2(n) s_2(n-k) \tag{7.25}$$

$$H_3(n+1,k) = H_3(n,k) + 2\mu e_3(n) s_3(n-k). \tag{7.26}$$

Furthermore, a stability condition similar to (7.21) has to be respected to prevent the routine from becoming unstable.

7.3 Predictive Filter Design for a Turbulent Boundary Layer

A feed-forward predictor can de designed using a system identification approach, using the data acquired in a turbulent boundary layer at free-stream velocity of 0.1 m/s . Two experimental campaigns were carried out, one using Liquid Crystal Thermography and the other one using Constant Temperature Anemometry. The boundary layer is tripped using a circular rod, of diameter 7 mm, located 70 mm downstream of the leading edge.

7.3.1 Experiments with Liquid Crystal Thermography

The predictor design by Liquid Crystal Thermography is performed using time series of hue, extracted at selected points, as described in Chapter 5.

The first logical step is to design a SISO adaptive filter, which receives a signal at point S as input and provides an output $c(n)$, which is the prediction/estimation of the signal observed at point C. These points marked at a certain time instant in the liquid crystal map are shown in Figure 7.10. At these points in particular, the time series of the hue value $h' = (h - \bar{h})$ are extracted, where $\bar{h}$ is the local mean value of hue. The observation time is 250 seconds and the sampling frequency is 10 Hz. Following the discucssion in Chapter 5, the sampling frequency should be high enough to capture at least the fluctuations related to largest scales in the near-wall flow. The computation

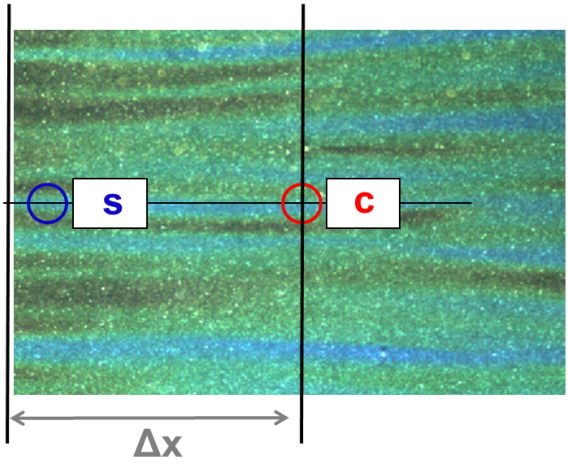

Figure 7.10: A sensor and a control point with generic streamwise separation Δx, marked in a liquid crystal image

of the filter weights is performed using the data of the first 200 seconds of the total observation time. A SISO Wiener filter and a LMS filter are designed, choosing a filter order of 50 in both cases. The LMS filter is designed with a step size of $\mu = 0.1$. Once the filter coefficients are computed, they can be used to estimate the signal at location C. This is done by using the data for the remaining 50 seconds of the time series. In order to evaluate the performance of the filters, the predicted and the actual signals are compared. The performance index that is used to evaluate the efficiency of the predictor is the cross-correlation coefficient between the predicted and the actual signal at zero time-lag. In fact, if the predictor works perfectly and the actual and the predicted signal at location C are identical, this coefficient would be equal to 1. The closer this coefficient is to 1, the better the prediction is. It has been verified that using this type of performance index is substantially equivalent to using the root-mean-square (RMS) error between the actual and the predicted signals, defined as

$$E_{RMS} = \sqrt{1/N \sum_{i}^{N} (c(n) - p(n))^2}. \tag{7.27}$$

Examples of signals used for the SISO filter design are shown in Figure 7.11. In this case the separation distance between the sensor and the control point is $\Delta x^+ = 150$, normalised in wall units. The sensor point is located at 0.8 m from the leading edge of the flat plate. Signal S appears to be very similar in shape to signal C, apart from a

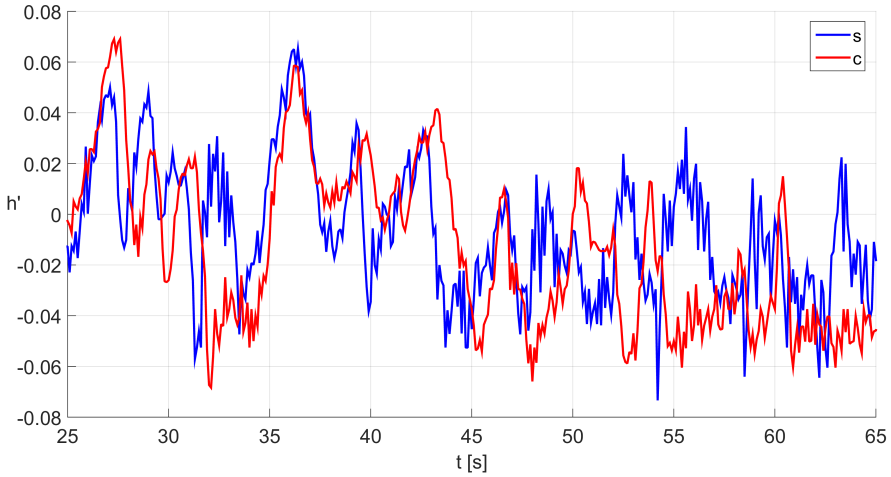

Figure 7.11: Hue fluctuation signals extracted at the sensor point S and at the control point C (with separation $\Delta x^+ = 150$) used to design the SISO Wiener and LMS filters

certain phase delay, due to the convection of the disturbances from point *S* to *C*.

The computed filter weights both for the Wiener filter and LMS filters are shown in Figure 7.12. Referring to equation (7.12), the index k is related to k-th time sample prior to the current sample computed at each step by the FIR filter. The absolute value

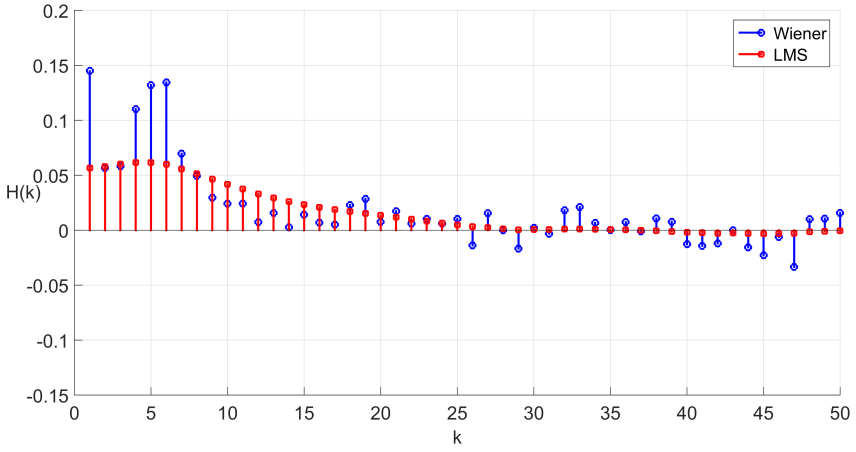

Figure 7.12: Coefficients of the Wiener and the LMS filters, designed with a separation distance of $\Delta x^+ = 150$

of the first weights is larger and decreases with k, both for the Wiener and the LMS filter. The maximum of the weights is observed at k =5-6 samples. This means that the most significant sample used by the FIR filter has a time lag of 0.5 - 0.6 seconds from

the current time sample. This value divided by the separation distance gives a convection velocity of about 0.056 m/s i.e. 11 u_τ. This value is very close to the convection velocity of the disturbances, estimated in Chapter 5.

The results of the prediction for both Wiener and LMS filters are shown in Figure 7.13. The actual signal extracted at the location C for the last 50 seconds of the obser-

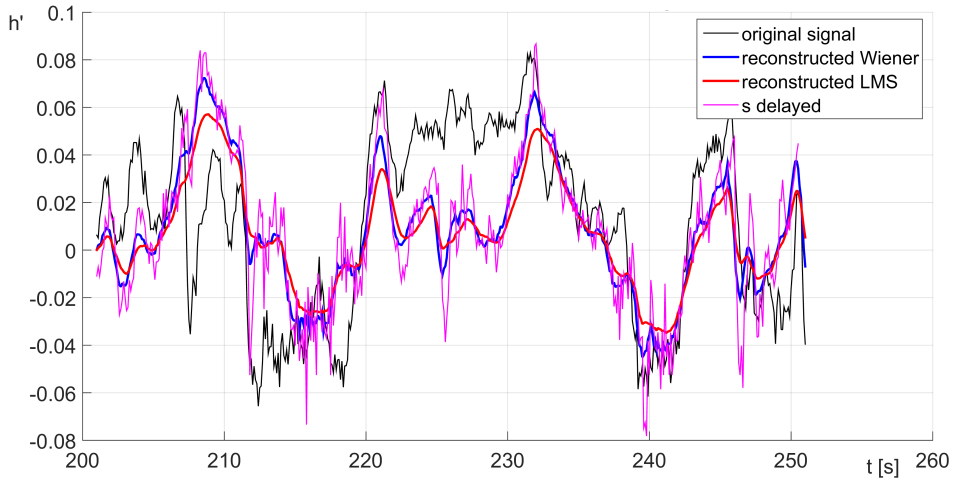

Figure 7.13: Comparison actual and predicted signals at point C with SISO Wiener and LMS filter (streamwise separation $\Delta x^+ = 150$)

vation time is plotted together with the predicted signals by the SISO Wiener and the SISO LMS filter. In addition, the signal observed at the position S (which is the input signal fed to the filters) and delayed by Δt_C is also plotted. Δt_C is the convection time of the disturbances at $u_c = 13\,u_\tau$, value obtained in Section 5.2.3. The output of both filters resembles signal observed at the position S delayed by Δt_C. Both Wiener and LMS filters appears to have two main effects:

- to isolate the frequency components which are most correlated between the signal at the sensor points and that at the control point (in this sense, the filter acts as a low-pass filter);
- to catch the movement of the disturbances, which are convected between the upstream points and the downstream point (in this sense, the filter acts as an all-pass delay filter).

The large fluctuations appear to be reconstructed by the filters and the convection velocity seems to be implicitly well established. However, the quality of the prediction

is, for example, not satisfactory in the interval 200 - 235 and, overall, the output of both filter is more similar to the input signal of the filter rather than to the actual signal observed at C. This may due to the short observation time on which the filters are designed, 200 seconds, limited by technological limits related to the experimental rig. A longer observation time is expected to improve the quality of the prediction.

The low-pass filtering effect of both filters is also observed in the power spectral density plots of the predicted signals compared with that of the actual signal, shown in Figure 7.14. The output of the filters has a lower frequency content of the actual sig-

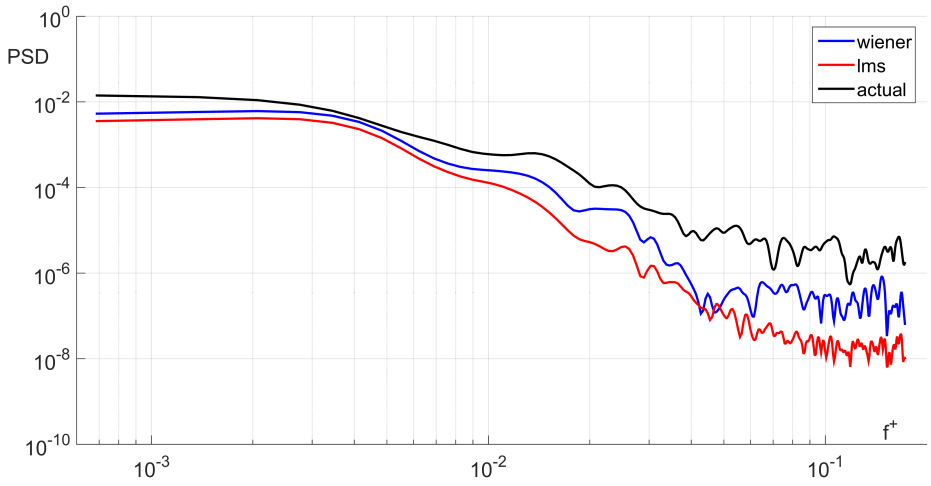

Figure 7.14: Comparison of the power spectral density of the actual signal and the predicted signals

nal. However, for $f^{+} < 0.006$ the power spectra density of the predicted signals is approximately the same as that of the actual signal. After this value, the power spectral density of the signal obtained with the Wiener filter seems to be higher than that of the signal obtained with the LMS filter. This means that the low-pass filtering effect of the adaptive LMS filter is more significant. In both cases, it seems possible to follow the largest scale fluctuations.

As mentioned above, the quality of the prediction can be estimated by using the cross-correlation coefficient between the output of the filter and the actual signal at the control point at zero time-lag. This value is computed by varying the separation Δx. Results are shown in Figure 7.15. The performance index for the Wiener and the LMS

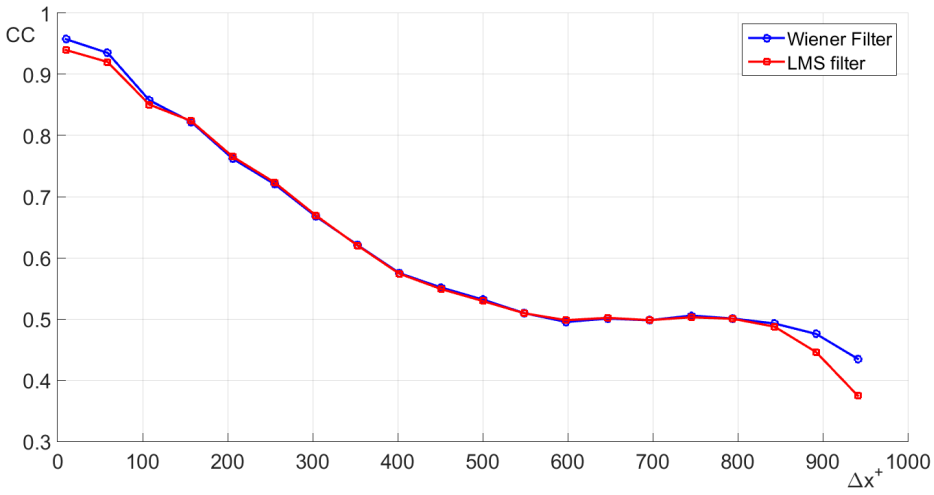

Figure 7.15: Variation of the performance index of the SISO Wiener and SISO LMS filter with Δx

filter are very close to each other. As expected, the performance index tends to decrease if Δx increases, as the degree of correlation between the signals at the sensor point and at the control point decreases if Δx increases. The quality of the prediction can be considered quite satisfactory if the performance index is higher than 0.6, which is verified if $\Delta x < 500$. For $\Delta x > 750$ the Wiener filter appears to be more performing. This is expected, as the Wiener filter is more accurate than the LMS filter, with the drawback of being more computationally intensive during its design.

A natural improvement to the SISO Wiener and LMS filters is the design of a MISO filter, following the work of Rathnasingham and Breuer [119, 84]. For this purpose a 3 input - 1 output system can be designed with same principle. In this case, time series of hue are extracted at the points marked in Figure 7.16. In this case both Δx and Δz can be varied. A FIR MISO Wiener filter and a LMS FIR filter are designed, in order to estimate the flow variables at location C based on the instantaneous signals extracted at the locations S_1, S_2 and S_3. The filter order is chosen to be 50 and the parameter μ for the LMS filter 0.01.

It is interesting to check whether the MISO filters improve the quality of the prediction with respect to the SISO filters. To do so, at first the MISO Wiener and LMS filters are designed with $\Delta z^+ = 50$, half the spacing of the sublayer streaks. The performance index, as a function of Δx^+ is compared with that of the SISO filters, 1 input - 1 output.

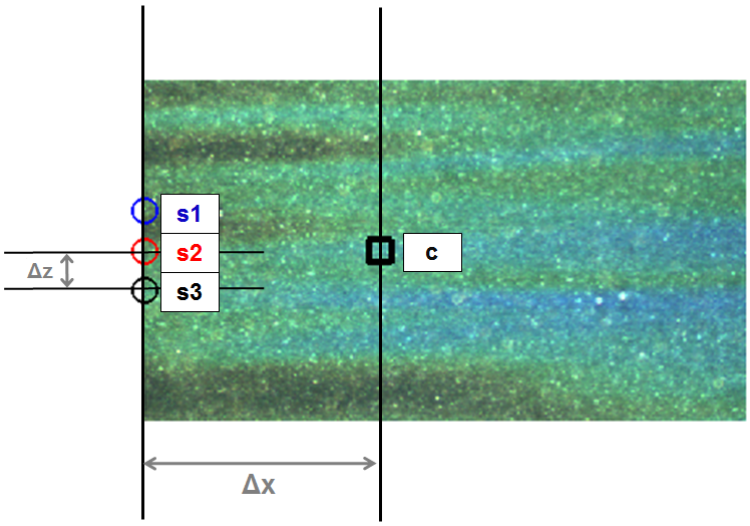

Figure 7.16: Sensor and control points with separation Δx used for the design of a MISO filter marked in a liquid crystal image

The results are shown in Figure 7.17. Surprisingly, the prediction with both MISO fil-

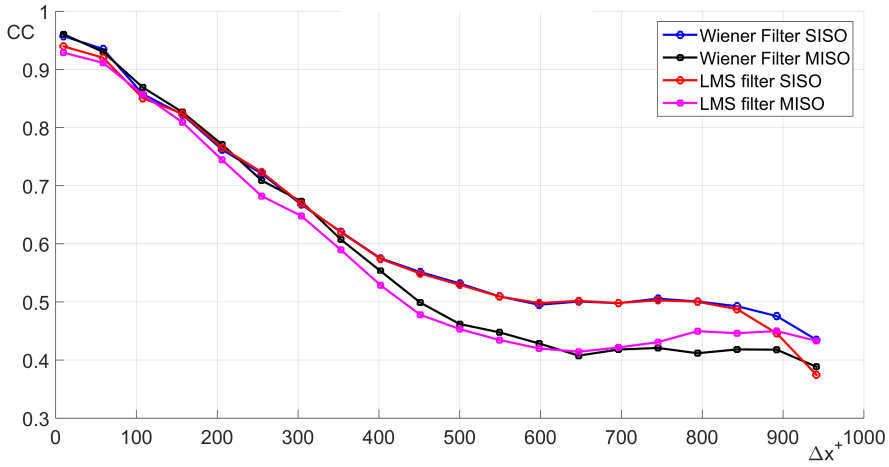

Figure 7.17: Comparison between the performance of SISO and MISO Wiener and LMS filters

ters does not seem to be better than with the SISO filters. In all cases, the performance index is the same for Δx^+ up to 350. For $\Delta x^+ > 350$ the performance index of the MISO filters is lower than that of the SISO filters. The lack of improvement could be attributed to the fact that the disturbances in the near-wall flow travel substantially in the streamwise direction. Therefore, the information from sensor S_2 is the most significant for the estimation of the signal at point C, whereas the information from sensor

points S_1 and S_3 is not very relevant and could be even redundant. This can explain the degradation of performance. These results are in agreement with those obtained by Rathnasingham and Breuer [119]. After a preconditioning routine on the input signals, they observed that the performance of the predictor in the SISO case (1 input - 1 output with Δx^+ =300) and in the MISO case (3 input - 1 output with Δx^+ =300 and Δz^+=40) is the same, with the RMS error between the actual and the predicted signal being 2.9% in both cases.

A more systematic study is carried out by varying both the separation Δz in spanwise direction between the upstream points and the distance Δx between the upstream sensors and that downstream. Figure 7.18 shows the result of this analysis for the MISO Wiener filter. The cross-correlation coefficient at zero time lag, taken as performance index, is the contour variable. The performance of the filter is more or less

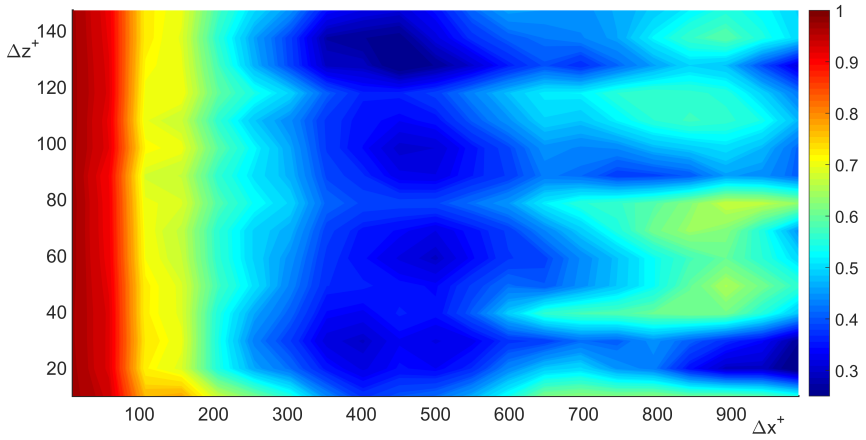

Figure 7.18: Performance of the MISO Wiener filter as a function of Δz^+ and Δx^+

independent of the spanwise separation Δz^+, at least within the area of investigation. This is in agreement with the results shown before. Therefore, given a certain streamwise separation Δx^+, the spanwise spacing of the sensor points could be increased up to Δz^+=140 without a substantial decrease of performance. The information coming from the signal S_2 is sufficient to build a successful predictor. The results for the LMS filter are shown in Figure 7.19. The conclusions are more or less the same.

The choice of the optimal spacing between the sensor and the control points in a MISO 3 input- 1 output system has to be made in all cases considering some technological constraints. Firstly, an actuator should be placed between the upstream points and

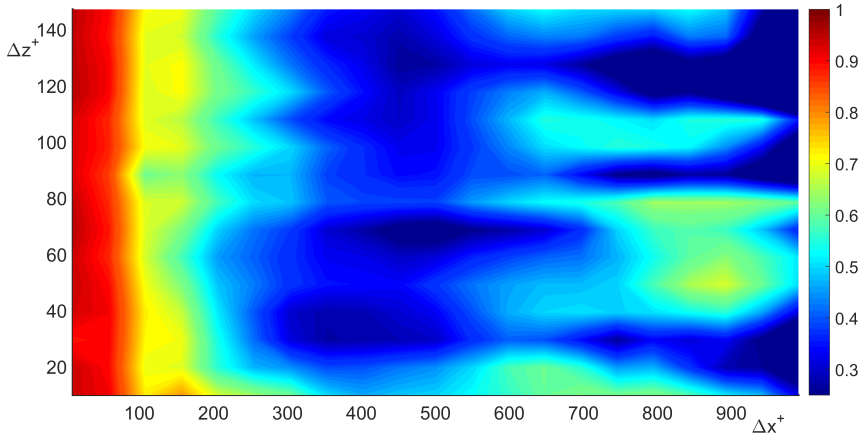

Figure 7.19: Performance of the MISO LMS filter as a function of Δz^+ and Δx^+

the downstream points (see also Figure 7.1). Therefore, it is necessary to guarantee a certain minimum streamwise separation because the disturbances generated by the actuator need some space to properly develop and yield the desired effect on the flow field. In this case, a minimum separation of Δx=50 mm is needed, i.e. $\Delta x^+ > 250$. In addition, the sensors themselves have a spanwise width, so it is not possible to place the sensor points too close. For classical wall probes (such as the Dantec 55R47 probes) a minimum spacing of $\Delta z = 8$ mm , corresponding to $\Delta z^+ = 40$ has to be set. As the performance strongly decreases with Δx^+, the minimum value imposed by the technological constraints has to be chosen, which is $\Delta x^+ = 250$. The value of Δz^+ does not seem to affect so much the performance, however to limit the intrusiveness it is better to place the wall probes in a configuration as much compact as possible. Therefore the minimum value of dictated by the technological constraint $\Delta z^+ = 40$ is chosen. Based on these results, for the prediction at single control point, a SISO system is perhaps more indicated because the MISO system involves a higher complexity and not a better performance.

7.3.2 Experiments with Constant Temperature Anemometry

The design of the feed-forward predictor is also performed using Constant Temperature Anemometry and using hot-film probes. Details on the experimental rig are given in Section 3.6.2. The location of the probes is sketched in Figure 7.20. An array of three Dantec 55R47 glue-on wall hot-film probes are installed at 0.67 m from the leading edge of the flat plate. The spanwise spacing of the probes is Δz = 8 mm, i.e. $\Delta z^+ = 40$.

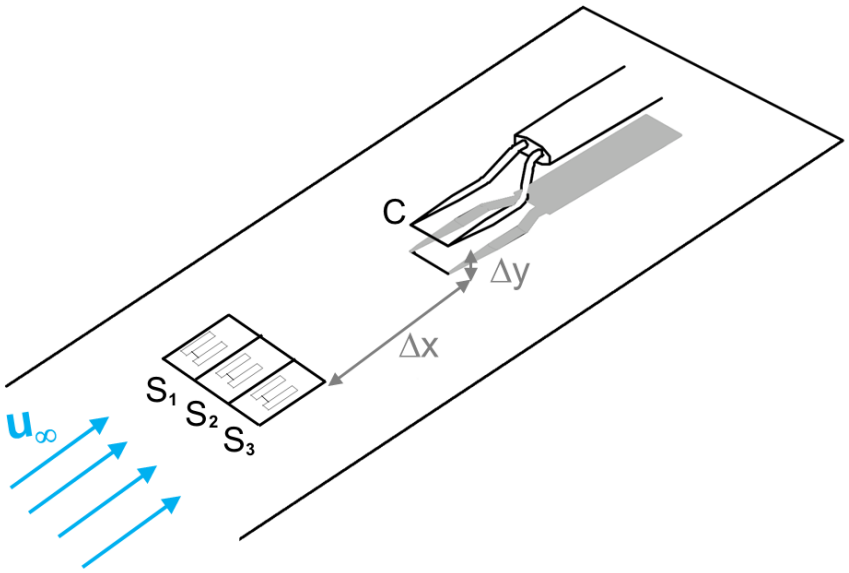

Figure 7.20: Constant Temperature Anemometry set-up used for the design of the feed-forward predictor

The points where the probes are located are referred to as "sensor points" hereafter and are indicated with the symbols S_1,S_2 and S_3. Downstream of the sensor points, a single hot-film probe is installed on a simple traverse system which enables the variation of both Δx and Δy within a certain range. The point where the hot-film probe is located is referred to as the "control point" and is denoted hereafter as C. Experiments are performed at the combination of Δx and Δy plotted in Figure 7.21, where the values of the separation are normalised in wall units. The three glue-on probes at the sensor

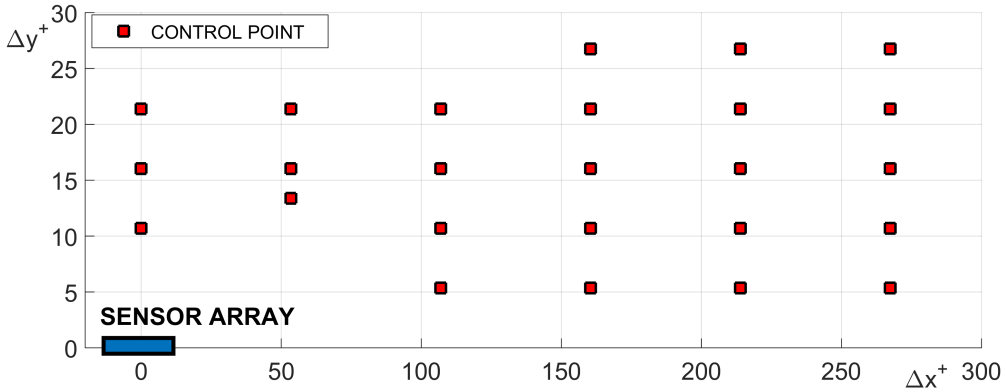

Figure 7.21: Combination of Δx^+ and Δy^+ of the CTA experiments

points are driven by a TSI IFA 300 CTA system, whereas the hot-film probe at the

control point is driven by a Dantec 55T42 mini-CTA system. All probes are operated at a overheat ratio of 1.1. The raw voltage signals output CTA anemometers are first low-pass filtered by an analogue (anti-aliasing) filter with a cut-off frequency of 100 Hz and then are sampled at 250 Hz. The total observation time for each test condition is 120 seconds. To remove any low frequency drift in the sensor (caused by particulate and fine air bubbles in the water flow) every signal is high-passed filtered at 0.1 Hz with a digital high-pass filter after data acquisition. In addition, also a digital low-pass filter at 7 Hz is applied to remove the high frequency noise generated by the analogue filter.

Firstly, the SISO case is examined, in which only the signals acquired at the points S_2 and C are taken into consideration. The objective of the adaptive filter is to estimate/predict the signal located at point C, given the signal at point S_2. The first 88 seconds of the time series are used to compute the filter coefficients. The last 32 seconds are used to evaluate the filter performance. For each raw signals $s(t)$, only the fluctuation component is considered, i.e. $s' = s(t) - \bar{s}$ where $\bar{s}$ is the mean value of the anemometer output voltage. The anemometer is not calibrated, as in this case only the fluctuations of the flow variables are of interest and not their mean value. A portion of the voltage signals acquired in a test at $\Delta x^+ = 160$ and $\Delta y^+ = 15$ is shown in Figure 7.22. As the voltage signals are outputs of different types of anemometer and probes,

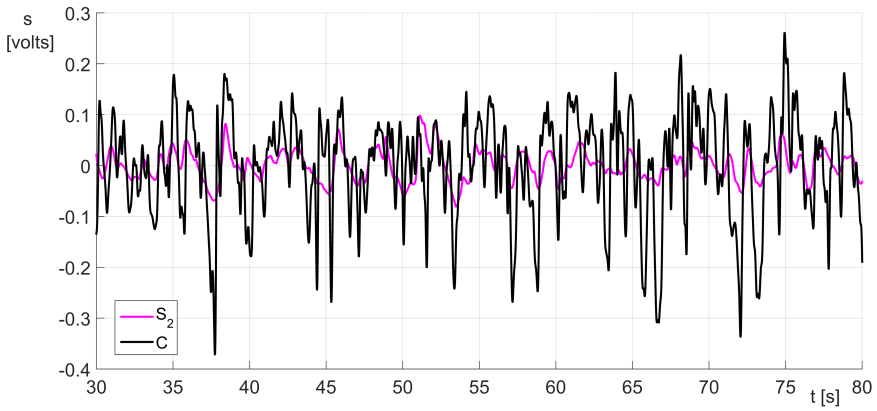

Figure 7.22: Voltage fluctuation signals used for the design of the SISO Wiener and LMS filters

the level of fluctuation around their mean value is different. This is not an issue, as the type of signals required as input and output of the adaptive filters can be of different

nature, as stated earlier in this chapter. In fact, in an efficient control system, the objective is to relatively reduce the level fluctuation of the flow variable at the control point in the controlled case compared to the uncontrolled case. For this purpose, a difference in the fluctuation level between the input and the output is not important. Two types of predictive filters are built, a SISO Wiener filter and a SISO LMS filter. In both cases, a filter order of 1250 is chosen, coherently with the filter order chosen in filter design with the Liquid Crystal Thermography. Indeed, in that case the filter order was 50 and the sampling frequency was 10 Hz. In this case the sampling frequency is 250 Hz, therefore to achieve the same temporal observation window of 5 seconds (about 150 T_τ viscous time units), the filter order needs to be set as $250 \cdot 5 = 1250$. As for the LMS filter, the parameter μ is chosen to be 0.01.

The computed filter coefficients at $\Delta x^+ = 160$ and $\Delta y^+ = 15$ are shown in Figure 7.23. Only the first 300 filter coefficients are shown (out of the total number of 1250).

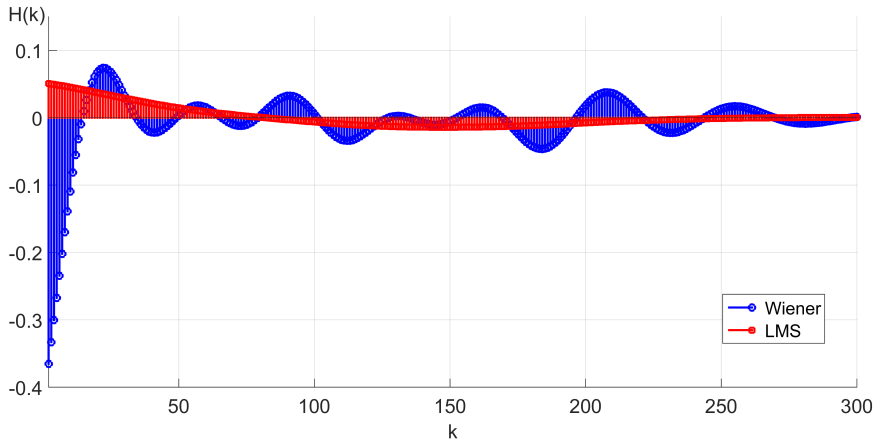

Figure 7.23: SISO Wiener and LMS filter coefficients computed in the case $\Delta x^+ = 160$ and $\Delta y^+ = 15$

The evaluation of the filter performance is performed on the last 32 seconds of the total observation time. The output of the filters is shown in Figure 7.24. The reconstructed signals have a certain resemblance with the actual signal measured at the control point. The main effects of the filters appears to be, firstly that of smoothing out the signal fluctuations, preserving only the frequency components which are more correlated between input and output; secondly that of shifting in time the input signals in order to account for the convective velocity of the disturbances. The low-pass filtering effect

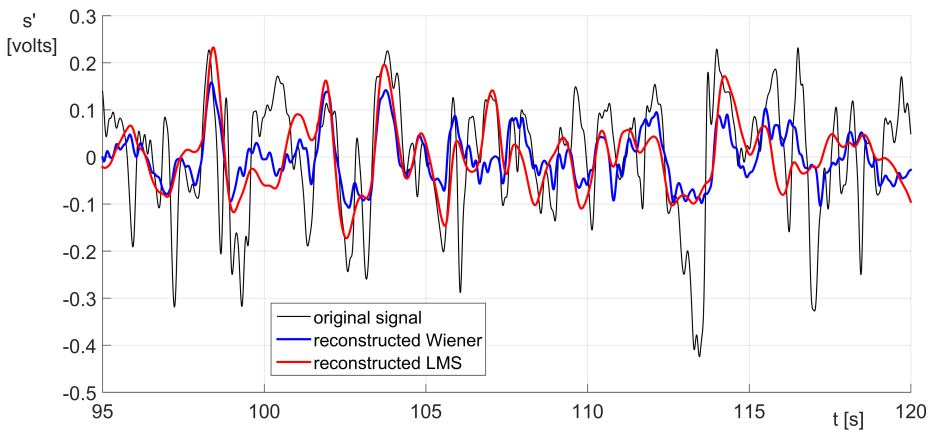

Figure 7.24: Comparison actual signals and predicted signals with SISO Wiener and SISO LMS filter in the case $\Delta x^+ = 160$ and $\Delta y^+ = 15$

is confirmed by the examination of power spectral density plots shown in Figure 7.25. The power spectral density is normalised in order to have unit area and is only shown

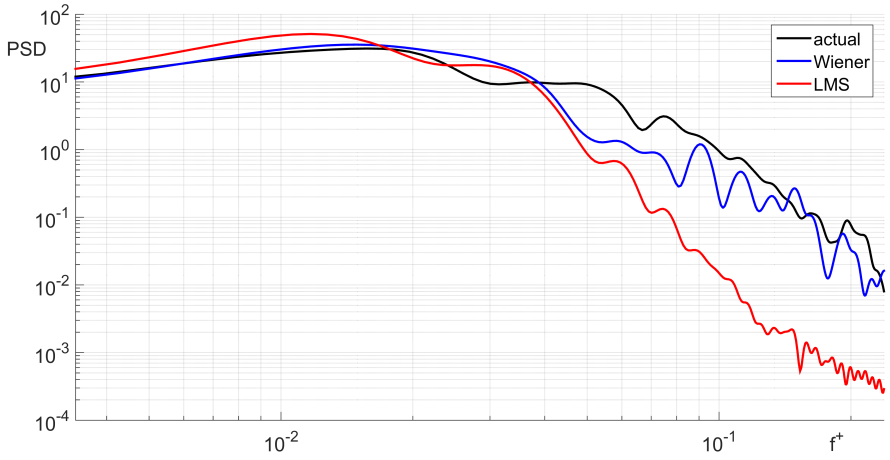

Figure 7.25: Comparison power spectral density of actual signals and predicted signals with the SISO Wiener and the SISO LMS filter in the case $\Delta x^+ = 160$ and $\Delta y^+ = 15$

between 0.1 and 7 Hz, since the signals are filtered in this frequency band. The LMS filter appears to smooth out all the fluctuations at f^+ higher than 0.04 (1.2 Hz). This value is in any case higher than the frequency of the sublayer streak passage, estimated to be $f^+ = 0.01$ - 0.15 in Section 5.2.2. Therefore, the large scale fluctuations are believed to be correctly followed.

In order to evaluate the performance of the filters, the value of the cross-correlation coefficient at zero time lag between the actual and the predicted signals is chosen as performance index. A systematic parametric study is carried out at all the tested combinations of Δx and Δy. The resulting parametric map for the Wiener filter, obtained by the interpolation of the scattered data points, is shown in Figure 7.26. The best results

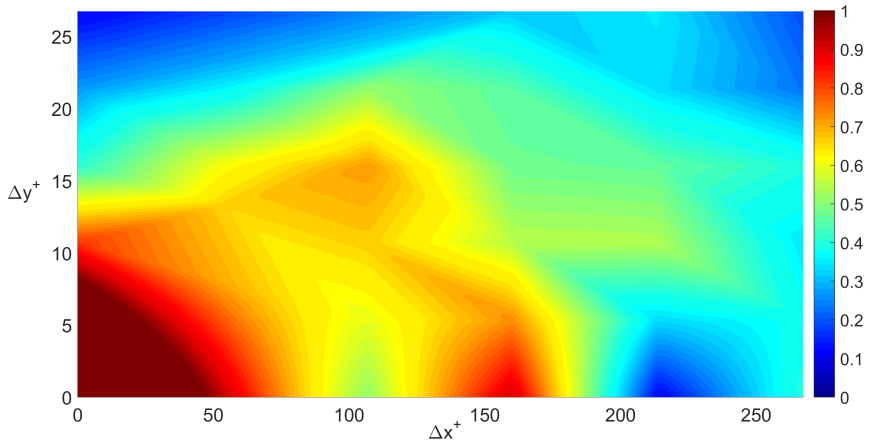

Figure 7.26: Performance index of the SISO Wiener Filter as a function of Δx^+ and Δy^+

are obtained for small values of Δx^+ and Δy^+, as the degree of correlation between the sensor point signal and the control point signal is higher. A level of correlation of 0.6 is achieved also at Δx^+ =100 and Δy^+ =15. The parametric map relatied to the LMS filer is shown in Figure 7.27. The contour levels are the same as those used for the Wiener filter. The LMS filer seems to be less performing than the Wiener filter, as the value of the performance index is lower, also for small values of Δx^+ and Δy^+.

The choice of the optimal values for Δx^+ and Δy^+ has to be made by taking into account some technological constraints. Since an actuator has to be located in between the sensor and the control point, at least a value of Δx^+ =250 has to be guaranteed. In addition, to avoid measurement errors due to the vicinity of the hot-film probe to the wall, the value of Δy^+ has to be greater than 10. Given that, the optimal parameter choice is Δx^+ =250 and Δy^+=10.

It is interesting also in this case to verify whether the use of MISO Wiener and LMS filters improves the performance of the prediction. MISO Wiener and LMS filters are designed with three inputs S_1,S_2 and S_3 and one output C. The filter order and the

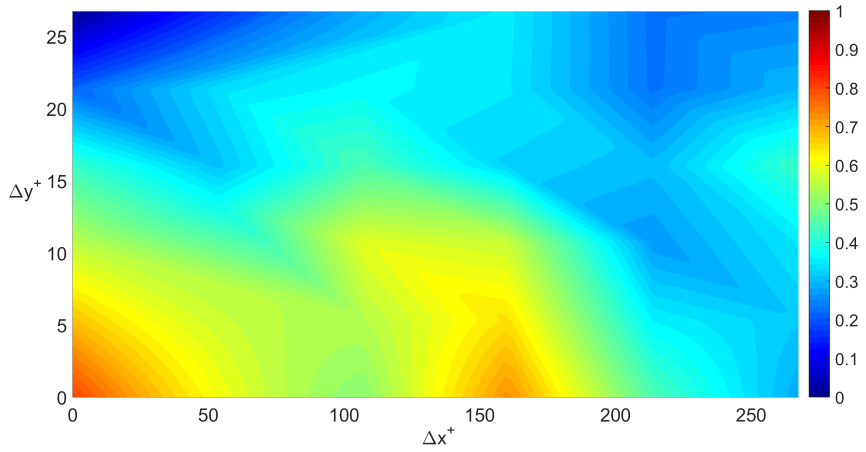

Figure 7.27: Performance index of the SISO LSM filter as a function of Δx^+ and Δy^+

other design parameters are the same as the SISO filters. Varying Δx^+ and Δy^+ it is possible to obtain a performance index map. In Figure 7.28 a comparison between performance maps of the MISO Wiener and of the SISO Wiener filters is shown in figure 7.28. Not a particularly improvement of the performance is obtained with the MISO

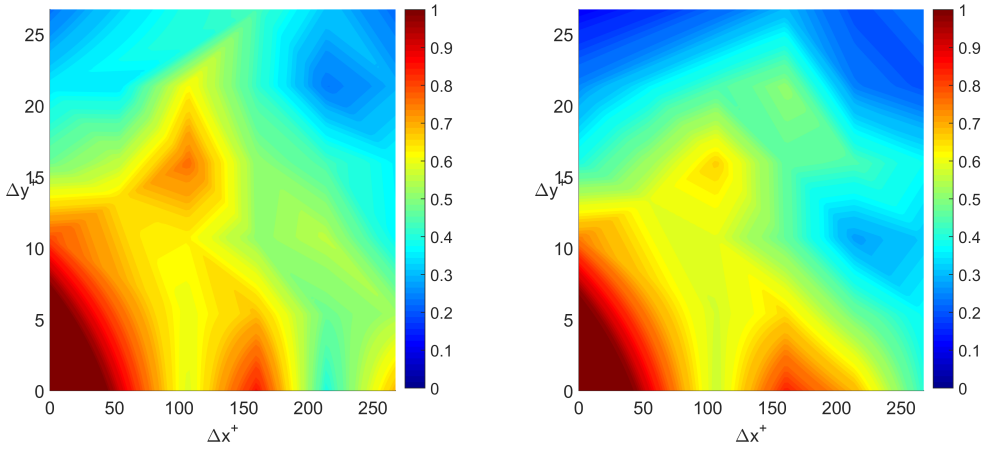

(a) SISO Wiener

(b) MISO Wiener

Figure 7.28: Comparison between the performance of a SISO and a MISO Wiener filter as function of Δx^+ and Δy^+

filter, confirming the results reported in Section 7.3.1. In Figure 7.29 a comparison between performance maps of the MISO LMS and of the SISO LMS filters is shown. The performance is seen to be greatly decreased, compared to the Wiener filter case, This might be due to convergence issued of the numerical routine for the LMS filter design. Further studies are required to clarify this point.

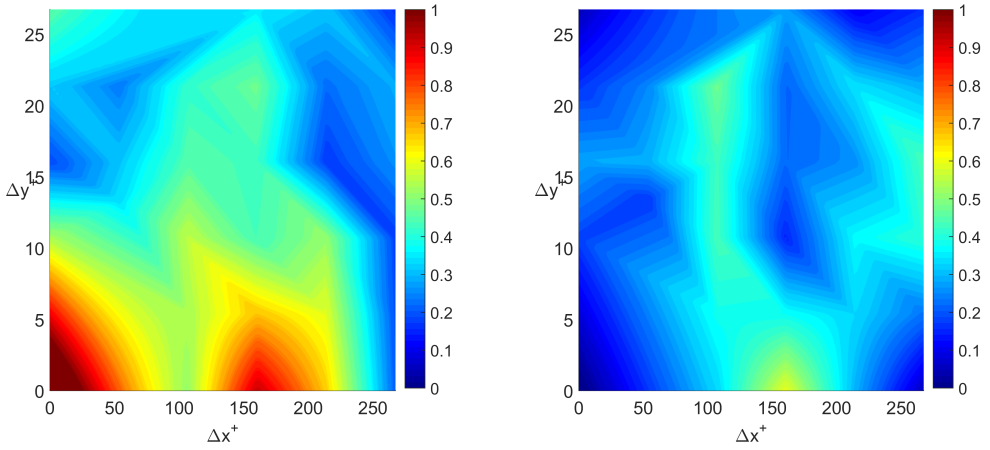

(a) SISO LMS (b) MISO LMS

Figure 7.29: Comparison between the performance of a SISO and a MISO LMS filter as function of Δx^+ and Δy^+

7.4 Summary of findings

In this chapter the design of a feed-forward predictor, key element of a feed-forward control strategy, in a turbulent boundary layer has been carried out using experimental data obtained with Liquid Crystal Thermography and Constant Temperature Anemometry. The typical designed control unit consits of a few sensors at the wall and a control point downstream in the boundary layer, either on the wall or at a certain distance from it. The objective of the study is to determine the optimal position the sensors upstream and of the control point downstream. Two types of linear adaptive filters are chosen as feed-forward predictors, namely the Wiener and the LMS filter.

With Liquid Crystal Thermography the predictor can be designed with both sensors and the control points at the wall. This study has shown that, if a single control point is established, a SISO filter, in which the sensor and the control point are aligned with the flow, is preferred to a MISO filter, in which more than one sensor upstream is used. This is because a SISO filter is less complex and its performance is not lower than a MISO filter. It is believed that this is due to the fact that the near-wall flow disturbances in a turbulent boundary layer tend to travel essentially along the streamwise direction, therefore the information coming from sensors not aligned with the control point in the streamwise direction is not relevant. This result is in good agreements with the findings of Rathnasingham and Breuer [119]. The streamwise separation between the

sensor point and the control point is dictated by technological constraint. An optimal values of Δx^+=250, about 40 mm, is chosen.

A similar study is carried out using Constant Temperature Anemometry, using which the possibility of placing a control point at a certain distance from the wall Δy^+ can also be considered. Also in this case SISO filters appear to provide a performance not inferior to that of MISO filters. The performance of the predictors is better at small values of both Δy^+ and Δx^+, as the degree of correlation between the signal upstream and downstream is higher. It is believed that not a good performance of the control system is obtained if the control point is very close to the wall, as the vicinity of the wall degrades the quality of measurement with the hot-film probes. Therefore a value of Δy^+=10 is considered optimal.

Chapter 8

Conclusions and Future Work

8.1 Conclusions

The aim of this research work was to explore the application of synthetic jets to control the near-wall coherent structures (streamwise streaks and vortices) in a turbulent boundary layer and to yield a skin friction drag reduction. To achieve this aim, experimental work was carried out using different experimental techniques. These techniques have included Particle Image Velocimetry, Liquid Crystal Thermography and Constant-Temperature Anemometry.

The experimental investigation has revealed that synthetic jets are capable of controlling streamwise streaks and vortices in a flow field. This has been shown in a laminar environment, achieving an almost complete cancellation of the streamwise streaks which develop in the near-wall region downstream of a circular cylinder vertically mounted across the boundary layer.
In addition, the capability of a synthetic jet array for producing regions of reduced skin friction in a turbulent boundary layer has been assessed and the physical mechanism behind it has been outlined.
The necessity of gathering some specific knowledge on the near-wall coherent structures to be controlled, has motivated an extension of the technique of Liquid Crystal Thermography. The technique has been applied for the first time for the quantitative spatial-temporal study of the near-wall structures in a turbulent boundary layer at low Reynolds number [146]. With some simple modifications, the performance of the technique can be significantly improved and is expected to have very promising applications as an exploratory tool not only for the dynamics of wall-bounded turbulence,

but also for turbulent flow control. However, with the current technology available the application of Liquid Crystal Thermography to the study and control of a turbulent boundary layer is constrained to low Reynolds number flows, especially because of its limited frequency response. For example, even for a subsonic aircraft the frequencies (i.e. the bursting frequency) that need to be resolved are of the order of 10^4 Hz. The frequency response of Liquid Crystal Thermography is very far away from these values and so a significant improvement has to be made to use it for full-scale application. The possibility of designing a simple feed-forward control system of a turbulent boundary layer has been explored. The system can be designed with a limited number of sensors and actuators. A preliminary design has been carried out, which has included the choice of suitable sensors and the definition of a preliminary geometry of the control unit (sensor and actuator arrangement).

Further details related to the specific conclusions drawn from the single objectives presented in chapter 1, are reported hereafter:

- *to assess the capability (in terms of modification of the velocity field) of a single synthetic jet actuators to control streamwise vortices and streaks in a laminar boundary layer and to determine the operating conditions at which the control effects are optimal.*

  A single synthetic jet is found to be effective in controlling the streaks generated by a cylinder of diameter 2 mm, mounted across a laminar boundary layer developing on a flat plate, in water at a free-stream velocity of 0.1 m/s. The synthetic jet is located at a distance of 0.71 m from the leading edge, the cylinder 30 mm downstream of it. A parametric study, in which the operating conditions of the synthetic jets are changed by varying the amplitude and frequency of the diaphragm oscillation is carried out. The optimal control effect, with an almost total cancellation of the streaks, is found at a velocity ratio VR=0.1, dimensionless stroke length L=1 and St=0.1.

- *to study the properties of the near-wall coherent structures in the turbulent boundary layer to be controlled.*

  The study of the near-wall structures in a turbulent boundary layer is performed with Liquid Crystal Thermography, in a rig appropriately designed for this purpose. The turbulent boundary layer develops on a flat plate, at a free-stream velocity of 0.1 m/s. In the area of investigation the Reynolds number based on the momentum thickness is 310. This study verifies that the Liquid Crystal

Thermography is able to capture the footprints at the wall of large scale coherent structures in the turbulent boundary layer. The technique revealed the presence of streamwise streaks of lower and higher velocity, which travel in the near-wall region. The physical properties of the streaks are determined. For instance, a spanwise spacing of 100 L_τ, a streamwise extent 500-1000 L_τ and convection velocity of 13-14 u_τ are found. These values are very similar to those reported in the literature. This information is important in designing a control system able to interact with these structures in a turbulent boundary layer. The technique also enabled a verification of Taylor's hypothesis. In particular, Taylor's hypothesis appears suitable for the study of the streamwise streaks with temporal information instead of spatial information, however its validity is limited to a spatial streamwise separation of 300 L_τ.

- *to examine the forcing effect of an array of circular synthetic jets on the near-wall region of a turbulent boundary layer and to identify the operating conditions that yield skin friction drag reduction.*

  A synthetic jet array is designed, based on the physical properties of the near-wall coherent structures determined before. The array is designed so as to produce artificial coherent structures, in particular hairpin vortices, of the same scale of the near-wall coherent structures of the turbulent boundary layer.

  The analysis of the flow field in the central plane with Particle Image Velocimetry revealed the presence of a region of lower mean velocity compared to the unforced turbulent boundary layer in the near-wall region, when synthetic jets are operated at VR=0.1 or lower. This region extends up to Δx^+=200 and is associated to a lower skin friction drag. At VR=0.2 or higher a region of higher velocity is observed in the near-wall region, associated to a higher skin friction drag.

  The phase-locked averaged velocity fields at VR=0.1 show that the region of lower mean velocity is related to a series of analogous regions that travel downstream at the different phases analysed within the period of oscillation of the synthetic jet diaphragm. At VR=0.2 or higher the region of higher mean velocity observed in the near-wall appears stationary. Above it regions of lower velocity, which move downstream and away from the wall during an oscillation period are observed.

  The frequency of actuation is varied between about $f^+ = 0.04$ and $f^+ = 0.15$

and the performance of the control system is not observed to be particularly dependent on this. In a full-scale application, for example again in the case of a subsonic aircraft, these values correspond to an actuation frequency of about 100 kHz. With the current technology, these actuation frequencies are not difficult to achieve.

The analysis of turbulent fluctuations suggests that the region of lower mean velocity at VR=0.1 is associated with a reduction of turbulence production and with an increased thickness of the viscous sublayer, but not enough evidence has been collected to confirm this. On the contrary at VR=0.2, turbulence production and the Reynolds stress in the near-wall region are observed to be increased.

The analysis of the flow field in planes in between two orifices revealed that the velocity near the wall is higher for all the operating conditions of the synthetic jets. The skin friction drag over the area in between two orifices is estimated. Also in the most favourable case, i.e. VR=0.1, a skin friction drag increase of 12% is observed.

The overall increase of skin friction is also observed with some preliminary liquid crystal flow visualisations. A wide region of higher wall temperature, and so higher wall shear stress for Reynolds analogy, which extends up to 300 L_τ downstream of the synthetic jet array at VR=0.1 and up to 500 L_τ at VR=0.2. The spatial resolution of the technique is not however sufficient to enable the visualisation of narrow regions of higher/lower temperature within the wide region.

- *to gain some knowledge about the physical mechanism which produces skin friction drag reduction/increase due to the synthetic jet array forcing*.

  The regions of lower velocity observed downstream the synthetic jet orifices at VR=0.1 or lower are believed to be induced by the passage of the train of hairpin vortices generated by the synthetic jets. In particular these regions appear to be related to the up-wash induced by the hairpin vortex legs. At VR=0.1 the hairpin vortices remain very close to the wall, at least for a distance of 200 L_τ downstream of the synthetic jet orifice. At VR=0.2 or higher, the hairpin vortices tend to leave the near-wall region almost immediately and appear to induce a pair of counter-rotating secondary vortices in the region just underneath the hairpin vortex legs. These secondary vortices create an up-wash in the region downstream of the synthetic jet orifices, with an increased velocity and an increased skin friction drag.

The legs of the hairpin vortices generated by adjacent synthetic jets are believed to merge and this is probably the reason for the increased velocity and skin friction drag observed in the region in between adjacent orifices. It is believed that an increased spanwise spacing between the synthetic jet orifices in the array will reduce the interaction between the hairpin vortices. In addition, the use of inclined jets would let the hairpin vortices travel closer to the wall for a longer distance downstream. Both these modifications are expected to increase the size of the skin friction drag reduction regions at the wall, but further investigations are needed to prove this point.

The region of reduced skin friction can be related to a decrease of turbulence production and to an increase of the thickness of the viscous sublayer. However, in this work not enough evidence has been collected on the statistics of velocity and of Reynolds shear stress to conclude this.

- *to lay the basis for the design of a feed-forward control system of a turbulent boundary layer based on wall-sensors and on an array of circular synthetic jets*.
  The design of the first leg of a feed-forward control system for a turbulent boundary layer is outlined and performed using Liquid Crystal Thermography and Constant Temperature Anemometry. The first leg consists of the design of a feed-forward predictor. The present studies focus on a feed forward predictor with a single control point. At the control point a certain control effect has to be achieved, such as the minimisation of the fluctuation of a flow variable (velocity, wall shear stress). The feed-forward predictor has to estimate the variation of this flow variable at the control point in an unforced turbulent boundary layer, in order to build a model of the flow system to be controlled. To achieve this, a single sensor can be employed upstream (SISO Single Input - Single Output predictor) aligned with the control point in the streamwise direction, or more than one sensor can be employed upstream (MISO Multiple Input - Single Output predictor). Due to the strong convective character of the disturbances in the near-wall region in the streamwise direction, it is observed that a SISO predictor is recommended as it is less complex than a MISO predictor and does not provide a worse performance. This conclusion is in agreement with the results reported in Rathnasingham and Breuer [119]. Similar results are obtained with the two measurement techniques employed. In particular, Liquid Crystal Thermography allowed a study in which all the sensors and the control points are

located at the wall. Given also some technological constraints of the flow control unit, the optimal streamwise separation between the sensor upstream and the control point downstream is determined to be 250 L_τ. Constant Temperature Anemometry also allowed the evaluation of a control point located at a certain distance from the wall. Given the technological constraints, a good performance can be achieved if the control point is located at a distance of 10 L_τ from the wall.

8.2 Recommendations for Future Work

In this work the potential for controlling streamwise vortices an streaks with a single synthetic jet in a laminar boundary layer is shown. The case of the streamwise vortices which develop in the near-wall region downstream of a circular cylinder, mounted vertically across a laminar boundary layer is examined. Although an almost total cancellation of the streak and the operating conditions of the synthetic jet at which this effect is achieved is shown, a thorough explanation of the physical mechanism behind it has not been provided. In order to do this, the analysis of the flow field in a plane still normal to the plate, but spanwise-oriented can be of great relevance, as the effects on the velocity field due to the two sets of vortices can be better analysed as well as the mechanism of their interaction. It is recommended that Stereo-PIV is employed, so as to measure all the three components of velocity, which can provide more information on the flow field.
Also the case of unsteady streamwise vortices can be studied, for example using a suction hole at the wall, which can be operated intermittently.

The case of turbulent boundary layer forcing with a synthetic jet array is analysed in this configuration: a synthetic jet orifice diameter of 5 mm and spacing of the orifices in the array of 9 mm. The diameter and the spacing can be varied in a certain range and this could provide better or worse effects in terms of overall skin friction drag reduction. As mentioned above, even the modification of a single design parameter, such as an increase in the spacing, could provide better results because it would probably reduce the interaction of hairpin vortices produced by adjacent synthetic jets. Since an experimental investigation of all cases would be too time-consuming and expensive, it is suggested that an investigation is carried out using numerical simulations

(using Large Eddy Simulations or Direct Numerical Simulations) to select the configurations which yield an overall drag reduction. Once these are found, an experimental investigation with Stereo-PIV should provide a validation of the numerical results and a better understanding of the flow physics of drag reduction.
It has been shown that the more the hairpin vortices remain in the near-wall region as they travel downstream of the synthetic jet orifice, the higher the skin friction drag reduction. Therefore, it is believed that the use of inclined and skewed synthetic jets could provide better results in terms of drag reduction than normal synthetic jets, because for the same value of VR the hairpin vortices generated by inclined and skewed synthetic jets tend to remain in the near-wall region for a larger distance downstream.
The mechanism of skin friction drag reduction can also be explored in terms of how the fluctuations of velocity are modified by the forcing. For this purpose experimental investigations with Constant-Temperature Anemometry, which yields a higher frequency response than Particle Image Velocimetry, are recommended. This could provide more detailed information, for example, on a possible reduction of velocity fluctuations at the edge of the buffer layer and on a possible reduction of the busting frequency.

Control results can be finally improved by using a reactive flow control method. A feed-forward predictor design was just outlined in this thesis. Given these results, a simple feed-forward control system could initially be built using a Liquid Crystal Thermography rig. This would give more flexibility in choosing the location of the sensors and of the control points, and possibly achieve best results in terms of drag reduction. Liquid Crystal Thermography can also immediately show whether and how the streaky pattern at the wall is modified by the control. Finally, based on these results a feed-forward control system can be be realised with a certain number of wall hot-film sensors.

The application of synthetic jets for turbulent drag reduction is a challenging task. However, this study has revealed the potential of the control method and has given some directions for future work.

Bibliography

[1] R.J. Adrian, C.D. Meinhart, and C.D. Tomkins. Vortex organization in the outer region of the turbulent boundary layer. *Journal of Fluid Mechanics*, 422:1–54, 2000.

[2] Ronald J. Adrian. Hairpin vortex organization in wall turbulencea). *Physics of Fluids (1994-present)*, 19(4):041301, 2007.

[3] Giancarlo Alfonsi. Coherent structures of turbulence: methods of eduction and results. *Applied Mechanics Reviews*, 59(6):307–323, 2006.

[4] P. Henrik Alfredsson and Arne V. Johansson. On the detection of turbulence-generating events. *Journal of Fluid Mechanics*, 139:325–345, 1984.

[5] Md. Shaukat Ali, Andallib Tariq, and B.K. Gandhi. Flow and heat transfer investigation behind trapezoidal rib using piv and lct measurements. *Experiments in fluids*, 54(5):1–15, 2013.

[6] Keith Amonlirdviman and Kenneth S. Breuer. Linear predictive filtering in a numerically simulated turbulent flow. *Physics of Fluids (1994-present)*, 12(12):3221–3228, 2000.

[7] J.B. Anders. Outer-layer manipulators for turbulent drag reduction. *Viscous Drag Reduction in Boundary Layers*, 123:263–284, 1990.

[8] Green Aviation. A better way to treat the planet. *National Aeronautics and Space Administration, NF-2010-07-500-HQ*, 2010.

[9] R.S. Azad and S. Burhanuddin. Measurements of some features of turbulence in wall-proximity. *Experiments in Fluids*, 1(3):149–160, 1983.

[10] P.R. Bandyopadhyay. Reviewmean flow in turbulent boundary layers disturbed to alter skin friction. *Journal of fluids engineering*, 108(2):127–140, 1986.

[11] G.K. Batchelor, H.K. Moffatt, and M.G. Worster. Perspectives in fluid dynamics. *Perspectives in Fluid Dynamics, Edited by GK Batchelor and HK Moffatt and MG Worster, pp. 644. ISBN 0521531691. Cambridge, UK: Cambridge University Press, December 2002.*, 1, 2002.

[12] James W. Baughn. Liquid crystal methods for studying turbulent heat transfer. *International Journal of Heat and Fluid Flow*, 16(5):365–375, 1995.

[13] J.W. Baughn and Xiaojun Yan. Liquid crystal methods in experimental heat transfer. *Proc. 32nd Heat Transfer and Fluid. California: Mechanics Institute Sacramento*, pages 15–40, 1991.

[14] Andrew Belmonte, Brian Martin, and Walter I. Goldburg. Experimental study of taylors hypothesis in a turbulent soap film. *Physics of Fluids (1994-present)*, 12(4):835–845, 2000.

[15] Theodore L. Bergman, Frank P. Incropera, and Adrienne S. Lavine. *Fundamentals of heat and mass transfer*. John Wiley & Sons, 2011.

[16] Neil S. Berman. Drag reduction by polymers. *Annual Review of Fluid Mechanics*, 10(1):47–64, 1978.

[17] R.F. Blackwelder and J.H. Haritonidis. Scaling of the bursting frequency in turbulent boundary layers. *Journal of Fluid Mechanics*, 132:87–103, 1983.

[18] A. Boomsma, S. Bhattacharya, D. Troolin, P. Vlachos, and S. Pothos. Piv uncertainty: computational and experimental evaluation of uncertainty methods. In *Proceedings, 11th International Symposium on Particle Image Velocimetry*, 2015.

[19] Kenneth S. Breuer and Kevin Wu. Models for adaptive feedforward control of turbulence. In *IUTAM Symposium on Flow Control and MEMS*, pages 219–227. Springer, 2008.

[20] C. Brossard, J.C. Monnier, P. Barricau, F.X. Vandernoot, Y. Le Sant, F. Champagnat, and G.Le. Besnerais. Principles and applications of particle image velocimetry. *Optical Diagnostics of Flows, ONERA Aerospace Lab Journal*, 2009.

[21] Hans H. Bruun. Hot-wire anemometry: principles and signal analysis. *Measurement Science and Technology*, 7(10):null, 1996.

[22] Guido Buresti. *Elements of fluid dynamics*. World Scientific, 2012.

[23] Dennis M. Bushnell. Turbulent drag reduction for external flows. *AIAA paper*, 227:1983, 1983.

[24] D.M. Bushnell. Aircraft drag reductiona review. *Proceedings of the Institution of Mechanical Engineers, Part G: Journal of Aerospace Engineering*, 217(1):1–18, 2003.

[25] Flavio Cannavó. Sensitivity analysis for volcanic source modeling quality assessment and model selection. *Computers & geosciences*, 44:52–59, 2012.

[26] Brian J. Cantwell. Organized motion in turbulent flow. *Annual review of fluid mechanics*, 13(1):457–515, 1981.

[27] Hnery A. Carlson and John L. Lumley. Active control in the turbulent wall layer of a minimal flow unit. *Journal of Fluid Mechanics*, 329:341–372, 1996.

[28] Haecheon Choi, Parviz Moin, and John Kim. Active turbulence control for drag reduction in wall-bounded flows. *Journal of Fluid Mechanics*, 262:75–110, 1994.

[29] Kwing-So Choi. Near-wall structure of a turbulent boundary layer with riblets. *Journal of fluid mechanics*, 208:417–458, 1989.

[30] Kwing-So Choi. Drag reduction. *Flow control: Fundamentals, Advances and Applications, VKI Lecture Series*, 2009.

[31] Kwing-So Choi, Jean-Robert DeBisschop, and Brian R. Clayton. Turbulent boundary-layer control by means of spanwise-wall oscillation. *AIAA journal*, 36(7):1157–1163, 1998.

[32] Kwing-So Choi, Timothy Jukes, and Richard Whalley. Turbulent boundary-layer control with plasma actuators. *Philosophical Transactions of the Royal Society of London A: Mathematical, Physical and Engineering Sciences*, 369(1940):1443–1458, 2011.

[33] Kurt J. Colella and William L. Keith. Measurements and scaling of wall shear stress fluctuations. *Experiments in fluids*, 34(2):253–260, 2003.

[34] European Commission et al. Flightpath 2050. europes vision for aviation. *Report of the High Level Group on Aviation Research, Publications Office of the European Union, Luxembourg*, 2011.

[35] Peter A. Davidson, Yukio Kaneda, and Katepalli R. Sreenivasan. *Ten Chapters in Turbulence*. Cambridge University Press, 2012.

[36] Juan del Álamo, Javier Jimenez, Paulo Zandonade, and Robert D. Moser. Self-similar vortex clusters in the turbulent logarithmic region. *Journal of Fluid Mechanics*, 561:329–358, 2006.

[37] Yiqing Du, V. Symeonidis, and G.E. Karniadakis. Drag reduction in wall-bounded turbulence via a transverse travelling wave. *Journal of Fluid Mechanics*, 457:1–34, 2002.

[38] A.J. Favre, J.J. Gaviglio, and R. Dumas. Space-time double correlations and spectra in a turbulent boundary layer. *Journal of Fluid Mechanics*, 2(04):313–342, 1957.

[39] V. Fink, A. Güttler, and B. Frohnapfel. Experimental and numerical investigation of riblets in a fully developed turbulent channel flow. *European Drag Reduction and Flow Control Meeting 2015 Cambridge*, 2015.

[40] Uriel Frisch. *Turbulence: the legacy of AN Kolmogorov*. Cambridge university press, 1995.

[41] Koji Fukagata, Kaoru Iwamoto, and Nobuhide Kasagi. Contribution of reynolds stress distribution to the skin friction in wall-bounded flows. *Physics of Fluids (1994-present)*, 14(11):L73–L76, 2002.

[42] Koji Fukagata, Nobuhide Kasagi, and Petros Koumoutsakos. A theoretical prediction of friction drag reduction in turbulent flow by superhydrophobic surfaces. *Physics of Fluids (1994-present)*, 18(5):051703, 2006.

[43] Mohamed Gad-el Hak. Modern developments in flow control. *Applied Mechanics Reviews*, 49(7):365–379, 1996.

[44] Mohamed Gad-el Hak and Ron F. Blackwelder. Selective suction for controlling bursting events in a boundary layer. *AIAA journal*, 27(3):308–314, 1989.

[45] Mohamed Gad-el Hak, Andrew Pollard, and Jean-Paul Bonnet. *Flow control: fundamentals and practices*, volume 53. Springer Science & Business Media, 2003.

[46] R. Garcıa-Mayoral, J. Seo, and A. Mani. Dynamics of gas-liquid interfaces in turbulent flows over superhydrophobic surfaces. *Proc. of the 2014 Summer Program of the CTR*, pages 295–304, 2014.

[47] Ricardo García-Mayoral and Javier Jiménez. Drag reduction by riblets. *Philosophical Transactions of the Royal Society of London A: Mathematical, Physical and Engineering Sciences*, 369(1940):1412–1427, 2011.

[48] Patrick Gaydecki. *Foundations of Digital Signal Processing: theory, algorithms and hardware design*, volume 15. Iet, 2004.

[49] Ari Glezer and Michael Amitay. Synthetic jets. *Annual Review of Fluid Mechanics*, 34(1):503–529, 2002.

[50] Salil Gogte, Peter Vorobieff, Richard Truesdell, Andrea Mammoli, Frank van Swol, Pratik Shah, and C. Jeffrey Brinker. Effective slip on textured superhydrophobic surfaces. *Physics of fluids*, 17(5):51701–51701, 2005.

[51] Zambri Harun, Jason P. Monty, and Ivan Marusic. The structure of zero, favorable and adverse pressure gradient turbulent boundary layers. In *TSFP DIGITAL LIBRARY ONLINE*. Begel House Inc., 2011.

[52] Monson H. Hayes. *Statistical digital signal processing and modeling*. John Wiley & Sons, 2009.

[53] D. Hooshmand, R. Youngs, J.M. Wallace, and J.L. Balint. An experimental study of changes in the structure of a turbulent boundary layer due to surface geometry changes. *AIAA paper*, (83-0230), 1983.

[54] H. Huang, D. Dabiri, and M. Gharib. On errors of digital particle image velocimetry. *Measurement Science and Technology*, 8(12):1427, 1997.

[55] Julian C.R. Hunt and David J. Carruthers. Rapid distortion theory and the problems of turbulence. *Journal of Fluid Mechanics*, 212:497–532, 1990.

[56] Abul Khair Muhammad Fazle Hussain and William C. Reynolds. The mechanics of an organized wave in turbulent shear flow. *Journal of Fluid Mechanics*, 41(02):241–258, 1970.

[57] Nicholas Hutchins and Kwing-So Choi. Accurate measurements of local skin friction coefficient using hot-wire anemometry. *Progress in Aerospace Sciences*, 38(4):421–446, 2002.

[58] Nicholas Hutchins and Kwing-So Choi. Towards a greater understanding of turbulent skin-friction reduction. In *ASME 2002 Joint US-European Fluids Engineering Division Conference*, pages 1449–1454. American Society of Mechanical Engineers, 2002.

[59] Nicholas Hutchins and Ivan Marusic. Evidence of very long meandering features in the logarithmic region of turbulent boundary layers. *Journal of Fluid Mechanics*, 579:1–28, 2007.

[60] Peter T. Ireland, Andrew J. Neely, David R.H. Gillespie, and Andrew J. Robertson. Turbulent heat transfer measurements using liquid crystals. *International Journal of Heat and Fluid Flow*, 20(4):355–367, 1999.

[61] P.T. Ireland and T.V. Jones. Liquid crystal measurements of heat transfer and surface shear stress. *Measurement Science and Technology*, 11(7):969, 2000.

[62] Yoichiro Iritani, Nobuhide Kasagi, and Masaru Hirata. Heat transfer mechanism and associated turbulence structure in the near-wall region of a turbulent boundary layer. In *Turbulent Shear Flows 4*, pages 223–234. Springer, 1985.

[63] M. Jabbal, S.C. Liddle, and W.J. Crowther. Active flow control systems architectures for civil transport aircraft. *Journal of Aircraft*, 47(6):1966–1981, 2010.

[64] Mark Jabbal. *Understanding the behaviour of synthetic jets in a boundary layer for flow separation control*. PhD thesis, The University of Manchester, 2008.

[65] Mark Jabbal and Shan Zhong. Particle image velocimetry measurements of the interaction of synthetic jets with a zero-pressure gradient laminar boundary layer. *Physics of Fluids (1994-present)*, 22(6):063603, 2010.

[66] Mark Jabbal and Shang Zhong. The near wall effect of synthetic jets in a boundary layer. *International Journal of Heat and Fluid Flow*, 29(1):119–130, 2008.

[67] Stuart A. Jacobson and William C. Reynolds. Active control of streamwise vortices and streaks in boundary layers. *Journal of Fluid Mechanics*, 360:179–211, 1998.

[68] Sejeong Jeon, Haecheon Choi, Jung Yul Yoo, and Parviz Moin. Space–time characteristics of the wall shear-stress fluctuations in a low-reynolds-number channel flow. *Physics of Fluids (1994-present)*, 11(10):3084–3094, 1999.

[69] Javier Jiménez. Cascades in wall-bounded turbulence. *Annual Review of Fluid Mechanics*, 44(1):27, 2011.

[70] Javier Jiménez and Alfredo Pinelli. The autonomous cycle of near-wall turbulence. *Journal of Fluid Mechanics*, 389:335–359, 1999.

[71] P.T. Jones, T.V. Ireland and Z. Wang. Liquid crystal heat transfer measurements. *VKI LS monographs: Measurement Techniques II*, 1995.

[72] T.V. Jones. The use of liquid crystals in aerodynamic and heat transfer testing. *Transport Phenomena in Heat and Mass Transfer*, 2:1242–1273, 1992.

[73] W.J. Jung, N. Mangiavacchi, and R. Akhavan. Suppression of turbulence in wall-bounded flows by high-frequency spanwise oscillations. *Physics of Fluids A: Fluid Dynamics (1989-1993)*, 4(8):1605–1607, 1992.

[74] Yong-Duck Kang, Kwing-So Choi, and Ho-Hwan Chun. Direct intervention of hairpin structures for turbulent boundary-layer control. *Physics of Fluids (1994-present)*, 20(10):101517, 2008.

[75] N. Kasagi, R.J. Moffat, and M. Hirata. Liquid crystals, handbook of flow visualization, chapter 8, ed. *WJ Yang, Hemisphere Pubi. corp*, 1989.

[76] Anthony Kendall and Manoochehr Koochesfahani. A method for estimating wall friction in turbulent wall-bounded flows. *Experiments in Fluids*, 44(5):773–780, 2008.

[77] Michael Kerho and C.A. Torrance. Active reduction of skin friction drag using low-speed streak control. In *AIAA 2002-271, 40th AIAA Aerospace Sciences Meeting and Exhibit, Reno, NV*, 2002.

[78] John Kim. Control of turbulent boundary layers. *Physics of Fluids (1994-present)*, 15(5):1093–1105, 2003.

[79] John Kim. Physics and control of wall turbulence for drag reduction. *Philosophical Transactions of the Royal Society of London A: Mathematical, Physical and Engineering Sciences*, 369(1940):1396–1411, 2011.

[80] John Kim and Fazle Hussain. Propagation velocity of perturbations in turbulent channel flow. *Physics of Fluids A: Fluid Dynamics (1989-1993)*, 5(3):695–706, 1993.

[81] John Kim, Parviz Moin, and Robert Moser. Turbulence statistics in fully developed channel flow at low reynolds number. *Journal of fluid mechanics*, 177:133–166, 1987.

[82] Joseph C. Klewicki. Reynolds number dependence, scaling, and dynamics of turbulent boundary layers. *Journal of fluids engineering*, 132(9):094001, 2010.

[83] S.J. Kline, W.C. Reynolds, F.A. Schraub, and P.W. Runstadler. The structure of turbulent boundary layers. *Journal of Fluid Mechanics*, 30(04):741–773, 1967.

[84] Karsten Knobloch. Real-time prediction of flow variables in a turbulent boundary layer. Technical report, Brown University Providence, 2000.

[85] Arthur G. Kravchenko, Haecheon Choi, and Parviz Moin. On the relation of near-wall streamwise vortices to wall skin friction in turbulent boundary layers. *Physics of Fluids A: Fluid Dynamics (1989-1993)*, 5(12):3307–3309, 1993.

[86] H.H. Ku. Notes on the use of propagation of error formulas. *Journal of Research of the National Bureau of Standards*, 70(4), 1966.

[87] P.K. Kundu, I.M. Cohen, and D.R. Dowling. Fluid mechanics, 920 pp, 2012.

[88] F. Laadhari, L. Skandaji, and R. Morel. Turbulence reduction in a boundary layer by a local spanwise oscillating surface. *Physics of Fluids (1994-present)*, 6(10):3218–3220, 1994.

[89] Jeffrey C. Lagarias, James A. Reeds, Margaret H. Wright, and Paul E. Wright. Convergence properties of the nelder–mead simplex method in low dimensions. *SIAM Journal on optimization*, 9(1):112–147, 1998.

[90] M.T. Landahl. On sublayer streaks. *Journal of Fluid Mechanics*, 212:593–614, 1990.

[91] Eli Lazar, Bradley DeBlauw, Nick Glumac, Craig Dutton, and Gregory Elliott. A practical approach to piv uncertainty analysis. In *27th AIAA Aerodynamic Measurement Technology and Ground Testing Conference*, volume 28, 2010.

[92] Conrad Y. Lee and D.B. Glodstein. Dns of micro jets for turbulent boundary layer control. *AIAA paper*, 1013:2001, 2001.

[93] Camilla Ljus, Bert Johansson, and A-E Almstedt. Frequency response correction of hot-film measurements in a turbulent airflow. *Experiments in fluids*, 29(1):36–41, 2000.

[94] Thomas Lorkowski, Ruben Rathnasingham, and Kenneth S. Breuer. *Small-scale forcing of a turbulent boundary layer*. PhD thesis, Fluid Dynamics Research Laboratory, Department of Aeronautics and Astronautics, Massachusetts Institute of Technology, 1997.

[95] J. L. Lumley. Drag reduction in turbulent flow by polymer additives. *Journal of Polymer Science: Macromolecular Reviews*, 7(1):263–290, 1973.

[96] I Marusic, R Mathis, and Nicholas Hutchins. Predictive model for wall-bounded turbulent flow. *Science*, 329(5988):193–196, 2010.

[97] Ivan Marusic, Gary J. Kunkel, and Fernando Porté-Agel. Experimental study of wall boundary conditions for large-eddy simulation. *Journal of Fluid Mechanics*, 446:309–320, 2001.

[98] Ivan Marusic, Romain Mathis, and Nicholas Hutchins. High reynolds number effects in wall turbulence. *International Journal of Heat and Fluid Flow*, 31(3):418–428, 2010.

[99] Ivan Marusic, B.J. McKeon, P.A. Monkewitz, H.M. Nagib, A.J. Smits, and K.R. Sreenivasan. Wall-bounded turbulent flows at high reynolds numbers: Recent advances and key issues. *Physics of Fluids (1994-present)*, 22(6):065103, 2010.

[100] Jean Mathieu and Julian Scott. *An introduction to turbulent flow*. Cambridge University Press, 2000.

[101] Meredith Metzger, Beverley McKeon, and Enrique Arce-Larreta. Scaling the characteristic time of the bursting process in the turbulent boundary layer. *Physica D: Nonlinear Phenomena*, 239(14):1296–1304, 2010.

[102] A.J. Musker. Explicit expression for the smooth wall velocity distribution in a turbulent boundary layer. *AIAA Journal*, 17(6):655–657, 1979.

[103] Douglas R. Neal, Andrea Sciacchitano, Barton L Smith, and Fulvio Scarano. Collaborative framework for piv uncertainty quantification: the experimental database. *Measurement Science and Technology*, 26(7):074003, 2015.

[104] V.D. Nguyen, A.M. Savill, and R.V. Westphal. Skin friction measurements following manipulation of a turbulent boundary layer. *AIAA journal*, 25(3):498–500, 1987.

[105] Jens M. Österlund, Björn Lindgren, and Arne V. Johansson. Flow structures in zero pressure-gradient turbulent boundary layers at high reynolds numbers. *European Journal of Mechanics-B/Fluids*, 22(4):379–390, 2003.

[106] Pradipta Kumar Panigrahi and Andallib Tariq. Liquid crystal heat transfer measurements in a rectangular channel with solid and slit rib. *Journal of visualization*, 6(4):407–416, 2003.

[107] Ronald L. Panton. Overview of the self-sustaining mechanisms of wall turbulence. *Progress in Aerospace Sciences*, 37(4):341–383, 2001.

[108] Jeongyoung Park and Haecheon Choi. Effects of uniform blowing or suction from a spanwise slot on a turbulent boundary layer flow. *Physics of Fluids (1994-present)*, 11(10):3095–3105, 1999.

[109] S.H. Park, I. Lee, and H.J. Sung. Effect of local forcing on a turbulent boundary layer. *Experiments in Fluids*, 31(4):384–393, 2001.

[110] Y.S. Park and H.J. Park, S.H .and Sung. Measurement of local forcing on a turbulent boundary layer using piv. *Experiments in fluids*, 34(6):697–707, 2003.

[111] Stephen B Pope. *Turbulent flows*. Cambridge university press, 2000.

[112] Maurizio Quadrio and Paolo Luchini. Integral space–time scales in turbulent wall flows. *Physics of Fluids (1994-present)*, 15(8):2219–2227, 2003.

[113] Maurizio Quadrio and Pierre Ricco. Critical assessment of turbulent drag reduction through spanwise wall oscillations. *Journal of Fluid Mechanics*, 521:251–271, 2004.

[114] Maurizio Quadrio and Pierre Ricco. The laminar generalized stokes layer and turbulent drag reduction. *Journal of Fluid Mechanics*, 667:135–157, 2011.

[115] Maurizio Quadrio, Pierre Ricco, and Claudio Viotti. Streamwise-travelling waves of spanwise wall velocity for turbulent drag reduction. *Journal of Fluid Mechanics*, 627:161–178, 2009.

[116] Markus Raffel, Christian E. Willert, Jürgen Kompenhans, et al. *Particle image velocimetry: a practical guide*. Springer, 2013.

[117] K. Narahari Rao, R. Narasimha, and MA Narayanan. The burstingphenomenon in a turbulent boundary layer. *Journal of Fluid Mechanics*, 48(02):339–352, 1971.

[118] Ruben Rathnasingham and Kenneth S. Breuer. System identification and control of a turbulent boundary layer. *Physics of Fluids (1994-present)*, 9(7):1867–1869, 1997.

[119] Ruben Rathnasingham and Kenneth S. Breuer. Active control of turbulent boundary layers. *Journal of Fluid Mechanics*, 495:209–233, 2003.

[120] Henry Rebbeck and Kwing-So Choi. A wind-tunnel experiment on real-time opposition control of turbulence. *Physics of Fluids (1994-present)*, 18(3):035103, 2006.

[121] J. Reneaux et al. Overview on drag reduction technologies for civil transport aircraft. *ONERA: Tire a Part*, 153:1–18, 2004.

[122] Pierre Ricco. Modification of near-wall turbulence due to spanwise wall oscillations. *Journal of Turbulence*, 5:20–20, 2004.

[123] Pierre Ricco and Stanislav Hahn. Turbulent drag reduction through rotating discs. *Journal of Fluid Mechanics*, 722:267–290, 2013.

[124] Pierre Ricco, Claudio Ottonelli, Yosuke Hasegawa, and Maurizio Quadrio. Changes in turbulent dissipation in a channel flow with oscillating walls. *Journal of Fluid Mechanics*, 700:77–104, 2012.

[125] Pierre Ricco and Shengli Wu. On the effects of lateral wall oscillations on a turbulent boundary layer. *Experimental thermal and fluid science*, 29(1):41–52, 2004.

[126] Stephen K. Robinson. Coherent motions in the turbulent boundary layer. *Annual Review of Fluid Mechanics*, 23(1):601–639, 1991.

[127] Jonathan P. Rothstein. Slip on superhydrophobic surfaces. *Annual Review of Fluid Mechanics*, 42:89–109, 2010.

[128] Peter W. Runstadler, Stephen Jay Kline, and William C. Reynolds. An experimental investigation of the flow structure of the turbulent boundary layer. Technical report, DTIC Document, 1963.

[129] D. Sabatino and C.R. Smith. Simultaneous velocity-surface heat transfer behavior of turbulent spots. *Experiments in fluids*, 33(1):13–21, 2002.

[130] D.R. Sabatino and C.R. Smith. Turbulent spot flow topology and mechanisms for surface heat transfer. *Journal of Fluid Mechanics*, 612:81–105, 2008.

[131] Philipp Schlatter, Ramis Örlü, Qiang Li, Geert Brethouwer, Arne V Johansson, P Henrik Alfredsson, and Dan S. Henningson. Progress in simulations of turbulent boundary layers. *TSFP-7, Ottawa, July*, 31, 2011.

[132] Herrmann Schlichting, Klaus Gersten, and Klaus Gersten. *Boundary-layer theory*. Springer Science & Business Media, 2000.

[133] W. Schoppa and F. Hussain. Coherent structure generation in near-wall turbulence. *Journal of fluid Mechanics*, 453:57–108, 2002.

[134] Wade Schoppa and Fazle Hussain. A large-scale control strategy for drag reduction in turbulent boundary layers. *Physics of Fluids (1994-present)*, 10(5):1049–1051, 1998.

[135] Andrea Sciacchitano, Douglas R. Neal, Barton L. Smith, Scott O. Warner, Pavlos P. Vlachos, Bernhard Wieneke, and Fulvio Scarano. Collaborative framework for piv uncertainty quantification: comparative assessment of methods. *Measurement Science and Technology*, 26(7):074004, 2015.

[136] Alvy Ray Smith. Color gamut transform pairs. In *ACM Siggraph Computer Graphics*, volume 12, pages 12–19. ACM, 1978.

[137] C.R. Smith, D.R. Sabatino, and T.J. Praisner. Temperature sensing with thermochromic liquid crystals. *Experiments in fluids*, 30(2):190–201, 2001.

[138] C.R. Smith and J.D. Walker. Sustaining mechanisms of turbulent boundary layers- the role of vortex development and interactions. *Self-sustaining mechanisms of wall turbulence(A 98-17710 03-34), Southampton, United Kingdom, Computational Mechanics Publications(Advances in Fluid Mechanics Series.*, 15:13–47, 1997.

[139] Alexander J. Smits, Beverley J. McKeon, and Ivan Marusic. High-reynolds number wall turbulence. *Annual Review of Fluid Mechanics*, 43:353–375, 2011.

[140] Il'ya Meerovich Sobol'. On sensitivity estimation for nonlinear mathematical models. *Matematicheskoe Modelirovanie*, 2(1):112–118, 1990.

[141] Philippe R. Spalart. Direct simulation of a turbulent boundary layer up to r θ= 1410. *Journal of Fluid Mechanics*, 187:61–98, 1988.

[142] D.B. Spalding. A single formula for the law of the wall. *Journal of Applied Mechanics*, 28(3):455–458, 1961.

[143] Emanuele Spinosa, Shanying Zhang, and Shan Zhong. Control of near-wall coherent structures in a turbulent boundary layer using synthetic jets. *European Drag Reduction and Flow Control Meeting, Cambridge*, 2015.

[144] Emanuele Spinosa and Shan Zhong. Control of streamwise vortices using synthetic jets. *4th International Conference on Experimental Fluid mechanics, Beijing (China)*, 2014.

[145] Emanuele Spinosa and Shan Zhong. Synthetic jet actuator experiments for turbulence control. *DIPART 2014 (The Airbus Flight Physics Distributed R&T Partnership) Bristol (UK)*, 2014.

[146] Emanuele Spinosa and Shan Zhong. Application of liquid crystal thermography for the investigation of the near-wall coherent structures in a turbulent boundary layer. *Sensors and Actuators A: Physical*, 233:207–216, 2015.

[147] Michel Stanislas, Laurent Perret, and Jean-Marc Foucaut. Vortical structures in the turbulent boundary layer: a possible route to a universal representation. *Journal of Fluid Mechanics*, 602:327–382, 2008.

[148] F. Sedat Tardu and C. Thanh Pham. Response of wall hot-film gages with longitudinal diffusion and heat conduction to the substrate. *Journal of heat transfer*, 127(8):812–819, 2005.

[149] Sedat F. Tardu. Active control of near-wall turbulence by local oscillating blowing. *Journal of Fluid Mechanics*, 439:217–253, 2001.

[150] Andallib Tariq, P.K. Panigrahi, and K. Muralidhar. Flow and heat transfer in the wake of a surface-mounted rib with a slit. *Experiments in fluids*, 37(5):701–719, 2004.

[151] Geoffrey Ingram Taylor. The spectrum of turbulence. In *Proceedings of the Royal Society of London A: Mathematical, Physical and Engineering Sciences*, volume 164, pages 476–490. The Royal Society, 1938.

[152] John R. Taylor and E.R. Cohen. An introduction to error analysis: the study of uncertainties in physical measurements. *Measurement Science and Technology*, 9(6):1015, 1998.

[153] Cameron Tropea, Alexander L. Yarin, and John F. Foss. *Springer handbook of experimental fluid mechanics*, volume 1. Springer Science & Business Media, 2007.

[154] Preetinder S. Virk. Drag reduction fundamentals. *AIChE Journal*, 21(4):625–656, 1975.

[155] Fabian Waleffe. On a self-sustaining process in shear flows. *Physics of Fluids (1994-present)*, 9(4):883–900, 1997.

[156] James M. Wallace. On the structure of bounded turbulent shear flow: a personal view. *Developments in theoretical and applied mechanics*, 11:509–521, 1982.

[157] John G. Webster and Halit Eren. *Measurement, Instrumentation, and Sensors Handbook: Spatial, Mechanical, Thermal, and Radiation Measurement*, volume 1. CRC press, 2014.

[158] Xin Wen and Hui Tang. On hairpin vortices induced by circular synthetic jets in laminar and turbulent boundary layers. *Computers & Fluids*, 95:1–18, 2014.

[159] Frank M White and Isla Corfield. *Viscous fluid flow*, volume 3. McGraw-Hill New York, 2006.

[160] W.W. Willmarth and S.S. Lu. Structure of the reynolds stress near the wall. *Journal of Fluid Mechanics*, 55(01):65–92, 1972.

[161] Daniel J Wise and Pierre Ricco. Turbulent drag reduction through oscillating discs. *Journal of Fluid Mechanics*, 746:536–564, 2014.

[162] W.W. Willmarthand C.W. Wooldridge. Measurements of the fluctuating pressure at the wall beneath a thick turbulent boundary layer. *J. Fluid Mech*, 14:187–210, 1962.

[163] Peng Xu and Kwing-So Choi. Boundary layer control for drag reduction by lorentz forcing. In *IUTAM Symposium on Flow Control and MEMS*, pages 259–265. Springer, 2008.

[164] Takashi Yoshino, Yuji Suzuki, and Nobuhide Kasagi. Drag reduction of turbulence air channel flow with distributed micro sensors and actuators. *Journal of Fluid Science and Technology*, 3(1):137–148, 2008.

[165] Shanying Zhang and Shan Zhong. Experimental investigation of flow separation control using an array of synthetic jets. *AIAA journal*, 48(3):611–623, 2010.

[166] Shanying Zhang and Shan Zhong. Turbulent flow separation control over a two-dimensional ramp using synthetic jets. *AIAA journal*, 49(12):2637–2649, 2011.

[167] S. Zhong, C. Kittichaikan, H.P. Hodson, and P.T. Ireland. A study of unsteady wake-induced boundary-layer transition with thermochromic liquid crystals. *Proceedings of the Institution of Mechanical Engineers, Part G: Journal of Aerospace Engineering*, 213(3):163–171, 1999.

[168] S. Zhong, C. Kittichaikan, H.P. Hodson, and P.T. Ireland. Visualisation of turbulent spots under the influence of adverse pressure gradients. *Experiments in fluids*, 28(5):385–393, 2000.

[169] S. Zhong, F. Millet, and N.J. Wood. The behaviour of circular synthetic jets in a laminar boundary layer. *Aeronautical Journal*, 109(1100):461–470, 2005.

[170] Shan Zhong, Mark Jabbal, Hui Tang, Luis Garcillan, Fushui Guo, Norman Wood, and Clyde Warsop. Towards the design of synthetic-jet actuators for full-scale flight conditions. *Flow, turbulence and combustion*, 78(3-4):283–307, 2007.

[171] Shan Zhong and Shanying Zhang. Further examination of the mechanism of round synthetic jets in delaying turbulent flow separation. *Flow, turbulence and combustion*, 91(1):177–208, 2013.

[172] Jue Zhou and Shan Zhong. Numerical simulation of the interaction of a circular synthetic jet with a boundary layer. *Computers & Fluids*, 38(2):393–405, 2009.

[173] Jue Zhou and Shan Zhong. Numerical simulations of flow separation control using an array of synthetic jets. *KATNet conference on Key Aerodynamic Technologies, Bremen, Germany*, 2009.

[174] Jue Zhou and Shan Zhong. Coherent structures produced by the interaction between synthetic jets and a laminar boundary layer and their surface shear stress patterns. *Computers & Fluids*, 39(8):1296–1313, 2010.